“Application of acousto-optical interactions in crystals to performing the spectrum analysis of radio-signals and shaping the multi-wave coupled states”

by

Sandra Eloísa Balderas Mata

Thesis submitted in partial fulfilment of the requirements for the PhD. degree in Optics in the National Institute for Astrophysics, Optics, and Electronics (INAOE).

Supervised by:

Dr. Alexander S. Shcherbakov

National Institute for Astrophysics, Optics, and Electronics

Sta. María Tonantzintla, Puebla.

August 2008.

To my parents

Rosa Ma. Mata H. and Federico Balderas M.

INDEX

Acknowledgements I

Statements II

CHAPTER 1

Introduction

1.1 Introduction: Historical survey 1

1.2 Propagation of plane polarized optical waves in crystalline materials 3

1.2.1 Electromagnetic waves in an anisotropic medium 3

1.2.2 Polarization of light waves in anisotropic medium 5

1.3 Propagation of polarized elastic waves through crystalline material 9

1.3.1 Elasticity 9

1.3.2 Propagation of plane acoustic waves in a non-piezoelectric medium 12

1.4 General explanation about acousto-optic effect 14

1.4.1 Acousto-optic effect 15

1.4.2 Thick grating model: Bragg acousto-optic interaction regime 16

1.4.3 Particle picture of acousto-optic interactions 20

1.4.4 Collinear acousto-optic interaction 25

1.5 Acousto-optical coupled states 26

1.5.1 Collinear acousto-optic coupled states 26

1.5.2 Three-wave non-collinear acousto-optic weakly-coupled states 28

1.5.3 Four-wave non-collinear acousto-optic weakly coupled states 29

1.6 Spectrum analyzers for radio-signals 31

1.6.1 Acousto-optical spectrum analyzers 31

1.6.2 Bank of filters vs. acousto-optical spectrum analyzers 33

References 35

CHAPTER 2

Acousto-optical interaction in TeO_2 crystal

2.1 Introduction 40

2.2 Analytical model for a multi-fold Bragg acousto-optical interaction 40

2.3 General approach to the analysis of acousto-optical interaction 43

2.4 A multi-fold Bragg acousto-optical interaction in anisotropic media 46

2.5 A two phonon acousto-optical interaction; the case of low efficiency 49

2.6 A two-fold light scattering ; bandwidth of a two-phonon interaction 51

2.7 A three phonon acousto-optical interaction 53

2.8 A three-fold light scattering; a simplified estimation for the bandwidth of a three-phonon interaction in a tellurium dioxide crystal 56

2.9 Optical activity in a tellurium dioxide crystal 58

2.10 Ellipticity of the polarization in a tellurium dioxide crystal 62

2.11 Photo-elastic effect in a tellurium dioxide crystal 64

2.12 Resolution of the acousto-optical modulators made of TeO_2 crystals 70

2.13 Estimations and experimental results 72

2.14 Conclusions 77

References 78

Chapter 3

Schematic arrangement of an acousto-optical spectrum analyzer and its potential performance data

3.1 Introduction 80

3.2 Schematic arrangement of an acousto-optical spectrum analyzer 80

3.2.1 Beam shaper: Beam expanding factor 81

3.2.2 Transmittance of a multi-prism beam shaper 85

3.2.3 An ideal thick lens as a Fourier transformer 90
3.3 Potential performance data of acousto-optical spectrum analyzer 95
3.3.1 Estimating the number of resolvable elements (spots) :
one-phonon light scattering regime 95
3.3.2 Estimating the number of resolvable elements (spots) :
two-phonon light scattering regime 100
3.3.3 The transfer function inherent in acousto-optical cell operating
in a two-phonon light scattering regime 103
3.3.4 Effect of acoustic attenuation along the aperture
of acousto-optical modulator 107
3.3.5 Gaussian apodization of the incoming light field distribution along
the acousto-optical cell aperture 112
3.3.6 Peculiarities of the lobe distributions in the Fourier transform plane 114
3.4 Conclusions 119
References 120

CHAPTER 4

Multi-wave acousto-optical coupled states

4.1 Introduction 122
4.2 Three-wave dissipative collinear weakly acousto-optical coupled states 122
4.2.1 General consideration of a three-wave collinear interaction
with the phase mismatches and the linear non-optical losses 123
4.2.2 The quasi-stationary background-free continuous-wave regime;
originating the localization condition 125
4.2.3 The quasi-stationary continuous-wave regime with $\Gamma \neq \mathbf{0}$;
appearing a background 132
4.2.4 Non-stationary regime of the pulsed non-optical wave and localizing
multi-pulse dissipative three –wave weakly coupled states 136

4.2.5 Preliminary estimations 139
4.2.6 Experiment with multi-pulse dissipative acousto-optical coupled states in a crystal with square-law nonlinearity and linear acoustic losses 142
4.3 Three-wave dissipative collinear strongly coupled acousto-optical states 145
4.3.1 A strong collinear co-directional acousto-optical interaction in presence of the linear acoustic losses 146
4.3.2 The real-valued evolution equations 150
4.3.3 Analysis for the light wave amplitude A_0 153
4.3.4 Analysis for the light wave amplitude A_1 156
4.3.5 Analysis for the acoustic wave amplitude U_0 159
4.4 Five-wave non-collinear acousto-optical coupled states 161
4.4.1 Originating five-wave Bragg non-collinear weakly coupled acousto-optical states 162
4.4.2 Five-wave non-collinear weakly coupled acousto-optical states in a TeO_2 crystal 166
4.4.3 Experimental data 168
4.5 Conclusions 170
References 171

General conclusions 174
Figure index 175
Table index 181

Acknowledgements

First of all, I want to thank God to letting me be in this very place and meet such a valuable people to me. Also, I want to thank my parents; Federico Balderas and Rosa Maria Mata; for their support, advice, and their love that they have been given me my whole life. To my sister and my brother, they have always been there for me and they make me want to become a better person every day. Thanks to be at any moment.

I want to thank my advisor, Dr. Alexander Shcherbakov for his help in the development of this thesis with his academic and personal advices, for his dedication to this work to improve it as much as possible. Also, for his enthusiasm during the time when the results were not the ones we expected to be. Thanks to all this, I did finish my PhD almost on time.

Thanks to my PhD examiners; Dr. Juan Castillo, Dr. Ruben Ramos, Dra. Svetlana Mansurova, Dr. Paco Renero, Dr. Gabriel Niconoff, they didn't just make remarks to improve the thesis but also because of their support and advice.

I also want to thank my friends and colleagues from which I have learned many things. Specially, those who were supporting me direct or indirectly in the process of this project; Mary Paz, Enrique, Aldo, Raul, Mauro, Luis, Mel, Malu, Ros, Juanita, Dr. Sabino, Dr. Paco, thanks for supporting me in the hard times and advising me in many others.

At last, but not less important, I want to thank Mexican people that through CONACyT help me economically to finish my PhD studies.

Statements

It is feasible to utilize a two-phonon as well as a three-phonon acousto-optical interaction for improving the frequency resolution of acousto-optic spectrum analyzers.

The transfer function can be formulated in analytical form for a two-phonon light scattering.

The dynamic range of an acousto-optical spectrometer can be determined by the second or another lobe instead of the first one.

Acousto-optical coupled states exist and can be observed in a collinear interaction regime even with acoustic losses and the corresponding localization conditions can be formulated as well.

Five-wave non-collinear acousto-optical coupled states exist and can be experimentally observed under the corresponding localization conditions.

Chapter 1

1.1 Introduction: Historical survey

Acoustic waves were studied extensively in the 19th century; surface acoustic waves were first described by Lord Rayleigh in 1885 as they pertained to earthquakes [1]. The acousto-optical effect was first studied or predicted by Brillouin in 1922 [2]. Physically, this effect describes the interaction between light and sound waves. This interaction produces the diffraction of light from the medium which was first perturbed by an acoustic wave. Later, in 1932 Debye and Sears [3] and Lucas and Biquard [4] verified it experimentally when optical sources of sufficiently high coherence become available. Surprisingly, a large number of diffracted orders were observed, symmetrically spaced about the undiffracted beam. Brillouin proposed that this effect was due to rescattering of light from the acoustic beam, it was quantified until a theoretical treatment using Feynman diagrams was presented in 1980 by Korpel and Poon [5]. This established a rigorous physical description of the multiple scattering of plane waves; a similar concept had been employed in a mathematical formalism first presented in 1960 [6].

The presence of multiple diffracted orders was first explained in a classic series of papers by Raman and Nath in 1935-1936 [7], who modeled the sound column as a phase grating acting in transmission to give rise to many diffracted orders by interference. They also considered the problem of oblique and arbitrary angle of incidence of light on the acoustic beam. Debye and Sears [3], who also derived a criteria for single- and multiple-order diffraction phenomena (Debye-Sears ratio).

A more quantitative distinction between single- and multiple-order diffraction was derived by Klein and Cook [8,9]. They derived the so-called Q-parameter or the Klein-Cook parameter, which is widely used today; it is interesting to note the Q-

parameter is simply a constant multiple of the Debye-Sears ratio. Many other investigators contributed to this early work, both theoretically and experimentally, a review of this is in [10].

However, it was not until the development of the laser in 1960s that acousto-optical techniques began to receive practical consideration. The earliest contemporary, published description of a light modulator is probably from Lieben in 1962 [11]. The first acousto-optic signal processing device, a correlators using a sound cell and a transmission mask was proposed in 1961 [12]; this work helped lay the foundation for the development of modern heterodyning techniques, which were demonstrated independently by Kind et al. [13] and Whitmann, Korpel, and Lotsoff, who investigated this effect in an interesting series of papers [14-16].

Beam deflectors were studied in 1965 [17]; this work was the first to note that the angular resolution of an AO deflector is related to the time bandwidth product. By the late 1960s, with the development of suitable materials for AO devices and transducer photolithography for surface acoustic wave (SAW) designs. In particular, diffraction of single order (Known as Bragg interaction [18]) has become increasingly important for optical signal processing applications. These diffraction phenomena were first demonstrated for acoustic fields by Korpel in 1966 [19], and developed independently by other authors [20, 21].

The fundamental concept of wave vector diagrams, previously presented by Debye and Sears [3], was more formally developed [22]. A generalized coupled-mode theory was proposed for arbitrary sound and light fields [23], and the Raman-Nath theory was extended to the important case of Gaussian sound fields [24]. The acousto-optics figure of merit now known as M_2 was proposed [25]. Earliest attempts were made to predict the elasto-optic coefficients [26]; tabulated of these parameters are available today [27].

Many researchers have studied the dependence of the diffracted light intensity on the angles of incidence, interaction lengths, and acoustic power [28, 29]. For anisotropic materials the diffraction efficiency is dependent on both the polarization of incident light [9] and of the acoustic wave [30]. For the case of SAW interaction, diffracted light intensity in the Bragg regime was observed to follow a sin functional dependence on the incident angle [31].

A great deal of theoretical work has been done, as reviewed [32-34]; most of the engineering applications concentrate on acousto-optic modulators and deflectors and optical spectrum analyzers [32, 33, 35, 36].

1.2 Propagation of plane polarized optical waves in crystalline materials

The electromagnetic propagation characteristics are determined by the $\mathbf{3 \times 3}$ symmetric permittivity matrix. This fact and the form of the Maxwell equations lead to a somewhat simpler form for the electromagnetic modes.

1.2.1 Electromagnetic waves in an anisotropic medium

When light travels through a crystal the birefringence or double refraction may manifest itself. Birefringence can be natural as a result from natural crystal anisotropy or can be artificial, which is produced by an electric field (electro-optic effect) or by a stress (photo-elastic effect). If the medium is isotropic the dielectric properties at optical frequencies are given by

$$\text{a)}\ \tilde{\vec{D}} = \varepsilon\, \vec{E}\ , \qquad \text{b)}\ \tilde{D}_i = \varepsilon_{ij} E_j\ , \quad (i,j = 1,2,3)\ , \tag{1.1}$$

where $\tilde{D}_i$ represents the components of the electric induction vector, E_j is the light electric field, $\varepsilon_{ij} = \varepsilon_0 \left(1 + \chi_{ij}\right)$ is the dielectric tensor of the medium, and ε_0 is

the dielectric constant in vacuum. It means that in any direction of the medium the relation between $\vec{\tilde{D}}$ and $\vec{E}$ from Eq.(1.1) holds. But this is not true for all materials; a crystal structure imposes severe constraints on the possible modes of propagation. Optical propagation in an arbitrary direction is, in general, only possible for two plane waves with the defined directions of $\vec{B}, \vec{H}, \vec{E}$, and $\vec{\tilde{D}}$.

As it can be seen from Eq.(1.1), $\vec{E}$ and $\vec{\tilde{D}}$ are not in the same direction. The convention of summation over repeated indices is observed, ε is a 3×3 symmetric matrix. The dielectric tensor is symmetric and has, in general, only six independent elements. This is assuming that the dielectric tensor ε is real.

$$\varepsilon_{ij} = \varepsilon_{ji}. \tag{1.2}$$

In the event that a lossless medium is described by a complex dielectric tensor, we have that

$$\varepsilon_{ij} = \varepsilon^*_{ji}, \tag{1.3}$$

where the asterisk denotes complex conjugate. Thus, the dielectric constant and refractive indexes both are complex in general, and one have only six independent elements. One can always find a coordinate system in, which the real system dielectric tensor is diagonal. Thus, one may redefine our coordinate system such that the constitutive relation simplifies to

$$\begin{bmatrix} \tilde{D}_1 \\ \tilde{D}_2 \\ \tilde{D}_3 \end{bmatrix} = \begin{bmatrix} \varepsilon_{11} & 0 & 0 \\ 0 & \varepsilon_{22} & 0 \\ 0 & 0 & \varepsilon_{33} \end{bmatrix} \cdot \begin{bmatrix} E_1 \\ E_2 \\ E_3 \end{bmatrix}. \tag{1.4}$$

The coordinate axes along, which the dielectric matrix becomes diagonal are called “the principal axes”.

1.2.2 Polarization of light waves in anisotropic medium

Since the crystal is made up of a regular periodic array of atoms with certain symmetry, the induced polarization will depend, both on its magnitude and its direction, and on the direction of the applied field. So, one has

$$\mathbf{P_i = \varepsilon_0 \chi_{ij} E_j}, \tag{1.5}$$

where the capital letters denote the complex amplitudes of the corresponding time-harmonic quantities. The $\mathbf{3 \times 3}$ array of the coefficients χ_{ij} is called the electric susceptibility tensor. It is always possible to choose a coordinate system in such a way that the off-diagonal elements vanish.

In anisotropic medium, the phase velocity of light depends on its state of polarization as well as its direction of propagation. The polarization state of a plane wave may vary as it propagates through the crystal. However, for a given direction of propagation in the medium, there exist, in general, two eigen-waves with well-defined eigen-phase-velocities and polarization directions. A light wave with polarization parallel to one of these directions will remain in the same polarization state as it propagates through the anisotropic medium.

The electric induction vector $\vec{\mathbf{D}}(\vec{\mathbf{r}}, \mathbf{t})$ passing through a crystal is given by

$$\vec{\mathbf{D}}(\vec{\mathbf{r}}, \mathbf{t}) = \mathbf{D}^{(\alpha)} \mathbf{i} \vec{\mathbf{e}}_{(\alpha)} \rho \exp\left[\mathbf{i} \varphi_{(\alpha)}\right], \tag{1.6}$$

where $\mathbf{D}^{(\alpha)} \exp\left[\mathbf{i} \varphi_{(\alpha)}\right]$ are the complex amplitudes, $\mathbf{k}_{(\alpha)} = \omega \mathbf{n}_{(\alpha)} / \mathbf{c}$, and α is the number of interacting electric induction vectors. Here, ρ is the measure of ellipticity for the polarization state, so that $\rho = \mathbf{0}$ for the linear polarization and $\rho = \pm \mathbf{1}$ for the circular polarization, right or left. With its moduli one can calculate the orts of polarization and can obtain the eigen-vectors of polarization for an

arbitrary polarized light beams incident on a crystal, which must have orthogonal states of polarization.

One can assume to have a pair of the electric induction vectors, that are passing through a crystal, Eq.(1.6) yield

$$\text{a)}\ \ \vec{D}^{(1)} = D^{(1)}\left(\vec{e}_1 + i\rho\,\vec{e}_2\right)\exp\left[i\left(k_1 x_3 - \omega t + \varphi_1\right)\right],$$

$$\text{b)}\ \ \vec{D}^{(2)} = D^{(2)}\left(i\rho\,\vec{e}_1 + \vec{e}_2\right)\exp\left[i\left(k_2 x_3 - \omega t + \varphi_2\right)\right]. \qquad (1.7)$$

It follows from Eqs.(1.7) that the vectors of polarization have the form

$$\text{a)}\ \ \vec{e}_1 + i\rho\,\vec{e}_2 = \begin{pmatrix} 1 \\ i\rho \end{pmatrix}, \qquad \text{b)}\ \ i\rho\,\vec{e}_1 + \vec{e}_2 = \begin{pmatrix} i\rho \\ 1 \end{pmatrix}. \qquad (1.8)$$

Their moduli can be calculated as

$$\text{a)}\ \ \left(\vec{e}_1 - i\rho\,\vec{e}_2\right)\left(\vec{e}_1 + i\rho\,\vec{e}_2\right) = (1, -i\rho)\begin{pmatrix} 1 \\ i\rho \end{pmatrix} = 1 + \rho^2,$$

$$\text{b)}\ \ \left(-i\rho\,\vec{e}_1 + \vec{e}_2\right)\left(i\rho\,\vec{e}_1 + \vec{e}_2\right) = (-i\rho, 1)\begin{pmatrix} i\rho \\ 1 \end{pmatrix} = \rho^2 + 1. \qquad (1.9)$$

Using Eqs.(1.9), one can normalize the vectors in Eq.(1.8) by $\sqrt{1+\rho^2}$ and write the orts of polarization as

$$\text{a)}\ \ \vec{\nu}_1 = \left(1+\rho^2\right)^{-1/2}\left(\vec{e}_1 + i\rho\,\vec{e}_2\right), \qquad \text{b)}\ \vec{\nu}_2 = \left(1+\rho^2\right)^{-1/2}\left(i\rho\,\vec{e}_1 + \vec{e}_2\right). \qquad (1.10)$$

The following scalar products illustrate the mutual orthogonality for the orts of polarization

$$\vec{\nu}_1^{+}\,\vec{\nu}_2 = \left(1+\rho^2\right)^{-1}\left(\vec{e}_1 - i\rho\,\vec{e}_2\right)\left(i\rho\,\vec{e}_1 + \vec{e}_2\right) = \left(1+\rho^2\right)^{-1}\left(i\rho - i\rho\right) = 0, \qquad (1.11)$$

$$\vec{\nu}_2{}^{+}\,\vec{\nu}_1 = \left(1+\rho^2\right)^{-1}\left(-i\rho\,\vec{e}_1+\vec{e}_2\right)\left(\vec{e}_1+i\rho\,\vec{e}_2\right)=\left(1+\rho^2\right)^{-1}\left(-i\rho+i\rho\right)=0\ .$$

(1.12)

The eigen-vectors of polarization for a pair of arbitrary polarized incident light beams whose states of polarization are, nevertheless, orthogonal to each other can be found as follows. If the main axes of the corresponding orts $\vec{\sigma}_{10}$ and $\vec{\sigma}_{20}$ coincide the main axes inherent in the elliptic polarization eigen-states in a crystal as

$$\text{a)}\quad \vec{\sigma}_{10} = \left(1+\rho_i^2\right)^{-1/2}\left(\vec{e}_1+i\rho_i\,\vec{e}_2\right),$$

$$\text{b)}\quad \vec{\sigma}_{20} = \left(1+\rho_i^2\right)^{-1/2}\left(i\rho_i\,\vec{e}_1+\vec{e}_2\right), \qquad (1.13)$$

where ρ_i is the ellipticity of the incident light polarization.

When the incident light is incoming in a crystal, the orts $\vec{\sigma}_1$ and $\vec{\sigma}_2$ become to be decomposed along the eigen-state orts, see Eq.(1.11). By this it means that one has

$$\vec{\sigma}_{1,2} = a_{1,2}\cdot\vec{\nu}_1 + b_{1,2}\cdot\vec{\nu}_2 =$$

$$= a_{1,2}\cdot\left(1+\rho^2\right)^{-1/2}\left(\vec{e}_1+i\rho\,\vec{e}_2\right)+b_{1,2}\cdot\left(1+\rho^2\right)^{-1/2}\left(i\rho\,\vec{e}_1+\vec{e}_2\right).$$

(1.14)

It can be easily shown that the factors $a_{1,2}$ and $b_{1,2}$ related to the case of an elliptic polarization of the incident light beams are

$$\text{a)}\quad a_{1E} = \frac{1}{\sqrt{\left(1+\rho^2\right)\left(1+\rho_i^2\right)}}\left[\left(1+\rho_i\rho\right)\cos\phi^* - i\left(\rho_i+\rho\right)\sin\phi^*\right],$$

$$\text{b)}\quad b_{1E} = \frac{1}{\sqrt{\left(1+\rho^2\right)\left(1+\rho_i^2\right)}}\left[\left(1-\rho_i\rho\right)\sin\phi^* + i\left(\rho_i-\rho\right)\cos\phi^*\right].$$

(1.15)

$$\text{a)}\quad \mathbf{a_{2E}} = -\frac{1}{\sqrt{(1+\rho^2)(1+\rho_i^2)}}\left[(1-\rho_i\rho)\sin\phi^* + i(\rho_i-\rho)\cos\phi^*\right],$$

$$\text{b)}\quad \mathbf{b_{2E}} = \frac{1}{\sqrt{(1+\rho^2)(1+\rho_i^2)}}\left[(1+\rho_i\rho)\cos\phi^* - i(\rho_i+\rho)\sin\phi^*\right], \tag{1.16}$$

where ϕ^* is an angle of rotation of the orts $\vec{\sigma}_1$ and $\vec{\sigma}_2$ main axes.

When the incident light is linearly polarized, i.e. $\rho_i = 0$, Eqs.(1.15) and (1.16) give [19]

$$\text{a)}\ \mathbf{a_{1L}} = \frac{1}{\sqrt{1+\rho^2}}\left[\cos\phi^* - i\rho\sin\phi^*\right], \qquad \text{b)}\ \mathbf{b_{1L}} = \frac{1}{\sqrt{1+\rho^2}}\left[\sin\phi^* - i\rho\cos\phi^*\right],$$

$$\text{c)}\ \mathbf{a_{2L}} = -\frac{1}{\sqrt{1+\rho^2}}\left[\sin\phi^* + i\rho\cos\phi^*\right], \qquad \text{d)}\ \mathbf{b_{2L}} = \frac{1}{\sqrt{1+\rho^2}}\left[\cos\phi^* + i\rho\sin\phi^*\right]. \tag{1.17}$$

When the incident light is circularly polarized, i.e. $\rho_i = 1$, Eqs.(1.15) and (1.16) give

$$\text{a)}\quad \mathbf{a_{1C}} = \frac{1+\rho}{\sqrt{2}\sqrt{1+\rho^2}}\left[\cos\phi^* - i\sin\phi^*\right],$$

$$\text{b)}\quad \mathbf{b_{1C}} = \frac{1-\rho}{\sqrt{2}\sqrt{1+\rho^2}}\left[\sin\phi^* + i\cos\phi^*\right],$$

$$\text{c)}\quad \mathbf{a_{2C}} = \frac{1-\rho}{\sqrt{2}\sqrt{1+\rho^2}}\left[-\sin\phi^* + i\cos\phi^*\right],$$

$$\text{d)}\quad \mathbf{b_{2C}} = \frac{1+\rho}{\sqrt{2}\sqrt{1+\rho^2}}\left[\cos\phi^* + i\sin\phi^*\right]. \tag{1.18}$$

Thus, Eqs.(1.14 – 1.18) realize the eigen-vectors of polarization for an arbitrary polarized incident light.

In summary, propagation of light in a uniaxial crystal in general consists of an ordinary and an extraordinary waves. The electric field vector $\vec{\mathbf{E}}$ (and the induction vector $\vec{\tilde{\mathbf{D}}}$) for the ordinary wave is always perpendicular to both the crystal principal axis and the propagation vector. The phase velocity for the ordinary wave is always $\mathbf{c}/\mathbf{n_o}$, regardless of the direction of propagation. The induction vector $\vec{\tilde{\mathbf{D}}}$ of the extraordinary wave, is perpendicular to the propagation vector, as is the electric field vector $\vec{\mathbf{E}}$ of the ordinary wave. The electric field vector $\vec{\mathbf{E}}$ of the extraordinary wave, however, is in general not perpendicular to the propagation vector. It lies in the plane formed by the propagation vector and the displacement vector. The electric field vectors of these two waves are mutually orthogonal.

1.3 Propagation of elastic waves through crystalline materials

1.3.1 Elasticity

Let us consider a homogeneous solid body; in which under the influence of external forces, the distances separating the different material points in a medium become modified; it is then said that it has undergone a ‘deformation’. The strain is a response of the crystal to an influence. This influence may be a stress (elasticity) or it may be to an electric field (piezoelectricity). In both cases, the magnitudes and directions of the principal strains are determined by the magnitude and orientation of the influence, as well as by the physical properties and the symmetry of the crystal. A strain may also be caused by a temperature change. In this case, the influence does not have an orientation, and is represented by a scalar. The relationship between stresses and strains for a given

medium inside the elastic limit can differ according to the intensity of the strain. Stresses and strains are represented by second rank tensors. When the strains are weak enough for the relation between stresses and strains to be linear; i.e. within the domain of validity of Hooke's law, these two tensors are related by a tensor of rank 4 known as a stiffness tensor. One can suppose that each component of a stress is a linear and homogeneous function of all the components of the strain tensor. The set of all these relations is

$$T_{ij} = c_{ijkl}\,\gamma_{kl} \ , \tag{1.19}$$

which constitutes what is known as the generalized Hooke's law, which is an extension of the simple Hooke's law ($T = Y\,\partial u / \partial x$ with Y being Young's modulus) relating to isotropic elastic bodies. The set c_{ijkl} (stiffness) is a tensor of rank 4. The γ_{kl} (strain) and T_{ij} (stress) components can vary from one point to another; on the other hand, in elastic media considered to be homogeneous, the c_{ijkl} are independent of spatial coordinates. Like all tensors of even rank, the stiffness tensor is centrosymmetric. Furthermore, the stress matrix is symmetric; i.e.,

$$T_{ij} = T_{ji}, \qquad i \neq j \tag{1.20}$$

Because there are three of these off-diagonal terms for each of the remaining six equations, the number of independent c_{ijkl} values is further reduced by 18 for a total of 36. Thus the symmetry conditions for the stress matrix (which are valid for all materials) result in the constraint

$$c_{ijkl} = c_{jikl} \ . \tag{1.21}$$

The stiffness tensor of the stress matrix is symmetrical as regards both the i and j and the k and l suffixes, this symmetry is for the stress T tensor.

There exists an easier form to write the stress and strain tensors, this is the matrix or Voigt notation, in which the **i** and **j** suffixes are grouped into one $(\mu = 1,2,3,...,6)$; and in the case of the stiffness tensor, the **k** and **l** suffixes are abbreviated according to Table 1.

Tensor notation	**l j** or **k l**	11	22	33	23, 32	31, 13	12, 21
Matrix notation	μ or λ	1	2	3	4	5	6

Table 1. Voigt notation.

It follows from Eq.(1.21) that the number of independent components can be reduced from 81 to 36. Thus, the relationship between $\mathbf{c_{ijkl}}$ and $\mathbf{c_{\mu\lambda}}$ in a compact form is [37]

$$\mathbf{c_{ijkl} = c_{\mu\lambda}} \tag{1.22}$$

The relation between the tensor and the matrix notation for the stress tensor has the form $\mathbf{T_{ij} = T_{\mu}}$, with $\mu = 1,2,3,4,5,6$; and for the strain tensor has the form $\gamma_{kl} = \gamma_{\lambda}$, with $\lambda = 1,2,3,4,5,6$, and $2\gamma_{kl} = \gamma_{\lambda}$, with $\lambda = 4,5,6$.

Hence Eq.(1.19) may be written as

$$\left[\mathbf{T_{\mu}}\right] = \left[\mathbf{c_{\mu\lambda}}\right]\left[\gamma_{\lambda}\right] \begin{matrix}\mu=1,2,...6 \\ \lambda=1,2,...6\end{matrix} . \tag{1.23}$$

$\left[\mathbf{T_{\mu}}\right]$ and $\left[\gamma_{\lambda}\right]$ are then matrices with 6 rows and one column and $\left[\mathbf{c_{\mu\lambda}}\right]$ is a $\mathbf{6 \times 6}$ square matrix. To transform the tensors into another axes, it is necessary to go back to the tensor notation in Eq.(1.19).

1.3.2 Propagation of the plane acoustic waves in a non-piezoelectric medium

The stress and the strain tensors have been defined, and thus the physical property which relates them under conditions where the generalized Hooke's law applies Eq.(1.19). The equation of motion for material particles in an elastic medium is given by

$$\frac{\partial T_{ij}}{\partial x_j} = \rho \frac{\partial^2 u_i}{\partial t^2}. \tag{1.24}$$

By taking T_{ij} from Eq.(1.19) and inserting it into Eq.(1.24), taking into account γ_{kl} and its symmetry in k and l, yields the wave equation

$$\rho \ddot{u}_i = c_{ijkl} u_{k,lj}. \tag{1.25}$$

Thus, a set of differential equations is obtained which governs the propagation of elastic waves, i.e., acoustic waves. The solution of Eqs.(1.25) completely defines the mechanical state of the crystal.

The polarization of the acoustic modes is defined as the direction of particle displacement and they have three orthogonal polarizations. Considering a monochromatic elastic wave in a crystal with a solution of the equations of motion in the form $u_i = u_{0i} \exp\left[i\left(\vec{K}\cdot\vec{r} - \Omega t\right)\right]$, where u_{0i} are constants, the relation between the wave vector $\vec{K}$ and the frequency Ω being such that this function actually satisfies Eq.(1.26). By substituting this solution into Eq.(1.26) one may obtain [38]

$$\rho \Omega^2 u_i = \lambda_{iklm} K_k K_l u_m. \tag{1.26}$$

Then, putting $u_i = \delta_{im} u_m$, Eq.(1.26) can be rewritten as

$$\left(\rho \Omega^2 \delta_{im} - \lambda_{iklm} K_k K_l\right) u_m = 0. \tag{1.27}$$

This is a set of three homogeneous equations of the first degree for the unknowns u_x, u_y, u_z. Such equations have non-zero solutions only if the determinant of the coefficients is zero. Thus one must has

$$\left| \lambda_{iklm} K_k K_l - \rho \Omega^2 \delta_{im} \right| = 0 . \qquad (1.28)$$

The dispersion equation determines the relation between the wave frequency and the wave vector, called the dispersion relation. Equation (1.28) has three roots $\Omega^2 = \Omega_j^2 \left(\vec{K} \right)$, which are in general different; so the dispersion relation has three branches. Substituting each root into Eqs.(1.27) and solving, one can find the directions of the displacement vector $\vec{u}$ in these waves – the directions of polarization of the waves; since the Eqs.(1.27) are homogeneous, they do not determine the magnitude of $\vec{u}$, which remain arbitrary.

The directions of polarization of the three waves with the same wave vector $\vec{K}$ are mutually perpendicular. Equations (1.27) determine the principal directions of $\lambda_{iklm} K_k K_l$, which are known to be mutually perpendicular. None of these directions is, however, in general either purely longitudinal or purely transverse with respect to the direction of $\vec{K}$.

The velocity with which the energy of wave is propagated (i.e. the group velocity) is given by [38]

$$\vec{U} = \partial \Omega / \partial \vec{K} . \qquad (1.29)$$

In crystals, the direction of propagation of the wave is in general different form that of $\vec{K}$. Only certain exceptional directions (the symmetry axes of the crystal) can be those of both $\vec{K}$ and $\vec{U}$. It is seen from the dispersion equation that, in a crystal, Ω is a first-order homogeneous function of the components of $\vec{K}$. Thus, $\vec{U}$ is a zero-order homogeneous function of K_i, K_j, K_k. In other words, the

velocity of propagation of the wave depends on its direction but not on the frequency.

If one constructs in $\vec{\mathbf{K}}$-space a surface of constant frequency, $\Omega\left(\vec{\mathbf{K}}\right) = \text{constant}$, for any branch of the dispersion relation, then the vector Eq.(1.29) is along the normal to the surface. If this surface is everywhere convex, a definite direction of $\vec{\mathbf{U}}$ corresponds to each direction of $\vec{\mathbf{K}}$, and vice versa. If, however, the constant-frequency surface is not everywhere convex, there is a gain one direction of $\vec{\mathbf{U}}$ for each direction of $\vec{\mathbf{K}}$, but a particular direction of $\vec{\mathbf{U}}$ may occur for various directions of $\vec{\mathbf{K}}$.

1.4 General explanation about acousto-optic effect

Practically, the most important phenomenon associated with the interaction of light with elastic waves is the diffraction of light by the acoustically perturbed medium. When an acoustic wave propagates in a medium, there is an associated strain field. The strain results in a change in the index of refraction. This is referred to as the acousto-optic effect. The strain field is a periodic function of position for a plane acoustic wave. The index of refraction of the medium becomes periodically perturbed, and therefore Bragg coupling takes place. In a crystalline solid, the acoustic wave produces regions of compression and rotation in the crystal lattice, followed by regions in which the lattice is relaxed. Similar phenomena occur in liquids, where compression waves propagate through the fluid. The modulation of light by acousto-optic interaction is used in a number of applications, including light modulators, beam deflectors, signal processors, tunable filters, and spectrum analyzers.

1.4.1 Acousto-optic effect

It is well known that the variations, $\Delta\left(1/n^2\right)_{ij}$, are related to the strain components γ_{kl}, by the centrosymmetric photo-elastic tensor of fourth-rank, which has the components p_{ijkl}, so one has that

$$\Delta\left(\frac{1}{n^2}\right)_{ij} = p_{ijkl}\,\gamma_{kl}. \tag{1.30}$$

Equation (1.30) is not sufficiently general to describe all phenomena. Nelson and Lax [39,40] have shown that not only shear but also local rotation may cause changes in $(1/n^2)$ if the medium is optically birefringent. Using Table 1.1, Eq.(1.30) can be written as

$$\Delta\left(\frac{1}{n^2}\right)_{\mu} = p_{\mu\lambda}\,\gamma_{\lambda}. \tag{1.31}$$

In isotropic media, the photo-elastic tensor p can be written in components $p_{\mu\lambda}$ as

$$\begin{bmatrix} p_{11} & p_{12} & p_{12} & 0 & 0 & 0 \\ p_{12} & p_{11} & p_{12} & 0 & 0 & 0 \\ p_{12} & p_{12} & p_{11} & 0 & 0 & 0 \\ 0 & 0 & 0 & (p_{11}-p_{12})/2 & 0 & 0 \\ 0 & 0 & 0 & 0 & (p_{11}-p_{12})/2 & 0 \\ 0 & 0 & 0 & 0 & 0 & (p_{11}-p_{12})/2 \end{bmatrix}. \tag{1.32}$$

It contains only two independent non-zero components p_{11} and p_{12}.

1.4.2 Thick grating model: Bragg acousto-optic interaction regime

As it has been mentioned in Section 1.1, there are two models to explain the propagation of a light beam passing through a sound column, i.e., single- and multiple-order of diffraction; the thick and the thin grating models, respectively. In reality, the grating often intentionally is made much thicker to improve the interaction efficiency. To analyze the thick grating problem, the wave equation has to be solved

$$\nabla^2\vec{\mathbf{E}} = \left[\frac{\mathbf{n}^2(\mathbf{x},\mathbf{t})}{\mathbf{c}^2}\right]\frac{\mathbf{d}^2\vec{\mathbf{E}}}{\mathbf{dt}^2}, \tag{1.33}$$

where $\Delta\mathbf{n}(\mathbf{x},\mathbf{t}) = \Delta\mathbf{n_o}\,\mathbf{sin}(\Omega\mathbf{t} - \mathbf{Kz} + \Phi)$ is the refractive index. To solve Eq.(1.24), the electric field of the diffracted light $\vec{\mathbf{E}}$ must be in terms of the incident light $\vec{\mathbf{E}}_\mathbf{0}$. The solution can be expressed quite general by the following Fourier series expansion as

$$\vec{\mathbf{E}} = \vec{\mathbf{E}}_\mathbf{0}\sum_{-\infty}^{\infty}\mathbf{A_q}(\mathbf{z})\,\mathbf{exp}\left[\mathbf{j}\left(\omega_\mathbf{q}\mathbf{t} - \vec{\mathbf{k}}_\mathbf{q}\cdot\vec{\mathbf{r}}\right)\right], \tag{1.34}$$

where $\mathbf{A_q}(\mathbf{z})$ is the amplitude of the $\mathbf{q}-$th Fourier component of light, and the propagation vector is given as

$$\vec{\mathbf{k}}_\mathbf{q}\cdot\vec{\mathbf{r}} = \mathbf{k_1}(\mathbf{z}\cos\theta + \mathbf{x}\sin\theta) + \mathbf{qKx}\ , \tag{1.35}$$

where $\vec{\mathbf{r}}$ indicates a general propagation vector, and it was assumed that the incident light is propagating in the $\mathbf{x}-\mathbf{z}$ plane at an angle θ with respect to the optic axis. Substituting Eq.(1.34) into Eq.(1.33) yields

$$\frac{\mathbf{dA_q}}{\mathbf{dz}} - \left(\frac{\pi\Delta\mathbf{n_0}}{\lambda_\mathbf{0}}\right)\left(\mathbf{A_{q-1}} - \mathbf{A_{q+1}}\right) = \frac{\mathbf{jqQ}(\mathbf{q}-\mathbf{2}\alpha)\mathbf{A_q}}{\mathbf{2L}}, \tag{1.36}$$

where $\mathbf{Q} = \mathbf{2}\pi\mathbf{L}\lambda_\mathbf{0}/\Lambda^\mathbf{2}\mathbf{n_0}$ is the Klein-Cook parameter, $\alpha = -(\mathbf{n_0}\Lambda/\lambda_\mathbf{0})\,\mathbf{sin}\theta$,

λ_0 is the wavelength of light in vacuum, Λ is the acoustic wavelength, and **L** is the interaction length.

It was assumed that the second derivate of $\mathbf{A_q}$ with respect to **z** is negligible in comparison with other terms. Eq.(1.36) defines a set of coupled-difference differential equations that relate the amplitudes of the Fourier series expansion. These plane wave amplitudes represent the diffracted modes, and the parameter $(\pi \Delta n_0 / \lambda_0)$ is the coupling coefficient between adjacent modes. Any given mode can couple energy only into the adjacent modes. The amount of energy transfer between adjacent modes depends not only on the coupling coefficient, but also on the degree of phase matching between them. If two adjacent modes are not phase matched, then there can not be an energy transfer between them regardless of how large the coupling coefficient becomes. The degree of phase matching is given by the right-hand side of Eq.(1.36); if this part of the equation is large, i.e., **Q** is large, then adjacent diffracted modes are poorly phase matched. If the phase mismatch is large, energy will not be transferred between diffracted modes; conversely, if the phase difference between orders is small, then energy can be transferred readily between diffracted orders. This can be accomplished in two ways:

1. by taking **Q** very small and θ near zero,

2. by operating at angles of incidence such that $\alpha = \pm \frac{1}{2}$ so that **Q** can be arbitrarily large.

The first case is known as Raman-Nath interaction, whereas the second is called Bragg diffraction. This **Q** parameter was first proposed by Klein and Cook, building on earlier work of Debye and Sears. These represent the two fundamental cases of acousto-optic interaction.

In Eq.(1.36), when $\mathbf{Q >> 1}$, the zero-th order can couple only to the plus and minus orders if $\alpha = \pm \frac{1}{2}$. If this condition is satisfied, the right-hand side of Eq.(1.36) goes to zero, and one has phase matching between the zero and the ± first orders. The light cannot be transferred from the first order into the second order or higher order because there is no phase matching between these orders.

An observer in the output plane behind the acousto-optic device will see only the undiffracted beam and a single diffracted order. Because the phase grating is thick, multiples diffraction occurs at every cross-section plane throughout the interaction length of the sound column. Only the single order that is phase matched will emerge as a diffracted beam; the other orders will be cancelled by destructive interference within the device interaction length. This type of interaction can be understood by visualizing the phase grating as a series of parallel, partially reflective planes, as shown in Fig.1.1. One may consider the grating as essentially stationary during the interaction, because the velocity of the acoustic wave is much less than the velocity of light. If one consider the incident plane wave AB and the diffracted wavefront CD, the optical path difference, $\mathbf{AB - CD = x\left(\cos\theta_i - \cos\theta_r\right)}$, to have phase matching, or constructive interference, must be an integral multiple of the optical wavelength

$$\mathbf{x\left(\cos\theta_i - \cos\theta_r\right) = m\lambda_0 / n}, \tag{1.37}$$

where θ_i is the angle of the incident light, and θ_r is the angle of the light reflected from the acoustic plane wavefront, and $\mathbf{m}$ is an integer. The preceding equation may be satisfied for all values of $\mathbf{x}$ if $\theta_i = \theta_r$, this is the case of isotropic materials; if the medium is anisotropic, these two angles will not be equal in general. The diffraction from other planes parallel to the acoustic wavefront and separated by one acoustic wavelength must add constructively. Thus, the path difference (AO + OB) in Fig.1.1 must equal to λ_0 / n, this yields the relation

$$\mathbf{2\Lambda \sin\theta_B = \lambda_0 / n}, \tag{1.38}$$

where the angle of incidence θ_B is now defined as the Bragg angle. Note that this expression for the Bragg angle also results by setting $\alpha = 1/2$ in Eq.(1.36).

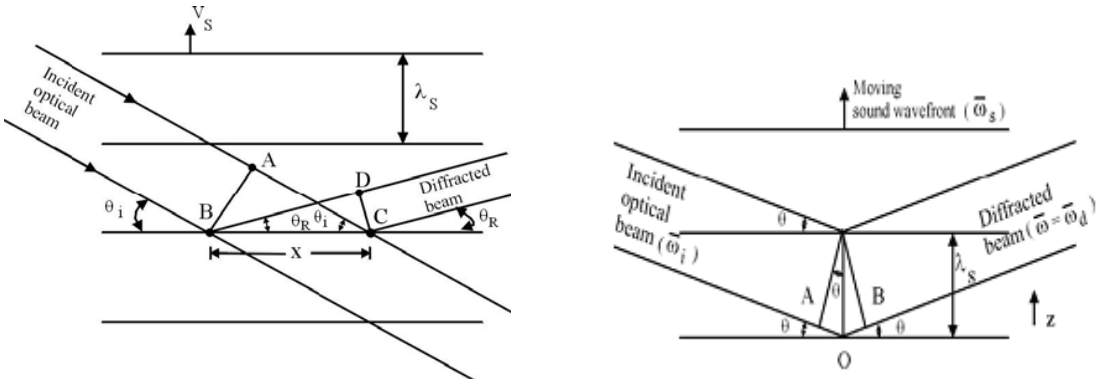

a) b)

Fig.1.1. Bragg interaction geometry.

Although Bragg interaction produces only a single diffracted order, one can choose one of two possible cases depending on the direction of incident light on the acoustic column. In Fig.1.1a, the incident light is up-shifted in frequency by the propagating acoustic wave. In Fig.1.1b, the diffracted light must be frequency down-shifted to preserve phase matching.

In optically isotropic media, the wave vector diagrams for Bragg interaction are isosceles; note that the Bragg angle condition follows directly from Fig.1.2 in the form

$$\sin\theta_B = \vec{K} / 2\vec{k}\,, \qquad (1.39)$$

where $\vec{K}$ and $\vec{k}$ are the wave vectors of the acoustic wave and the light, respectively.

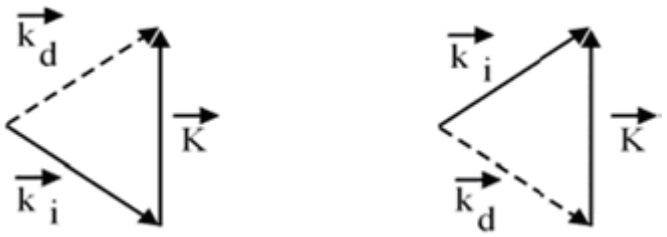

a) b)

Fig.1.2 Wave vector diagram for Bragg interaction: a) frequency upshifted, b) frequency downshifted.

One can apply these geometric results to the coupled-mode theory derived previously. From Eq.(1.36) and considering the case $\alpha = 1/2$ yields the set of equations

$$\text{a)}\quad \mathbf{dA_0/dz + (\pi \Delta n_0/\lambda_0)(A_1) = 0}$$

$$\text{b)}\quad \mathbf{dA_1/dz - (\pi \Delta n_0/\lambda_0)(A_0) = jQ(1-2\alpha)A_1}. \qquad (1.40)$$

The solution for Eqs.(1.35) with the angle of incidence exactly equal to the angle of Bragg is

$$\mathbf{I_0(L) = I_0 \cos^2(\pi \Delta n_0 L/\lambda_0 \theta)}\ , \qquad (1.41)$$

$$\mathbf{I_1(L) = I_0 \sin^2(\pi \Delta n_0 L/\lambda_0 \theta)}\ , \qquad (1.42)$$

where $\mathbf{I_0}$ is the incident optical power. Note that with no acoustic beam present, $\mathbf{\Delta n_0 = 0}$ and there is no diffracted beam; all of the optical power is transmitted in the zero order.

1.4.3 Particle picture of acousto-optic interactions

The diffraction of light by sound can be deduced if we take advantage of the dual particle-wave nature of light and sound. A light beam with a propagation vector $\vec{\mathbf{k}}_0$ and frequency ω_0 can be considered to consist of a stream of particle (photons)

with the momentum $\hbar\vec{\mathbf{k}}_{\mathbf{0}}$ and energy $\hbar\omega_{\mathbf{0}}$. The sound wave, likewise, can be thought of as made up of particle (phonons) with momentum $\hbar\vec{\mathbf{K}}$ and the energy $\hbar\Omega$.

The diffraction of light by an approaching sound beam, can be described as a sum of single collisions, each of which involves the annihilation of one incident photon at ω and one phonon and simultaneous creation of a new (diffracted) photon at a frequency $\omega_{\mathbf{1}} = \omega_{\mathbf{0}} + \Omega$, which propagates along the direction of the scattered beam. The conservation of momentum requires that the momentum $\hbar\left(\vec{\mathbf{k}}_{\mathbf{0}} + \vec{\mathbf{K}}\right)$ of the colliding particles be equal to the momentum $\hbar\vec{\mathbf{k}}_{\mathbf{1}}$ of the scattered photon, so that

$$\vec{\mathbf{k}}_{\mathbf{1}} = \vec{\mathbf{k}}_{\mathbf{0}} \pm \vec{\mathbf{K}}, \tag{1.43}$$

which is is equivalent to the Bragg condition. The conservation of energy takes the form

$$\omega_{\mathbf{1}} = \omega_{\mathbf{0}} + \Omega. \tag{1.44}$$

Thus the diffracted beam is shifted in frequency by an amount equal to the sound frequency. Since the interaction involves the annihilation of a phonon, conservation of energy implies that the shift in frequency is such that $\omega_{\mathbf{1}} > \omega_{\mathbf{0}}$ and the phonon energy is added to that of the annihilated photon to form a new photon. Or, the scattered process could be considered as one in which a new photon (diffracted photon) and a new phonon are generated while the incident photon is annihilated. In this case, the conservation of energy principle yields

$$\omega_{\mathbf{1}} = \omega_{\mathbf{0}} - \Omega. \tag{1.45}$$

The relation between the sing of the frequency change and the sound propagation direction is consistent with the Doppler-shift arguments.

The linkage between wave vectors of interacting particles can be expressed in the form of wave vector diagrams on cross-sections of the wave vector surfaces inherent in a crystal. Similar diagrams represent a graphic version of the conservation laws, see Eqs.(1.43)-(1.45), and they may be exploited for the analysis of scattering. For example, Fig.1.3a illustrates an opportunity for one-fold scattering of the incident photon by one acoustic phonon in a single-axis crystal, when the initial and ultimate states of polarization for these photons are different. Then, under certain conditions, i.e. at set angles of light incidence on the phonon beam and at fixed angular frequencies of phonons, one can observe the phenomenon of two-fold scattering of light caused by participating two acoustic phonons [41].

The main peculiarity of this phenomenon lies in conserving both the energy and the momentum for two transitions simultaneously. In their own turn, these laws determine the angular frequencies and wave vectors of all three interacting waves

$$\text{a)}\ \ \omega_{\mathbf{p}} = \omega_{\mathbf{0}} + \mathbf{p}\Omega\,, \qquad \text{b)}\ \ \vec{\mathbf{k}}_{\mathbf{p}} = \vec{\mathbf{k}}_{\mathbf{0}} + \mathbf{p}\vec{\mathbf{K}}\,, \tag{1.46}$$

where $\omega_{\mathbf{p}}$ and $\vec{\mathbf{k}}_{\mathbf{p}}\,(\mathbf{p} = \mathbf{1,2,3})$ are the angular frequencies and wave vectors of interacting photons. This fact leads to originating two orders of scattering, apart the zero-th one, each by itself satisfies the conservation laws, described by Eqs.(1.46). Figure 1.3 presents the diagram of wave vectors, dealing with the two- and three-phonon scattering of light quanta in a uniaxial crystal. Such a diagram offers rather small angles of deflection and occurs at the specific angular frequency of acoustic phonons, which can be determined as

$$\text{a)}\ \ \Omega_{\mathbf{2}} = \mathbf{2}\pi\lambda^{-\mathbf{1}}\mathbf{V}\sqrt{\left|\mathbf{n}_{\mathbf{0}}^{\mathbf{2}} - \mathbf{n}_{\mathbf{1}}^{\mathbf{2}}\right|}\,, \qquad \text{b)}\ \ \Omega_{\mathbf{3}} = \pi\lambda^{-\mathbf{1}}\mathbf{V}\sqrt{\mathbf{2}\left|\mathbf{n}_{\mathbf{0}}^{\mathbf{2}} - \mathbf{n}_{\mathbf{1}}^{\mathbf{2}}\right|}\,. \tag{1.47}$$

Here $\mathbf{n}_{\mathbf{p}}$ is the corresponding refractive index, so $\mathbf{n}_{\mathbf{0}} = \mathbf{n}_{\mathbf{2}} \neq \mathbf{n}_{\mathbf{1}}$.

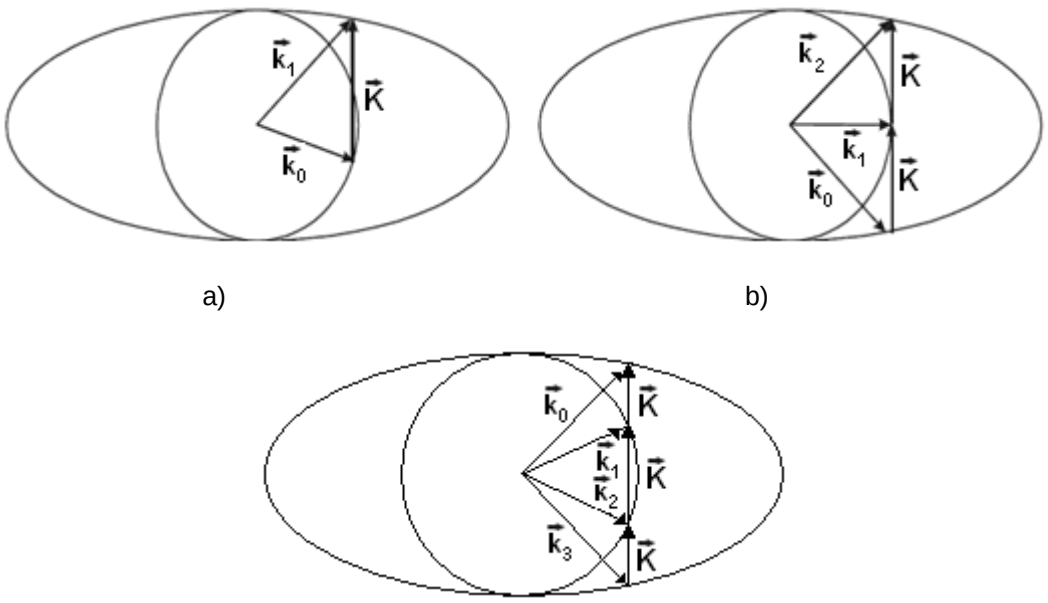

a) b)

c)

Fig.1.3. Wave vector surfaces and wave vector diagrams inherent in a one-fold (a), two-fold (b), and three-fold (c) light scattering of a photon by acoustic phonons in a uniaxial crystal.

The polarization states of light in various orders of scattering can be orthogonal to each other, whereas the frequencies of light beams in the first, second, and third orders are shifted by Ω_2 and $2\Omega_2$ or Ω_3, $2\Omega_3$, and $3\Omega_3$, as the case requires, relative to the zero order light beam, see Fig.1.4.

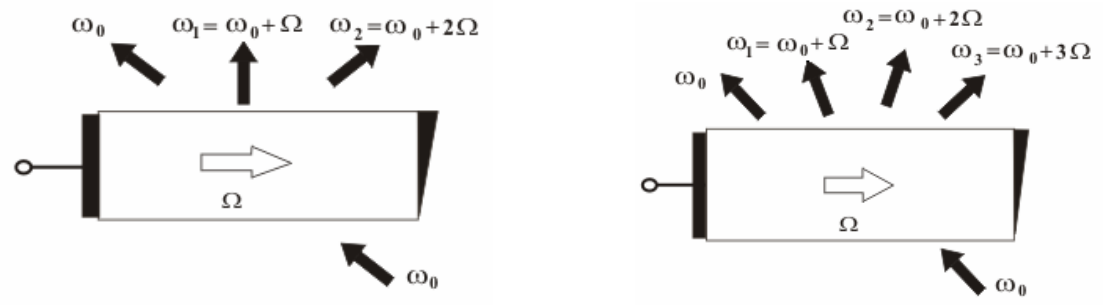

a. b.

Fig.1.4. General arrangement of optical beams in a two-phonon (a) and three-phonon (b) processes of light scattering; light arrows show the corresponding acoustic waves passing through crystals from the piezo-electric transducers to the absorbers.

In an anisotropic medium, the refractive index associated with a light beam is, in general, dependent on the direction of propagation. Since the diffracted light beam, in general, propagates in a different direction from the incident beam, the magnitudes of the wave vectors are no longer nearly the same. In some cases, there may even be a change of the polarization state between the incident and the diffracted beam. And, since they are in general different, the triangle is not isosceles even if we neglect the small differences between ω_0 and ω_1. Assuming that a pure shear wave with linear polarization propagates in the direction of the optical $\mathbf{z}$-axis. The shear wave causes orthogonal scattering of extraordinary incident wave, propagating in the $\mathbf{y}-\mathbf{z}$ plane, into an ordinary wave propagating in the same plane. Such a construction is shown in Fig.1.5a.

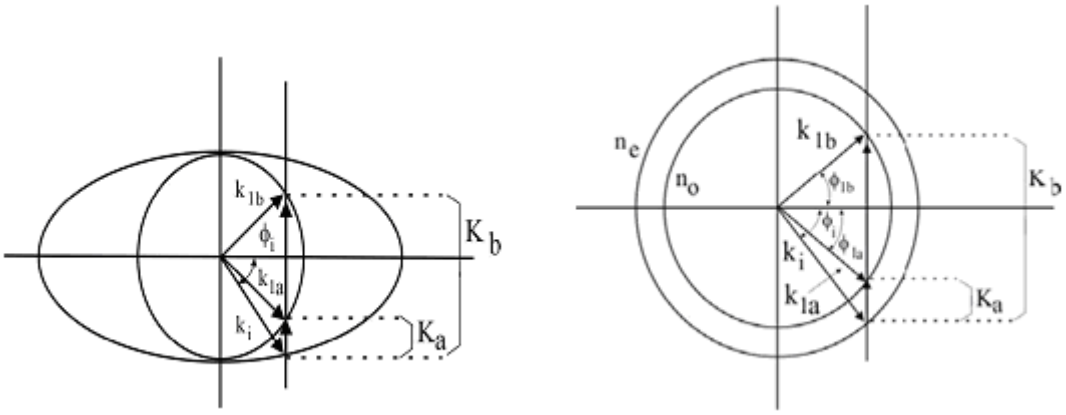

a) b)

Fig.1.5. Anisotropic interaction in positive uniaxial crystal.
a) shear wave along optical axis, light wave in **xy** plane, b) all waves in **xy** plane.

Note that for a given $\vec{\mathbf{k}}_\mathbf{i}$, two $\vec{\mathbf{k}}_\mathbf{1}$'s are possible: $\vec{\mathbf{k}}_\mathbf{1a}$ mediated by $\vec{\mathbf{K}}_\mathbf{a}$ and $\vec{\mathbf{k}}_\mathbf{1b}$ mediate by $\vec{\mathbf{K}}_\mathbf{b}$. When $\phi_\mathbf{i}$ increases, $\vec{\mathbf{K}}_\mathbf{a}$ will decrease, indicating Bragg angle behaviour for frequencies down to zero. In this limit, $\vec{\mathbf{k}}_\mathbf{1}$ and $\vec{\mathbf{k}}_\mathbf{1a}$ are parallel and opposite to $\vec{\mathbf{K}}_\mathbf{a}$. In Fig.1.5a, for instance, there does not exist, in general, a second wave vector $\vec{\mathbf{K}}'_\mathbf{a}$, equal in length to $\vec{\mathbf{K}}_\mathbf{a}$ and directed upward, that would

re-scatter the $\vec{k}_{1a}$ on the circle into $\vec{k}'_{1a}$ on the ellipse, in this case the light is non-collinear incidence, that means the light wave and the acoustic wave are interacting in orthogonal directions [10].

Anisotropic interactions generally offer an increase in efficiency and in both acoustic and optical bandwidth. They are used almost universally in large aperture devices. The reduction in the acoustic velocity, seen in shear-mode tellurium dioxide, lends this material to be used in high resolution deflectors.

1.4.4 Collinear acousto-optic interaction

Collinear acousto-optical interaction was initially predicted and studied by Dixon in the middle of 1960s [1] and then, starting form the 1970s has been successfully exploited in various applications [2-6]. During the process of collinear interaction of stationary Bragg light scattering by a coherent wave in an optically uniaxial crystal [7,8], the polarizations of the incident and scattered light beams are orthogonal to each other, while their wave vectors $\vec{k}_0$ and $\vec{k}_1$ lie along the acoustic wave vector $\vec{K}$. Recently the existence of a new branch of studies an applications of collinear acousto-optical interaction, which is associated with three-wave coupled states, has been manifested [10,11].

An example of an acousto-optic collinear interaction is sketched in Fig.1.5a which shows two orthogonally polarized optical beams propagating along the **x**-axis coupled by an acoustic wave in a calcium molybdate crystal. The collinear phase matching condition for this case is, $(\omega/c)(n_o - n_e) = (\Omega/V)$, where n_o is the ordinary index of refraction, and n_e is the extraordinary index of refraction. For the two waves to be coupled by the acoustic one, it is necessary that the photo-elastic tensor $p_{ijkl} \neq 0$. Since in $CaMoO_4$, $p_{ijkl} = p_{45}$ is finite, the coupling can be accomplished.

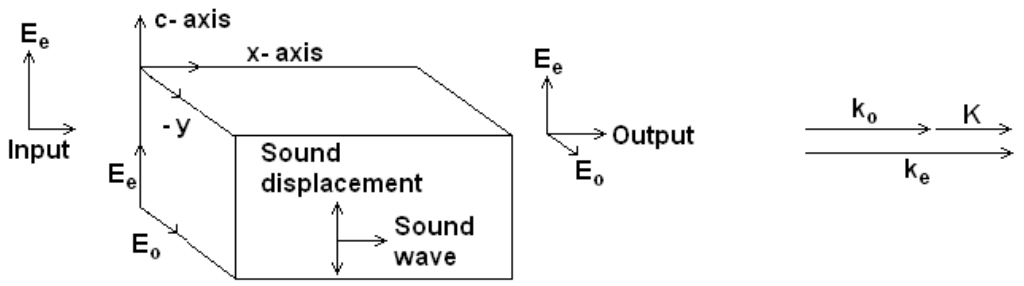

a) b)

Fig.1.6. a) Collinear coupling between a **z**-polarized and a **y**-polarized optical beams by a shear acoustic, b) collinear phase matching in a birefringent crystal [49].

Figure 1.6b shows the vector diagram for the phase matching condition which has to be fulfilled in order to collinear interaction in anisotropic medium takes place.

1.5 Acousto-optical coupled states

1.5.1 Collinear acousto-optic coupled states

In many cases the analysis of three-wave processes leads to finding various solitary waves in the form of coupled states, where waves of the same or even different nature become to be mutually trapped and propagate together [42-44]. The dynamics of localization the acousto-optical coupled states with collinear scattering has been studied both theoretically and experimentally [43,45,46]. They can be shaped via stationary co-directional collinear interaction of two optical modes with some non-optical third wave in a dispersive waveguide due to the balance action of the square-law nonlinearity. The profiles of all the waves are steady at three different current frequencies, because the interaction exhibits itself as a mechanism of stabilizing self-action. The reduced set of three combined nonlinear partial differential equations which describe the stationary coupled states can be written as [44]

a) $\frac{dC_0}{dx} = -C_1 C_2^* \exp(2i\eta x)$, b) $\frac{dC_1}{dx} = C_0 C_2 \exp(-2i\eta x)$,

$$\text{c)}\quad \frac{dC_2}{dx} = -C_1 C_0^* \exp(2i\eta x), \tag{1.48}$$

where x is the spatial coordinate, C_k $(k = 0,1,2)$ are the normalized complex amplitudes; and 2η is the wave numbers mismatch. Assuming that $C_k = a_k \exp(i\varphi_k)$ then Eqs.(1.48) can be converted into equations for real amplitudes a_k and real phases φ_k, which have the following solutions [47]

$$a_k^2 = \alpha_k^2 + b_k^2, \qquad b_0^2 = \sigma^2 cn^2[\mu(x - x_0); \hat{\kappa}],$$

$$b_1^2 = \sigma^2 sn^2[\mu(x - x_0); \hat{\kappa}], \qquad b_2^2 = \mu^2 dn^2[\mu(x - x_0); \hat{\kappa}].$$

where α_k are parameters that specify the background, the parameters σ, μ, and $\kappa = \sigma/\mu$ are independent of the coordinate x. They are determined by the boundary conditions and the mismatch. The b_k terms represent the oscillating portions of solutions, evaluating the extent of localization for the coupled states. Using the motion equations $d^2 b_i / dx = -dU_i / db_i$ for some particles in the real-valued potentials $U_i(b_i)$,

$$\text{a)}\quad \frac{d^2 b_k}{dx^2} = 2\vartheta_k b_k^3 + p_k b_k, \qquad \text{b)}\quad U_k(b_k) = -\frac{\vartheta_k}{2} b_k^4 - \frac{p_k}{2} b_k^2 + H_k. \tag{1.49}$$

For $k = 1$ with $b_1(x_0) = 0$, Eq.(1.49b) gives the potential that has a local minimum at $b_1 = 0$ and two absolute maxima at $b_1 = \pm\sqrt{F_1/2}$, where F_1 is a constant. Substituting this potential into Eq.(1.49a) gives a kink soliton solution of the form, $b_1(x) = \pm\sqrt{F_1/2} \cdot \tanh\left[\sqrt{F_1/2}\,(x - x_0)\right]$, which represents a shock wave of envelope or a dark optical coupled state. In the case of $k = (0,2)$, the potential exhibit the only one local maximum at $b_k = 0$.

The waves $\mathbf{b_0}$ and $\mathbf{b_2}$ shape the bright components of the coupled states $\mathbf{b_0(x)=\pm\sqrt{F_0}\cdot sech\left[\sqrt{F_0}\,(x-x_0)\right]}$ and $\mathbf{b_2(x)=\pm\sqrt{-F_2}\cdot sech\left[\sqrt{-F_2}\,(x-x_0)\right]}$ with $\mathbf{b_k\,(x\to-\infty)=b_k\,(x\to+\infty)}$. At any finite distance the symmetry in these waves tends to be broken, because the absolute minima of the potential is degenerated and they can be reached in two different points instead of one. Since the symmetrical states with the least energy at $\mathbf{b_k=0}$ are unstable, either of two signs can be set in the relations $\mathbf{b_k(x_0)=\pm\left|b_k(x_0)\right|}$. This is known as the spontaneous breaking of symmetry [48] that is inherent in topologically uncharged bright components of coupled states.

1.5.2 Three-wave non-collinear acousto-optic weakly-coupled states

The well-known set of combined differential equations of the first order that governs the evolution of the complex amplitudes $\mathbf{C_0(x)}$ and $\mathbf{C_1(x)}$ of light waves and describes a one-phonon Bragg non-collinear acousto-optic interaction [43] is denoted by

$$\text{a)}\ \frac{\mathbf{dC_0}}{\mathbf{dx}}=-\mathbf{q_1C_1\exp(2i\eta x)},\qquad \text{b)}\ \frac{\mathbf{dC_1}}{\mathbf{dx}}=\mathbf{q_0C_0\exp(-2i\eta x)}. \tag{1.50}$$

The factors $\mathbf{q_{0,1}}$ can be approximated as $\mathbf{q_0\approx q_1\approx q_2=2\pi\Delta n/(\lambda\cos\theta)}$, where $\mathbf{\Delta n}$ is the amplitude of the variations of the refractive indices due to the action of continuous-wave ultrasound reflects the photo-elastic properties of a crystal and includes the amplitude of the acoustic wave, θ is the angle of incidence of the wave $\mathbf{C_0}$, and $\mathbf{2\eta=k_{0,x}-k_{1,x}}$ represents the angular frequency mismatch. Using the boundary conditions $\mathbf{\left|C_0(x=0)\right|^2=1}$, $\mathbf{C_1(x=0)=0}$, and the conservation law $\mathbf{\left|C_0\right|^2+\left|C_1\right|^2=1}$, the solutions to Eqs.(1.50) in terms of the light intensities are

$$\text{a)}\quad |C_0|^2 = \frac{\eta^2}{q+\eta^2} + \frac{q^2}{q+\eta^2}\cos^2\left(x\sqrt{q^2+\eta^2}\right),$$

$$\text{b)}\quad |C_1|^2 = \frac{q^2}{q+\eta^2}\sin^2\left(x\sqrt{q^2+\eta^2}\right). \qquad (1.51)$$

The first summand in Eq.(1.51a) is independent on the coordinate **x** and exhibits the contribution of some background; while the second one, represents the oscillating portion of the solution describing the localization of the incident light field. Equations (1.51) yield that $L\sqrt{q^2+\eta^2} = \pi N$, where **L** is the spatial length of interaction and **N** is an integer. When $N = 1$ yields one-pulse weakly coupled state, and when $N > 1$, the distribution of $|C_1|^2$ over the transverse extent of elastic wave has **N** partial peaks in its envelope, while the intensity $|C_0|^2$ has **N** holes [50], and the efficiency of localization is given as $\hat{\rho} = q_0(q_1)^{-1}q^2\left(q^2+\eta^2\right)^{-1}$.

1.5.3 Four-wave non-collinear acousto-optical weakly coupled states

A set of equations for the amplitudes $C_m(x)$ of light waves ($m=0,1,2$), with stationary two-phonon light scattering in Bragg regime is given by [10,32]

$$\text{a)}\quad \frac{dC_0}{dx} = -qC_1\exp(-i2\eta_0 x),$$

$$\text{b)}\quad \frac{dC_1}{dx} = q\left[C_0\exp(i2\eta_0 x) - C_2\exp(-i2\eta_1 x)\right],$$

$$\text{c)}\quad \frac{dC_2}{dx} = qC_1\exp(i2\eta_1 x). \qquad (1.52)$$

The parameters $2\eta_m = k_{m,x} - k_{m+1,x}$, explained in terms of **x**-components for the light wave vectors, represent the joint angular-frequency mismatches. The factor **q** describes both the material properties and the acoustic power density and it is set equal to a constant. Analyzing Eqs.(1.52) with the boundary conditions $|C_0(x=0)|^2 = I^2$, $C_{1,2}(x=0) = 0$ and exploit the conservation law $|C_0|^2 + |C_1|^2 + |C_2|^2 = I^2$, where I^2 is the intensity of continuous wave incident light. The exact solutions to Eqs.(1.52) in this regime are [50]

$$C_0(x) = iI\left\{1 + \frac{q^2(2\eta - a_0)}{a_0(a_0 - a_1)(a_0 - a_2)}\left[1 - \exp(-ia_0x)\right] - \frac{q^2(2\eta - a_1)}{a_1(a_2 - a_1)(a_0 - a_1)} \times \right.$$

$$\left. \times \left[1 - \exp(-ia_1x)\right] + \frac{q^2(2\eta - a_2)}{a_2(a_2 - a_1)(a_0 - a_2)}\left[1 - \exp(-ia_2x)\right]\right\}, \tag{1.53}$$

$$C_1(x) = \frac{qI(2\eta - a_0)}{(a_0 - a_1)(a_0 - a_2)}\exp\left[i(\eta_0 - a_0)x\right] - \frac{qI(2\eta - a_1)}{(a_2 - a_1)(a_0 - a_1)} \times$$

$$\times \exp\left[i(\eta_0 - a_1)x\right] + \frac{qI(2\eta - a_2)}{(a_2 - a_1)(a_0 - a_2)}\exp\left[i(\eta_0 - a_2)x\right], \tag{1.54}$$

$$C_2(x) = iq^2 I\left\{\frac{1 - \exp\left[i(2\eta - a_0)x\right]}{(a_0 - a_1)(a_0 - a_2)} + \frac{1 - \exp\left[i(2\eta - a_0)x\right]}{(a_2 - a_1)(a_0 - a_1)} - \right.$$

$$\left. - \frac{1 - \exp\left[i(2\eta - a_0)x\right]}{(a_2 - a_1)(a_0 - a_2)}\right\}. \tag{1.55}$$

Here the numbers a_m are real roots of the cubic algebraic equation $a^3 - (2\eta_0 + 2\eta)a^2 - (2q^2 - 2\eta\eta_0)a + q^2 2\eta = 0$ and $\eta = \eta_0 + \eta_1$. As follows from Eqs.(1.53)-(1.55), the intensities $|C_m(x)|^2$ are periodic in **x**, such values x_n

exist that $|C_0(x_n = 0)|^2 = I^2$, $C_{1,2}(x_n = 0) = 0$. Thus, the intensities of scattered waves are zero outside tue area occupied by the acoustic wave. Inside this area, the spatial distributions of the scattered waves contain a number of peaks, and simultaneously the distribution of incident light has holes at the same positions. If $\eta_0 = \eta_1 = 0$, then

$$\text{a)}\ |C_0(x)|^2 = \cos^4\left(qx/\sqrt{2}\right), \qquad \text{b)}\ |C_1(x)|^2 = \frac{1}{2}\sin^2\left(qx\sqrt{2}\right),$$

$$\text{c)}\ |C_2(x)|^2 = \sin^4\left(qx/\sqrt{2}\right). \tag{1.56}$$

The condition of localization for the scattered components in Eqs.(1.56) within the spatial interval $(0, x_n)$ has the form of $x_n q = \pi n\sqrt{2}$.

1.6 Spectrum analyzers for radio-signals

Usually, a spectrum analyzer displays a power spectrum over a given frequency range in real time, changing the output as the properties of the signal change. These devices are used commonly in radio-astronomy to analyze the radio-signals detected by the radio-telescopes. Radio-signals can be from radio galaxies, pulsars, masers, and the cosmic microwave background radiation. There are different kinds of spectrum analyzers, in the next subsection it will be discussed two of them.

1.6.1 Acousto-optical spectrum analyzers

The interaction of light beams with a sound wave in a photo-elastic medium exhibit many interesting effects. These effects can be used to build light modulators, beam deflectors, tunable filters, spectral analyzers, and signal processors.

The use of acousto-optic cells to obtain the power spectra of unknown signals began with the early work [12, 52], using acoustic waves launched in a fluid and Raman-Nath diffraction. It was not until the late 1960s, with the development of suitable crystalline solids, that Bragg regime devices became available. Acousto-optic interactions offer the possibility of manipulating a laser beam or processing a signal radiation at high speed, since no mechanical moving parts are involved. The idea of deflecting a beam of light by changing the frequency of the sound leads naturally to the concept of an acousto-optic frequency analyzer. One of the earliest applications for the acousto-optical spectrum analyzer was in the field of radio-astronomy.

The principle of the acousto-optical spectrometer was first described by Lambert in 1962. It can be described as follows; the intermediate frequency signal from the telescope receiver is converted to an ultrasonic wave through a piezo-electric transducer bonded to an acousto-optical crystal cell (Brags cell), and the wave travels through the material maintaining the spectrum information of the radio frequency (RF) signal.

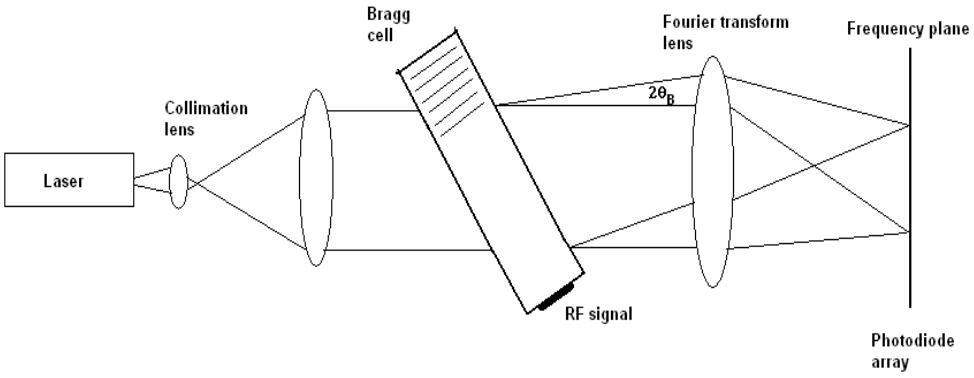

Fig.1.7. Basic acousto-optic spectrum analyzer.[51]

The Bragg cell is illuminated by laser light that has been expanded to cover the entire acousto-optical cell's aperture, spatially filtered, and collimated. The acoustic wave diffracts the incident light into a single order via Bragg diffraction. Within the range of linearity, the diffraction angle and the diffracted light intensity

are proportional to the frequency and power of the input signal, respectively. The first radio observations using this technique were made by Cole in 1973.

Figure 1.7 shows a basic scheme of an acousto-optic spectrum analyzer. In this scheme, the Fourier transform lens produces the frequency transform one focal length from the lens, and the information is read out using a self-scanned photodetector array. For each beam angle out of the Bragg cell there is a discrete point focus in the frequency plane, and since the angle is proportional to the frequency, there is a one-to-one correspondence of the light image in the frequency plane to the input signal. The limiting resolution (or spot size) of the system is determined by the illumination, and the Fourier transform indicates the sidelobe level and skirt width of the spot.

1.6.2 Bank of filters vs. acousto-optical spectrum analyzers

An electronic receiver can be made to scan a desired bandwidth and measure the signal energy over a narrow range of frequencies. As we reduce the receiver bandwidth to improve the sensitivity, the scan rate must also be reduced, in a noisy signal environment; this means that the probability of intercepting the desired signal is reduced proportionally. To avoid this problem, receivers are design with a large bank of narrow bandpass filters operating in parallel; such devices also are called channelizers. However, this complicates the design and limits the number of frequency channels that can be implemented electronically, as the number of channels depends on the time-bandwidth product of the system.

In contrast, the optical spectrum analyzer can use an acousto-optic cell with a time-bandwidth product of 1000-2000; many more channels can be realized in a more compact space than if an electronic implementation were used. The number of resolvable channels also is limited by the photo-detector array. The resulting parallel signal processing structure offers a high probability of intercept over a broad frequency bandwidth, with sharp frequency resolution.

Acousto-optical spectrum analyzers can be used to replace banks of filters constructed with conventional electronic components. This new type of radio-spectrometer is potentially superior for millimeter-wave spectroscopy.

A complete system consists of only three active components (laser, photo-detector array, and acousto-optics device), so that the power requirements also are much lower than in conventional electronic systems [53]. In addition, these devices are usually very compact; a packaged unit can measure only about 5-15 cubic in. in volume. A system of this size easily can be placed very close to the receiving microwave antenna, so that the received signals need not be conveyed over long distances prior to processing.

The dynamic range, which is fundamentally limited by the square law photo-detection process, can be increased by using heterodyne detection; a separate optical path is provided to deliver a reference beam to the detector. In practice, we may think of the output as representing a sampled version of the actual Fourier transform. Additionally, it is possible to integrate in both space and time as done in the so-called hybrid spectrum analyzers [54]. Several detailed treatments of various acousto-optic spectrum analyzer designs are available in the literature [14-16, 55-57].

A summary of the features of different types of spectrometers used for radio-astronomy are presented in Table I.

Table I.

Bank of filters	Autocorrelators	Acousto-optics
It is the most direct form to obtain the spectrum of a radio-signal Each filter must be designed individually It is cheap It has problems with stability due to the number of filters It needs a constant maintenance or to restrict the bandwidth	It is fast and cheap It can reach wider bandwidths at higher frequencies (hundreds of GHz) It requires high energy levels	It has a high spectral resolution It does not require high energy levels It is not so versatile with respect to resolution and bandwidth

As can be inferred from Table 1, acousto-optical spectrum analyzers are one of the best choices in terms of energy levels, size, and spectral resolution. In the other hand, the resolution and the bandwidth must be enhanced or improved.

References

1. Lord Rayleigh, “On waves propagated along the plane surfaces of an elastic solid”. Proc. London Math. Soc., **17**, 4-11 (1885).
2. L. Brillouin, “Diffusion de la lumiere et des rayonnes X par un corps transparent homogene; influence del'agitation thermique”. Ann. Phys., **17**, 88 (1922).
3. P. Debye and F. W. Sears, “On the scattering of light by supersonic waves”. Proc. Nat. Acad. Sci. U.S., **18**, 409-414 (1932).

4. R. Lucas and P. Biquard, “Optical properties of solids and liquids under ultrasonic vibrations,” J. Phys. Rad., **3**, 464 (1932).
5. A. Korpel and T. C. Poon, “Explicit formalism for Acousto-optic multiple plane-wave scattering”, J. Optical Society of America, **70**, 817 (1980).
6. M. V. Berry, The diffraction of light by ultrasound, (Academic Press, New York, 1966).
7. C. V. Raman and N. S. N. Nath, “Diffraction of light by high frequency sound waves, Parts I and II”, Proc. Indian Academic of Science, **2**, 406 (1935), “Diffraction of light by supersonic waves, Part III”, **3**, 75 (1936), “Part IV”, **3**, 119 (1936), “Part V”, **3**, 459 (1936), “Generalized theory”, **4**, 222 (1936).
8. W.R. Klein and B.D. Cook, “Light diffraction by ultrasonic gratings”, Acoustica, **15**, 67-74 (1965).
9. W.R. Klein and B.D. Cook, “Unified approach to ultrasonic light diffraction”, IEEE Trans. On sonics and ultrasonics, **SU-14**, 123 (1967).
10. A. Korpel, Acousto-Optics. (Marcel Dekker, New York, 1988).
11. W. Liebe, “Some applications ofan ultrasonic light modulators”, J. Acosutical Society of America, **34**, 860 (1962).
12. A.H. Rosenthal, “Applications of ultrasonic light modulation to signal recording, display, analysis and communication”, IRE Trans. On ultrasonic engineering, **SU-8**, 1 (1961).
13. M. King, W.R. Benett, L.B. Lambert, and M. Arm, “Real time electro-optic signal processors with coherent detection”, Applied Optics, **6**, 1367 (1967).
14. R. Withman, A. Korpel, and S. Lossof, “Applications of acoustic Bragg diffraction to optical processing techniques”, Proc. Symp. Modern Optics (Polytechnic Press, Brooklyn, NY, 1967) p. 243.
15. R.L. Whitman and A. Korpel, “Probing of acoustic surfaces perturbations by coherent light”, Applied Optics, **8**, 1567 (1969).
16. A. Korpel and R.L. Whitman, “Visualization of a coherent light field by heterodyning with a scanning laser beam”, Applied Optics, **8**, 1577 (1969).
17. A. Korpel, R. Alder, P. DEsmares, and T:M: Smith, “An Ultrasonic Light deflection system”, IEEE J. Quantum Electronics, **QE-1**, 60 (1965).

18. W.H. Bragg and W.L. Bragg, “The relection of X-rays of crystals”, Proc. Royals Society of London, **A88**, 428 (1913).
19. A. Korpel, “Visualization of the cross section ofa sound beam by Bragg diffraction light”, Applied Physics Letters, **9**, 425 (1966).
20. C.S. Tsai and H:V. Hance, “Optical imaging of the cross section of a microwave acoustic beam in rutile by Bragg diffraction of a lasee beam”, J. Acoustical Society of America, **42**, 1345 (1967).
21. G. Wade, C.J. Landry, and A.A. de Souza, “Acoustical transparencies for optical imaging and ultrasonic diffraction”, in A.F. Metherell, H.M.A: EL-Sum, and L. Larmore, eds., Acoustical Holography, 1 (Plenum Press, New York, 1969), p. 159.
22. N.M. Kroll, “Parametric amplification in spatially extended media and application to the design of tunable oscillators at optical frequencies”, Phys. Rev., **127**, 1207 (1962).
23. A. Korpel, “Acousto-optics”, in R. Wolf, ed., Applied Solid State Science, 3, (Academic Press, New York, 1972).
24. O. Leroy and J.M. Claeys, “Diffraction of light by profiled ultrasound”, Acoustica, **55**, 21 (1984).
25. T.M. Smith and A. Korpel, “Measurements of light-sound interaction efficiencies in solids”, IEEE J. Quantum Electronics, **QE-1**, 283 (1965).
26. D.A. Pinnow, “Guidelines for the selection of acousto-optic materials”, IEEE J. Quantum Electronics, **QE-6**, 223 (1970).
27. R.J. Pressley, ed., Handbook of lasers with selected data of optical technology, (CRC Press, Cleveland, 1971).
28. R.R. Aggarwal, “Diffraction of light by ultrasonic waves (Deduction of the different theories from the generalized theory of Raman and Nath)”, Proc. Indian Academic Science, **A31**, 417 (1950).
29. P. Pharisean, “On the diffraction of light by progressive supersonic waves, oblique incidence: Intensities in the neighbourhood of the Bragg angle”, Proc. Indian Academic Science, **A44**, 165 (1957).

30. C.F. Quate, C.D. Wilkinson, and D.K. Winslow, “Interaction of light and microwave sound”, Proc. IEEE, **53**, 1604 (1965).
31. L. Klun, M.L. Dakss, P.F. Heidrich, and B.A. Scott, “Deflection of an optical guided wave by a surface acoustic wave”, Appl. Phys. Lett.,**17**, 265 (1970).
32. V.I. Balakshy, V.N. Parigin, and L.E. Chirkov, Physical principles of acousto-optics, (Radios i Sviaz, Moscow, 1985).
33. S.V. Kulakov, Acousto-optic devices for spectrum and correlation signal analysis, (Nauka, Leningrad, 1978).
34. L.N. Magdih and V.Y. Molchanov, Acousto-optical devices and their applications, (Moscow, Soviet Radio, 1978).
35. Z.M. Gorbachevskaya, UHF signal identification receiving devices for modern radio defense systems, (Moscow: CNII Elektronika, 1982).
36. N.A. Esepkina, N.F. Ryzhov, and S.V. Pruss Zhukovskiy, Acousto-optic spectrograph for radio-astronomy, (preprint, Leningrad (SO AN USSR N.11L), 1984).
37. T.S.Narasimhamurty, *Photoelastic and Electro-optic Properties of Crystals*, (Plenum Press, New York, 1981). p.152.
38. Landau and Lifshitz. *Theory of elasticity : Course of theoretical physics Vol.7*, USSR Academy Science, Moscow USSR (2005).
39. D.F. Nelson and M. Lax, “New Symmetry for Acousto-Optic Scattering”. Phys. Rev. Lett., **24**, 379 (1970).
40. D.F. Nelson and M. Lax, “Theory of the Photo-elastic Interaction”. Phys. Rev. B, **3**, 2778 (1971).
41. N.N.Syrbu, R.V.Cretu. “The superposition of one- and two-phonon absorption and radiation in TeO2 crystal”. Elsevier Science (www.sciencedirect.com), infrared physics & Technology, **37**, 769-775 (1997).
42. A.P. Sukhorukov. *Nonlinear wave interactions in optics and radiophysics*, (Nauka Press, Moscow, 1988).
43. A.S. Shcherbakov, “A three-wave interaction. Stationary coupled states”, (St.Petersburg State Technical University Press, St.Petersburg. 1998).

44. R.K. Dodd, J.C. Eilbeck, J.D. Gibbon, and H.C. Morris. *Solitons and nonlinear wave equations.* (Academic Press, Orlando. 1984).
45. O.I.Belokurova, A.S.Shcherbakov. "Dynamics of shaping the components of coupled acousto-optical state." *Techn. Phys. Lett.* **16,** 612-614 (1990).
46. A.S.Shcherbakov, I.B.Pozdnov. "Localization dynamics of weakly-coupled acousto-optical states." *Techn. Phys. Lett.,* **20,** 687-689 (1994).
47. A.S.Shcherbakov. "Shaping the optical components of solitary three-wave weakly coupled states in a two-mode crystalline waveguide." in *Nonlinear Guided Waves and Their Applications,* OSA Technical Digest (Optical Society of America, Washington DC, 2002), NLMD7, pp. 1.3.
48. R.Rajaraman, *Solitons and Instantons*, (North-Holland Publising Company, Amsterdam, 1982).
49. A. Yariv, *Quantum Electronics* (John Wiley & Sons, Inc., 1989)
50. A.S.Shcherbakov and A.Aguirre Lopez. "Observation of the optical components inherent in multi-wave non-collinear acousto-optical coupled states." Optics Express, **10**, 1398-1403 (2002), http://www.opticsexpress.org/abstract.cfm?URI=OPEX-10-24-1398.
51. P.K. Das and C.M. DeCusatis, *Acousto-Optic Signal Processing: Fundamentals and Applications* (Artech House Inc, Norwood, MA, 1991).
52. L.B. Lambert, "Wideband instantaneous spectrum analyzers employing delay line light modulators", in IRE Int. Conf. Rec., **10**, 69 (1962).
53. J.N. Lee and A. Vander Lugt, "Acousto-optic signal processing and computing", IEEE Proc.,**77**, 1528 (1989).
54. P. Kellman, H.N. Shaver, and J.W. Murray, "Integrating acousto-optic channelized receivers", Proc. IEEE, **69**, 93 (1981).
55. http://www.mt-berlin.com/frames_ao/acousto_frames.htm
56. I.J. Abramovitz and D. Greenfield, "Surface wave acousto-optic processors in one and two dimensions" (Proc. DOD Conf. Electro-Acousto-Optic Technology, Orlando, FL, 1986).
57. P. Kellman and T. Bader, "Acousto-optic channelized receivers", Opt. Eng., **23**, 2 (1984).

Chapter 2

Acousto-optical interaction in TeO_2 crystals

2.1 Introduction

Usually, the Bragg acousto-optical process includes three waves, the incident and scattered light modes as well as the acoustic mode. In general, a specially chosen geometry of acousto-optical interaction in anisotropic medium, i.e., tellurium dioxide (TeO_2) crystal, allows a two- as well as a three-fold light scattering by the acoustic wave. Under certain conditions, i.e. at a set of the angles of light incidence on selected crystal cut and at a specially fixed frequency of the acoustic wave, one will be able to observe the Bragg multi-fold light scattering. These effects can be exploited for creating optical modulators with improved frequency and/or angular resolution [1]. The analytical models for multi-phonon acousto-optical interaction without phase mismatches are briefly discussed for a TeO_2 crystal; attention is paid to the two- and three-fold scattering regimes. In a two-fold light scattering the effective anomalous light diffraction is involved in this process, whereas for the three-fold light scattering includes both anomalous and normal mechanisms of scattering whose ratio should be estimated, in which the account contributions from the phenomenon of optical activity are considered. The feasibility of applying such a phenomenon to upgrading the frequency resolution of spectrum analyzers for radio-astronomy spatial modulation of light is analyzed.

2.2 Analytical model for a multi-fold Bragg acousto-optical interaction

Attention will be focused on a novel approach to the Bragg regime of **N**-fold, namely, a one-, two- or three-fold light scattering in an optically anisotropic media

[2,3] caused by multi-phonon processes, wherein a plane elastic wave with the angular frequency Ω and wave number **K** is traveling along the **y**-axis. Under action of such an elastic wave the dielectric permeability ε becomes to be a function of the coordinate **y** and time **t**, so it is varied as

$$\varepsilon(y,t) = \varepsilon_0 + \varepsilon_1 \sin(K y - \Omega t + \Phi), \tag{2.1}$$

where ε_0 is the dielectric permeability for a non-perturbed medium, ε_1 is the amplitude of variations in the dielectric permeability, Φ is the phase of the acoustic wave which is constant for a uniform plane wave. Then, let us assume that the area of propagation for the elastic wave is bounded by two planes $x = 0$ and $x = L$, and interacts with **N** plane electromagnetic waves of the form

$$E_{in} = \sum_{p=0}^{N} A_p \exp\left[i\left(k_p x \cos\theta_p + k_p y \sin\theta_p - \omega_p t + \varphi_p\right)\right], \tag{2.2}$$

which strike the plane $x = 0$, at θ_p angles with respect to the **x**-axis. Here, $p = 0,1,2,...,N$; while A_p, φ_p, ω_p, and k_p are the normalized real amplitude, initial phase, angular frequency, and wave number of the **p**-th incident light wave, respectively; where $\omega_p = \omega_0 + p\Omega$ and $k_p = \left|\vec{k}_p\right| = \omega_p \varepsilon_0^{1/2} c^{-1}$. Without lossing generality, one may put that all the fields are independent of the third coordinate. Because the directions of the light waves are pre-assigned by the Bragg conditions, a scalar version of the wave equation, governing the electric component $E(x,y,t)$ of the electromagnetic wave in the area of interaction, may be used. It would be natural to represent the project solution in the area $x \in [0,L]$ as a sum of partial waves with the normalized complex amplitudes $C_p(x)$, so one have that

a) $$\frac{\partial^2 E}{\partial x^2} + \frac{\partial^2 E}{\partial y^2} - \frac{1}{c}\frac{\partial^2(\varepsilon E)}{\partial t^2} = 0 \ ,$$

$$\text{b)}\quad \mathbf{E}=\sum_{p=0}^{N} C_p(x)\exp\left[i\left(k_{p,x}\,x+k_{p,y}\,y-\omega_p\,t\right)\right], \qquad (2.3)$$

where $k_{p,y}=k_0\sin\theta_0+pK$ and $k_{p,x}=\sqrt{k_p^2-k_{p,y}^2}$, which are the wave numbers of the **p-**th incident light wave in the **y** and **x** directions, respectively. Equation (2.3b) does not contain any waves, being reflected by the dynamic acoustic grating in the medium. The reflected waves become to be essential when the angles of scattering are close to **90°**, for instance, for the collinear acousto-optical interaction. In the chosen approximation, we obtain the following set of ordinary equations [2]

$$\frac{dC_p(x)}{dx}=q_{p-1}C_{p-1}(x)\exp\left[i\left(2\eta_{p-1}x+\Phi\right)\right]-q_{p+1}C_{p+1}(x)\exp\left[i\left(2\eta_p x+\Phi\right)\right], \qquad (2.4)$$

$$\text{a)}\quad q_p=\varepsilon_1 k_p^2\left(4k_{p,x}\varepsilon_0\right)^{-1}, \qquad \text{b)}\quad 2\eta_p=k_{p,x}+K_x-k_{p+1,x}, \qquad (2.5)$$

where q_p is a parameter which describes the efficiency of the acousto-optical interaction, ε_0 is the dielectric constant for a non-perturbed medium, ε_1 is the amplitude of variations in the dielectric constant, and Φ is the initial phase of elastic wave. It follows from Eqs.(2.4) that only the neighboring pairs of orders govern the redistribution of optical energy in each p-th order of scattering. When the angles θ_p of incidence for all the light beams are chosen in an arbitrary way, all the values $2\eta_p L$ far exceed π, so the scattering is not sufficiently effective. Nevertheless, for specific angles θ_p, being close to the above-mentioned Bragg angles, a few values $2\eta_p L$ turn out to be small, so rather effective scattering into the corresponding p-th order takes place.

2.3 General approach to the analysis of acousto-optical interaction

One way of finding the general solution to Eqs.(2.4) and (2.5) in isotropic medium [2] lies in exploiting a $(M+N+1)$- dimensional vector $\vec{C}(x)$ with the components $C_{-N}, C_{-N+1}, ..., C_0, ..., C_M$ together with

$$\hat{H}(x) = \begin{pmatrix} 0 & b_{-N} & 0 & 0 & \cdots & 0 \\ a_{-N+1} & 0 & b_{-N+1} & 0 & \cdots & 0 \\ 0 & a_{-N+2} & 0 & b_{-N+2} & \cdots & 0 \\ \cdots & \cdots & \cdots & \cdots & \cdots & 0 \\ 0 & 0 & 0 & 0 & \cdots & a_M \end{pmatrix}, \qquad (2.6)$$

which is a square matrix with rank equal to $(M+N+1)$ and where $a_p = q_p \exp(2i\eta_{p-1}x)$; $b_p = -q_p \exp(-2i\eta_p x)$ with $M \geq p \geq -N$. Then, Eqs.(2.4) can be written as $d\vec{C}/dx = \hat{H}(x)\vec{C}(x)$ and by integrating them from 0 to L, one has

$$\vec{C}(L) = \vec{C}(0) + \int_0^L \hat{H}(x)\vec{C}(x)\,dx. \qquad (2.7)$$

The boundary condition for the current consideration is taken in the form of $C(0) = (0, 0, \ldots, 0, 1, 0, \ldots, 0)$. The solution to Eq.(2.7) can be found with the help of the following recurrent formula

$$\vec{C}^{(i)}(L) = \vec{C}(0) + \int_0^L \hat{H}(x)\vec{C}^{(i-1)}(x)\,dx, \qquad (2.8)$$

where one can select $\vec{C}^{(0)}(x) = \vec{C}(0)$ at the zero approximation. In this approximation, only the zero-order amplitude with $p = 0$ is initially non-zero. Each next approximation gives two additional non-zero amplitudes, so that a p-th non-

zero amplitude appears in the **p**-th approximation. Figure 2.1 illustrates the process of originating the non-zero amplitudes for a few steps of sequential approximations in Eq.(2.10). Generally, one can see from Fig.2.1 that each **p**-th amplitude can be represented in the form of the series, as follows

$$C_p(L) = \sum_{i=0}^{\infty} C_p^{(p+2i)}, \tag{2.9}$$

where the an **i**-th term of this series is proportional to $\left(\varepsilon_1/\varepsilon_0\right)^{p+2i}$ being the parameter of smallness. The first term of series in Eq.(2.9) is the **p-**fold integral

$$C_p^{(p)}(L) = \int_0^L a_p(x_p) \int_0^{x_p} a_{p-1}(x_{p-1}) \cdots \int_0^{x_3} a_2(x_2) \int_0^{x_2} a_1(x_1)\, dx_1\, dx_2 \ldots dx_p, \tag{2.10}$$

which describes the shortest path form zero to **p**-th order of scattering via the scheme $\mathbf{0 \to 1 \to 2 \to \cdots \to p}$. The second term in Eq.(2.9) corresponds to all the paths from zero to **p**-th order of scattering path. The general form of the second term in Eq.(2.9) is given by

$$C_p^{(p+2)}(L) = \sum_{m=0}^{p+1} \int_0^L a_p(x_{p+2}) \cdots \int_0^{x_{m+3}} a_m(x_{m+2}) \int_0^{x_{m+2}} b_{m-1}(x_{m+1}) \cdots \int_0^{x_2} a_1(x_1) dx_1\, dx_2 \ldots dx_{p+2}. \tag{2.11}$$

The third term in Eq.(2.9) characterizes all the paths from zero to **p**-th orders of scattering with two-fold back-scattering paths and so on. It should be noted that all the integrals could be calculated analytically, although these calculations are rather cumbersome due to a large amount of multi-fold integrals. Nevertheless, such an approach gives the algorithm for general solution to the problem of acousto-optical interaction in isotropic medium. To illustrate how it works lets consider the simplest description for the limiting case of a one-phonon Bragg light

scattering in isotropic medium. In this case, only two orders of scattering with **p** = **0,1** exist and one can put $\mathbf{q_1 \approx q_0}$. A few steps of originating the non-zero amplitudes for sequential approximations in Eq.(2.8) are shown in Fig.2.2. Then, for simplicity one can assume that the Bragg angular condition is satisfied exactly, see Fig.2.3a, so $\eta_0 = 0$ and the matrix $\hat{H}(x)$ takes the form

$$\hat{H}(x) = \begin{pmatrix} 0 & -q_0 \\ q_0 & 0 \end{pmatrix}. \qquad (2.12)$$

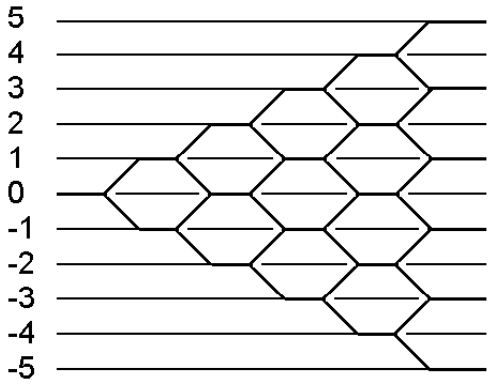

Fig.2.1 General diagram of originating the orders of scattering governed by Eq.(2.8) with the boundary condition $\mathbf{C(0) = (0, 0, \ldots, 0, 1, 0, \ldots, 0)}$.

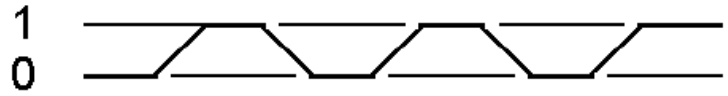

Fig.2.2. Diagram of originating the scattered orders governed by Eq.(2.8) in the regime of a one-phonon light scattering with the boundary condition $\mathbf{C(0) = (1,0)}$.

The corresponding series, see Eq.(2.9), can be easily summarized, and they give the well-known result

a) $$\mathbf{C_0(L) = \sum_{i=0}^{\infty} \frac{(-1)^i}{2i!} (q_0 L)^{2i} = \cos(q_0 L)},$$

b) $$C_1(L)=\sum_{i=0}^{\infty}\frac{(-1)^i}{(2i+1)!}(q_0 L)^{2i+1}=\sin(q_0 L).\qquad (2.13)$$

Equations (2.13) represent the amplitudes for the two orders of scattering during the process of a one-phonon light scattering. As one can noticed they are complementary trigonometric functions.

2.4 A multi-fold Bragg acousto-optical interaction in anisotropic media

Broadly speaking, Eq.(2.4) and (2.5) should be generalized to be applicable to all the regimes of light scattering in anisotropic media. However, leaving aside the most general combined regimes one can nevertheless sake the simplicity of mathematical description and exploit these equations in the most important particular regimes under some restricting conditions. In so doing, let us start from the surfaces' cross-sections for the wave vectors characterizing the acousto-optical interaction in crystals, see Fig.2.3.

Attention will be focused on a two- and three-fold light scattering in optically anisotropic media [2] caused by multi-phonon processes, wherein the plane elastic wave is traveling almost normal to the incident light. In these regimes, the conservation laws are given by $\omega_{m+1}=\omega_m+\Omega$ and $\vec{k}_{m+1}=\vec{k}_m+\vec{K}$ simultaneously (ω_m, $\vec{k}_m$ and Ω, $\vec{K}$ are the cyclic frequencies and the wave vectors of light and acoustic waves, respectively; and $m=0,1,2,3$ as the case requires).

Multi-phonon processes occur at various angles θ_0 of light incidence and the characteristic acoustic frequencies Ω, see Eqs.(1.47), peculiar to just a two- or three-phonon Bragg scattering of light, which are characterized by [2]

Two-fold scattering: $$\sin\theta_0=\left(n_0\right)^{-1}\sqrt{\left|n_0^2-n_1^2\right|}\ , \qquad (2.14)$$

Three-fold scattering: $$\sin\theta_0=3\left(4n_0\right)^{-1}\sqrt{2\left|n_0^2-n_1^2\right|}\ , \qquad (2.15)$$

where $n_0 \neq n_1$ are the refractive indices of a crystal.

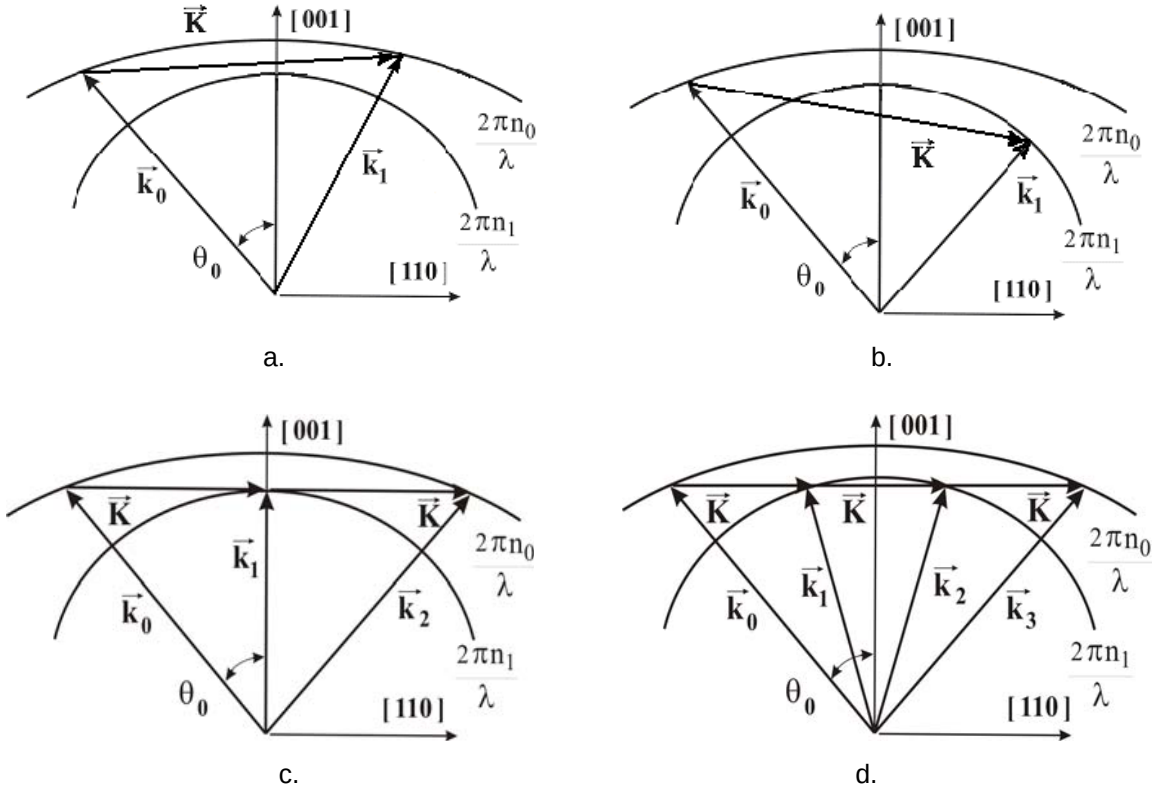

Fig.2.3. Feasible geometries of the acousto-optical interaction in a tellurium dioxide single crystal normal (a) and anomalous (b) one-phonon regime; a two-phonon regime (c), and a three-phonon regime (d).

As a result, the above-used description for isotropic medium, see Eqs.(2.12) and (2.13), can be applied to a one-phonon Bragg light scattering in anomalous regime, with $q_0 \neq q_1$, so that the matrix $\hat{H}(x)$ from Eq.(2.8) takes the form [4]

$$\hat{H}_1(x)=\begin{bmatrix} 0 & -q_1\exp\left(-2i\eta_0 x\right) \\ q_0\exp\left(2i\eta_0 x\right) & 0 \end{bmatrix}. \qquad (2.16)$$

The matrix $\hat{\mathbf{H}}_1(\mathbf{x})$ is in correspondence with Fig.2.2 and the wave vector diagram in Fig.2.3b. When varying the light frequency during the process of light scattering can be omitted as before, the diagrams in Figs.2.3c and 2.3d give the forms of the matrix $\hat{\mathbf{H}}(\mathbf{x})$ in a two-phonon light scattering regime, where $\mathbf{q_0} \approx \mathbf{q_1} \approx \mathbf{q_2}$, and the regime of a three-phonon light scattering, where $\mathbf{q_1} \approx \mathbf{q_2} = \mathbf{q_n}$ and $\mathbf{q_0} \approx \mathbf{q_3} = \mathbf{q_a}$, respectively,

$$\hat{\mathbf{H}}_2(\mathbf{x}) = \begin{bmatrix} 0 & -\mathbf{q_0}\exp(-2i\eta_0 \mathbf{x}) & 0 \\ \mathbf{q_0}\exp(2i\eta_0 \mathbf{x}) & 0 & -\mathbf{q_0}\exp(-2i\eta_1 \mathbf{x}) \\ 0 & \mathbf{q_0}\exp(2i\eta_0 \mathbf{x}) & 0 \end{bmatrix}, \tag{2.17}$$

$$\hat{\mathbf{H}}_3(\mathbf{x}) = \begin{bmatrix} 0 & -\mathbf{q_a}\exp(-2i\eta_0 \mathbf{x}) & 0 & 0 \\ \mathbf{q_a}\exp(2i\eta_0 \mathbf{x}) & 0 & -\mathbf{q_n}\exp(-2i\eta_1 \mathbf{x}) & 0 \\ 0 & \mathbf{q_n}\exp(2i\eta_1 \mathbf{x}) & 0 & -\mathbf{q_a}\exp(-2i\eta_2 \mathbf{x}) \\ 0 & 0 & \mathbf{q_a}\exp(2i\eta_2 \mathbf{x}) & 0 \end{bmatrix}, \tag{2.18}$$

In these two cases, Eq.(2.8) leads to the diagrams presented in Fig.2.4.

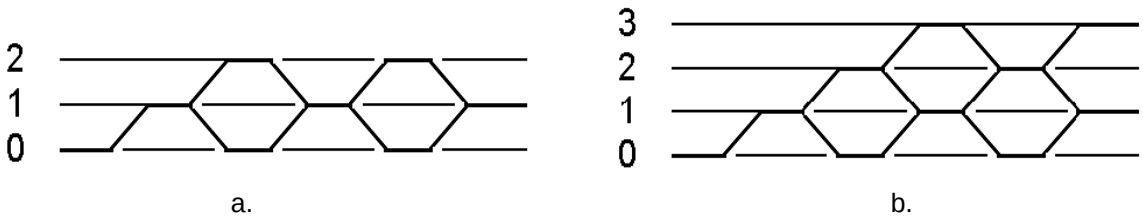

a. b.

Fig.2.4. Diagrams of originating the scattered orders, Eq.(2.8): (a) two-phonon light scattering regime with $\mathbf{C}(0) = (1,\ 0,\ 0)$; (b) three-phonon light scattering regime with $\mathbf{C}(0) = (1,\ 0,\ 0,\ 0)$.

Exploiting the procedure described in Section 2.3 to solve Eq.(2.8) for these regimes with $\eta_p = 0$, in a two-phonon light scattering regime, Eq.(2.9) gives [4]

$$\text{a)}\quad C_0(q_0 x) = 1 - \frac{1}{2}\sum_{i=0}^{\infty}\frac{1}{(2i+2)!}\left(q_0 x\sqrt{2}\right)^{2i+2} = \cos^2\left(\frac{q_0 x}{\sqrt{2}}\right),$$

$$\text{b)}\quad C_1(q_0 x) = \frac{1}{\sqrt{2}}\sum_{i=0}^{\infty}\frac{(-1)^i}{(2i+1)!}\left(q_0 x\sqrt{2}\right)^{2i+1} = \frac{1}{\sqrt{2}}\sin\left(q_0 x\sqrt{2}\right),$$

$$\text{c)}\quad C_2(q_0 x) = \frac{1}{\sqrt{2}}\sum_{i=0}^{\infty}\frac{1}{(2i+2)!}\left(q_0 x\sqrt{2}\right)^{2i+2} = \sin^2\left(\frac{q_0 x}{\sqrt{2}}\right). \qquad (2.19)$$

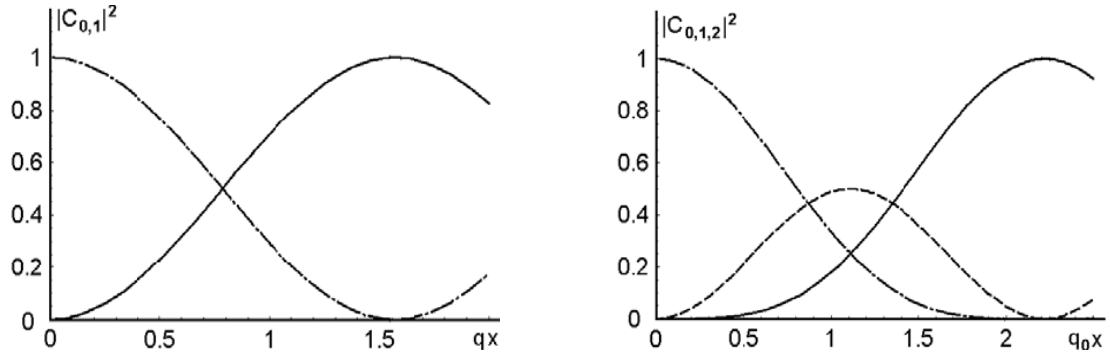

a. b.

Fig.2.5. Intensity distributions: (a) one-phonon light scattering regime with $q = \sqrt{q_0\, q_1}$ (dot-dashed line for $|C_0(qx)|^2$ and solid line for $|C_1(qx)|^2$); (b) two-phonon light scattering regime (dot-dashed line for $|C_0(q_0 x)|^2$, dashed line for $|C_1(q_0 x)|^2$, and solid line for $|C_2(q_0 x)|^2$).

Figure 2.5 shows the intensity distributions for the regimes of a one- and two-phonon light scattering [4].

2.5 A two phonon acousto-optical interaction; the case of a low efficiency

A two-phonon process occurs at an angle θ_0 of light incidence and the characteristic frequency $\Omega = \Omega_2$, peculiar to a two-fold Bragg scattering of light,

as in Eqs.(2.14). And, having that the $\hat{H}(x)$ matrix for this particular regime is given by Eq.(2.17) with $q_0 \approx q_1 \approx q_2$.

Let us estimate the minimal contribution to the second order of scattering. When the efficiency of scattering is small enough, one can do just two iterative steps operating over Eq.(2.7). In this case, the initial amplitude of zero order can be taken to be unity, while the first order's amplitude can be estimated at the first iterative step within a one-fold integrating in Eq.(2.7)

$$\begin{pmatrix} C_0^{(1)} \\ C_1^{(1)} \\ C_2^{(1)} \end{pmatrix} = \begin{pmatrix} 1 \\ 0 \\ 0 \end{pmatrix} + \int_0^L \hat{H}_2(x) \begin{pmatrix} 1 \\ 0 \\ 0 \end{pmatrix} dx = \begin{pmatrix} 1 \\ 0 \\ 0 \end{pmatrix} + \int_0^L \begin{pmatrix} 0 \\ q_0 \exp(2i\eta_0 x) \\ 0 \end{pmatrix} dx \ , \tag{2.20}$$

so that partial amplitudes are given by

$$\text{a) } C_0^{(1)} = 1 \ , \qquad \text{b) } C_0^{(1)} = (q_0 L) \exp(i\eta_0 L) \frac{\sin(\eta_0 L)}{\eta_0 L} \ , \qquad \text{c) } C_2^{(1)} = 0 \ . \tag{2.21}$$

Then, one has to make the second iterative step substituting Eqs.(2.21) in the right hand side of Eq.(2.7), which gives

$$\begin{pmatrix} C_0^{(2)} \\ C_1^{(2)} \\ C_2^{(2)} \end{pmatrix} = \begin{pmatrix} 1 \\ 0 \\ 0 \end{pmatrix} + \int_0^L \hat{H}_2(x) \begin{pmatrix} 1 \\ (q_0 \eta_0^{-1}) \exp(i\eta_0 x) \sin(\eta_0 x) \\ 0 \end{pmatrix} dx \ . \tag{2.22}$$

Using Eq.(2.17), one can find from Eq.(2.22) that [5]

$$C_2^{(2)} = (q_0^2 \eta_0^{-1}) \int_0^L \exp(3i\eta_0 x) \sin(\eta_0 x) \, dx = \\ = 4 q_0^2 L^2 \exp(2i\eta_0 L) \frac{\sin^2(\eta_0 L)}{(\eta_0 L)^2} \ . \tag{2.23}$$

The right hand side of Eq.(2.23) describes the desired minimal contribution to the second order of scattering within a two-phonon acousto-optical interaction.

2.6 A two-fold light scattering; bandwidth of a two-phonon interaction

Using Eq.(2.4), one obtains the evolution equations describing a two-fold light scattering. In this case, see Fig.2.3c, Eq.(2.4) can be considerably simplified by disregarding all the amplitudes $\mathbf{C_P(x)}$ with the exception of $\mathbf{C_0}$, $\mathbf{C_1}$, and $\mathbf{C_2}$, so that

$$\text{a)}\ \frac{\mathbf{dC_0(x)}}{\mathbf{dx}} = -\,\mathbf{q_1 C_1(x)\exp\left(-2i\eta_0 x\right)},$$

$$\text{b)}\ \frac{\mathbf{dC_1(x)}}{\mathbf{dx}} = \mathbf{q_0 C_0(x)\exp\left(2i\eta_0 x\right) - q_2 C_2(x)\exp\left(-2i\eta_1 x\right)},$$

$$\text{c)}\ \frac{\mathbf{dC_2(x)}}{\mathbf{dx}} = \mathbf{q_1 C_1(x)\exp\left(2i\eta_1 x\right)}\ . \qquad (2.24)$$

It may be tolerated on the above-mentioned assumption that the shifts in carrier angular frequencies of light waves, included in the amplitude coefficients for different orders, can be neglected. All the parameters $\mathbf{q_P}$ with $\mathbf{p = 0, 1, 2}$ describe the efficiency of interaction with changing the polarization state of light, and these two steps of scatterings are provided by the same photo-elastic constants. That is why one can put $\mathbf{q_0 = q_1 = q_2 \equiv q}$. The exact solution to Eqs.(2.24) with the simplest boundary conditions $\left|\mathbf{C_0(x=0)}\right|^2 = \mathbf{1}$ and $\mathbf{C_{I,2}(x=0) = 0}$, related to $\mathbf{C_2(x)}$ in this regime [6] can be written as

$$C_2(x) = iq^2 \left\{ \frac{1-\exp\left[i(2\eta - a_0)x\right]}{(a_0 - a_1)(a_0 - a_2)} + \right.$$

$$\left. + \frac{1-\exp\left[i(2\eta - a_1)x\right]}{(a_2 - a_1)(a_0 - a_1)} - \frac{1-\exp\left[i(2\eta - a_2)x\right]}{(a_2 - a_1)(a_0 - a_2)} \right\}. \tag{2.25}$$

Here, a_m are roots of $a^3 - 2(\eta_0 + \eta)a^2 - (2q^2 - 4\eta\eta_0)a + 2q^2\eta = 0$ and $\eta = \eta_0 + \eta_1$ is the mismatch. Generally, as it follows from Eq.(2.25), the intensity of this scattered light wave is periodic in x. When $\eta_0 = \eta_1 = 0$, one can obtain $a_0 = 0$ and $a_{1,2} = \pm q\sqrt{2}$, so that $C_2(x) = \sin^2\left(qx/\sqrt{2}\right)$. Consequently, even 100% of the incident light can be scattered into the second order at $qx = \pi/\sqrt{2}$. One can assume a precise angular alignment and extend η_0 and η_1 into a series in terms of the only frequency detuning $f - f_2$ for the current frequency f relative to the central frequency f_2 determined by Eq.(2.47b). In the second approximation with respect to $f - f_2$, one can obtain from Eq.(2.5b) and the wave vectors diagram, see Fig.2.3c, that [2]

$$\text{a)} \quad 2\eta_0 \approx -\pi\lambda\, n_0^{-1} V^{-2} (f - f_2)^2,$$

$$\text{b)} \quad 2\eta_1 \approx -4\pi\lambda\, n_0^{-1} V^{-2} f_2 (f - f_2) - 7\pi\lambda\, n_0^{-1} V^{-2} (f - f_2)^2. \tag{2.26}$$

Consequently, in the first approximation with respect to $f - f_2$ yields [7]

$$\text{a)} \quad \eta_0 \approx 0, \qquad \text{b)} \quad \eta_1 \approx -2\pi\lambda\, n_0^{-1} V^{-2} f_2 (f - f_2). \tag{2.27}$$

Exploiting Eqs.(2.27) for the sake of simplicity and substituting Eqs.(2.27) into Eq.(2.24), one can draw a three-dimensional distribution for $|C_2(x)|^2$, see Fig.2.6a, and estimate the dependence of the light intensity $|C_2(x)|^2$ on the product $\eta_1 x$, where the mismatch η_1 is connected with the frequency detuning

$(f - f_2) \approx \eta_1 n_0 V^2 (2\pi\lambda f_2)^{-1}$. By taking $\eta_1 x = \pi/2$ with $x = L$, see Fig.2.6b, one can find the frequency bandwidth $\Delta f_2 = 2(f - f_2)$ of a two-phonon light scattering in the form

$$\Delta f_2 \approx \frac{n_0 V^2}{2\lambda f_2 L} \quad . \tag{2.28}$$

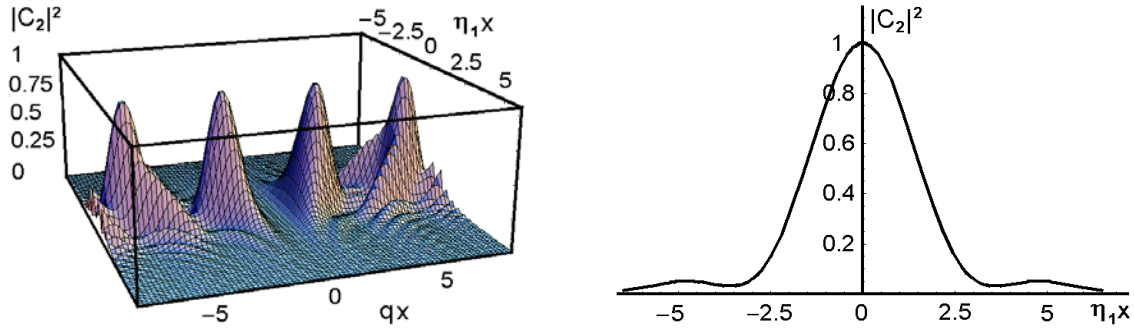

a. b.

Fig.2.6. A three-dimensional distribution (a) for $|C_2(qx, \eta_1 x)|^2$ and (b) the cross-section of that distribution at $qx = \pi/\sqrt{2}$ (b).[7]

It is seen from Fig.2.6a that the first maxima of unity level in this distribution can be reached at $qx = \pm \pi/\sqrt{2}$.

2.7 A three phonon acousto-optical interaction

In the regime of a three-phonon light scattering, one can obtain a quartet of series having the form of Eq.(2.9). After summarizing these cumbersome series and taking $q = q_a/q_n$, one can obtain [4]

$$C_0(q_n L) = \frac{1+\sqrt{1+4q^2}}{2\sqrt{1+4q^2}} \cos\left(\frac{q_n L}{\sqrt{2}} \sqrt{1+2q^2-\sqrt{1+4q^2}} \right) +$$

$$+ \frac{\sqrt{1+4q^2}-1}{2\sqrt{1+4q^2}} \cos\left(\frac{q_n L}{\sqrt{2}} \sqrt{1+2q^2+\sqrt{1+4q^2}} \right),$$

(2.29)

$$C_1(q_n L) = \frac{\sqrt{1+4q^2}-1}{2q\sqrt{2\left(1+4q^2\right)}} \sqrt{1+2q^2+\sqrt{1+4q^2}} \quad \sin\left(\frac{q_n L}{\sqrt{2}} \sqrt{1+2q^2-\sqrt{1+4q^2}} \right) +$$

$$+ \frac{\sqrt{1+4q^2}+1}{2q\sqrt{2\left(1+4q^2\right)}} \sqrt{1+2q^2-\sqrt{1+4q^2}} \quad \sin\left(\frac{q_n L}{\sqrt{2}} \sqrt{1+2q^2+\sqrt{1+4q^2}} \right),$$

(2.30)

$$C_2(q_n L) = \frac{q}{\sqrt{1+4q^2}} \cos\left(\frac{q_n L}{\sqrt{2}} \sqrt{1+2q^2-\sqrt{1+4q^2}} \right) -$$

$$- \frac{q}{\sqrt{1+4q^2}} \cos\left(\frac{q_n L}{\sqrt{2}} \sqrt{1+2q^2+\sqrt{1+4q^2}} \right),$$

(2.31)

$$C_3(q_n L) = \frac{\sqrt{1+2q^2+\sqrt{1+4q^2}}}{\sqrt{2\left(1+4q^2\right)}} \quad \sin\left(\frac{q_n L}{\sqrt{2}} \sqrt{1+2q^2-\sqrt{1+4q^2}} \right) -$$

$$- \frac{\sqrt{1+2q^2-\sqrt{1+4q^2}}}{\sqrt{2\left(1+4q^2\right)}} \quad \sin\left(\frac{q_n L}{\sqrt{2}} \sqrt{1+2q^2+\sqrt{1+4q^2}} \right).$$

(2.32)

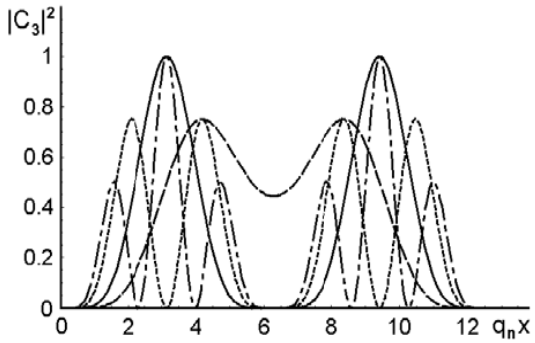

Fig.2.7. Distributions of the light intensity $|\mathbf{C_3}(\mathbf{x})|^2$ vs. $\mathbf{q_n x}$: dashed line: **q = 0.559**, solid line: **q = 0.866**, dotted line: **q = 1.414**, and dot-dashed line: **q = 1.936** [4].

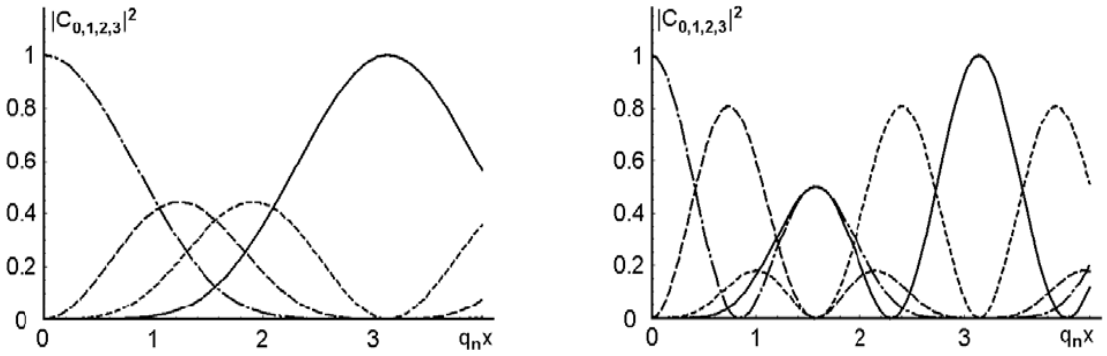

a. b.

Fig.2.8. Distributions of the light intensities with a three-phonon light scattering vs. $\mathbf{q_n x}$: (a) **q = 0.866**, and (b) **q = 1.936**. Dot-dashed lines for $|\mathbf{C_0}(\mathbf{x})|^2$; dashed lines for $|\mathbf{C_1}(\mathbf{x})|^2$; dotted lines for $|\mathbf{C_2}(\mathbf{x})|^2$; and solid lines for $|\mathbf{C_3}(\mathbf{x})|^2$ [4].

As it is seen from Section 2.2, the efficiency of acousto-optical interaction is described by the parameter $\mathbf{q_p}$, which includes the properties of the crystal and is connected with the acoustic power **P**. The acoustic power density $\mathbf{P}/(\mathbf{Lh})$ can be expressed in terms of the deformation γ as $\mathbf{P}/(\mathbf{Lh}) = \tilde{\rho}\mathbf{V}^3\gamma^2/\mathbf{2}$, where $\tilde{\rho}$ is the material density of a TeO_2-crystal. The deformation is connected with the variation ε_1 of the dielectric permeability as $\varepsilon_1 = \varepsilon_0^2 \mathbf{p_{eff}}\,\gamma$, where $\mathbf{p_{eff}}$ is an effective photo-elastic constant, and with Eq.(2.5a) lead to

$$q_p = \frac{\pi}{\lambda \cos\theta_p}\sqrt{\frac{n^6 p_{eff}^2 P}{2\tilde{\rho} V^3 L h}} = \frac{\pi}{\lambda \cos\theta_p}\sqrt{\frac{M_2 P}{2Lh}}, \qquad (2.33)$$

where $M_2 = n^6 p_{eff}^2 / (\tilde{\rho} V^3)$ is the figure of acousto-optical merit inherent in a crystalline material. Figure 2.3 shows that there are two possible types of interactions, noted above as normal and anomalous regimes. It is well known [8] that the anomalous regime in a TeO_2-crystal with the crystallographic orientation shown in Fig.2.3 is characterized by extremely high efficiency due to $p_{eff,an} = 0.5(p_{11} - p_{12})$ and $M_2 = 1.2 \cdot 10^{-15}$ s^3/g.

2.8 A three-fold light scattering; a simplified estimation for the bandwidth of a three-phonon interaction in a tellurium dioxide crystal

Now one can disregard all the amplitudes $C_p(x)$ in Eq.(2.4) with the exception of the amplitudes $C_0, C_1, C_2,$ and C_3, as shown in Fig.2.3d. In so doing, one obtains the following set of only four simplified ordinary differential equations for the amplitudes of the scattered light modes [2],

a) $$\frac{dC_0(x)}{dx} = -q_1 C_1(x) \exp(-2i\eta_0 x),$$

b) $$\frac{dC_1(x)}{dx} = q_0 C_0(x) \exp(2i\eta_0 x) - \tilde{q}_2 C_2(x) \exp(-2i\eta_1 x),$$

c) $$\frac{dC_2(x)}{dx} = \tilde{q}_1 C_1(x) \exp(2i\eta_1 x) - q_3 C_3(x) \exp(-2i\eta_2 x),$$

d) $$\frac{dC_3(x)}{dx} = q_2 C_2(x) \exp(2i\eta_2 x). \qquad (2.34)$$

In Eqs.(2.34), the parameters $\mathbf{q_p}$ ($\mathbf{p = 0,1,2,3}$) can be rewritten in terms of normal and anomalous scattering of light in a uniaxial crystal as $\mathbf{\tilde{q}_1 = \tilde{q}_2 = q_n}$ and $\mathbf{q_0 = q_3 = q_a}$. The factors $\mathbf{q_n}$ and $\mathbf{q_a}$ describe both the material properties relative to normal and anomalous processes of light scattering and the acoustic power density, and they can be taken to be constants at a fixed acoustic signal. Generally $\mathbf{q_n \neq q_a}$, because these factors include different components of the photo-elastic tensor inherent in the selected crystal.

As before, one assume a precise angular alignment and extend η_0, η_1, and η_2 into a series in terms of the only frequency detuning $\mathbf{f - f_3}$ for the current frequency $\mathbf{f}$ relative to the central frequency $\mathbf{f_3}$ determined by Eq.(2.15b). In the first approximation with respect to $\mathbf{f - f_3}$, one can obtain from Eq.(2.5b) and the wave vectors diagram, see Fig.2.3d, that [9]

$$\text{a)}\ \ 2\eta_0 \approx \pi\lambda\, n_0^{-1} V^{-2} f_3 \left(f - f_3\right), \qquad \text{b)}\ \ \eta_1 \approx -3\eta_0, \qquad \text{c)}\ \ \eta_2 \approx -7\eta_0 . \tag{2.35}$$

Substituting Eqs.(2.35) into Eqs.(2.34), one can estimate the dependence of the light intensity $\left|C_3(x)\right|^2$ on the product $\mathbf{q_n x}$. The corresponding plot in Fig.2.9a shows the case inherent in a TeO_2 crystal [10] with the ratio $\mathbf{q = q_a / q_n \approx 4.44}$. Such a value of the ratio $\mathbf{q}$ provides unfortunately a non-monotonic growing of the light intensity $\left|C_3(x)\right|^2$ with $\mathbf{q_n x}$, but includes an opportunity of reaching the 100% maximum intensity at $\mathbf{q_n x \approx 2.82}$ and $\mathbf{q_n x \approx 3.46}$. These two circumstances lead to two possibilities. The first one is connected with operating on an interval of $\mathbf{q_n x}$ between zero and approximately 0.75, so that the efficiency of modulation will not exceed 15%. The second one gives potentially a chance to reach just 100% efficiency, but needs exploiting a bias for the incoming electronic signals associated with the magnitudes $\mathbf{q_n x \approx 2.5}$ or $\mathbf{q_n x} = \pi$ in Fig.2.9a [7].

In the case of $\mathbf{q_n\, x = 2.82}$, one can consider the dependence of the light intensity $\left|\mathbf{C_3(x)}\right|^{\mathbf{2}}$ on the product $\mathbf{2\eta_0\, x}$, see Fig.2.9b, where $\boldsymbol{\eta_0}$ is connected with the frequency detuning $\mathbf{f - f_3 \approx 2\eta_0\, n_0\, V^2 \left(\pi \lambda\, f_3\right)^{-1}}$.

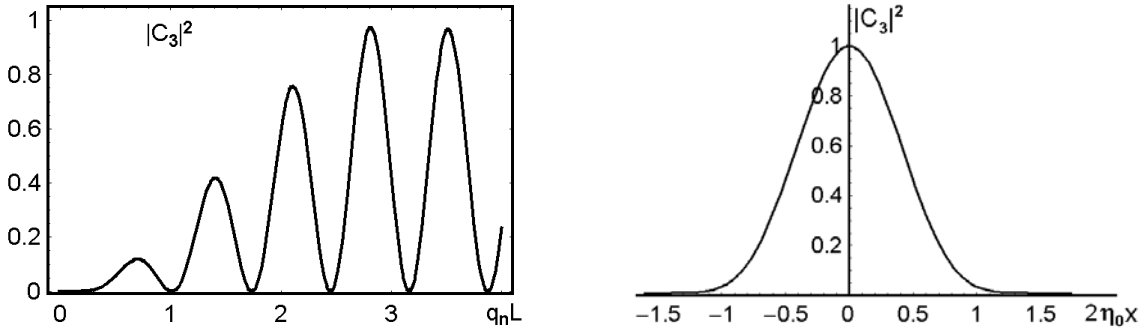

a. b.

Fig.2.9. (a) Distribution of the light intensity $\left|\mathbf{C_3(x)}\right|^{\mathbf{2}}$ vs. $\mathbf{q_n\, x}$ with $\mathbf{q = 4.44}$;

(b) dependence of $\left|\mathbf{C_3(x)}\right|^{\mathbf{2}}$ on $\boldsymbol{\eta_0}\,\mathbf{x}$ with $\mathbf{q_n\, x = 2.82}$ [7].

By analogy with the previous section, one has to take $\mathbf{2\eta_0\, x \approx \pi/6}$ at $\mathbf{x = L}$. Such a selection makes possible determining the bandwidth of a three-phonon light scattering as

$$\Delta \mathbf{f_3 = 2\left(f - f_3\right) \approx \frac{n_0\, V^2}{3\lambda\, f_3\, L}}\ . \qquad (2.36)$$

2.9 Optical activity in a tellurium dioxide crystal

In the optics of crystals, it is worthwhile to analyze the dependence of the electric field strength $\vec{\mathbf{E}}\mathbf{(\vec{r}, t)}$ on the electric field induction $\vec{\mathbf{D}}\mathbf{(\vec{r}, t)}$, as it has been mentioned in Chapter 1, this relation has the form of $\vec{\mathbf{E}}\mathbf{(\vec{r}, t) = \kappa\, \vec{D}(\vec{r}, t)}$ in the local case, where $\boldsymbol{\kappa}$ is the dielectric impermeability tensor whose eigen-values are inverse squares of the main refractive indices inherent in a crystal. However, crystals are characterized by spatial non-locality.

Physically, spatial non-locality means that the electric field strength $\vec{\mathbf{E}}(\vec{\mathbf{r}},\mathbf{t})$ is determined by the electric field induction $\vec{\mathbf{D}}(\vec{\mathbf{r}},\mathbf{t})$ not only at the point $\vec{\mathbf{r}}$, but by values of the electric field induction in some vicinity of a point $\vec{\mathbf{r}}$ as well. In the non-local case, it can be said that one is dealing with the spatial dispersion. When the electric field induction $\vec{\mathbf{D}}(\vec{\mathbf{r}},\mathbf{t})$ is homogeneous in behavior, so that its magnitudes in some vicinity of a point $\vec{\mathbf{r}}$ are equal to its magnitude at the point $\vec{\mathbf{r}}$, the spatial dispersion does not manifest itself. That is why the spatial dispersion can be represented as the dependence of $\vec{\mathbf{E}}(\vec{\mathbf{r}},\mathbf{t})$ on both $\vec{\mathbf{D}}(\vec{\mathbf{r}},\mathbf{t})$ and its spatial derivatives [11]. The effect of the optical activity can be observed in crystals, which exhibit such a dependence on just the first spatial derivatives of the electric field induction $\vec{\mathbf{D}}(\vec{\mathbf{r}},\mathbf{t})$, so that in the first approximation one can write $\vec{\mathbf{E}}(\vec{\mathbf{r}},\mathbf{t}) = \kappa\,\vec{\mathbf{D}}(\vec{\mathbf{r}},\mathbf{t}) + \hat{\mathbf{g}}\,[\partial\vec{\mathbf{D}}(\vec{\mathbf{r}},\mathbf{t})/\partial\vec{\mathbf{r}}]$, where the tensor $\hat{\mathbf{g}} \neq \mathbf{0}$. Due to $\partial\vec{\mathbf{D}}(\vec{\mathbf{r}},\mathbf{t})/\partial\vec{\mathbf{r}} = \mathbf{i}\vec{\mathbf{k}}\vec{\mathbf{D}}$ for the monochromatic light wave with the wave vector $\vec{\mathbf{k}}$ yields

$$\text{a)}\ \ \mathbf{E_j} = \left(\kappa_{\mathbf{jl}} + \mathbf{i}\,\mathbf{g}_{\mathbf{jlm}}\,\mathbf{k_m}\right)\,\mathbf{D_l}\ , \qquad \text{b)}\ \ \vec{\mathbf{E}} = \left(\kappa + \mathbf{i}\,\hat{\mathbf{g}}\cdot\vec{\mathbf{k}}\right)\,\vec{\mathbf{D}}\ . \tag{2.37}$$

The expression in brackets is a modified tensor of the dielectric impermeability. This admixture has an order of the ratio $\mathbf{a}/\lambda$, where $\mathbf{a}$ is the atomic cell size in a crystal, λ is the light wavelength corresponding to the wave vector $\vec{\mathbf{k}} = (\mathbf{2}\pi/\lambda)\,\vec{\mathbf{m}}$, and $\vec{\mathbf{m}}$ is unit vector of the wave normal. If the crystal is optically transparent, a modified tensor of the dielectric impermeability is Hermitian, so that its real-valued part is symmetrical and its imaginary-valued part is anti-symmetrical in behavior. Thus, the tensor $\hat{\mathbf{g}}$ is anti-symmetrical in the first pair of indices, i.e. $\mathbf{g}_{\mathbf{jlm}} = -\,\mathbf{g}_{\mathbf{ljm}}$, while the pseudo-tensor $\hat{\mathbf{G}}$, being dual to the tensor $\hat{\mathbf{g}}$ with an accuracy of the scalar factor $\lambda/(\mathbf{2}\pi)$, can be introduced as

$$\text{a)}\ \ \mathbf{G_{ln}} = \frac{\pi}{\lambda}\hat{\delta}_{\mathbf{jkl}}\,\mathbf{g_{kjn}}\ , \qquad \text{b)}\ \ \frac{\mathbf{2}\,\pi}{\lambda}\delta_{\mathbf{jkl}}\,\mathbf{g_{kjn}} = \hat{\delta}_{\mathbf{jkl}}\,\mathbf{G_{ln}}\ , \tag{2.38}$$

where $\hat{\delta}_{jkl} = (1/2)(j-k)(k-l)(l-j)$ is the unit anti-symmetric Levi-Chivita tensor. Using Eq.(2.38), one can rewrite Eq.(2.37) as

$$\text{a)}\ \ E_j = \left(\kappa_{jl} + i\hat{\delta}_{jlm} G_{mn} m_n\right) D_l\ , \qquad \text{b)}\ \ \vec{E} = \kappa\vec{D} + i\vec{D}\times\hat{G}\cdot\vec{m}\ . \qquad (2.39)$$

Let us take the coordinate system whose axes X_1 and X_2 oriented along the main axes of a crystal, while $X_3 \,||\, \vec{m}$. In these coordinates, Eqs.(2.39) give

$$\text{a)}\ \ E_1 = n_{01}^{-2} D_1 + iG_{33} D_2\ , \qquad \text{b)}\ \ E_2 = n_{02}^{-2} D_2 - iG_{33} D_1\ , \qquad (2.40)$$

because $D_3 = 0$, $\kappa_{12} = 0$, $\kappa_{11} = n_{01}^{-2}$, and $\kappa_{22} = n_{02}^{-2}$. Here, n_{01} and n_{02} are the refractive indices for light waves in absence of the spatial dispersion and $n_{01} \geq n_{02}$. Maxwell's equations for plane waves require that $\vec{E} - \vec{m}\vec{m}\cdot\vec{E} = n^{-2}\vec{D}$. In the chosen coordinate system, it leads to $E_{1,2} = n^{-2} D_{1,2}$. Exploiting these relations, one can exclude the values $E_{1,2}$ from Eq.(2.40), write a set of two homogeneous equations for the values $D_{1,2}$, and obtain the characteristic equation for that set in the form of $(n_{01}^{-2} - n^{-2})(n_{02}^{-2} - n^{-2}) - G_{33}^2 = 0$. Solving this algebraic equation relative to n and taking into account that $|G_{33}| << n_{01}, n_{02}$, one can find [12]

$$\text{a)}\ \ n_1 = n_{01} + \frac{1}{2} n_{01}^3 \rho\, G_{33}\ , \qquad \text{b)}\ \ n_2 = n_{02} - \frac{1}{2} n_{02}^3 \rho\, G_{33}\ , \qquad (2.41)$$

$$\rho = \frac{1}{2G_{33}}\left[\sqrt{(n_{02}^{-2} - n_{01}^{-2})^2 + (2G_{33})^2} - (n_{02}^{-2} - n_{01}^{-2})\right]\ . \qquad (2.42)$$

Equation (2.42) is the main formula for the light polarization ellipticity. Here, $|\rho| \leq 1$ due to $n_{01} \geq n_{02}$, and $\mathbf{sign}\,\rho = \mathbf{sign}\, G_{33}$.

If $\vec{\mathbf{m}}$ is parallel to the optical axis, then $\mathbf{n_{01} = n_{02} = N_o}$ (where $\mathbf{N_o}$ is the main refractive index for the ordinary light wave) and $\rho = \mathbf{sign}\, \mathbf{G_{33}}$, so that two circularly polarized light wave pass along the optical axis and Eqs.(2.41) take the forms [12]

$$\text{a)}\ \ \mathbf{n_1 = N_o + \frac{1}{2} N_o^3 \left| G_{33} \right|}\ , \qquad \text{b)}\ \ \mathbf{n_2 = N_o - \frac{1}{2} N_o^3 \left| G_{33} \right|}. \qquad (2.43)$$

These formulas describe the plots for cross-sections of the refractive index surfaces in the vicinity of an optical axis inherent in a TeO_2 crystal, see Fig.2.10 [12]. If birefringence is not very small, the parameter ρ decreases with deviating the wave normal $\vec{\mathbf{m}}$ from optical axis by an angle ϑ. When $\mathbf{(n_{02}^{-2} - n_{01}^{-2})^2 \approx (2G_{33})^2}$ in Eq.(2.42), yields $\left|\rho\right| = \sqrt{2} - 1 \approx 0.4$. One can calculate that this value leads to the expression $\mathbf{\sin\vartheta = \sqrt{|2G_{33}\,(N_e^{-2} - N_o^{-2})^{-1}|}}$, where $\mathbf{N_e}$ is the main refractive index for the extraordinary light wave. Usually, $\mathbf{G_{33} \approx 10^{-4} - 10^{-5}}$ and $\mathbf{(N_e^{-2} - N_o^{-2}) \approx 0.02 - 0.06}$, therefore ϑ is about a few degrees.

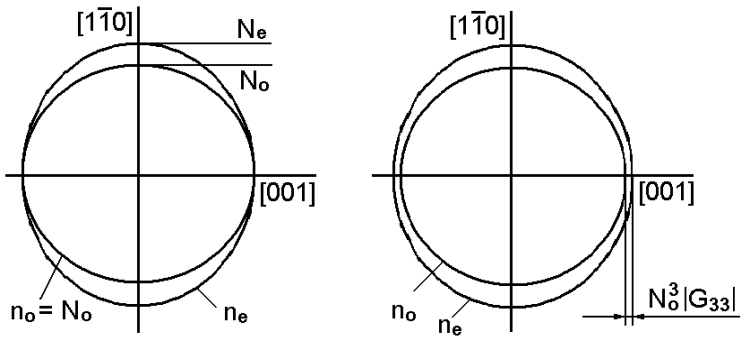

a. b.

Fig.2.10. Two cross-sections of refractive index surfaces in a TeO_2 crystal: (a) hypothetic plot without the effect of optical activity; (b) illustration to the effect of optical activity.

As one can see from the diagrams in Fig.(2.3), one has to take into account the acousto-optical effect in TeO_2, as shown in Fig.(2.10b), because without it the multi-fold interaction of Bragg scattering in anisotropic medium cannot be studied,

since in the ideal situation, Fig.(2.10a), these interactions cannot occur in the $[\mathbf{001}]$-axis.

2.10 Ellipticity of the polarization in a tellurium dioxide crystal

Tellurium dioxide is a uniaxial crystal, so that $\mathbf{n_{02} = N_o}$ is the main refractive index for the ordinary state of polarization, while $\mathbf{n_{01} = n_e(x,z)}$ depends on the direction $\mathbf{(x,z)}$ in a crystal and has the form of an ellipse $\dfrac{\mathbf{x^2}}{\mathbf{N_e^2}} + \dfrac{\mathbf{z^2}}{\mathbf{N_o^2}} = \mathbf{1}$. One is interested in rather small tips from **[001] || z**-axis. Therefore, one can consider the coordinates $\mathbf{(x_0, z_0)}$ of a cross-point of this ellipse with a direct line $\mathbf{x = z\,\tan(\pi\vartheta/180)}$ when the angle ϑ of tip from the **[001]**-axis is measured in angular degrees. In fact, one needs the length of linear segment between the origin of coordinate and this cross-point. These coordinates are given by

$$\text{a)}\ \ \mathbf{x_0} = \frac{\mathbf{N_e N_o \tan(\pi\vartheta/180)}}{\sqrt{\mathbf{N_e^2 + N_o^2\,\tan^2(\pi\vartheta/180)}}}\ , \qquad \text{b)}\ \ \mathbf{z_0} = \frac{\mathbf{N_e N_o}}{\sqrt{\mathbf{N_e^2 + N_o^2\,\tan^2(\pi\vartheta/180)}}}\ , \tag{2.44}$$

consequently,

$$\mathbf{n_e^2 = x_0^2 + z_0^2} = \frac{\mathbf{N_e^2 N_o^2\,[1+\tan^2(\pi\vartheta/180)]}}{\mathbf{N_e^2 + N_o^2\,\tan^2(\pi\vartheta/180)}} \geq \mathbf{n_0^2 \equiv N_o^2}\ . \tag{2.45}$$

Finally, one can write

$$\rho(\vartheta) = \frac{1}{2G_{33}}\left[\sqrt{(N_o^{-2} - n_e^{-2})^2 + (2G_{33})^2} - (N_o^{-2} - n_e^{-2})\right]. \tag{2.46}$$

Dependences of the ellipticity ρ of polarization for the light waves versus the angle ϑ of deflection from the **[001]**-axis in a TeO_2-crystal for a few light wavelengths are depicted in Fig.2.11.

Physically, possible magnitudes of the angle ϑ coincide with the angles θ of incidence or scattering the light beams as $\theta = \vartheta$. The estimations, performed for a TeO_2-crystal for the above-discussed orientation, show that the normal regime of light scattering (using the ordinary state of polarization) meets: 1) $\theta = \mathbf{0.786^o}$ at $\lambda = \mathbf{633\ nm}$, $\mathbf{f = 60\ MHz}$; 2) $\theta = \mathbf{0.657^o}$ at $\lambda = \mathbf{488\ nm}$, $\mathbf{f = 67\ MHz}$; and 3) $\theta = \mathbf{0.505^o}$ at $\lambda = \mathbf{442\ nm}$, $\mathbf{f = 58\ MHz}$. In regard to the anomalous regime of light scattering, it is worthwhile to consider the particular case of a geometry presented in Fig.2.12, because such geometry provides the most wideband acousto-optical interaction with polarization rotation [13]. This geometry requires specific magnitude $\mathbf{f_0}$ of elastic waves frequency [8], but can lead to manifesting a two-phonon light scattering [6] with applying rather powerful acoustic signal to a cell. Under this restricting condition of a small enough acoustic signals, one can calculate that the light incidence angles are determined by $\mathbf{\sin\theta_0 \approx \theta_0 = \lambda f_0 / (n_0 V)}$, so that: 1) $\theta_0 = \mathbf{0.919^o}$ at $\lambda = \mathbf{633\ nm}$, $\mathbf{f_0 = 37.4\ MHz}$; and 2) $\theta_0 = \mathbf{1.132^o}$ at $\lambda = \mathbf{488\ nm}$, $\mathbf{f_0 = 63.3\ MHz}$. The angles of scattering in this regime are definitely smaller than the values of θ_0, as it follows from Fig.2.12.

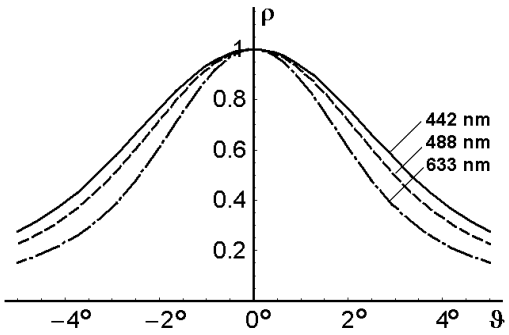

Fig.2.11. The ellipticity ρ of polarization of the light waves vs. the angle ϑ of a tip from the **[001]**-axis in a TeO_2-crystal.

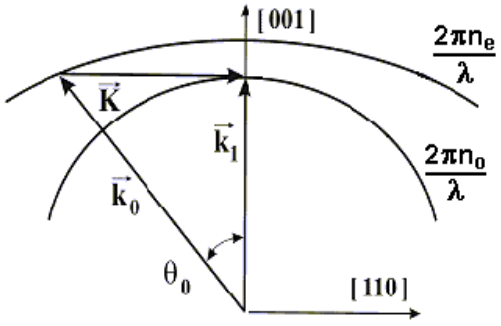

Fig.2.12. A wide-band geometry for the anomalous regime of light scattering in a TeO_2-crystal.

The obtained estimations for the angles show that the range of varying them lies approximately in a limit of $\mathbf{0.5^o - 1.5^o}$. Therefore, the angular dependence for the ellipticity of polarization in Fig.2.11 is perfectly adequate to the real situation in a TeO_2-single crystal [19]. Consequently, the magnitudes of ρ lie between 0.75 and 0.97 in visible optical range, as it can be concluded from Fig.2.11, and moreover, the magnitude of ρ grows as the light wavelength decreases.

2.11 Photo-elastic effect in a tellurium dioxide crystal

Generally, the dielectric impermeability tensor κ becomes to be perturbed under action of the mechanical deformations in a medium and takes the form $\kappa + \hat{\zeta}$, where the symmetrical tensor $\hat{\zeta}$ of second rank represents a small admixture to the tensor κ. One can write

$$\text{a)}\ \ \hat{\zeta} = \mathbf{p}\gamma \qquad \text{b)}\ \ \zeta_{ij} = \mathbf{p}_{ijkl}\,\gamma_{kl}\ , \tag{2.47}$$

because even the first approximation is quite enough for crystalline materials. As it has mentioned in Chapter 1, $\hat{\mathbf{p}}$ is the tensor of the fourth rank for photo-elastic coefficients. Mechanical deformations are described in the first approximation by the symmetric deformation tensor as

$$\text{a)}\ \ \gamma_{kl} = \frac{1}{2K}\left(\frac{\partial \vec{u}_k}{\partial x_l} + \frac{\partial \vec{u}_l}{\partial x_k}\right), \qquad \text{b)}\ \ \gamma_{kl} = \gamma_{lk}\ , \tag{2.48}$$

where $\vec{\mathbf{u}}$ is the unit vector of displacement in the acoustic wave. Due to $\partial \vec{\mathbf{u}}(\vec{\mathbf{r}}, \mathbf{t})/\partial \vec{\mathbf{r}} = \mathbf{i}\vec{\mathbf{K}} \cdot \vec{\mathbf{u}}$ for the monochromatic plane acoustic wave with the wave vector $\vec{\mathbf{K}} = \mathbf{K}\vec{\mathbf{m}}$, yields $\gamma = \frac{1}{2}\left(\vec{\mathbf{u}} \cdot \vec{\mathbf{m}} + \vec{\mathbf{m}} \cdot \vec{\mathbf{u}}\right)$. Practically, it is more convenient to operate by these tensors in so-called matrix notations, $\zeta_\lambda = \zeta_{ij}$, $\mathbf{p}_{\lambda\mu} = \mathbf{p}_{ijkl}$, and $\gamma_\mu = \gamma_{kl}$, so that $\zeta_\lambda = \mathbf{p}_{\lambda\mu}\gamma_\mu$.

The characteristic surface of the dielectric impermeability tensor can be written as $\vec{\mathbf{r}}\cdot\boldsymbol{\kappa}\cdot\vec{\mathbf{r}}=\mathbf{1}$ or in components as $\kappa_{ij}\,x_i\,x_j=1$. It represents the optical indicatrix. Physical axes of the optical indicatrix determine orientation for a pair of the eigen-vectors of electric induction in a crystal. That is why the quadratic form

$$\text{a)}\ \ p_{eff}=\vec{d}^{(s)}\cdot\hat{\zeta}\cdot\vec{d}^{(i)}\ , \qquad \text{b)}\ \ p_{eff}=d_i^{(s)}\zeta_{ij}d_j^{(i)}\ , \tag{2.49}$$

describes the effective photo-elastic constant p_{eff} of scattering, i.e. the efficiency of converting the initial state of light polarization, described by the unit electric induction vector $\vec{d}^{(i)}$ into the scattered state of light polarization, characterized by the unit electric induction vector $\vec{d}^{(s)}$ due to the photo-elastic effect in a crystal. In the particular case of a TeO_2-crystal whose point symmetry group is **422**, Eq.(1.32) becomes [14],

$$p_{\lambda\mu}=\begin{pmatrix} p_{11} & p_{12} & p_{13} & 0 & 0 & 0\\ p_{12} & p_{11} & p_{13} & 0 & 0 & 0\\ p_{31} & p_{31} & p_{33} & 0 & 0 & 0\\ 0 & 0 & 0 & p_{44} & 0 & 0\\ 0 & 0 & 0 & 0 & p_{44} & 0\\ 0 & 0 & 0 & 0 & 0 & p_{66} \end{pmatrix}. \tag{2.50}$$

Then, let us assume that slow shear acoustic wave is passing along the $[1\bar{1}0]$-axis in a TeO_2-crystal whose vector of displacement is oriented along the **[110]**-axis. It means that $\vec{m}=(1/\sqrt{2})(1,-1,0)$ and $\vec{u}=(1/\sqrt{2})(1,1,0)$. The corresponding normalized tensor of deformations is given by

$$\text{a)}\ \ \gamma_{kl}=\frac{1}{2}\begin{pmatrix} 1 & 0 & 0\\ 0 & -1 & 0\\ 0 & 0 & 0 \end{pmatrix}, \qquad \text{b)}\ \ \gamma_{\mu}=\left(1,-1,0,0,0,0\right). \tag{2.51}$$

Performing the matrix multiplication and converting the product $p_{\lambda\mu}\gamma_{\mu}$ from the matrix notation to the conventional one, yield

$$\zeta_{ij} = p_{ijkl}\,\gamma_{kl} = \frac{1}{2}\left(p_{11} - p_{12}\right)\begin{pmatrix} 1 & 0 & 0 \\ 0 & -1 & 0 \\ 0 & 0 & 0 \end{pmatrix}. \qquad (2.52)$$

Now, the eigen-state orts of polarization, see Chapter 1, can be applied to estimate the scattering photo-elastic properties of a TeO_2-crystal for the above-mentioned orientation. For this purpose, one may exploit a two-dimensional reduced version of the matrix admixtures $\tilde{\zeta}_{ij}$ to the dielectric impermeability tensor κ instead of Eq.(2.52), which is additionally normalized by the factor $(p_{11} - p_{12})/2$. It can be done, because all the angles of incidence and scattering are rather small, lie in a range of $0.5^o - 1.5^o$, and do not exceed two angular degrees. One can find magnitudes of the effective photo-elastic constants, normalized by the factor $(p_{11} - p_{12})/2$, in the regime with conserving the state of polarization, i.e. with the normal regime of scattering, as

$$\text{a)}\ \left|2\rho G_{33}\right| << \left|1-\rho^2\right|, \qquad \text{b)}\ \tilde{p}_{eff}(2\to 2) = \vec{\nu}_2^{\,+}\,\tilde{\zeta}_{ij}\,\vec{\nu}_2 = \frac{\rho^2 - 1}{1+\rho^2}. \qquad (2.53)$$

Together with this, one can obtain magnitudes of the normalized effective photo-elastic constants in the regime with changing the state of polarization, i.e. with the anomalous regime of scattering, as

$$\text{a)}\ \tilde{p}_{eff}(1\to 2) = \vec{\nu}_2^{\,+}\,\tilde{\zeta}_{ij}\,\vec{\nu}_1 = \frac{-2i\rho}{1+\rho^2}\exp\left[i\left(\varphi_1 - \varphi_2\right)\right],$$

$$\text{b)}\ \tilde{p}_{eff}(2\to 1) = \vec{\nu}_1 + \vec{\zeta}_{ij}\,\vec{\nu}_2 = \frac{2i\rho}{1+\rho^2}\exp\left[i\left(\varphi_2 - \varphi_1\right)\right]. \qquad (2.54)$$

Then, one can estimate the scattering photo-elastic properties of a TeO_2-crystal in the above-mentioned orientation when optical activity has been taken into account.

In the case when Eq.(2.40) is included in consideration, a two-dimensional reduced version of the matrix admixtures $\tilde{\zeta}_{ij}$ to the dielectric impermeability tensor κ has the form $\tilde{\zeta}_{ij} = \begin{pmatrix} 1 & iG_{33} \\ -iG_{33} & -1 \end{pmatrix}$. Again, one can consider the regime with conserving the polarization state, i.e. with the normal regime of scattering, as

$$\text{a)}\ \ \hat{\rho}_{eff}(1 \to 1) = \vec{\nu}_1^{+}\,\tilde{\zeta}_{ij}\,\vec{\nu}_1 = \frac{1-\rho^2-2\rho G_{33}}{1+\rho^2}\ ,$$

$$\text{b)}\ \ \hat{\rho}_{eff}(2 \to 2) = \vec{\nu}_2^{+}\,\tilde{\zeta}_{ij}\,\vec{\nu}_2 = \frac{\rho^2-1+2\rho G_{33}}{1+\rho^2}\ . \qquad (2.55)$$

In the regime with changing the polarization state, i.e. with the anomalous regime of scattering, one can obtain [12]

$$\text{a)}\ \ \hat{\rho}_{eff}(1 \to 2) = \vec{\nu}_2^{+}\,\tilde{\zeta}_{ij}\,\vec{\nu}_1 = \frac{-2i\rho - i(1-\rho^2)G_{33}}{1+\rho^2}\exp\left[i(\varphi_1-\varphi_2)\right],$$

$$\text{b)}\ \ \hat{\rho}_{eff}(2 \to 1) = \vec{\nu}_1^{+}\,\tilde{\zeta}_{ij}\,\vec{\nu}_2 = \frac{2i\rho + i(1-\rho^2)G_{33}}{1+\rho^2}\exp\left[i(\varphi_2-\varphi_1)\right].$$

(2.56)

Let us start our estimations from Eqs.(2.55), one has to compare $\left|1-\rho^2\right|$ and $\left|\ 2\rho G_{33}\ \right|$ with each other. In the worst case $\vartheta = 0.5^{o}$, one can take: 1) $\rho = 0.97$, $G_{33} = 5.60 \cdot 10^{-5}$ and find $\left|1-\rho^2\right| = 0.05910$, $\left|2\rho G_{33}\right| = 0.00011$ at $\lambda = 442\ nm$; 2) $\rho = 0.96$, $G_{33} = 2.83 \cdot 10^{-5}$ and calculate $\left|1-\rho^2\right| = 0.07841$, $\left|2\rho G_{33}\right| = 0.00005$ at $\lambda = 633\ nm$. These estimations show that $\left|2\rho G_{33}\right| << \left|1-\rho^2\right|$ in a TeO_2-crystal, so that one can practically exploit Eqs.(2.53) instead of Eqs.(2.55).

Then, comparing $|2\rho|$ and $\left|(1-\rho^2)G_{33}\right|$ in Eqs.(2.56). The worst case is associated with $\vartheta = 1.5^o$, and one can take: 1) $\rho = 0.85$, $G_{33} = 5.60 \cdot 10^{-5}$ and find $\left|(1-\rho^2)G_{33}\right| = 0.000016$, $|2\rho| = 1.700000$ at $\lambda = 442\ nm$; 2) $\rho = 0.75$, $G_{33} = 2.83 \cdot 10^{-5}$ and calculate $\left|(1-\rho^2)G_{33}\right| = 0.000012$, $|2\rho| = 1.500000$ at $\lambda = 633\ nm$. These calculations demonstrate that $\left|(1-\rho^2)G_{33}\right| << |2\rho|$ in a TeO_2-crystal, so that practically one can use Eqs.(2.54) instead of Eqs.(2.56). Finally, let us use Eqs.(2.53) and (2.54) to estimate the modulus of the normalized effective photo-elastic constants in terms of the eigen-states of polarization as

$$\text{a)}\ \left|\tilde{p}_{eff}(i \to i)\right| = \left|\frac{1-\rho^2}{1+\rho^2}\right|, \qquad \text{b)}\ \left|\tilde{p}_{eff}(i \to j)\right| = \left|\frac{2\rho}{1+\rho^2}\right|,$$

$$\text{c)}\ \ q = \frac{\left|\tilde{p}_{eff}(i \to j)\right|}{\left|\tilde{p}_{eff}(i \to i)\right|} = \left|\frac{2\rho}{1-\rho^2}\right|, \tag{2.57}$$

where $(i, j) = (1, 2)$, and $\left|\tilde{p}_{eff}(i \to i)\right| < \left|\tilde{p}_{eff}(i \to j)\right|$ with $\rho \in [0.7, 1.0]$. Thus, the efficiency of anomalous light scattering exceeds the efficiency of normal scattering in a TeO_2-crystal under the chosen orientation. Using $\tilde{\zeta}_{ij}$ to estimate the effective photo-elastic constants under action of an external light beams conserving the state of light polarization, one can exploit $\vec{\sigma}_1$ and $\vec{\sigma}_2$ and write [12]

$$\text{a)}\ p^*_{eff}(1 \to 1) = \vec{\sigma}_1{}^{+}\,\tilde{\zeta}_{ij}\,\vec{\sigma}_1 = \frac{1-\rho_i^2}{1+\rho_i^2}, \qquad \text{b)}\ p^*_{eff}(2 \to 2) = \vec{\sigma}_2{}^{+}\,\tilde{\zeta}_{ij}\,\vec{\sigma}_2 = \frac{\rho_i^2-1}{1+\rho_i^2}. \tag{2.58}$$

One can also obtain magnitudes of the normalized effective photo-elastic constants in the regime with changing the state of polarization inherent in an external beam, i.e. with the anomalous regime of scattering, that

a) $p^{*}_{eff}(1\to 2)=\vec{\sigma}_2{}^{+}\,\tilde{\zeta}_{ij}\,\vec{\sigma}_1=$

$$=\frac{-1}{1+\rho_i^2}\left[2i\rho_i\cos(2\phi)+(1+\rho_i^2)\sin(2\phi)\right]\exp\left[i(\psi_1-\psi_2)\right],$$

b) $p^{*}_{eff}(2\to 1)=\vec{\sigma}_1{}^{+}\,\tilde{\zeta}_{ij}\,\vec{\sigma}_2=$

$$=\frac{1}{1+\rho_i^2}\left[2i\rho_i\cos(2\phi)-(1+\rho_i^2)\sin(2\phi)\right]\exp\left[i(\psi_2-\psi_1)\right].$$

(2.59)

The corresponding plots are show in Fig.2.13.

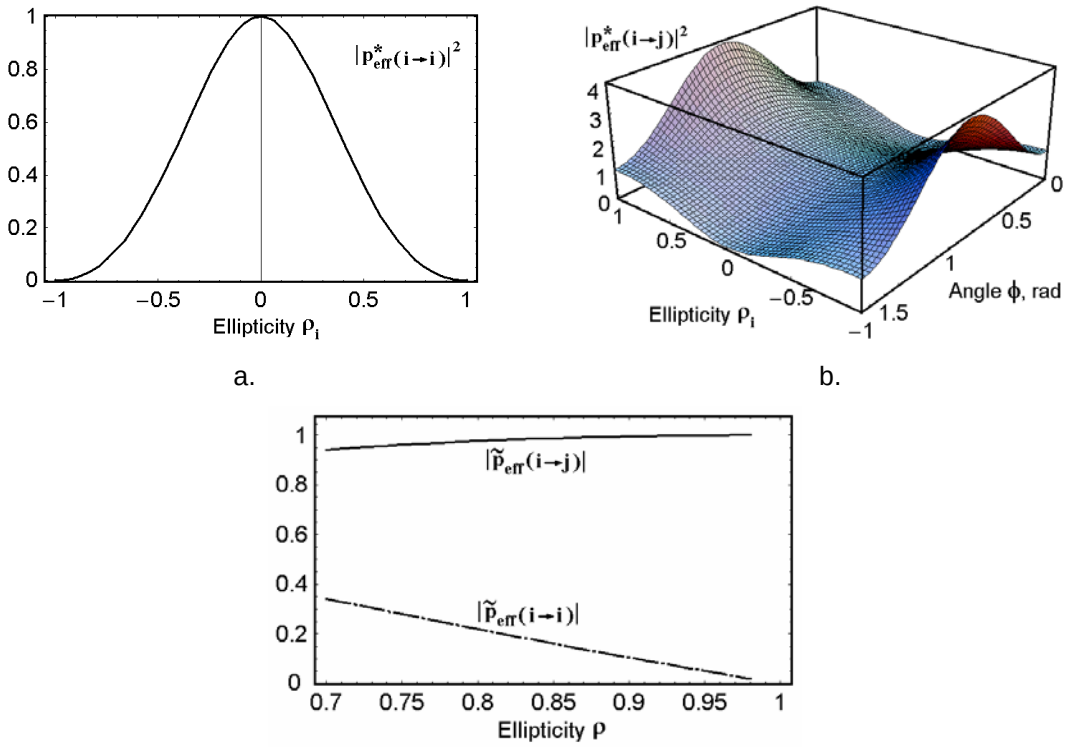

a. b.

c.

Fig.2.13. Squared moduli of the normalized effective photo-elastic constants (a) $\left|p^{*}_{eff}(i\to i)\right|$, (b) $\left|p^{*}_{eff}(i\to j)\right|$ vs. the ellipticity ρ_i as well as the rotation angle ϕ.[19], and (c) $\left|\tilde{p}_{eff}(i\to i)\right|$ and $\left|\tilde{p}_{eff}(i\to j)\right|$ vs. the ellipticity ρ in a TeO_2-crystal.

It is well known [2] that the anomalous regime in a TeO_2-crystal with the crystallographic orientation shown in Fig.2.10 is characterized by extremely high efficiency due to $\mathbf{p_{eff,\,an} = 0.5\,(p_{11} - p_{12})}$ and $\mathbf{M_2} = 1.2 \cdot 10^{-15}$ s^3/g. By contrast, the theoretically predicted magnitude of the effective photo-elastic constant $\mathbf{p_{eff,\,n}}$ in the normal regime is much smaller than in the case of the same orientation for a crystal.

2.12 Resolution of the acousto-optical modulators made of TeO_2 crystals

Generally, the momentum $\mathbf{p}$ of a photon is connected with the wave number $\mathbf{k}$ as $\mathbf{p = hk/(2\pi)}$, where $\mathbf{h}$ is the Planck constant, so one may spect an uncertainty $\mathbf{\delta p = h(\delta k)/(2\pi)}$ in the momentum related to the uncertainty in the wave number $\mathbf{\delta k}$ of a photon. Also, the momentum $\mathbf{\tilde{P}}$ of a phonon is connected with the wave number $\mathbf{K}$ as $\mathbf{\tilde{P} = hK/(2\pi)}$, and an uncertainty $\mathbf{\delta\tilde{P} = h(\delta K)/(2\pi)}$ in the momentum related to the uncertainty in the wave number $\mathbf{\delta K}$ of a phonon is spected. Then, because the phonon wave number is $\mathbf{K = 2\pi f/V}$, one can note that an uncertainty of the phonon wave number, in its turn, can be explained in terms of an uncertainty in the phonon frequency $\mathbf{\delta f}$ as $\mathbf{\delta K = 2\pi(\delta f)/V}$. The limiting case of Bragg light scattering in acousto-optics is determined by the well-known [15] dimensionless inequality $\mathbf{\lambda f^2 L/V^2 >> 1}$. In this limit an uncertainty in the momentum of the issuing photon is characterized by the relation $\mathbf{\delta p \approx \delta P}$, and consequently, $\mathbf{\delta k \approx \delta K}$, because they both are localized inside the same spatial area determined by the aperture $\mathbf{D}$. Together with this, the value of $\mathbf{\delta k}$ is significantly smaller than the photon wave number variation connected with scattering from the order $\mathbf{j}$ to the order $\mathbf{j+1}$, i.e. $\mathbf{\left|\vec{k}_{j+1} - \vec{k}_j\right| \approx K >> \delta K \approx \delta k}$. By

this is meant that the wave numbers of both the photons and the phonons are well determined in the Bragg limit of acousto-optical interaction. Due to the Heisenberg uncertainty principle [16] proclaims that $\delta p\, \delta x \sim h$ with $\delta x \approx D$, one can find that

$$\delta f \approx V/D. \tag{2.60}$$

This value determines the frequency resolution of acousto-optical modulators independently on the number of phonons taking part in a process of the Bragg light scattering. The number N_m of resolvable spots for each of the light scattering regimes under consideration has the form of $N_m = \Delta f_m / \delta f$. In so doing, one can use Eqs.(2.28) and (2.36) for two- and three-phonon processes and compare them with the numbers N_1 for the normal one-phonon light scattering [2,3],

$$\text{a)}\ N_1 = \frac{2nVD}{\lambda f_1 L}, \qquad \text{b)}\ N_2 = \frac{n_0 VD}{2\lambda f_2 L}, \qquad \text{c)}\ N_3 = \frac{n_0 VD}{3\lambda f_3 L}. \tag{2.61}$$

Then, one can consider the angular resolution of the acousto-optical modulators in these three regimes and take the following angular-frequency dependences

$$\sin\theta_m = \frac{m}{2}\frac{K}{k_m} = \frac{m}{2}\frac{\lambda f_m}{n_0 V}, \tag{2.62}$$

which are true within the limits of the corresponding bandwidths Δf_m. These equations directly follow from Fig.2.3c for $m = 2$, and from Fig.2.3d for $m = 3$, respectively. It is easily to find from Eq.(2.62) that small variations $\mathbf{var}\,\theta_m$ of the angles θ_m are connected with the corresponding variations $\mathbf{var}\, f_m$ of the frequencies f_m as

$$\mathbf{var}\ \theta_m = \frac{m\lambda}{2n_0 V \cos\theta_m}\ \mathbf{var}\ f_m. \tag{2.63}$$

The angular size of a resolvable spot is determined by the width of the light beam or the modulator's aperture D as $\delta\theta \approx \lambda/(n_0 D)$, which is the angular spreading

of the optical beam. Using this ratio, one can estimate the number of resolvable spots $\mathbf{M_m}$ located inside a two-side small angular interval of varying as

$$\mathbf{M_m = \frac{2\,var\ \theta_m}{\delta\theta} = m\left(\frac{D}{V\cos\theta_m}\right)\ var\ f_m}\ , \qquad (2.64)$$

where practically $\mathbf{\cos\theta_m \approx 1}$. In Eq.(2.64), the term $\mathbf{T = D/V\cos\theta_m}$ describes the time of scanning the light beam through just one resolvable spot, i.e. characterizes the speed of modulator's operation. Among other things one can put that values of the variations $\mathbf{var\ f_m}$ are the same for all $\mathbf{m = (1, 2, 3)}$. In this particular case, Eq.(2.64) shows that one and the same modulator operating in one and the same frequency bandwidth provides the number of resolvable spots directly proportional to the number $\mathbf{m}$ of phonons taking part in the light scattering process. In other words, the exploitation of a two- or/and three-phonon light scattering provides growing the specific resolution of modulators under consideration.

2.13 Estimations and experimental results

It is worthwhile to consider the experimental data from a few practical estimations. A TeO_2 single crystal has been selected as a material for the acousto-optical cell. This crystal has rather dispersive refractive index $\mathbf{n_0}$, whose values are $\mathbf{n_0}$ = 2.26 at λ = 633 nm, $\mathbf{n_0}$ = 2.33 at λ = 488 nm and $\mathbf{n_0}$ = 2.35 at λ = 442 nm [17], and the acoustic wave velocity is $\mathbf{V = 0.616 \cdot 10^5}$ cm/s for the slow shear acoustic mode running exactly along the $\mathbf{[1\bar{1}0]}$-axis with the displacement vector directed along **[110]**-axis [17]. The figure of merit for this shear mode wave in a TeO_2-crystal is $\mathbf{M_2 = 1200 \cdot 10^{-18}}$ s^3/g [8,17], which is the highest one for solid-state acousto-optical materials in the visible range known up to now. At first, one has to check the realization of just Bragg regime for light scattering in the chosen cell. In

such a regime, the Klein-Cook parameter [15] $\mathbf{Q = \lambda L f^2 / (n V^2)}$ should exceed unity. Operating at $\lambda = \mathbf{488}$ nm and at the lowest expected acoustic wave frequency $\mathbf{f = 40}$ MHz with $\mathbf{L = 1.0}$ cm one can calculate $\mathbf{Q \approx 10}$, which confirms the Bragg character of light scattering in the regime selected within the visible range of light spectrum. Then, to estimate the frequency bandwidth $\Delta \mathbf{f_1}$ of acousto-optical interaction with the anomalous one-phonon light scattering [13] as well as a two- and three-phonon processes of scattering one can use Eqs.(2.28) and (2.36) with substituting $\delta\varphi = \mathbf{V/(L f)}$ by the enlarged value of $\delta\varphi_{\mathbf{E}} = \mathbf{20.7}\,\delta\varphi$ due to the contribution from the acoustic anisotropy in the (**110**)-plane of TeO_2 crystal [18]. Thus, one can write [7]

$$\text{a)}\ \ \Delta \mathbf{f_1} \approx \mathbf{2V}\sqrt{\mathbf{2n_0}\,|\mathbf{n_0^2 - n_1^2}|^{1/2}\,\lambda^{-1}\Delta\varphi_{\mathbf{E}}}\ , \qquad \text{b)}\ \ \Delta \mathbf{f_2} \approx \frac{\mathbf{n_0 V}}{\mathbf{2}\lambda}\Delta\varphi_{\mathbf{E}}\ ,$$

$$\text{c)}\ \ \Delta \mathbf{f_3} \approx \frac{\mathbf{n_0 V}}{\mathbf{3}\lambda}\Delta\varphi_{\mathbf{E}}\ . \qquad (2.65)$$

Using Eqs.(2.28) and (2.36), i.e. with $\delta\varphi \approx \mathbf{10^{-3}}$ rad, the following set of values can be obtained: $\Delta \mathbf{f_1} \approx$ 33 MHz at $\lambda = \mathbf{633}$ nm, $\Delta \mathbf{f_2} \approx$1.4 MHz at $\lambda = \mathbf{488}$ nm, and $\Delta \mathbf{f_3} \approx$1.2 MHz at $\lambda = \mathbf{442}$ nm. By contrast, numerical estimations based on Eqs.(2.65), give $\Delta \mathbf{f_1} \approx$ 151 MHz at $\lambda = \mathbf{633}$ nm, $\Delta \mathbf{f_2} \approx$28 MHz at $\lambda = \mathbf{488}$ nm, and $\Delta \mathbf{f_3} \approx$15 MHz at $\lambda = \mathbf{442}$ nm. Practically, of course, both these sets of data should be considered only as lower and upper limits of bandwidths, respectively, for acousto-optical processes under analysis, because the first set does not include the acoustic anisotropy, while the second one does not take into account a number of the restricting external factors. Nevertheless, Eqs.(2.65) predict that the contributions caused by the acoustic anisotropy are able to enlarge the frequency bandwidth of acousto-optical interaction in comparison with the case of pure acoustic diffraction.

The experimental studies consist in two parts. The first one include measuring the bandwidths of acousto-optical interaction in the regimes of a one-, two-, and three-phonon light scattering. General schematic arrangement of the corresponding set-up for these measurements is presented in Fig.2.14 [7]. Lasers with three different wavelengths were exploited to observe a triplet of the wide-band intensity-frequency distributions, Fig.2.15 [7]. A set of the values recorded during these experiments with the same TeO_2–cell includes: $\Delta \mathbf{f_1} \approx$ 31 MHz at $\lambda = \mathbf{633}$ nm, $\Delta \mathbf{f_2} \approx 16$ MHz at $\lambda = \mathbf{488}$ nm, and $\Delta \mathbf{f_3} \approx 4.5$ MHz at $\lambda = \mathbf{442}$ nm. The measured acousto-optic bandwidth $\Delta \mathbf{f_1} \approx \mathbf{31}$ MHz is close to estimation without the acoustic anisotropy. Moreover, the value of $\Delta \mathbf{f_1} \approx \mathbf{31}$ MHz represents approximately an octave at the central frequency 60 MHz, see Fig.2.15a.

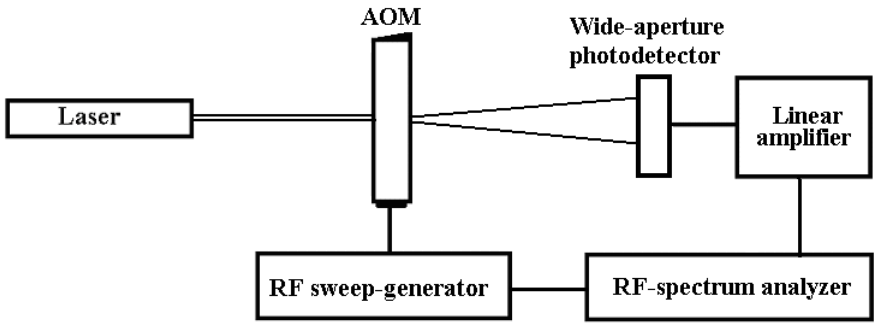

Fig.2.14. General schematic arrangement for measuring the frequency bandwidths of a TeO2-modulator in various regimes of multi-phonon light scattering.

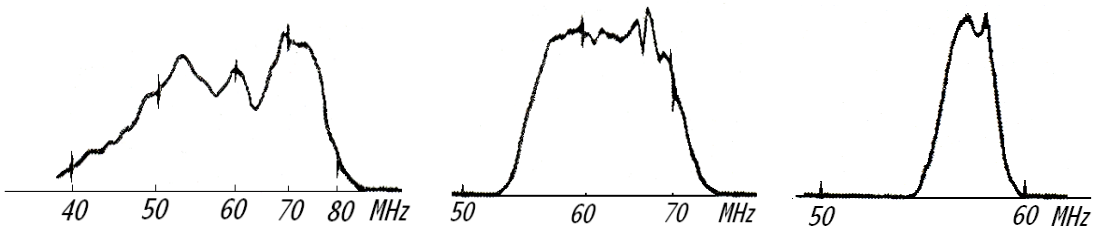

a. b. c.

Fig.2.15. The intensity-frequency distributions for a one-phonon (a), two-phonon (b), and three-phonon (c) light scattering processes in tellurium dioxide single crystal.

These facts mean that Δf_1 is mainly determined by the bandwidths of piezoelectric transducer by itself, so that acoustic anisotropy has no chances to manifest itself in the regime of a one-phonon anomalous light scattering. The restriction appearing from the transducer covers the effect of acoustic anisotropy, and that is why the experimental value of 31 MHz is too close to the numerical estimation of 33 MHz. The measured acousto-optical bandwidths $\Delta f_2 \approx 16$ MHz and $\Delta f_3 \approx 4.5$ MHz are rather far from both the above-made estimations, see Figs.2.15b and 2.15c. Because all the measurements had been done with the same acousto-optical cell, it is unlikely that influence of the piezoelectric transducer took place in the last two cases. However, together with broadening the bandwidth due to that anisotropy, other physical factor exists, which has the restricting effect. This effect is connected with varying the wave vectors on the diagrams in Figs.2.3c and 2.3d, because it is ultimately conditioned by the necessity of meeting the conservation laws at all the intermediate stages of multi-phonon light scattering. That is why a contribution from the acoustic anisotropy is not able to exhibit itself by the full measure; experimentally one can observe a sort of balance between the contributions inherent in anisotropic spreading of the acoustic beam and approximate fulfilling of the conservation laws in intermediate stages. The proposed analytical model in Section 2.11 of a multi-phonon light scattering in anisotropic medium as well as the optical modulators based on TeO_2 crystal ($V = 0.616\ 10^5$ cm/s) with $L = 10$ mm were examined experimentally in the visible range. At an accurate alignment of the Bragg angle θ_B, the acoustic carrier frequency $f = \Omega/2\pi$ tuned from 50 to 80 MHz and with the acoustic power density P/Lh varied as well. In particular, it has been observed almost 100% efficiency within a two-phonon light scattering into the optical mode C_2 at $P/Lh \approx 2$ mW/mm^2 and $\lambda = 488$ nm, see Fig.2.15b. Within a three-phonon process, the efficiency of light scattering into the optical mode C_3 was about 12% at $P/Lh \approx 4$ mW/mm^2 and $\lambda = 442$ nm, see Fig.2.15c.

The last result means that the value of **q** lies in a range between 4 and 5 and can be rather adequately characterized by $\mathbf{q} = \mathbf{4.44}$ in agreement with recently obtained data [7].

The second part of the experiments was related to estimate the possible resolution of modulators under consideration. In so doing, the experimental set-up was re-arranged at the scheme shown in Fig.2.16 [7], with scanning very narrow slit diaphragm was applied to our needs. This technique gives an opportunity to fix the continuous distribution of light intensity in the lobes of an individual spot really carefully in rather wide dynamic range of about 25 dB. In parallel, the corresponding numerical estimations have been carried out to provide the possibility of comparison with the experimental data obtained.

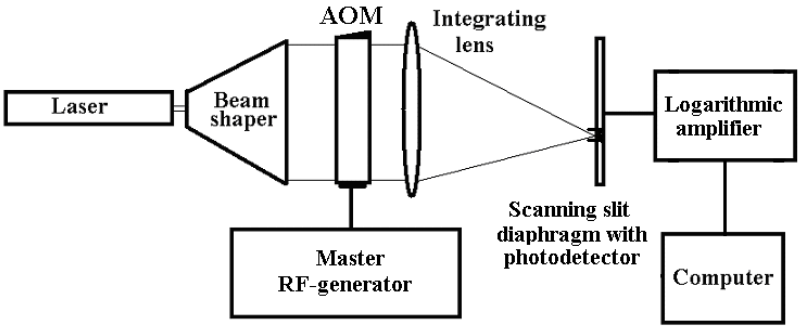

Fig.2.16. Schematic arrangement to measure the intensity profile of an individual spot.

The fulfilled measurements have shown an expected result that the intensity distributions of individual spots, corresponding to the regimes of a one-, two-, and three-phonon light scattering, are very similar to each other. Such a result is caused by the fact that the angles of light scattering in these regimes do not exceed a few degrees in the case of a TeO_2 acousto-optical modulator, so that conditions for a one-, two-, or three-fold scattering of light are almost the same; mainly, they are determined by optical quality of a crystal and homogeneity of the acoustic beam inside the modulator. Because of this only one example of the intensity distributions at an individual spot, related to a two-fold light scattering, is

presented in Fig.2.17a [7]; numerical estimation at the same conditions is displayed in Fig.2.17b [7].

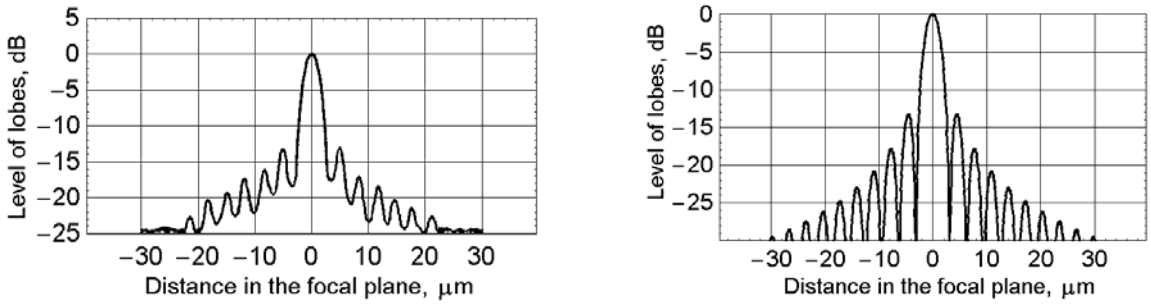

a. b.

Fig.2.17. The intensity distributions of an individual spot in focal plane of the integrating lens for a two-phonon light scattering in a TeO_2 acousto-optical modulator:
(a) experimental plot, (b) numerical simulation.

One can see that the measured level of the first lobes lie around –13 dB with initially homogeneous lighting of the modulator's aperture, which is in agreement with the well-known theoretical prediction [19] and looks practically acceptable from the viewpoint of application a multi-phonon light scattering to spectral analysis of radio-wave and optical signals.

2.14 Conclusions

- A special approach to Bragg scattering of light in optically uniaxial crystals marked by the inclusion of multi-fold or multi-phonon processes has been developed.
- The configurations related to two- and three-phonon scattering processes to highlight both the angular-frequency conditions and the characteristics that can be optimized in TeO_2 for realizing 100% efficiency, from the viewpoint of applications to light modulation, have been analyzed.
- The analysis and numerical simulations in terms of the eigen-vectors for light modes in anisotropic medium and the effect of optical activity in TeO_2 have been formulated.

- The estimations for a two-phonon light scattering are based on well-grounded data regarding to the anomalous regime, which exhibits a high efficiency of acousto-optical interaction. By contrast, the estimations for a three-phonon light scattering require the comparison of the effective photo-elastic constants, inherent in normal and anomalous regimes, with each other. An attempt of such a comparison has been developed.
- The problems regarding to the bandwidth and an improved frequency resolution of light modulators, have been investigated and experimentally examined.

References

1. A.S.Shcherbakov, E.Tepichin Rodriguez, Yu.N.Ledeneva, and A.Aguirre López. "Spatial modulators exploiting a multi-phonon light scattering in crystals", Proc. SPIE, Vol.6311, A1 – A10 (2006).
2. V.I.Balakshy, V.N.Parygin, L.E.Chirkov. *Physical Principles of Acousto-Optics.* (Radio i Svyaz. Moscow. 1985).
3. A.Korpel. *Acousto-Optics. (*Marcel Dekker. New York. 1997).
4. **A.S.Shcherbakov, S.E.Balderas Mata, Yu.N.Ledeneva, and A.Aguirre López**. "**Amplitude and frequency characteristics of a multi-phonon light scattering in tellurium dioxide single crystal", Proc. SPIE, Vol.6455, 6455-19 (2007).**
5. **A.S.Shcherbakov, Je.Maximov, E.Tepichin Rodriguez, S.E.Balderas Mata, A.Luna Castellanos, and J.G.Aguilar Soto, "Applying a two-phonon light scattering in crystals to the spectrum analysis of radio-signals", Proc. SPIE, Vol. 6695, 6695-0W (2007).**
6. A.S.Shcherbakov and A.Aguirre Lopez, "Observation of the optical components inherent in multi-wave non-collinear acousto-optical coupled states", Optics Express, Vol.10, 1398-1403 (2002).

7. A.S.Shcherbakov, A.Luna Castellanos, and S.E.Balderas Mata. "Upgrading the frequency resolution of spectrum analyzers for radio-astronomy due to exploiting a multi-phonon light scattering in the TeO_2 crystalline modulators", Proc. SPIE, Vol.6796, (2007).

8. N.Uchida and N.Niizeki, "Acousto-optic deflection materials and techniques", Proc. IEEE, Vol.61, 1073-1092 (1973).

9. V.B.Voloshinov, V.N.Parygin, L.E.Chirkov, "Some peculiarities of the anisotropic Bragg diffraction", Bulletin of the Moscow State University. Physics & Astronomy, no.3, 305-311 (1976).

10. A.S.Shcherbakov, S.E.Balderas Mata, and Je.Maximov, "Shaping five-wave non-collinear weakly coupled acousto-optical states in a TeO_2 single crystal", Proc. SPIE, Vol. 6729 (2007).

11. Yu.I.Sirotin and M.P.Shaskolskaya. *Fundamentals of Crystal Physics.* (Mir Publishers. Moscow. 1982).

12. A.S.Shcherbakov, A.Luna Castellanos, S.E.Balderas Mata, "Optical modulators exploiting a multi-phonon light scattering in TeO_2-structures", Proc. SPIE, Vol.6796, (2007).

13. R.W.Dixon, "Acoustic diffraction of light in anisotropic media", IEEE Journal of Quantum Electronics, Vol.QE-3, 85-93 (1967).

14. W.A.Wooster. *Tensors and Group Theory for the Physical Properties of Crystals* (Clarendon Press. Oxford, 1973).

15. R.W.Klein and B.D.Cook, "A unified approach to ultrasonic light diffraction", IEEE Trans., Vol.SU-14, 123-134 (1967).

16. P.A.M.Dirac. *The principles of quantum mechanics*. 4-th Ed. (Yeshiva University, N.Y., 1964), Chapter 4.

17. V.G.Dmitriev, G.G.Gurzadyan, and D.N.Wikogosyan. *Handbook of nonlinear optical crystals.* (Springer-Verlag, New-York, 1999).

18. Y.Ohmashi, N.Uchida, and N.Niizeki, "Acoustic wave propagation in TeO_2 - single crystal". Journ. Acoust. Soc.Am, Vol.51, 164-168 (1972).

19. J.W.Goodman: *Introduction to Fourier ptics.* 2-nd Ed. (McGraw Hill. New York. 1996) Chapter 4.

Chapter 3

Schematic arragement of an acousto-optical spectrum analyzer and its potential performance data

3.1 Introduction

In this Chapter, the schematic arrangement of an acousto-optical spectrometer for radio-astronomy will be described. Its main physical parts will be discussed. In doing so, the beam shapper which will be utilized to expand the laser beam to enter the acousto-optical cell is studied. The distribution of the intensity profile of the light beam in the Fourier plane transform is illustrated. The number of resolvable spots in one- and two- phonon light scattering regimes is determined. Also, the two-phonon light scattering regime in a uniaxial crystal is analyzed. Finally, the acoustic attenuation along the acousto-optical cell aperture is discussed and the effect of a ligth beam apodization for the enhacement of the cell's potential dynamic range is described.

3.2 Schematic arrangement of an acousto-optical spectrum analyzer

The experimental setup to perform the acousto-optical spectrum analyzer, Fig.2.1, consists of a laser, a beam shaper, which is an arrangement of 4 prisms, an acousto-optical modulator (AO modulator) and a multi-lens system to obtain a multi-channel Fourier pattern on a CCD linear array.

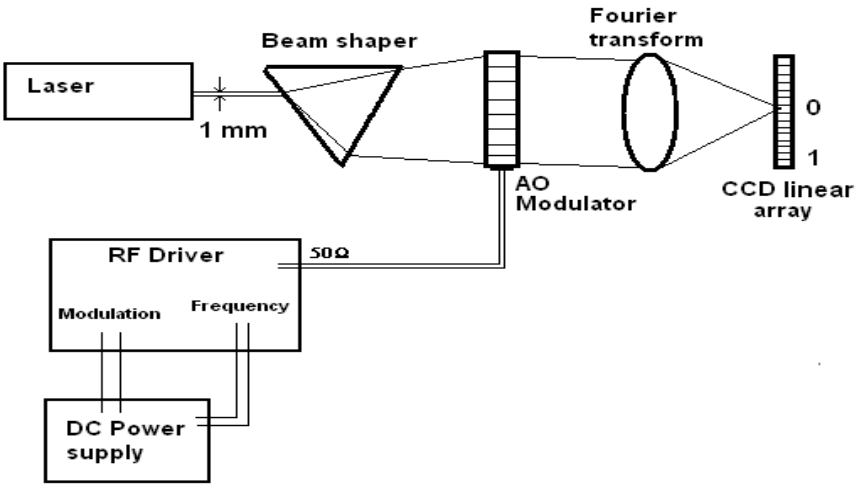

Fig.3.1 Schematic arragemente for the implementation of an acousto-optical spectrum analyzer.

To design the optical scheme; the beam shaper and the multi-lens system, some considerations must be taken into account. First of all, the beam shaper requires to perform a special ratio between the size of the entrance beam and the output of it. And second, the multi-lens system needs to be treated as a thick lens, which will act as a Fourier transformer; the size of the diffraction orders must match the size of the CCD linear array pixels, which has 2048 elements of 14 μm in width, and 14 μm in height, the array length is about 29 mm.

3.2.1 Beam shaper: beam expanding factor

One has to find the ratio between the width of the beam at the end of the prism and the width at its entrance. This ratio must be in terms of the angle of incidence of the beam, and the angle and the index of refraction of the prism; this is because, it is necesary to have control of the output beam width at the end of the prism by controlling the angle of incidence, since the width of the beam as well as the angle and refraction index of the prism are fixed. To obtain this kind of ratio, one applies the well known Snell's law [1] for the first interface (air-glass) of a prism (Fig.3.2) with $\mathbf{n_0 = 1}$, it has the form $\mathbf{\sin\varphi = n \sin\theta}$, so the angle of refraction is

$$\theta = \sin^{-1}\left[\frac{\sin\varphi}{n}\right]. \tag{3.1}$$

From Fig.3.3, one may see that, $\sin\beta = \frac{d_0}{c_1}$; where $\beta = \pi/2 - \varphi$, and $\cos\eta = \frac{d}{c_1}$; where $\eta = \theta$. So, the ratio, d_0/d, is given as

$$\frac{d_0}{d} = \frac{\sin\beta}{\cos\theta} = \frac{\sin(\pi/2 - \varphi)}{\cos\theta}, \tag{3.2}$$

where θ is given by Eq.(3.1).

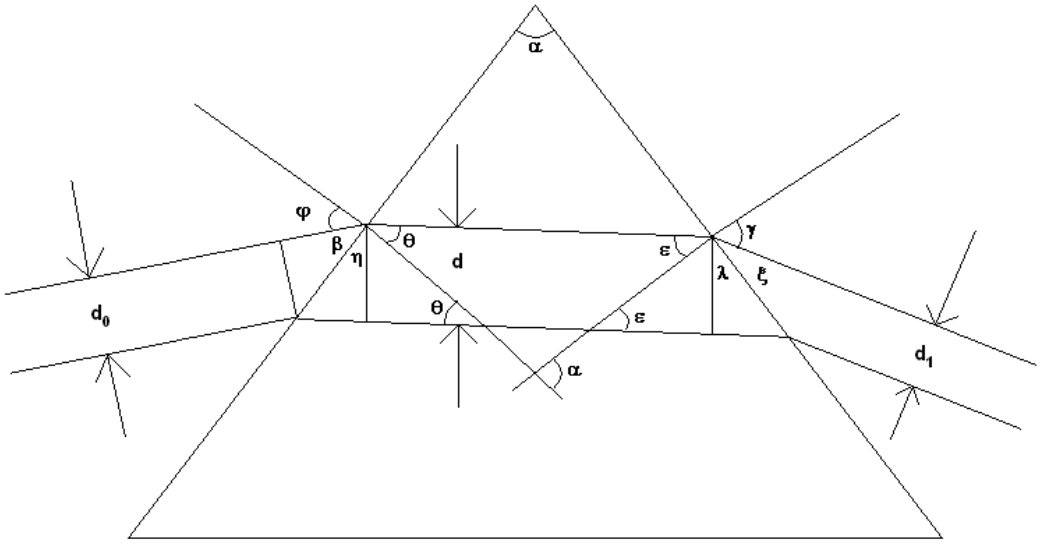

Fig.3.2 Diagram of the interaction of a light beam passing through a prism.

For the second surface, Snell's law gives us, $n\sin\varepsilon = \sin\gamma$, so the angle of incidence in the second surface is given as

$$\varepsilon = \sin^{-1}\left[\frac{\sin\gamma}{n}\right], \tag{3.3}$$

from Fig.3.3 one has that

$$\varepsilon = \alpha - \theta \ . \tag{3.4}$$

And, also $\cos\lambda = \frac{d}{c_2}$; where $\lambda = \varepsilon$, and $\sin\xi = \frac{d_1}{c_2}$; where $\xi = \pi/2 - \gamma$. So, the ratio d_1/d is

$$\frac{d_1}{d} = \frac{\sin\xi}{\cos\varepsilon} = \frac{\sin(\pi/2-\gamma)}{\cos\varepsilon}, \tag{3.5}$$

where ε is given by Eq.(3.3). To obtain the ratio between d_1 and d_0 one has to combined Eqs.(3.2) and (3.5), which gives us

$$\frac{d_1}{d_0} = \frac{\sin(\pi/2-\gamma)\cos\theta}{\sin(\pi/2-\varphi)\cos\varepsilon}. \tag{3.6}$$

Knowing that, $\sin(a-b) = \sin a\cos b - \cos a\sin b$, then

$$\frac{d_1}{d_0} = \frac{[\sin(\pi/2)\cos(\gamma) - \cos(\pi/2)\sin(\gamma)](\cos\theta)}{[\sin(\pi/2)\cos(\varphi) - \cos(\pi/2)\sin(\varphi)](\cos\varepsilon)} = \frac{\cos\gamma\cos\theta}{\cos\varphi\cos\varepsilon}. \tag{3.7}$$

Using Snell's law in the second interface (glass-air) of a prism, see Fig.3.3, one may obtain that $\gamma = \sin^{-1}(n\sin\varepsilon)$, and using Eq.(3.4), gives us

$$\gamma = \sin^{-1}[n\sin(\alpha-\theta)]. \tag{3.8}$$

Substituting Eq.(3.8) into Eq.(3.7) and knowing that, $\cos\left(\sin^{-1}x\right) = \sqrt{1-x^2}$, where $x = n\sin(\alpha-\theta)$, one obtains

$$\frac{d_1}{d_0} = \frac{\sqrt{1-n^2\sin^2(\alpha-\theta)}}{\cos\varphi\cos(\alpha-\theta)}\cos\theta.$$

Introducing Eq.(3.1) into the cosine and by doing some algebra, one obtain the ratio between the width of the output beam and the width of the input beam; in terms of the top angle of the prism α, the angle of incidence θ, and the refractive index n. And, it is given by

$$\frac{d_1}{d_0} = \frac{\sqrt{1-n^2\sin^2(\alpha-\theta)}\sqrt{n^2-\sin^2\varphi}}{n\cos\varphi\cos(\alpha-\theta)} \quad . \tag{3.9}$$

Finally, the factor of beam expanding is given as [2]

$$B_1 = \frac{d_1}{d_0} = \frac{\sqrt{(n^2-\sin^2\varphi)[1-n^2\sin^2(\alpha-\delta)]}}{n\cos\varphi\cos(\alpha-\delta)} \quad , \tag{3.10}$$

where $\delta = \arcsin\left(\frac{\sin\varphi}{n}\right)$. In the simplest case, when all the glass prisms are identical to each other and the angles φ of incidence are the same for all of them, one can write $B_m = (B_1)^m$.

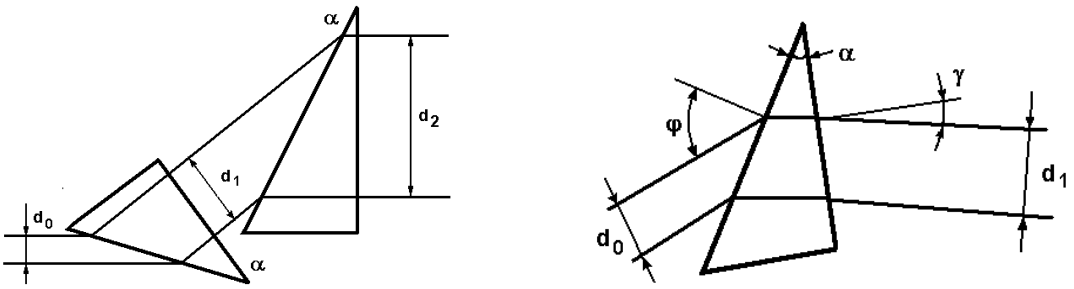

a. b.

Fig.3.3. The light beam passing through a glass prism: (a) $m = 1$, (b) $m = 2$.

Even in this simplest case of identical prisms, one can take more than one prism to provide the needed expanding factor. If the number of prisms is even, the beam direction can be saved with an accuracy of some spatial parallel shift, see Fig.3.3. That is why the numbers $m = \{1,2,4\}$ are taken for consideration within this work.

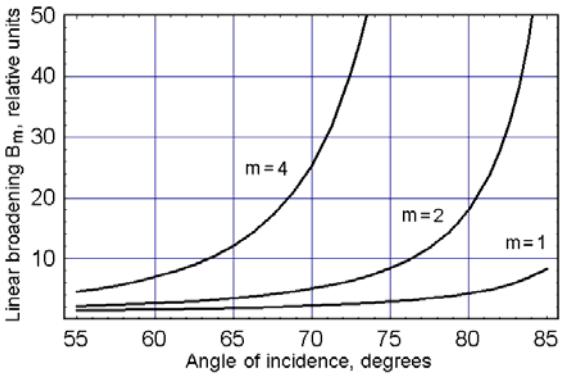

Fig.3.4. Linear expanding factor $\mathbf{B_m}$ for $\mathbf{m}$ prisms with $\mathbf{n = 1.5}$ and $\boldsymbol{\alpha}$ **= 30°**.

With the initial laser beam diameter of about $\mathbf{d_0 = 1}$ mm and the needed optical aperture for an acousto-optical cell of about, for example, $\mathbf{D = 35}$ mm, one can consider the cases with $\mathbf{m = 2}$ or $\mathbf{m = 4}$. The corresponding angles φ of incidence become to be rather large. The plots illustrating the possibilities of light beam expansion by triplet of sets including $\mathbf{m = \{1,2,4\}}$ prisms with $\mathbf{n = 1.5}$ and $\boldsymbol{\alpha}$ **= 30°** are presented in Fig.3.4 [2].

3.2.2 Transmittance of a multi-prism beam shaper

Now, one has to calculate the transmittance of each prism, to do so, one has to use the Fresenel's formulae for the transverse ($\mathbf{T_\perp}$) and parallel ($\mathbf{T_{||}}$) transmittance; which are given as [1]

$$\mathbf{T_\perp = \frac{4n_t \cos\theta_t \sin^2\theta_t \cos\theta_i}{\sin^2(\theta_i + \theta_t)}}, \tag{3.11}$$

and,

$$\mathbf{T_{||} = \frac{4n_t \cos\theta_t \sin^2\theta_t \cos\theta_i}{\sin^2(\theta_i + \theta_t)\cos^2(\theta_i - \theta_t)}}, \tag{3.12}$$

assuming that $\mathbf{n_i = 1}$.

Knowing from Snell's law that, $n_t \sin\theta_t = \sin\theta_i$, introducing this into Eqs.(3.11) and (3.12); and having that, $\sin 2a = 2\sin a \cos a$, yields

$$T_{\perp} = \frac{(2\sin\theta_t \cos\theta_t)(2\sin\theta_i \cos\theta_i)}{\sin^2(\theta_i + \theta_t)} = \frac{\sin 2\theta_t \sin 2\theta_i}{\sin^2(\theta_i + \theta_t)}, \tag{3.13}$$

$$T_{\parallel} = \frac{(2\sin\theta_t \cos\theta_t)(2\sin\theta_i \cos\theta_i)}{\sin^2(\theta_i + \theta_t)\cos^2(\theta_i - \theta_t)} = \frac{\sin 2\theta_t \sin 2\theta_i}{\sin^2(\theta_i + \theta_t)\cos^2(\theta_i - \theta_t)}. \tag{3.14}$$

The total transmittance of the prism is given by the product of the transmittance of the two interfaces involved in the path of the beam through the prism as

$$T_{tot\perp} = T_{1\perp} * T_{2\perp}. \tag{3.15}$$

The transmittance of the first interface (air-glass) of the prism, see Fig.3.2, with $\theta_i = \varphi$ and $\theta_t = \theta$, Eq.(3.13) takes the form

$$T_{1\perp} = \frac{\sin 2\theta \sin 2\varphi}{\sin^2(\varphi + \theta)}. \tag{3.16}$$

The following relations are used to obtain a relation for $T_{1\perp}$,

a) $\sin 2a = 2\sin a \cos a$,

b) $\sin(\theta - \varphi) = \sin\theta\cos\varphi - \cos\theta\sin\varphi$,

c) $\sin(\theta + \varphi) = \sin\theta\cos\varphi + \cos\theta\sin\varphi$. (2.17)

And, by adding or subtracting Eqs.(3.17b) and (3.17c) one obtain

a) $\sin(\theta - \varphi) + \sin(\theta + \varphi) = 2\sin\theta\cos\varphi$,

b) $\sin(\theta + \varphi) - \sin(\theta - \varphi) = 2\sin\varphi\cos\theta$. (3.18)

By applying Eq.(3.17a) with Eqs.(3.18) into Eq.(3.16) gives us

$$T_{1\perp} = \frac{\sin 2\theta \sin 2\varphi}{\sin^2(\varphi+\theta)} = \frac{(2\sin\theta\cos\varphi)(2\sin\varphi\cos\theta)}{\sin^2(\varphi+\theta)} = \frac{\sin^2(\theta+\varphi)-\sin^2(\theta-\varphi)}{\sin^2(\varphi+\theta)}.$$

Arranging the terms, the transmittance of the first interface is given by

$$T_{1\perp} = 1 - \frac{\sin^2(\theta-\varphi)}{\sin^2(\theta+\varphi)}. \tag{3.19}$$

For the transmittance of the second interface $T_{2\perp}$ one can do a similar process as before, except that in this case, $\theta_i = \varepsilon$, and $\theta_t = \gamma$, and taking into account Eq.(3.4), one has that

$$T_{2\perp} = 1 - \frac{\sin^2(\gamma-\alpha+\theta)}{\sin^2(\gamma+\alpha-\theta)}. \tag{3.20}$$

So, the total transverse transmittance, Eq.(3.15), can be rewritten as [2],

$$T_{tot\perp} = \left[1 - \frac{\sin^2(\theta-\varphi)}{\sin^2(\theta+\varphi)}\right] * \left[1 - \frac{\sin^2(\gamma-\alpha+\theta)}{\sin^2(\gamma+\alpha-\theta)}\right]. \tag{3.21}$$

The parallel transmittance for the first interface (air-glass) with $\theta_i = \varphi$, and $\theta_t = \theta$ is

$$T_{1||} = \frac{\sin 2\theta \sin 2\varphi}{\sin^2(\varphi+\theta)\cos^2(\varphi-\theta)}, \tag{3.22}$$

By doing the same procedure as in the case of the transverse transmittance, one has

$$T_{1||} = \frac{[2\sin\theta\cos\varphi][2\sin\varphi\cos\theta]}{\sin^2(\varphi+\theta)\cos^2(\varphi-\theta)} = \frac{\sin^2(\varphi+\theta)-\sin^2(\varphi-\theta)}{\sin^2(\varphi+\theta)\cos^2(\varphi-\theta)}.$$

By arranging the terms, the transmittance of the first interface is given as

$$T_{1||} = \frac{1}{\cos^2(\varphi-\theta)} - \frac{\tan^2(\varphi-\theta)}{\sin^2(\varphi+\theta)}. \tag{3.23}$$

For the transmittance of the second interface $\mathbf{T_{2||}}$ a similar process as before has to be done, except that in this case $\theta_i = \varepsilon$, and $\theta_t = \gamma$, so one obtain

$$\mathbf{T_{2||}} = \frac{\mathbf{1}}{\mathbf{\cos^2(\varepsilon - \gamma)}} - \frac{\mathbf{\tan^2(\varepsilon - \gamma)}}{\mathbf{\sin^2(\varepsilon + \gamma)}}. \tag{3.24}$$

By introducing Eq.(3.4) into Eq.(3.24) yields

$$\mathbf{T_{2||}} = \frac{\mathbf{1}}{\mathbf{\cos^2(\alpha - \theta - \gamma)}} - \frac{\mathbf{\tan^2(\alpha - \theta - \gamma)}}{\mathbf{\sin^2(\alpha - \theta + \gamma)}}. \tag{3.25}$$

The total parallel transmittance, $\mathbf{T_{tot\,||} = T_{1||} * T_{2||}}$, can be written as [2],

$$\mathbf{T_{tot||}} = \left[\frac{\mathbf{1}}{\mathbf{\cos^2(\varphi - \theta)}} - \frac{\mathbf{\tan^2(\varphi - \theta)}}{\mathbf{\sin^2(\varphi + \theta)}}\right] * \left[\frac{\mathbf{1}}{\mathbf{\cos^2(\alpha - \theta - \gamma)}} - \frac{\mathbf{\tan^2(\alpha - \theta - \gamma)}}{\mathbf{\sin^2(\alpha - \theta + \gamma)}}\right]. \tag{3.26}$$

In the particular case of one glass prism ($\mathbf{m = 1}$) with $\mathbf{n = 1.5}$ and $\alpha = \mathbf{30^0}$, the plots illustrating Eqs.(3.13) and (3.14) are depicted in Fig.3.5. It is seen from Fig.3.5 that always $\mathbf{T_1(\perp) < T_1(||)}$ and, consequently, $\mathbf{T_m(\perp) < T_m(||)}$ where $\mathbf{T_m(\perp) = [T_1(\perp)]^m}$ and $\mathbf{T_m(||) = [T_1(||)]^m}$. Therefore, only the last case related to $\mathbf{T_m(||)}$ will be further considered here later.

Restricting into the particular case of laying the light polarization in the beam-expanding plane, one arrives at the following combined diagram for both the beam expanding and the optical energy transmission, which is shown in Fig.3.6 [2]. The plots for the optical energy transmission in Fig.3.6 are governed by $\mathbf{T_m(||)}$ for $\mathbf{m = \{1, 2, 4\}}$. This combined diagram gives various practical possibilities. For instance, selecting the beam expansion factor as $\mathbf{B = 35}$, one can find the two options: 1) $\mathbf{m = 2}$, $\varphi_2 \approx \mathbf{83°}$, $\mathbf{B_2 \approx 35}$, and $\mathbf{T_2 \approx 0.4}$ (i.e. 40 %)

or 2) $\mathbf{m = 4}$, $\mathbf{\varphi_4 \approx 72°}$, $\mathbf{B_4 \approx 35}$, and $\mathbf{T_4 \approx 0.7}$ (i.e. 70 %), as they follow from the combined diagram in Fig.3.6.

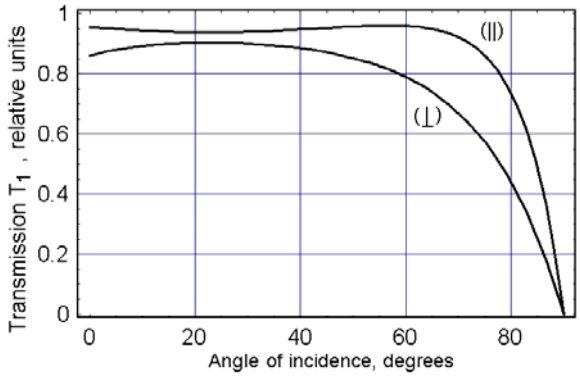

Fig.3.5. Comparison of the transmissions inherent in one glass prism with $\mathbf{n = 1.5}$ and $\mathbf{\alpha = 30°}$ for two states of light polarization.

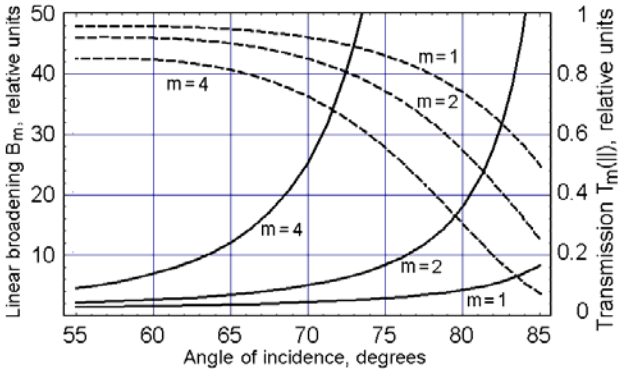

Fig.3.6. The combined diagram illustrating both the beam expanding and the transmission in glass prism shapers with $\mathbf{m = \{1, 2, 4\}}$, $\mathbf{n = 1.5}$, and $\mathbf{\alpha = 30^0}$.

Then, the top angle α of glass prisms can be optimized. Again, one takes $\mathbf{m = \{2, 4\}}$ and $\mathbf{n = 1.5}$ for the same case of laying the light polarization in a beam expanding plane and find the contribution of the top angle α, see Fig.3.7 [2].

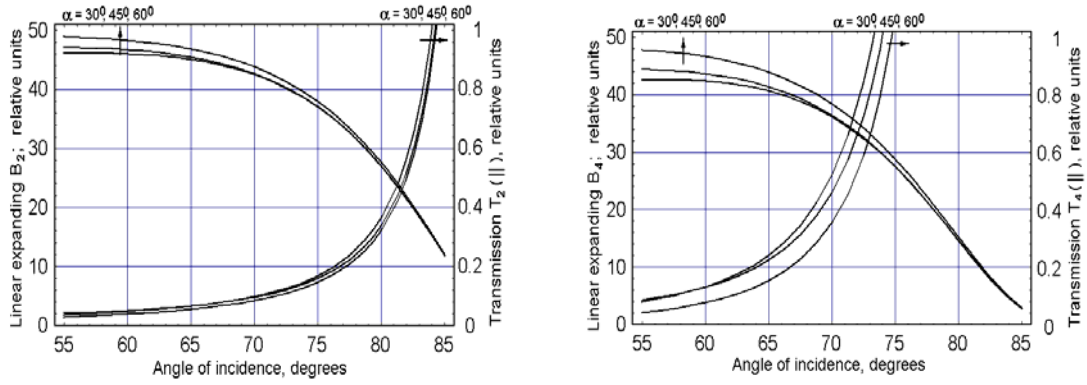

a. b.

Fig.3.7. Diagrams illustration the effect of varying the prism top angle α:

(a) $\mathbf{m = 2}$, and (b) $\mathbf{m = 4}$.

One can see that the influence of this angle is not too much, but it can be considerable in a view of precise optimization of the prism shaper performances.

3.2.3 An ideal thick lens as a Fourier transformer

There are two main kinds of lenses in optics, thin lenses and thick ones. In the case of a thin lens, the spacing between its two surfaces is negligible. In the other hand, the separation along the optical axis between the two surfaces of a thick lens is nonnegligible, with such lenses one can obtain short focal lengths. In this case is of great importance to have such a short focal length so that the acousto-optical spectrometer can be optimized in size. One of the most remarkable and useful properties of a converging lens is its inherent ability to perform Fourier transforms. The systems studied are coherent systems, linear in complex amplitude, and the distribution of light amplitude across a particular plane behind the lens is of interest. In some cases this is the back focal plane of the lens, which by definition is a plane normal to the lens axis, situated at the distance $\mathbf{F_L}$, focal length, behind the lens.

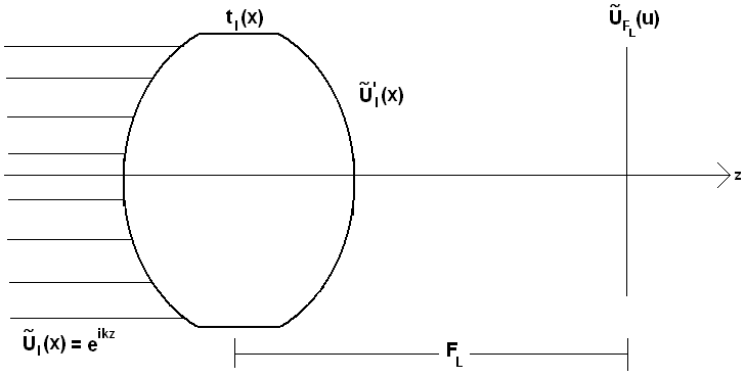

Fig.3.8. Scheme to perform the Fourier transfrom with a thick positive lens, which is illuminated by a plane wave [3].

To find the Fourier transform of the incident field $\tilde{U}_l(x)$ in a thick lens the Fresnel diffraction formula with $z = F_L$, can be used [3]

$$\tilde{U}_{F_L}(u) = \exp(ikz)\exp\left(i\frac{k}{2z}u^2\right)\int_{-\infty}^{\infty}\tilde{U}_l'(x)\exp\left(i\frac{k}{2F_L}x^2\right)\exp\left(-i\frac{2\pi}{\lambda F_L}xu\right)dx. \tag{3.26}$$

The complex field $\tilde{U}_l'(x,y)$ across the plane immediately behind the lens is related to the field $\tilde{U}_l(x,y)$ incident on a plane inmediately in front of the lens as $\tilde{U}_l'(x) = t_l(x)\tilde{U}_l(x)$. The phase transformation representing the lens is

$$t_l(x,y) = \exp(i\hat{\phi}), \tag{3.27}$$

with $\hat{\phi}(x) = kn\Delta(x)[n-1] + k\Delta_0$ which is the total phase delay suffered by the wave at the coordinate **x** when passing through the lens, Δ_0 is the maximum thickness of the lens on its axis, **Δ(x)** is the thickness at the coordinate **x**, see Fig.3.9, and **n** is the refraction index of the lens. The first term on the right-hand side of the above equation is the delay caused by the lens and the second one refers to the delay produced by the remaining region of free space between planes.

The problem is to find the thickness function $\Delta(x)$, which can be assume to be of the form $\Delta(x)=\Delta_1(x)+\Delta_2(x)+\Delta_3(x)$, because the lens has been splitted in three parts, see Fig.3.9.

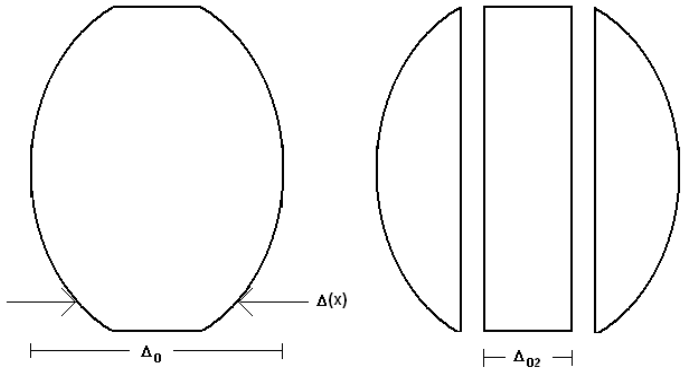

Fig.3.9. Side view of a thick lens and how it is possible to split it in three parts.

Referring to the geometries in Fig.3.10, the thickness function for the first and the third component are given by

$$\Delta_1(x)=\Delta_{01}-R_1\left(1-\sqrt{1-\frac{x^2}{R_1^2}}\right),\qquad \Delta_3(x)=\Delta_{03}-R_2\left(1-\sqrt{1-\frac{x^2}{R_2^2}}\right),$$

respectively. The second component of the thickness function comes from a region of constant thickness Δ_{02}, see Fig.3.9. The total thickness is

$$\Delta(x)=\Delta_0-R_1\left(1-\sqrt{1-\frac{x^2}{R_1^2}}\right)+R_2\left(1-\sqrt{1-\frac{x^2}{R_2^2}}\right),$$

where $\Delta_0=\Delta_{01}+\Delta_{02}+\Delta_{03}$.

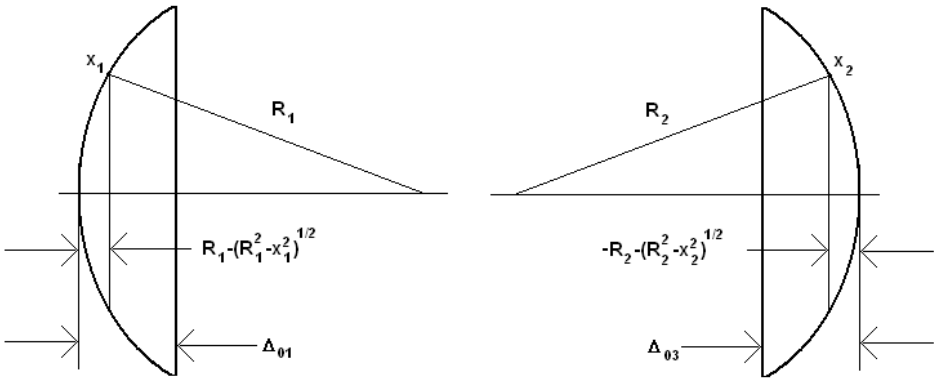

Fig.3.10. Calculation of the thickness function. Geometry for Δ_1 and Δ_3.

The thickness function can be simplified if attention is restricted to portions of the wavefront that lie near the lens axis, i.e., paraxial rays. Considering only values of **x** and **y** sufficiently small to allow the following approximations

$$\sqrt{1-\frac{x^2+y^2}{R_1^2}} \approx 1-\frac{x^2+y^2}{R_1^2}, \qquad \sqrt{1-\frac{x^2+y^2}{R_2^2}} \approx 1-\frac{x^2+y^2}{R_2^2}.$$

Then, the thickness function can be rewritten as

$$\Delta(x) = \Delta_0 - R_1\left(\frac{x^2}{R_1^2}\right) + R_2\left(\frac{x^2}{R_2^2}\right) = \Delta_0 - \frac{x^2}{R_1} + \frac{x^2}{R_2}. \tag{3.28}$$

The first term of the thickness function Δ_0 using the paraxial approximation theory, has the form [4]

$$\frac{1}{F_L} = (n-1)\left(\frac{1}{R_1} - \frac{1}{R_2}\right) + \frac{\Delta_0 (n-1)^2}{R_1 R_2 n}. \tag{3.29}$$

so one has that

$$\Delta_0 = \frac{R_1 R_2 n}{(n-1)^2 F_L} + \frac{n}{(n-1)}(R_2 - R_1). \tag{3.30}$$

Introducing Eq.(3.30) into Eq.(3.28) yields

$$\Delta(x)=\frac{R_1R_2n}{(n-1)}+\frac{n}{(n-1)}(R_2-R_1)-\frac{x^2}{R_1}+\frac{x^2}{R_2}\ , \tag{3.31}$$

Then, Eq.(3.27) with Eq.(3.31), and having that $\frac{1}{F_L^*}=(n_1-1)\left(\frac{1}{R_1}-\frac{1}{R_2}\right)$, can be written as

$$t_l(x,y)=\exp[ikn\Delta_0]\exp\left[i\frac{k}{2F_L^*}x^2\right], \tag{3.32}$$

Substituting Eq.(3.32) into Eq.(3.26) and having that the field behaind the lens is $\tilde{U}_l'(x)=A\exp(ikz)\,t_l(x)\,P(x)$ with the pupil function $P(x)=1$, yields

$$\tilde{U}_{F_L}(u)=A\exp(ikz)\ \frac{\exp\left(i\frac{k}{2F_L^*}u^2\right)}{i\lambda F_L^*}\exp(ik\Delta_0 n)\int_{-\infty}^{\infty}\exp\left(-i\frac{2\pi}{\lambda F_L^*}xu\right)dx. \tag{3.33}$$

By restricting the diameter of the lens to be **2a,** i.e., from **-a** to **a**, Eq.(3.33) takes the form

$$\tilde{U}_{F_L}(u)=A\exp\ (ikz)\ \frac{\exp\left(i\frac{k}{2F_L^*}u^2\right)}{i\lambda F_L^*}\exp(ik\Delta_0 n)\int_{-a}^{a}\exp(-i2\pi f_x x)dx, \tag{3.34}$$

where the spatial frequency is given by $f_x=\frac{u}{\lambda F_L^*}$. Then,

$$\tilde{U}_{F_L}(u)=A\ \frac{\exp\left(i\frac{k}{2F_L^*}u^2\right)}{i\lambda F_L^*}\exp[ik(\Delta_0 n+z)]\ [a\,\mathrm{sinc}(-i2\pi f_x x)]. \tag{3.35}$$

And, the intensity is given as

$$I(u) = |A|^2 a^2 \left| \mathrm{sinc}\left(2\pi f_x a\right)\right|^2 . \qquad (3.36)$$

It can be seen from Eq.(3.36) that the intensity profile of the focal spot of a light beam before passing through a thick lens has a sinc distribution. The width of this distribution will depend on the physical dimensions of the thick lens.

3.3 Potential performance data of the acousto-optical spectrum analyzer

In this Section, the discussion on how to estimate the number of resolvable spots of an acousto-optical spectrometer for the cases of one-phonon anomalous light scattering regime and for two-phonon regime is performed. Also, the comparisson of the transfer function for one- and two phonon light scattering regimes; and how it is possible, having the transfer function to determine the angular bandwith of a cell is analyzed. Finally, the effect of the acoustic attenuation as well as the Gaussian apodization of the incident beam profile along the cell's aperture is studied.

3.3.1 Estimating the number of resolvable elements (spots): one-phonon light scattering regime

Acousto-optical interaction by itself leads to deflection of light beam by certain angle proportional to the frequency of an acoustic wave. At first, let us consider basic relations characterizing the parameters of acousto-optical deflectors based on one- and two-phonon light scattering. The most important of them is the number of resolvable elements. The number N_m of resolvable elements corresponds to either the number of resolvable frequencies in the plane of Fourier transform or the number of resolvable spots in the plane of pattern. This number can be determined as a ratio $N_m = \Delta\theta/\delta\theta$ of the maximal angle range $\Delta\theta$ of deflection for the scattered light beam to the angular spreading $\delta\theta = \lambda/(n_0 D)$ of

optical beam, where **D** is the beam width or the acousto-optical cell's aperture and $\mathbf{n_0}$ is the refractive index of the crystal. At this stage, one has met the problem: how to explain the maximal angle range $\Delta\theta$ of deflection in terms of the cell's frequency bandwidth $\Delta \mathbf{f}$. For this purpose, one has to analyze the corresponding vector diagrams [5], see Fig.3.11.

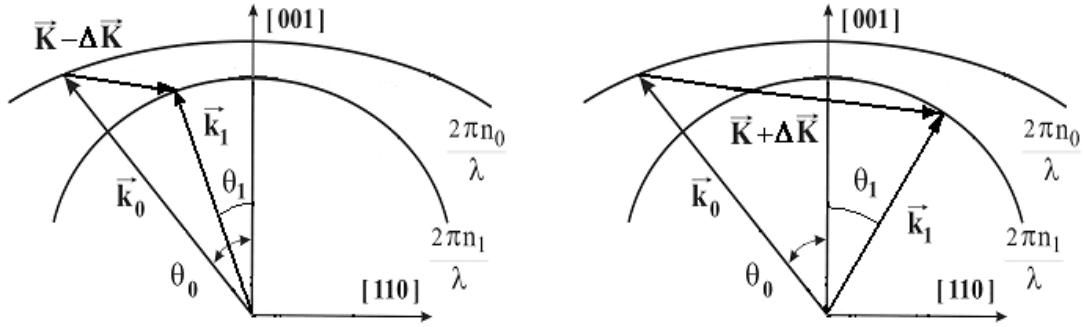

Fig.3.11. Vector diagram for a one-phonon light scattering, being non-degenerated by a two-phonon process, in a tellurium dioxide crystal.

The corresponding angular frequency dependences are given by

$$\text{a)}\quad \sin\theta_0 = \frac{K}{2n_0 k}\left[1+\left(\frac{k}{K}\right)^2\left(n_0^2-n_1^2\right)\right],$$

$$\text{b)}\quad \sin\theta_1 = \frac{K}{2n_1 k}\left[1-\left(\frac{k}{K}\right)^2\left(n_0^2-n_1^2\right)\right], \qquad (3.39)$$

where $K=\left|\vec{K}\right|$, $k_0=\left|\vec{k}_0\right|=n_0 k$, $k_1=\left|\vec{k}_1\right|=n_1 k$, n_0 and n_1 are the current refractive indices of TeO_2 crystal in the crystallographic plane presented in Fig.3.11, k is the light wave number in a vacuum. It follows from Fig.3.11 that the angle θ_0 of incidence is almost constant, while the angle θ_1 of scattering is varied in accordance to Eq.(3.39b) reflecting the corresponding Bragg condition. By differentiating Eq.(3.39a), one can find that the central acoustic frequency f_0,

providing similar situation and being in fact optimized for a one-phonon anomalous light scattering in a crystalline material, is given by

$$f_0 = \frac{V}{\lambda}\sqrt{2n_0(n_0 - n_1)}, \tag{3.40}$$

where λ is the light wavelength in a vacuum. Rewriting Eqs.(3.39) in terms of the acoustic frequency, one can obtain [5] the following approximate relation between the frequency deviation $(f - f_0)$ from the central acoustic frequency f_0 and the incident angle variation $[\theta_0(f) - \theta_0(f_0)]$ in the angle of incidence

$$(f - f_0) \approx 2f_0\sqrt{[\theta_0(f) - \theta_0(f_0)]\cos\theta_0\,\frac{\lambda f_0}{V(n_0 - n_1)}}\,. \tag{3.41}$$

The incident angle variation is determined by $\varphi_S = \Lambda/L = V/(Lf_0)$, which is the angle of the acoustic beam spreading, where L can be considered in rather good approximation as the characteristic size of the radiating acoustic aperture. Consequently, one can write $\theta_0(f) - \theta_0(f_0) = V/(Lf_0)$. Then, the bandwidth includes a doubled frequency deviation, i.e. $\Delta f = 2(f - f_0)$, because the deviation represents a function being approximately symmetric relative to the central frequency f_0. Using these relations, one can obtain from Eq.(3.41) that

$$\Delta f = 2V\sqrt{\frac{2n_0\cos\theta_0}{\lambda L}}\,. \tag{3.42}$$

Because the output light beam is deflected by the angle

$$\Delta\theta_1 = \frac{\lambda\Delta f}{n_0 V\cos\theta_0} = 2\sqrt{\frac{2\lambda}{n_0 L\cos\theta_0}}\,, \tag{3.43}$$

one can estimate the number N of resolvable spots as

$$N_m = \frac{\Delta\theta_1}{\delta\theta} = 2D\sqrt{\frac{2n_0}{\lambda L\cos\theta_0}}\,. \tag{3.44}$$

At the first glance, Eq.(3.44) does not include any frequency dependence, but it is not quite true because λ and $\mathbf{f_0}$ are not independent on each other for the optimized regime of a one-phonon anomalous light scattering under consideration. To resolve this difficulty one may use the data taken from Ref.[6]. These data consists of the following three measured points: $\lambda =$ **488** nm, $\mathbf{f_0} =$ **63.3** MHz; $\lambda =$ **633** nm, $\mathbf{f_0} =$ **37.7** MHz; and $\lambda =$ **1060** nm, $\mathbf{f_0} =$ **15.6** MHz. Using these data, one can create an approximate formula $\lambda[\mu m] = h_1 + h_2\,(f_0[MHz] + h_3)^{-1}$ including these three points; here $h_1 = 0.25077$, $h_2 = 16.009$, and $h_3 = 4.183$. Inserting this approximate formula into Eq.(3.44) and assuming that $\cos\theta_0 \approx 1$, one can obtain [2]

$$N_1 \le 2D\sqrt{\frac{2n_0}{L\left[h_1 + h_2\,(f_0 + h_3)^{-1}\right]}}\,. \qquad (3.45)$$

The acoustic beam spreading along a path of the light beam propagation condition is the second geometrical limitation of the number N_m. The condition, bounding the piezoelectric transducer length L with the distance to the point of half power level in the near-field zone of acoustic wave, being practically equivalent to D, is $D = L^2 f_0/(2V)$. Then, the Bragg regime of a one-phonon light scattering is provided when the well-known Klein-Cook parameter [7] $Q = (2\pi/n_0)\cdot(\lambda L f_0^2/V^2)$ does not exceed 2π (here n is an averaged refractive index of a crystalline material). Therefore, one can estimate that $L = n_0 Q V^2/(2\pi\lambda f_0^2)$ with a value of Q as the case requires. Substituting two last expressions for D and L into Eq.(3.45) yields [2]

$$N_2 \le \frac{n_0^2 Q^{3/2} V^2}{2\pi^{3/2}\,[h_1 + h_2\,(f_0 + h_3)^{-1}]^2 f_0^2}\,. \qquad (3.46)$$

The third principle limitation is connected with the acoustic attenuation. It can also be represented as function of the acoustic frequency $\mathbf{f_0}$. Let us use the factor Γ of acoustic attenuation expressed in dB/(cm GHz^2), so that a $\mathbf{B}$-dB level of attenuation will require the aperture of $\mathbf{D \le B \gamma^{-1} f_0^{-2}}$. Substituting this formula into Eq.(3.45), one can find [2]

$$\mathbf{N_3 \le \frac{2B}{\gamma V f_0^2} \sqrt{\frac{2n_0}{L\,[h_1 + h_2\,(f_0 + h_3)^{-1}]}}} \; . \qquad (3.47)$$

Thus, the number $\mathbf{N_m}$ of resolvable elements is restricted by a triplet of the above-mentioned independent limitations. In the particular case of a one-phonon optimized anomalous light scattering in a TeO_2 crystal, one can take, for example, the following values inherent in this crystalline material: $\mathbf{V}$ = 0.616 10^5 cm/s, λ = 488 nm, $\mathbf{n}$ = 2.3, and Γ = 240 dB/(cm GHz^2). The numerical estimations have been realized for $\mathbf{D = 1, 2, 3, 4}$ cm; the attenuation factors along the full aperture $\mathbf{B = 3, 4, 6}$ (dB/aperture), and the Klein-Cook parameter as $\mathbf{Q = 2\pi}$, see Fig.3.12 [2].

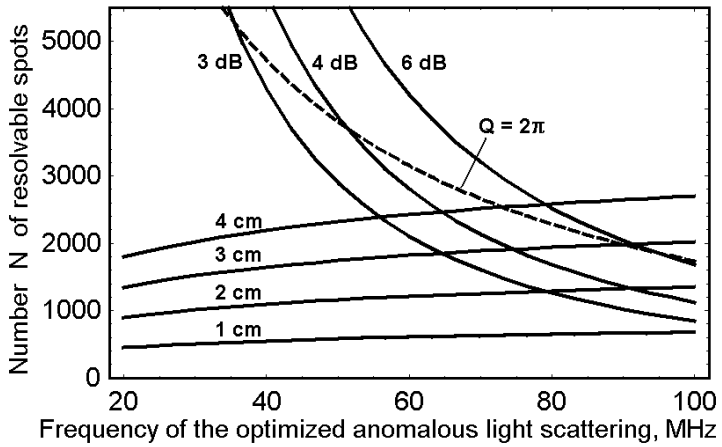

Fig.3.12. The combined diagram illustrating the effect of a triplet of the restricting factors. Solid slowly growing lines for $\mathbf{N_1}$ with **D = 1, 2, 3,** and **4** cm. Dashed line for $\mathbf{N_2}$ with $\mathbf{Q = 2\pi}$. Solid hyperbolic-like falling curves illustrate $\mathbf{N_3}$ and reflect contributions of the acoustic attenuation; **B = 3, 4**, and **6** dB along the aperture.

One can see that a TeO_2 acousto-optical cell with $\mathbf{D = 4}$ cm, $\mathbf{Q = 2\pi}$, and $\mathbf{B = 4}$ (dB/aperture) is capable to provide $\mathbf{N_m \approx 2500}$ resolvable spots in a one-phonon optimized anomalous light scattering regime at a frequency $\mathbf{f_0}$ of about **65** MHz.

3.3.2 Estimating the number of resolvable elements (spots) : two-phonon light scattering regime

As in the case of one-phonon light scattering regime; one has to make use of the ratio between the maximal angle range of deflection for the scattered light beam and the angular spreading of the optical beam, $\mathbf{N = \Delta\theta/\delta\theta}$. Once more, one has met the problem how to explain the maximal angle range $\Delta\theta$ of deflection in terms of the frequency bandwidth $\Delta \mathbf{f}$ of a cell. For this purpose, one has to analyze the corresponding vector diagrams, see Fig. 2.3a.

For the case of a two-phonon light scattering, Fig.2.3a should be considered. A triangular of the wave vectors with $\theta_2 = \theta_0 + \Delta\theta_2$ leads to the formula

$$4\left[K + (\Delta K)\right]^2 = 2k^2\left[1 - \cos\left(2\theta_0 + \Delta\theta_2\right)\right], \qquad (3.48)$$

where $k = \left|\vec{k}_0\right| = \left|\vec{k}_2\right|$. All the angles are really small, so $\cos\theta_0 \approx 1$, $\cos\Delta\theta_2 \approx 1$, $\sin\theta_0 = K/k$, and $\sin\Delta\theta_2 \approx \Delta\theta_2$. Considering Eq.(3.48) in the first order approximation and ignoring the term $(\Delta K)^2$ in the right hand side. After obvious simplifications, one can find $2\Delta K = k\,\Delta\theta_2$. Now, $\Delta K = 2\pi\Delta f_2/V$, where Δf_2 is the frequency bandwidth of a cell based on a two-phonon light scattering, and $k = 2\pi n_0/\lambda$. After these substitutions, it yields in terms of the maximal angle range of deflection, $\Delta\theta_2$, [8]

a) $\Delta f_2 = \frac{n_0 V}{2\lambda}\Delta\theta_2$, b) $\Delta\theta_2 = \frac{2\lambda}{n_0 V}\Delta f_2$, c) $N_m = \frac{\Delta\theta_2}{\delta\theta} = 2T\Delta f_2$.

(3.49)

However, as it has been shown in previous section in terms of the angles, the frequency bandwidth of a two-phonon light scattering can be estimated as $\Delta f_2 \approx \Delta f_1/4$ at a level of -4 **dB** (this estimation is in direct agreement with the result from Ref.[10]), so that a two-phonon light scattering in a cell with the same aperture provides as twice as less number N_m together with as twice as higher angular (and frequency) resolution in comparison with a one-phonon regime of light scattering.

For high-quality deflectors, the number N_m should be as much as possible, however, the magnitude of N_m is restricted by at least two geometrical factors and acoustic attenuation. The first geometrical factor is maximally acceptable cell's aperture D. A two-phonon light scattering admits the inequality $\Delta f_2 \le f_2/8$. That is why in connection with the first restricting factor one can write [8]

$$N_1 \le \frac{D f_2}{4V}. \qquad (3.50)$$

The second geometrical limitation of the number N, as before is in conection with the bounding of the piezo-electric transducer length L with the distance to the point of half power level in the near-field zone of acoustic wave, being practically equivalent to D, is $D = L^2 f_2/(2V)$. The Bragg regime of a two-phonon light scattering is provided when the well-known Klein-Cook parameter $Q = (2\pi/n)\cdot(\lambda L f_2^2/V^2)$ exceeds 2π (here n is an averaged refractive index of a material). Therefore, $L = nQV^2/(2\pi\lambda f_2^2)$ with a value of Q as the case requires. Substituting two last expressions for D and L into Eq.(3.50), yields [8]

$$N_2 \le \frac{n^2 Q^2 V^2}{32\pi^2 \lambda^2 f_2^2}. \qquad (3.51)$$

Equation (3.51) includes the product $\lambda^2 f_2^2$ whose multiplicands λ and f_2 are not independent on each other for a two-phonon light scattering. To resolve this difficulty one may use, as before, the data taken from Ref.[6], which gives us an approximate formula $\lambda[\mu m] = h_1 + h_2 (f_0[MHz] + h_3)^{-1}$, where $h_1 = 0.25077$, $h_2 = 16.009$, and $h_3 = 4.183$. Inserting this approximate formula into Eq.(3.50), one can obtain [8]

$$N_2 \le \frac{n^2 Q^2 V^2}{32\pi^2 f_2^2} \left(h_1 + \frac{h_2}{f_2 + h_3} \right)^{-2}. \qquad (3.52)$$

The third principle limitation is connected with the acoustic attenuation. It can also be represented as function of the acoustic frequency f_2. Let us use the factor Γ of acoustic attenuation expressed in dB/(cm GHz^2), so that a B-dB level of attenuation will require the aperture of $D \le m\gamma^{-1} f_2^{-2}$. Substituting this formula into Eq.(3.50), one can find [8]

$$N_3 \le \frac{B}{4\gamma V f_2}. \qquad (3.53)$$

Thus, the number N_m of resolvable elements (spots) is restricted by a triplet of these independent limitations. In the particular case of a two-phonon light scattering in a TeO_2 crystal, one can take the following values V = 0.616 10^5 cm/s, λ = 488 nm, n = 2.3, and Γ = 240 dB/(cm GHz^2).

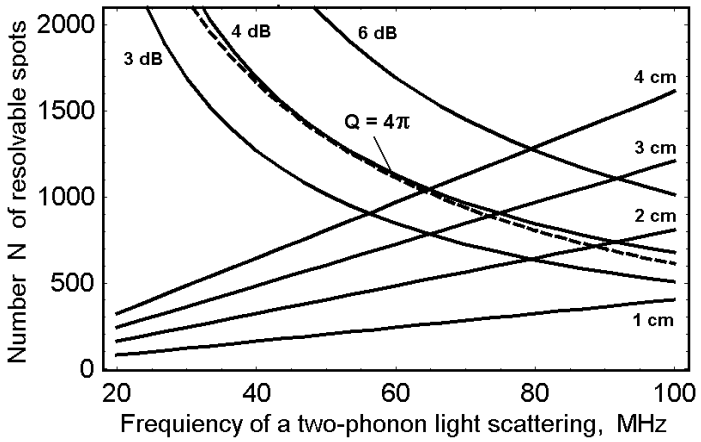

Fig.3.13. Combined diagram illustrating the effect of a triplet of the restricting factors. Solid straight lines for $\mathbf{N_1}$, **D = 1, 2, 3,** and **4** cm. Dashed line for $\mathbf{N_2}$ with **Q = 4** π. Solid hyperbolic-like for $\mathbf{N_3}$ and **B = 3, 4,** and **6** dB along the aperture.

The numerical estimations have been realized for $\mathbf{D = 1, 2, 3, 4}$ cm; $\mathbf{B = 3, 4, 6}$ (dB/aperture), and $\mathbf{Q = 4\pi}$, see Fig.3.13 [8]. One can see that a TeO_2 acousto-optical cell with $\mathbf{D = 4}$ cm, $\mathbf{Q = 4\pi}$, and $\mathbf{B = 4}$ (dB/aperture) is capable to provide $\mathbf{N_m \approx 1000}$ resolvable spots in a two-phonon light scattering regime with the twice frequency resolution at a frequency $\mathbf{f_2}$ of about 60 MHz.

3.3.3 The transfer function inherent in acousto-optical cell operating in a two-phonon light scattering regime

There are a lot of optical systems, which can be considered as linear in behavior under quite natural restrictions. An assumption about the linearity of any system simplifies its analysis in a marked degree. For example, the analysis related to passing an arbitrary signal through a linear system can be performed on the basis of only system's responses to some simple perturbations and the principle of superposition. One of similar simple perturbations is an impulse signal. In this case, one can write the ratio bounding the input signal $\mathbf{s_1(z)}$ and the output one $\mathbf{s_2(z)}$ as

$$s_2(z_2) = \int_{-\infty}^{+\infty} s_1(z_1)\, h(z_1, z_2)\, dz_1 \,. \qquad (3.54)$$

The function $h(z_1, z_2)$ represents the impulse response and characterizes the light field distribution at the output of optical system conditioned by the light source at the point z_1. For an spatially invariant system, one can put that $h(z_1, z_2) = h(z_2 - z_1)$, so that Eq.(3.54) takes the form of a convolution integral. Performing the Fourier transform over such a convolution integral, one can find $S_2(\theta) = S_1(\theta) H(\theta)$, where $S_2(\theta)$ and $S_1(\theta)$ are the spatial spectra of the signals $s_1(z)$ and $s_2(z)$; $H(\theta)$ is the transfer function of this spatially invariant optical system. Thus, the analysis of such a system boils down to finding $h(z_2 - z_1)$ or $H(\theta)$.

The transfer function of free space which characterizes the angular spectrum of the scattered light governed by two-phonon processes is given as

$$E_2(\theta_2) = 4 q_0^2 L^2 \frac{k_0}{2\pi} \times \int_{-\infty}^{\infty} \left\{ E_0(\theta_0) \frac{\sin^2\left[2\eta(\theta_0, \theta_2) L\right]}{\left[2\eta(\theta_0, \theta_2) L\right]^2} \times \right.$$

$$\left. \times \left[\int_{-\infty}^{\infty} U(K)\, \delta(k_0 \sin\theta_0 + 2K - k_2 \sin\theta_2)\, dK \right] \right\} d\theta_0 \,. \qquad (3.55)$$

The introduced spectral functions $E_0(\theta_0)$ and $E_2(\theta_2)$ are connected with the amplitudes of the incident and scattered light waves at the central plane $x = L/2$. Using Eq.(3.55) for the angular spectrum, one can find the light field scattered due to a two-phonon acousto-optical interaction at any arbitrary point. To do so, one should multiply $E_2(\theta_2)$ by the corresponding transfer function and then calculate the reversed Fourier transform. The simplest results can be obtained in a far zone of light diffraction or in the focal plane of a lens placed behind the interaction area.

In both these cases, the amplitude distribution of the scattered light coincides formally with Eq.(3.55) within an inessential constant factor [3]. It should be noted that an acousto-optical cell could be considered as a linear optical system under certain limitations. In particular, it is true when efficiency of a two-phonon light scattering is rather low. If the monochromatic acoustic wave $\mathbf{u(z,t) = u_0\ exp\,[i(K_0\,z - \Omega_0\,t)]}$ is passing through a cell, the spectrum $\mathbf{U(K) = 2\pi\,u_0\ exp\,(-i\Omega_0\,t)\,\delta(K_0 - K)}$ of this acoustic signal includes only one component. Substituting the last formula into Eq.(3.55), one can obtain

$$\mathbf{E_2(\theta_2) = exp\,(-2i\Omega_0\,t)} \int_{-\infty}^{\infty} \left\{ \mathbf{E_0(\theta_0)\ \tilde{T}(\theta_0)\ \delta(\theta_2 - \frac{\lambda K_0}{\pi n} - \theta_0)} \right\} \mathbf{d\theta_0}\ , \tag{3.56}$$

where

$$\mathbf{\tilde{T}(\theta_0) = 4q_0^2 L^2 \frac{k_0}{2\pi}\ \frac{sin^2[2K_0 L(\theta_0 - \theta_B)]}{[2K_0 L(\theta_0 - \theta_B)]^2}}\ . \tag{3.57}$$

Equation (3.56) makes it possible to consider acousto-optical cell as a linear optical system with the transfer function $\mathbf{\tilde{T}(\theta_0)}$, which is real-valued and positive in the transmission bandwidth. This system shifts the spectrum of optical signal by the value $\mathbf{2\Omega_0}$, but does not carry in any phase distortions. The profiles of $\mathbf{\tilde{T}(\theta_0)}$ for both one- and two-phonon regimes are shown in Fig.3.14. With the help of the function profile $\mathbf{\tilde{T}(\theta_0)}$ makes is possible to determine the angular bandwidth $\Delta\theta$ of a cell. One can see that the bandwidth in a two-phonon regime is about 4 times narrower in comparison with a one-phonon regime of light scattering at a level of $\mathbf{-4}$ dB.

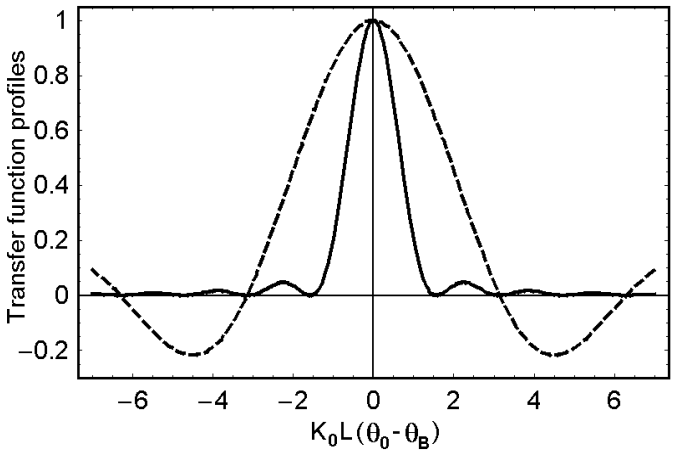

Fig.3.14. The profiles of transfer functions: solid line is for a two-phonon light scattering, dashed line for a one phonon regime is presented for a comparison.

The transfer function does not give the complete description for the process of passing optical signals through an acousto-optical cell, because it does not account the finiteness of cell's aperture along the z-axis. This function characterizes only variations in the signal spectrum, conditioned by selective properties of a cell. To take into account the finite aperture of a cell one can use a system including an infinite cell and an aperture diaphragm behind of a cell. Operating over such a system, one can first exploit the above-obtained transfer function for infinite cell. Then, the spectrum of signal at the output of already finite-aperture system can be estimated as the convolution between $E_2(\theta_2)$ and the Fourier transform of that limiting aperture diaphragm. Finally, it is seen from Eq.(3.57) that with n_0, n_1 = const, the angular range of a cell does not depend on a type and geometry of acousto-optical interaction, but it is determined by only the spreading angle $\varphi_S = V/(2fL)$ of an acoustic wave. Often, even in the cases that the dependences $n_{0,1}(\theta_0,\theta_2)$ exist in anisotropic media, one may ignore these angular dependences due to the ranges of varying $\theta_{0,2}$ are small.

3.3.4 Effect of acoustic attenuation along the aperture of acousto-optical modulator

The Bragg regime of light diffraction occurs with a large length **L** of interaction between light and acoustic waves. In this case, the dynamic acoustic grating is rather thick, so during the analysis of diffraction one has to take into account the phase relations between waves in different orders. Such a regime can be realized only when the angle θ_B of light incidence on a thick acoustic grating meets the Bragg conditions and $Q = \lambda L / \Lambda^2 >> 1$, where λ is the light wavelength and Λ is the acoustic wavelength. Usually, the Bragg regime includes the incident and scattered light modes as well as the acoustic mode, see Fig.3.15a. In this regime, the light intensities are governed by trigonometric function dependences in the forms [10]

$$\text{a)}\ I_0 = \cos^2(qz), \qquad \text{b)}\ I_1 = \sin^2(qz), \tag{3.58}$$

where the parameter $q = \pi(\lambda \cos\theta_B)^{-1}\sqrt{2M_2 P S^{-1}}$, M_2 is the acousto-optic figure of merit, P/S is the acoustic power density and $S = Lh$. Figure 3.15b illustrates the light intensities in the Bragg regime. One can see from Fig.3.15b that the Bragg regime provides principal opportunity of realizing 100% efficiency of light scattering.

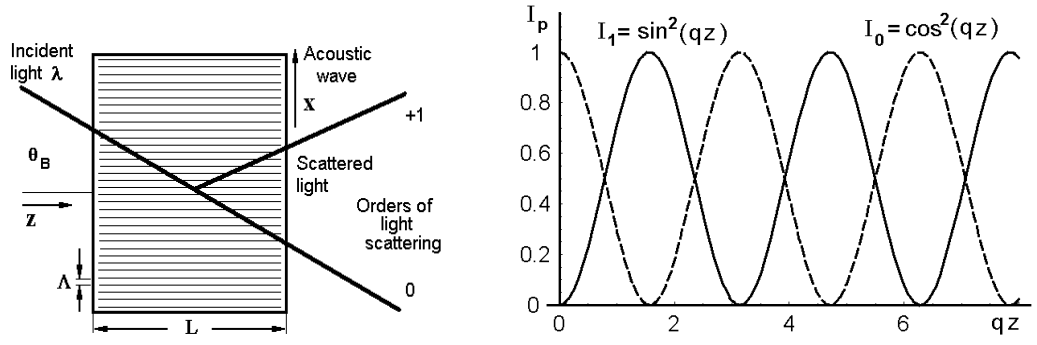

Fig.3.15. Optical scheme for scattering light by a thick dynamic acoustic grating (a) and the corresponding light intensity distributions (b).

Taking into account the full energy in a volume of a deformed body in the second apprximation [11], one can find both the acoustic power density and the parameter $\mathbf{q}$ as [12]

$$\text{a)}\ \ \frac{\mathbf{P}}{\mathbf{S}} = \frac{\mathbf{1}}{\mathbf{2}}\,\tilde{\rho}\,\mathbf{V}^{\mathbf{3}}\,\mathbf{A}_{\mathbf{1}}^{\mathbf{2}}\,\exp(-\mathbf{2}\alpha\mathbf{x})\ ,$$

$$\text{b)}\ \ \mathbf{q} = \pi\,\mathbf{A}_{\mathbf{1}}\exp(-\alpha\mathbf{x})\,(\lambda\cos\theta_{\mathbf{B}})^{-\mathbf{1}}\sqrt{\tilde{\rho}\,\mathbf{V}^{\mathbf{3}}\,\mathbf{M}_{\mathbf{2}}}\ . \qquad (3.59)$$

where α is the coefficient of linear losses, and $\mathbf{V}$ is the acoustic wave velocity.

During the spectrum analysis the partial magnitude of the parameter $\mathbf{q}$ for each individual spectral component of a radio-signal is really small, so that one can approximate Eq.(3.58b) as $\mathbf{I_1} = \sin^{\mathbf{2}}(\mathbf{qz}) \approx \mathbf{qz}$. In this case, the real-valued amplitude $\mathbf{E_1}$ of the scattered light field, i.e. the issuing light amplitude at the output facet of acousto-optical cell is directly proportional to the parameter $\mathbf{q}$, so that one can obtain

$$\text{a)}\ \ \mathbf{E_1}(\mathbf{x},\mathbf{z}) = \mathbf{E_1}(\mathbf{z})\,\mathbf{E_1}(\mathbf{x})\ , \qquad \text{b)}\ \ \mathbf{E_1}(\mathbf{x}) = \exp(-\alpha\mathbf{x})\ ,$$

$$\text{c)}\ \ \mathbf{E_1}(\mathbf{z}) = \pi\,\mathbf{z}\,\mathbf{A_1}\,(\lambda\cos\theta_{\mathbf{B}})^{-\mathbf{1}}\sqrt{\rho\,\mathbf{V_S^3}\,\mathbf{M_2}}\ . \qquad (3.60)$$

To simplify further consideration one can normalize $\mathbf{E_1}(\mathbf{x},\mathbf{z})$ putting $\mathbf{E_1}(\mathbf{z}) = \mathbf{1}$. After that the total normalized intensity of the issuing light (the index 1 will be further omitted) is given by

$$\frac{\mathbf{I}(\alpha\mathbf{D})}{\mathbf{I}(\mathbf{0})} = \frac{\mathbf{1}}{\mathbf{D}}\int_{\mathbf{0}}^{\mathbf{D}}\mathbf{E_1^2}\,(\mathbf{x})\,\mathbf{dx} = \frac{\mathbf{1}-\exp(-\mathbf{2}\alpha\mathbf{D})}{\mathbf{2}\alpha\mathbf{D}}\ . \qquad (3.61)$$

Thus, a part of the scattered light will be lost. Moreover, the acoustic losses affect the size of the resolvable spot, i.e. some influence on the frequency resolution will

take place. The normalized light intensity associated with a resolvable spot in the focal plane of the integrating lens can be estimated as

$$\frac{I(\alpha D,u)}{I(\alpha D,0)}=\frac{\sin^2(\pi u)+\sinh^2(\alpha D/2)}{\left[1+(2\pi u/\alpha D)^2\right]\ \sinh^2(\alpha D/2)}\ , \qquad (3.62)$$

where $u = x_1 D/\lambda F_L$, x_1 is the coordinate in the focal plane, F_L is the lens' focal distance. The corresponding plot, shown in Fig.3.16a, reflects growing the level of aside lobes. It is perturbed only slightly, if $\alpha \le 6$ dB/cm. The effect of total acoustic losses along the aperture on a spot maximum is defined by

$$\frac{I(\alpha D,0)}{I(0,0)}=\left[\frac{1-\exp(-\alpha D)}{\alpha D}\right]^2\ , \qquad (3.63)$$

and it is illustrated by the decreasing curve in Fig.3.16b.

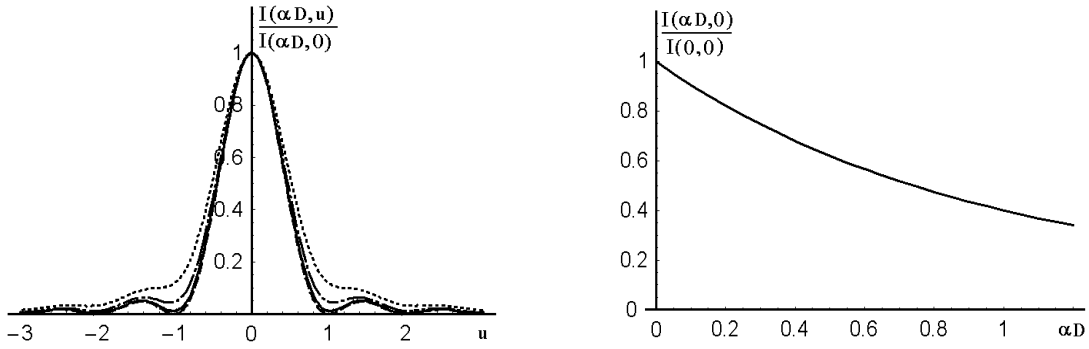

a. b.

Fig.3.16. Effect of acoustic attenuation: (a) normalized light intensity in the focal spot; solid line, $\alpha = 0$ dB/cm, dashed line, $\alpha = 3$ dB/cm, dash-dotted line, $\alpha = 6$ dB/cm, and dotted line, $\alpha = 10$ dB/cm; (b) light intensity in a maximum of the focal spot as a function of αD.

For the case of one-phonon Bragg light scattering, normal or anomalous. In this regime, the scattered light intensities are governed by trigonometric function dependences [10]

$$\text{a)}\ I_0^{(1)}=\cos^2\left(\frac{qz}{2}\right), \qquad \text{b)}\ I_1^{(1)}=\sin^2\left(\frac{qz}{2}\right), \qquad (3.64)$$

where the parameter **q** is the same as in the case of Eq.(3.58). Together with this, one can consider the so-called two-phonon Bragg light scattering. This regime involves one incident light mode, one acoustic mode, and three scattered light modes. In the last case, the scattered light intensities are again governed by trigonometric function dependences but in other forms [10]

$$\text{a)}\ \ I_0^{(2)} = \cos^4\left(\frac{q z}{2\sqrt{2}}\right),\quad \text{b)}\ \ I_1^{(2)} = \frac{1}{2}\sin^2\left(\frac{q z}{\sqrt{2}}\right),\quad \text{c)}\ \ I_2^{(2)} = \sin^4\left(\frac{q z}{2\sqrt{2}}\right). \tag{3.65}$$

One can see from Eqs.(3.64) and (3.65) that the Bragg regime provides principal opportunity of realizing 100% efficiency of light energy conversion into the highest orders of scattering, i.e. $I_1^{(1)}$ and $I_2^{(2)}$. Taking into account the attenuation of total energy in a volume of a deformed body, one can find both the acoustic power density and the modulation parameter **q** as

$$\text{a)}\ \ \frac{P}{S} = \frac{1}{2}\rho V^3 U^2 \exp(-2\alpha x),$$

$$\text{b)}\ \ q = \pi U \exp(-\alpha x)(\lambda \cos\theta_B)^{-1}\sqrt{\rho V^3 M_2}, \tag{3.66}$$

where **U** is the amplitude of the elastic wave. During the spectrum analysis the partial magnitude of the parameter **q** for each individual spectral component of a radio-signal is really small, so that one can approximate Eqs.(3.64b) and (3.65c) in the acousto-optical cell with linear acoustic losses. For the regime of a one-phonon light scattering, such an approximation can be successfully done in a vicinity of the point $qz = 0$. In this case, the real-valued amplitude $E_1^{(1)}(x,z)$ of the scattered light field is directly proportional to the modulation parameter **q**, so that one can obtain

$$\text{a)}\ \ E_1^{(1)}(x,z) = E_1^{(1)}(z)\,E_1^{(1)}(x),\qquad \text{b)}\ \ E_1^{(1)}(x) = \exp(-\alpha x),$$

$$\text{c)}\quad \mathbf{E_1^{(1)}(z)=\frac{\pi\, z U}{2\lambda\cos\theta_B}\sqrt{\rho V^3 M_2}}\,. \tag{3.67}$$

However, similar approach to the regime of a two-phonon light scattering gives

$$\text{a)}\quad \mathbf{E_2^{(2)}(x,z)=E_2^{(2)}(z)\,E_2^{(2)}(x)}\,,\qquad \text{b)}\quad \mathbf{E_2^{(2)}(x)=\exp(-2\alpha x)}\,,$$

$$\text{c)}\quad \mathbf{E_2^{(2)}(z)=\frac{\pi^2 U^2 z^2 \rho V^3 M_2}{8\lambda^2\cos^2\theta_B}}\,. \tag{3.68}$$

It is clearly seen from Eq.(3.68) that exploiting a vicinity of the point $\mathbf{qz=0}$ for a two-phonon light scattering leads to the twiced magnitude $\mathbf{2\alpha}$ of the acoustic attenuation factor in $\mathbf{E_2^{(2)}(x)}$ and to a square-law dependence of $\mathbf{E_2^{(2)}(z)}$ on the acoustic signal amplitude $\mathbf{U}$, which both are practically undesirable. These difficulties can be avoided through exploiting a vicinity of the point $\mathbf{qz=\pi}$. In this area, one can find that $\mathbf{E_2^{(2)}(x,z)=A+Bqz}$ with

$$\text{a)}\quad \mathbf{A=\sin\left(\frac{\pi}{2\sqrt{2}}\right)\left[\sin\left(\frac{\pi}{2\sqrt{2}}\right)-\frac{\pi}{\sqrt{2}}\cos\left(\frac{\pi}{2\sqrt{2}}\right)\right]}\,,$$

$$\text{b)}\quad \mathbf{B=\frac{1}{\sqrt{2}}\sin\left(\frac{\pi}{2\sqrt{2}}\right)\cos\left(\frac{\pi}{2\sqrt{2}}\right)}\,. \tag{3.69}$$

Such an approach implies the existence of a background $\mathbf{A}$, but leads to the desirable properties of a cell at the expense of exploiting that background. Assuming that now $\mathbf{qz=E_2^{(2)}(z)\,E_2^{(2)}(x)}$, one can estimate

$$\text{a)}\quad \mathbf{E_2^{(2)}(x)=\exp(-\alpha x)}\,,\qquad \text{b)}\quad \mathbf{E_2^{(2)}(z)=\frac{\pi\, z\, U}{\lambda\cos\theta_B}\sqrt{\rho V^3 M_2}}\,,$$

(3.70)

so in the last case the factor of acoustic attenuation in Eq.(3.70a) is the same that in Eq.(3.67b) and $\mathbf{E_2^{(2)}(z)}$ depends now linearly on the acoustic signal amplitude $\mathbf{U}$, because Eq.(3.70b) is quite similar to Eq.(3.67c).

3.3.5 Gaussian apodization of the incoming light field distribution along the acousto-optical cell aperture

Now, one makes an attempt to describe the effect of apodizating the incoming light beam on the potential dynamic range of acousto-optical spectrum analyzer. Reasoning from the fact that the electric field profile $\mathbf{E(x)}$, inherent in the issuing beam of the gas laser (where $\mathbf{x}$ is the physical coordinate across a beam, measured in centimeters) and reaching the acousto-optical cell aperture, is usually close to the Gaussian shape, see Fig.3.17a, one can write that

$$\mathbf{E(y) = E_0\ exp\left(-\tilde{\sigma}x^2\right) = E_0\ exp\left(-\beta y^2\right)}, \qquad (3.71)$$

where $\mathbf{y = x/D}$ is the normalized dimensionless coordinate, $\mathbf{D}$ is the physical cell's aperture measured in centimeters, while $\tilde{\sigma}$ and $\beta = \tilde{\sigma}\mathbf{D^2}$ are physical and dimensionless parameters of the Gaussian profile function, whose variations with the parameter β are depicted in Fig.3.17b.

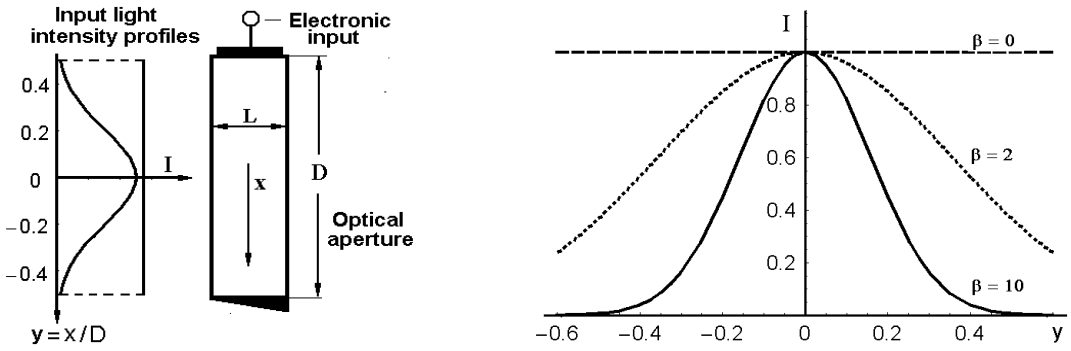

a. b.

Fig.3.17. Optical arrangement of lighting the acousto-optical cell (a) and a role of the parameter β (b).

When the electric field profile of a laser beam has Gaussian shape, its total optical power is fixed by

$$I_T = \left[\int_{-\infty}^{+\infty} \exp(-\beta y^2)\, dy \right]^2 = \frac{\pi}{\beta} . \qquad (3.72)$$

The size of the optical aperture inherent in acousto-optical cell is fixed as well and one can assume that $D = 1$, so that the absolute value of available optical power is given by

$$I_A = \left[\int_{-1/2}^{+1/2} \exp(-\beta y^2)\, dy \right]^2 = \frac{\pi}{\beta} \mathrm{Erf}^2\left(\frac{\sqrt{\beta}}{2} \right) . \qquad (3.73)$$

Thus, one can scale the initial profile and correlate it with the available aperture of the cell. The ratio I_A / I_T represents the coefficient of utilization for the incident optical power; it grows, when the absolute level of optical power decreases, see Fig.3.18. Then, just the value of I_A has to be exploited for normalizing the light spots in the Fourier-transform plane. The shape of light distribution peculiar to an individual spot in the Fourier-transform plane can be estimated analytically as

$$E(u_1) = \sqrt{\frac{\beta}{\pi}}\, \mathrm{Erf}^{-1}\left(\frac{\sqrt{\beta}}{2} \right) \int_{-1/2}^{+1/2} \exp(-\beta y^2) \exp(-2i\pi u_1 y)\, dy =$$

$$= \frac{i}{2} \mathrm{Erf}^{-1}\left(\frac{\sqrt{\beta}}{2} \right) \exp\left(\frac{\pi^2 u_1^2}{\beta} \right) \left[\mathrm{Erfi}\left(\frac{2\pi u_1 - i\beta}{2\sqrt{\beta}} \right) - \mathrm{Erfi}\left(\frac{2\pi u_1 + i\beta}{2\sqrt{\beta}} \right) \right] . \qquad (3.74)$$

Figure 3.19 [13] illustrates the dependence of light intensity profiles in the Fourier transform plane on the parameter β.

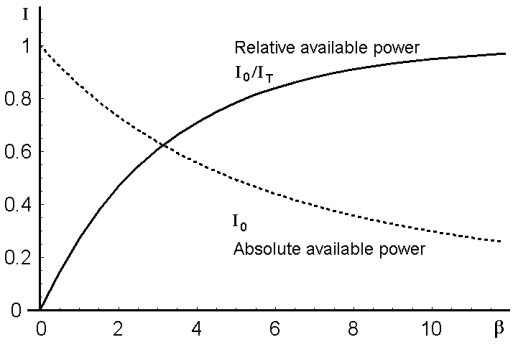

Fig.3.18. Available optical powers.

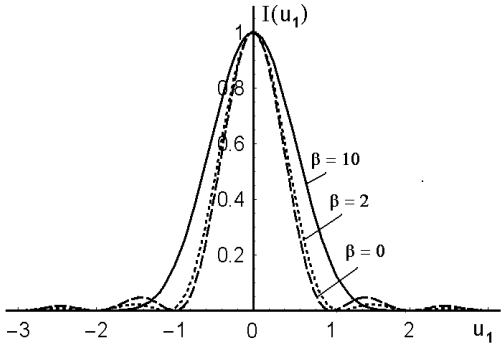

Fig.3.19. Light intensity plots for: $\beta = 0$ (dashed line), $\beta = 2$ (dotted line), and $\beta = 10$ (solid line).

One can see from Fig.(3.19) that as β grows the spot of the beam increases in its width, as a result the absolute available power decreases.

3.3.6 Peculiarities of the lobe distributions in the Fourier transform plane

As it has been noted, Fig.3.19 illustrates the tendencies of redistributions for light intensity profiles in the Fourier transform plane on the parameter β. However, each particular distribution can manifest unexpected peculiarities. In order to investigate this problem let us consider a three-dimensional plot of the lobes neighboring the main, i.e. zero or maximal one, see Fig.3.20 [12,13]. One can see that the first lobe exceeds the second one only for a limited area of values for β. Moreover, when the parameter β becomes to be large enough, one can see that the second lobe begins to exceed the first one. That is why a few particular distributions, Fig.3.21 [12,13], should be now considered. It is seen from Figs.3.20 and 3.21 that starting from the value of $\beta = \mathbf{6.7}$ already the second diffractive lobe becomes to be dominating. Consequently, for the region of $\beta > \mathbf{6.7}$ the dynamic range should be estimated in terms of the second diffractive lobe instead of the first one.

Using the data from Fig.3.21, one can estimate both the potential dynamic range, see Fig.3.22 [12,13], and broadening of a resolvable spot at the intensity level of half a maximum of the main lobe, see Fig.3.23 [12,13].

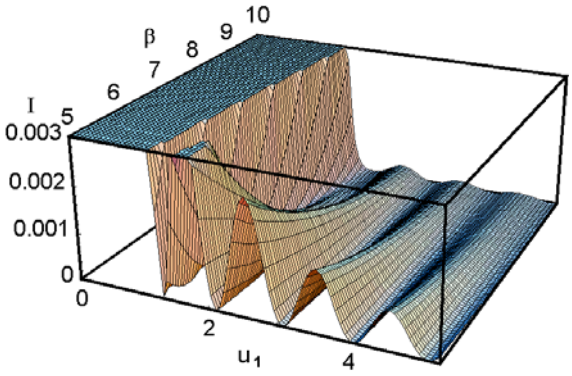

Fig.3.20. A three-dimensional plot of the lobes illustrating the tendency of dominating the second lobe.

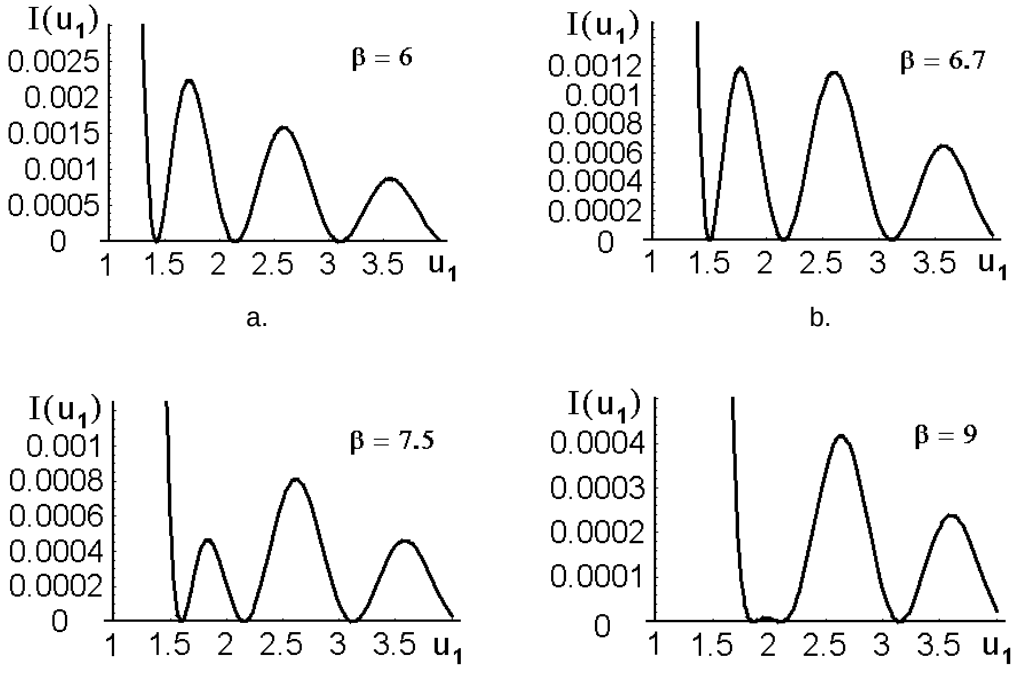

Fig.3.21. Estimations for the maximal side lobe and spot's width with varying β; the level of the side lobes is measured relative to the maximal intensity of the main lobe.

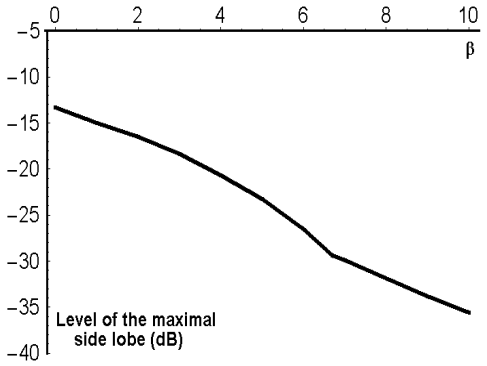

Fig. 3.22. Level of the maximal side lobe relative to the maximum intensity of the main lobe.

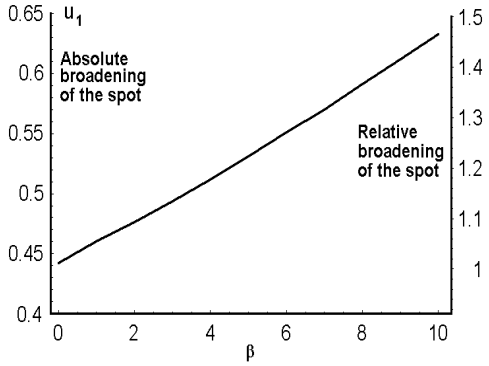

Fig. 3.23. Broadening of a resolvable spot at the intensity level of half a-maximum of the main lobe.

It has been mentioned that the shape of light field distribution $\mathbf{E(u_1)}$ peculiar to an individual resolvable spot in the Fourier-transform plane, Eq.(3.74), by introducing the acoustic losses, Eq.(3.74) takes the form

$$\mathbf{E(u)=\int_0^1 \exp\left[-\beta(y-0.5)^2\right]\ \exp\left(-\alpha_0\, y\right)\ \exp\left(-2i\pi u\, y\right) dy =}$$

$$\mathbf{=\frac{1}{2}\sqrt{\frac{\pi}{\beta}}\ \exp\left[-\beta\left(\frac{1}{4}-\tilde{\nu}^2\right)\right]\ \left\{Erf\left[\sqrt{\beta}\,(1+\tilde{\nu})\right]-Erf\left[\sqrt{\beta}\ \tilde{\nu}\right]\right\}.}$$

(3.75)

Here, the parameter $\alpha_0=\alpha D$ describes now the total acoustic losses along the cell's optical aperture and it can be expressed in decibels as well as in dimensionless form, because $\alpha[cm^{-1}]=0.23\cdot\alpha[dB/cm]$; where $\tilde{\nu}=\left(\frac{\alpha_0}{2\beta}-\frac{1}{2}\right)+i\frac{\pi u}{b}$. Let us introduce $\tilde{\nu}(u=0)=\tilde{\nu}_0=\left(\frac{\alpha_0}{2\beta}-\frac{1}{2}\right)$, then one can write

$$\mathbf{E(u=0)=\frac{1}{2}\sqrt{\frac{\pi}{\beta}}\ \exp\left[-\beta\left(\frac{1}{4}-\tilde{\nu}_0^2\right)\right]\ \left\{Erf\left[\sqrt{\beta}\,(1+\tilde{\nu}_0)\right]-Erf\left[\sqrt{\beta}\ \tilde{\nu}_0\right]\right\},}$$

(3.76)

which is real-valued in behavior. Using Eqs.(3.75) and (3.76), the normalized distribution $\mathbf{I(u)}$ of light intensity peculiar to an individual resolvable spot in a focal plane of the integrating lens can be written as

$$\mathbf{I(u) = E(u)\,E^{*}(u)\,E^{-2}(u = 0)} \ . \tag{3.77}$$

Generally, $\mathbf{u = \tilde{w} D/\lambda F_L}$, where $\tilde{\mathbf{w}}$ is the physical spatial coordinate in the focal plane. In the particular case of $\boldsymbol{\beta \equiv 0}$, Eq.(3.77) can be simplified as

$$\mathbf{I(u, \beta = 0) = \frac{\sin^2(\pi u) + \sinh^2(\alpha_0/2)}{\left[1 + (2\pi u/\alpha_0)^2\right] \sinh^2(\alpha_0/2)}} \ . \tag{3.78}$$

Figure 3.24 [14] shows the results of numerical simulations, based on Eqs.(3.77) and (3.78). It is seen that increasing the total losses α_0 leads to growing of side lobes and minima of the normalized light intensity distribution inherent in each individual resolvable spot in the focal plane. Together with this, increasing the parameter β provides suppressing side lobes and minima of light distributions, so that the dynamic range could be increased. Let us estimate now potential limitations for the dynamic range in a scheme of acousto-optical spectrometer. The most critical limitation is connected with the maximal level of the first side lobe if the apodization parameter β is not too large [12,13].

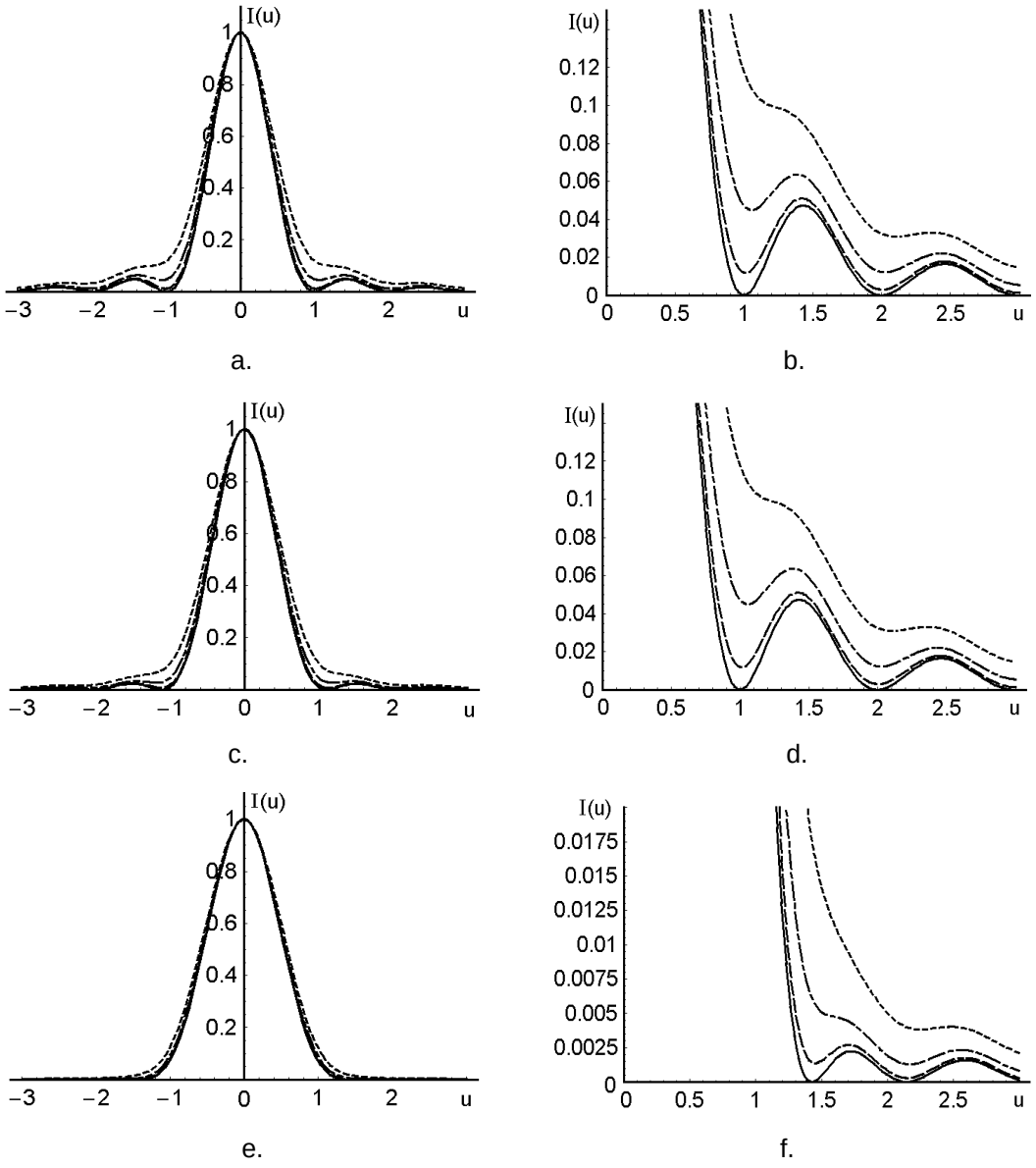

Fig.3.24. Combined effects of both the incident light apodization and the acoustic attenuation on the normalized light intensity in the focal plane: (a) and (b) are for $\beta = 0$, (c) and (d) are for $\beta = 2$, (e) and (f) are for $\beta = 6$. Then, everywhere, solid lines are for $\alpha_0 = 0$, dashed lines are for $\alpha_0 = 3$ dB, dashed-dotted lines are for $\alpha_0 = 6$ dB, and dotted lines are for $\alpha_0 = 10$ dB.

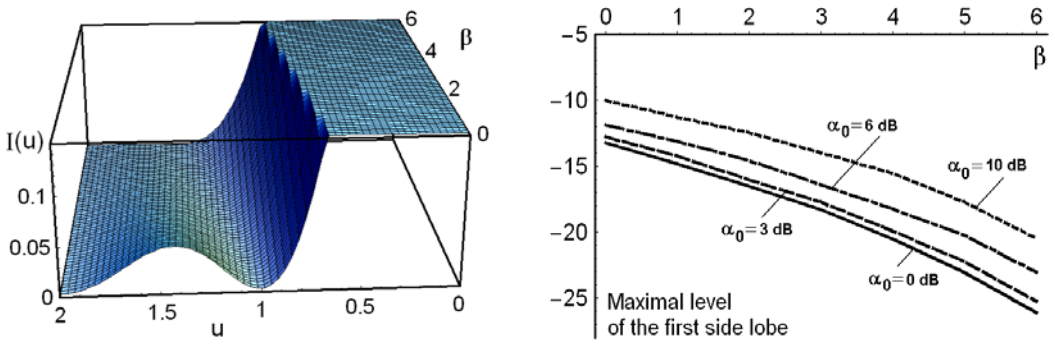

a. b.

Fig.3.25. The general plot of the first side lobe inherent in an individual resolvable spot in a Fourier plane (a) and maximal levels of the first side lobe versus the apodization parameter β (b), the solid line is for $\alpha_0 = 0$, the dashed line is for $\alpha_0 = 3$ dB, the dashed-dotted line is for $\alpha_0 = 6$ dB, and the dotted line is for $\alpha_0 = 10$ dB.

Figure 3.25 [14] illustrates the effect of maximal side lobe on the dynamic range, so that one can clearly see that acoustic attenuation decreases the potential dynamic range, which grows by itself with escalating the parameter β.

3.4 Conclusions

- The principle aspects of implementing and designing the glass-prism-made optical beam shaper using even numbers of prisms for the optical scheme of acousto-optical spectrometer have been studied.
- The procedure of optimizing by maximizing the potential resolution of an acousto-optical cell based on a one-phonon anomalous light scattering by acoustic phonons has been investigated. And, also in connection with a two-phonon light scattering in the acousto-optical cells in technically important particular case when the efficiency of acousto-optical interaction is so low that the first-order approximation in the problem of scattering becomes to be applicable and effective, have been investigated.

- The combined influence of both the geometric limitations and the acoustic attenuation on the number of resolvable spots for the regimes of a one-phonon anomalous light scattering and for a two-phonon light scattering has been created for the first time.
- In order to estimate the angular bandwidth of crystalline acousto-optical cell exploiting in a two-phonon light scattering regime the approach based on the transfer function inherent in linear optical systems, has been successfully applied.
- Practical capabilities of the incident light beam apodization connected with improving the dynamic range of acousto-optical spectrometer as a whole while still independently on the contribution from acoustic attenuation and also together with its contribution in an acousto-optical cell, have been studied.

References

1. M.Born and E.Wolf. *Principles of Optics.* 3-d Ed. (Pergamon Press, 1970, Oxford – London), Chapter 1.
2. **A.S.Shcherbakov, S.E.Balderas Mata, E.Tepichin Rodriguez, A.Luna Castellanos, D.Sanchez Lucero, and Je.Maximov, "The main peculiarities of arranging the optical scheme of acousto-optical spectrometer for the Mexican Large Millimeter Telescope", Proc. SPIE, Vol. 6663, 6663-0O (2007).**
3. J.W.Goodman: *Introduction to Fourier ptics.* 2-nd Ed. (McGraw Hill. New York. 1996) Chapter 5.
4. V. Mahajan. *Optical Imaging and Aberrations: Part I. Ray Geometrical Optics.* (SPIE Press Monograph Vol.PM45) Chapter 1.
5. R.W.Dixon. Acoustic diffraction of light in anisotropic media. IEEE Journal of Quantum Electronics, Vol.QE-3, 85-93 (1967).
6. N.Uchida and N.Niizeki. Acousto-optic deflection materials and techniques. Proc. IEEE, Vol.61, 1073-1092 (1973).
7. R.W.Klein and B.D.Cook. A unified approach to ultrasonic light diffraction. IEEE Transactions, Vol.SU-14, 123-134 (1967).

8. A.S. Shcherbakov, Je.Maximov, E.Tepichin Rodriguez, S.E.Balderas Mata, A.Luna Castellanos, and J.G.Aguilar Soto, "Applying a two-phonon light scattering in crystals to the spectrum analysis of radio-signals", Proc. SPIE, Vol. 6695, 6695-0W (2007).

9. A.S.Shcherbakov, E.Tepichin Rodriguez, Y.N. Ledeneva, and A.Aguirre López. Spatial modulators exploiting a multi-phonon light scattering in crystals. Proc. SPIE, Vol.6311, OA1 – OA10 (2006).

10. V.I.Balakshij, V.N.Parygin, L.E.Chirkov. Physical Principles of Acousto-Optics. (Radio I Svyaz, Moscow, 1985).

11. L.D.Landau and E.M.Liwshits. *Theory of Elasticity: Volume 7*. (Pergamon Press, Oxford, 1999).

12. **A.S.Shcherbakov, S.E.Balderas Mata, and D.Sanchez Lucero. "Estimating the factors restricting potential dynamic range in the optical scheme of acousto-optical spectrometer for the Mexican Large Millimeter Telescope", Proc. SPIE, Vol.6667, OM1 – OM10 (2007).**

13. **.S.Shcherbakov, S.E.Balderas Mata, "Potential dynamic range inherent in the optical scheme of acousto-optical spectrometerfor the Mexican Large Millimeter Telescope", Proc. of SOMI XXII (2007).**

14. **A.S.Shcherbakov, A.Luna Castellanos, E.Tepichin Rodriguez, and S.E.Balderas Mata, "Potential dynamic range in a scheme of acousto-optical spectrometer providing light beam apodization for a large-aperture crystalline cell with linear acoustic losses", Proc. SPIE, Vol. 6890 (2008).**

Chapter 4

Multi-wave acousto-optical coupled states

4.1 Introduction

The interaction of light with acoustic waves in a photo-elastic medium makes possible shaping multi-wave solitary waves, whose field components differ in physical nature, but are trapped by each other [1]. Such a type of Bragg solitary waves, so called coupled states, have recently been revealed and investigated in the systems with a square-law nonlinearity, namely, in two-mode waveguides [2,3], where spatial-temporal coupled states could be formed with a collinear geometry of acousto-optical interaction, and in crystals [4], allowing the existence of three- and four-wave coupled states with a non-collinear scattering of light by coherent acoustic phonons.

4.2 Three-wave dissipative collinear weakly acousto-optical coupled states

In some cases the analysis of three-wave processes leads to solitary waves in the form of coupled states, where waves of the same or even different nature become mutually trapped and propagate together [4-6]. Such coupled states can be shaped via stationary co-directional collinear interaction of two optical modes with a non-optical third wave in a dispersive waveguide due to the balancing action of the square-law nonlinearity. The profiles of all the waves are steady at three different current frequencies, because the interaction exhibits itself as a mechanism of stabilizing self-action.

A new specific regime is considered, which is related to shaping multi-pulse dissipative Bragg weakly-coupled states within a three-wave collinear interaction in a medium with linear losses for a slow non-optical wave. Both stationary and non-stationary analytic models are derived for describing the localization processes for multi-pulse dissipatvie three-wave coupled states. Computer simulations are performed and their behavior is discussed.

4.2.1 General consideration of a three-wave collinear interaction with phase mismatches and linear non-optical losses

As it has been mentioned, a three-wave co-directional collinear interaction with the mismatched wave numbers in a two-mode medium is described by a set of three nonlinear partial differential equations [7]. A regime of weak coupling [2,3] is considered, in which two light modes are scattered by a relatively slow wave, being non-optical by its nature and exhibiting linear losses, and the essentially effective Bragg scattering of light can be achieved without any observable influence of the scattering process on that non-optical wave, because the number of interacting photons is a few orders less than the number of the scattering quanta injected into a medium. The velocities of light modes can be approximated by the same value $\mathbf{c}$, because usually the length of crystalline waveguide does not exceed $\mathbf{10}$cm. In this regime, the above-mentioned set of equations falls into an equation for the complex amplitude $\mathbf{U(x,t)}$ of a slow wave and a pair of combined equations for the complex amplitudes $\mathbf{C_0(x,t)}$ and $\mathbf{C_1(x,t)}$ of the incident (pumping) light wave and scattered one, respectively [8-10],

$$\text{a)}\ \frac{\partial \mathbf{U}}{\partial \mathbf{x}} + \frac{\mathbf{1}}{\mathbf{V}}\frac{\partial \mathbf{U}}{\partial \mathbf{t}} = -\alpha \mathbf{U}, \qquad \text{b)}\ \frac{\partial \mathbf{C_0}}{\partial \mathbf{x}} + \frac{\mathbf{1}}{\mathbf{c}}\frac{\partial \mathbf{C_0}}{\partial \mathbf{t}} = -\mathbf{q_1}\,\mathbf{C_1 U^*}\,\exp\left(2\mathbf{i}\eta\,\mathbf{x}\right),$$

$$\text{c)}\ \frac{\partial \mathbf{C_1}}{\partial \mathbf{x}} + \frac{\mathbf{1}}{\mathbf{c}}\frac{\partial \mathbf{C_1}}{\partial \mathbf{t}} = \mathbf{q_0}\,\mathbf{C_0 U}\exp\left(-2\mathbf{i}\eta\,\mathbf{x}\right). \qquad (4.1)$$

Here, the factor α describes losses of the non-optical wave, $\mathbf{V}$ is the velocity of that slow wave, $\mathbf{q_{0,1}}$ are the constants of interaction, and $\mathbf{2\eta}$ is the mismatch of wave numbers inherent in the interacting waves. Now, one goes to the tracking coordinates $\mathbf{(x, \tau = t - x/c)}$ and assume that the non-optical wave, governed by Eq.(4.1a) and described by $\mathbf{U = u[x(1 - V/c) - V\tau]\ exp(-\alpha x)\ exp(i\varphi)}$, has the constant phase φ, so that one can convert Eqs.(4.1b) and (4.1c) into equations of the second order as

$$\frac{\partial^2 C_{0,1}}{\partial x^2} - \left(\frac{1}{u}\frac{\partial u}{\partial x} - \alpha \pm 2i\eta \right) \frac{\partial C_{0,1}}{\partial x} + q_0\, q_1\, u^2 \exp\left(-2\alpha x\right) C_{0,1} = 0 . \qquad (4.2)$$

By putting $\mathbf{C_{0,1} = a_{0,1}(x, t)\ exp[\, i\tilde{\Phi}_{0,1}(x, t)\,]}$, $\gamma_{0,1} = \partial\tilde{\Phi}_{0,1}/\partial x$ and then divide real and imaginary parts in Eqs.(4.2), one yields

$$\frac{\partial^2 a_{0,1}}{\partial x^2} - \left(\frac{1}{u}\frac{\partial u}{\partial x} - \alpha \right) \frac{\partial a_{0,1}}{\partial x} + \left[q_0\, q_1\, u^2 \exp\left(-2\alpha x\right) - \gamma_{0,1}^2 \pm 2\eta\,\gamma_{0,1} \right] a_{0,1} = 0 , \qquad (4.3)$$

$$2\left(\gamma_{0,1} \mp \eta\right) \frac{\partial a_{0,1}}{\partial x} + \left(\frac{\partial \gamma_{0,1}}{\partial x} - \frac{\gamma_{0,1}}{u}\frac{\partial u}{\partial x} + \alpha\gamma_{0,1} \right) a_{0,1} = 0 . \qquad (4.4)$$

Equations (4.4) have the following general solutions

$$\gamma_{0,1} = \pm\eta\, u\, a_{0,1}^{-2} \exp(-\alpha x) \times \int u^{-1} \left(\frac{\partial a_{0,1}^2}{\partial x} \right) \exp(\alpha x)\, dx + \tilde{\Gamma}_{0,1} u\, a_{0,1}^{-2} \exp(-\alpha x) , \qquad (4.5)$$

where $\tilde{\Gamma}_{0,1}$ are the two integration constants.

4.2.2 The quasi-stationary background-free continuous-wave regime; originating the localization condition

At first, restricting ourselves by considering the simplest choice of $\Gamma_{0,1} = 0$ in Eqs.(4.5) and study the phenomenon in the continuous-wave regime for the incident light and the non-optical wave when $u[x(1-V/c)-V\tau] = U_0$ is constant. Equations (4.3) and (4.4) can be analyzed with the fixed magnitude of the mismatch η and the practically natural boundary conditions $a_0(x=0,t)=1$, $(\partial a_0/\partial x)(x=0,t)=0$, $a_1(x=0,t)=0$, and $(\partial a_1/\partial x)(x=0,t)=q_0U_0$ in a half-infinite medium. In so doing, one can estimate $\gamma_{0,1}$ approximately. At first, one can assume that, due to smallness of the factor α, one can suggest that the spatial scale of varying the term $\exp(\alpha x)$ is much larger than the scale of varying $\partial a_{0,1}^2/\partial x$ in Eq.(4.5), so the term $\exp(\alpha x)$ can be factored out from the integral. As a result one can yield $\gamma_{0,1} \approx \pm\eta$ and $-\gamma_{0,1}^2 \pm 2\eta\gamma_{0,1} = \eta^2$. It should be noted that the same result could be obtained, even if $\gamma_{0,1}$ will be calculated to the first approximation in powers of α in that integral term, i.e. estimated as [8-10]

$$\text{a)}\ \gamma_{0,1} \approx \pm\eta\left(1-\alpha\, a_{0,1}^{-2}\int a_{0,1}^2\,dx\right), \qquad \text{b)}\ \gamma_{0,1}^2 \approx \eta^2\left(1-2\alpha\, a_{0,1}^{-2}\int a_{0,1}^2\,dx\right). \tag{4.6}$$

The second approximation in powers of α in the same integral term gives

$$-\gamma_{0,1}^2 \pm 2\eta\gamma_{0,1} = \eta^2\left[1-2\alpha^2\, a_{0,1}^{-4}\int\left(a_{0,1}^2\int a_{0,1}^2\,dx\right)dx\right]. \tag{4.7}$$

Thus, with the notation $q_0 q_1 U_0^2 = \sigma^2$, Eq.(4.3) takes the form

$$\frac{\partial^2 a_{0,1}}{\partial x^2} + \alpha\,\frac{\partial a_{0,1}}{\partial x} + \left[\sigma^2\exp(-2\alpha x) + \eta^2\right]a_{0,1} = 0. \tag{4.8}$$

Recently, Eq.(4.8) has been analyzed in the case of $\alpha = 0$ and $\eta \neq 0$ [2,3], while now another possibilities will be considered. It should be noted that Eq.(4.8) has the following exact analytical solution in terms of Bessel functions

$$a_{0,1} = B_{0,1} \exp\left(-\frac{\alpha x}{2}\right) J_{\nu}\left[\exp(-\alpha x)\frac{\sigma}{\alpha}\right] + \tilde{D}_{0,1} \exp\left(-\frac{\alpha x}{2}\right) J_{-\nu}\left[\exp(-\alpha x)\frac{\sigma}{\alpha}\right]. \tag{4.9}$$

where $B_{0,1}$ and $\tilde{D}_{0,1}$ are the integration constants; and $\nu = (2\alpha)^{-1}\sqrt{\alpha^2 - 4\eta^2}$. In the regime of an exact phase synchronism, i.e. with $\eta = 0$ and $\alpha \neq 0$, when the indices of Bessel functions in Eq.(4.9) are equal to $\pm 1/2$, these solutions can be reduced to

$$a_{0,1} = K_{0,1} \sin\left\{\frac{\sigma}{\alpha}\left[1 - \exp(-\alpha x)\right]\right\} + L_{0,1} \cos\left\{\frac{\sigma}{\alpha}\left[1 - \exp(-\alpha x)\right]\right\}, \tag{4.10}$$

with the following relations between the integration constants

$$B_{0,1}\sqrt{\frac{2\alpha}{\pi\sigma}} = K_{0,1}\cos\left(\frac{\sigma}{\alpha}\right) + L_{0,1}\sin\left(\frac{\sigma}{\alpha}\right), \quad \text{and}$$

$$\tilde{D}_{0,1}\sqrt{\frac{2\alpha}{\pi\sigma}} = K_{0,1}\sin\left(\frac{\sigma}{\alpha}\right) + L_{0,1}\cos\left(\frac{\sigma}{\alpha}\right).$$

Applying the above-mentioned boundary conditions to Eq.(4.10), one can obtain

$$\text{a)} \quad \left|C_0(x)\right|^2 = \cos^2\left\{\frac{\sigma}{\alpha}\left[1 - \exp(-\alpha x)\right]\right\},$$

$$\text{b)} \quad \left|C_1(x)\right|^2 = \frac{q_0}{q_1}\sin^2\left\{\frac{\sigma}{\alpha}\left[1 - \exp(-\alpha x)\right]\right\}. \tag{4.11}$$

It is seen from Eqs.(4.11) that the contribution of the linear losses from the non-optical wave exhibits itself like some spatial scaling in light scattering, while the efficiency of light scattering can achieve 100% with $\eta = 0$ and $\alpha \neq 0$.

However, the general solution form to Eq.(4.8) represented by Eq.(4.9) is not quite convenient in practically important cases of large phase mismatches $\eta > \alpha$. To construct another form of the solution one can use the conservation law $q_0 a_0^2 + q_1 a_1^2 = q_0$ - const, resulting from Eqs.(4.1). Combining Eqs.(4.8) for a_0 and a_1, one can obtain a pair of the following equations:

$$\frac{\partial (a_{0,1}^2)}{\partial x} = 2\sqrt{a_{0,1}^2 (q_{0,1}^{-1} q_0 - a_{0,1}^2)\,[\sigma^2 \exp(-2\alpha x) + \eta^2\,]}, \qquad (4.12)$$

whose solutions with arbitrary integration constants $\theta_{0,1}$ are given by

$$\text{a)}\ \ a_{0,1}^2 = q_{0,1}^{-1} q_0 \sin^2\left[\theta_{0,1} + G(x)\right], \qquad \text{b)}\ \ G(x) = \int \sqrt{\sigma^2 \exp(-2\alpha x) + \eta^2}\ dx. \qquad (4.13)$$

Using the above-noted boundary conditions, one arrive at [10]

$$\text{a)}\ \ \theta_0 = \arcsin\left[\sigma^{-1}\sqrt{\sigma^2 + \eta^2}\,\right] - G(0), \qquad \text{b)}\ \ \theta_1 = -G(0),$$

$$\text{c)}\ \ G(x) = \frac{1}{\alpha}\left[-\sqrt{\eta^2 + \sigma^2 \exp(-2\alpha x)} + \right.$$

$$\left. + \eta \ln\left\{ 2\alpha\eta^{-2}\left[\eta \exp(\alpha x) + \sqrt{\sigma^2 + \eta^2 \exp(2\alpha x)}\,\right]\right\}\right].$$

$$\text{d)}\ \ G(0) = \frac{1}{\alpha}\left(-\sqrt{\eta^2 + \sigma^2} + \eta \ln\left\{ 2\alpha\eta^{-2}\left[\eta + \sqrt{\sigma^2 + \eta^2}\,\right]\right\}\right), \qquad (4.14)$$

So that the stationary intensities of the pumping and scattered light waves can be expressed as

$$\text{a)}\ \ |C_0(x)|^2 = \frac{\eta^2}{\sigma^2 + \eta^2} + \frac{\sigma^2}{\sigma^2 + \eta^2} \cos^2\left[G(x) - G(0)\right],$$

b) $$\left|\mathbf{C_1(x)}\right|^2 = \frac{q_0}{q_1}\frac{\sigma^2}{\sigma^2+\eta^2}\ \sin^2\left[\mathbf{G(x)-G(0)}\right]. \qquad (4.15)$$

These solutions include contributions of two types. The first summand in Eq.(4.15a) represents a background determined by the phase mismatch η; while the second one gives the oscillations imposed on that background. The scattered light wave intensity Eq.(4.15b) contains only some oscillations, so that one can write the localization condition as

$$\mathbf{G(x)-G(0)} = \pi\mathbf{N}, \qquad (4.16)$$

where ($\mathbf{N = 1,2,}\ldots$). Of course, when $\eta = \mathbf{0}$, it yields $\mathbf{G(x)} = -\alpha^{-1}\sigma\ \mathbf{exp(-\alpha x)}$, $\theta_0 = \alpha^{-1}\sigma + (\pi/2)$, and $\theta_1 = \alpha^{-1}\sigma$, so that Eqs.(4.15) take the form of Eqs.(4.11). The fact of the existance of this localization condition means the dissipative collinear three-wave coupled states appearing in a two-mode medium with sqaure-law nonlinearity and linear losses for a slow non-optical wave; and they can include more than one pulse when $\mathbf{N > 1}$.

Additionally, it should be noted that a pair of the obtained solutions for the intensities $\mathbf{I_{0,1}} = \left|\mathbf{C_{0,1}}\right|^2$, Eqs.(4.15), satisfies the following ordinary differential equations of the second order

$$\left(\frac{dG}{dx}\right)^{-2}\frac{\partial^2 I_0}{\partial x^2} + \alpha\left(\frac{dG}{dx}\right)^{-4}\left[\left(\frac{dG}{dx}\right)^2 - \eta^2\right]\frac{\partial I_0}{\partial x} + 4I_0 = 2\left(\frac{\sigma^2+2\eta^2}{\sigma^2+\eta^2}\right), \qquad (4.17)$$

$$\left(\frac{dG}{dx}\right)^{-2}\frac{\partial^2 I_1}{\partial x^2} + \alpha\left(\frac{dG}{dx}\right)^{-4}\left[\left(\frac{dG}{dx}\right)^2 - \eta^2\right]\frac{\partial I_1}{\partial x} + 4I_1 = \frac{2q_0}{q_1}\left(\frac{\sigma^2}{\sigma^2+\eta^2}\right), \qquad (4.18)$$

with the previously noted boundary conditions $\mathbf{I_0(x=0)} = \mathbf{1}$, $\mathbf{I_1(x=0)} = \mathbf{0}$ and $\mathbf{(\partial I_0/\partial x)(x=0)} = \mathbf{(\partial I_1/\partial x)(x=0)} = \mathbf{0}$. Of course, the relation $\mathbf{q_0\,(\partial I_0/\partial x)} = -\mathbf{q_1\,(\partial I_1/\partial x)}$ takes place, within the process under consideration.

Then, the number $\mathbf{N}$ of bright or dark pulses in the corresponding component of the coupled state is conditioned by both the frequency mismatch η as well as by the losses α. Let us consider two particular cases. In the first lossless case of $\alpha = 0$ and $\eta \neq 0$, one can obtain from Eq.(4.16)

$$\text{a)}\ \ \eta^2 = \pi^2 N^2 x_C^{-2} - \sigma^2, \qquad \text{b)}\ \ G(x) - G(0) = \frac{\pi N x}{x_C}\ , \tag{4.19}$$

where x_C is the spatial length of localization. One can substitute this formula into Eq.(4.15b) and yield the dependence of the scattered light intensity I_1 on the number $\mathbf{N}$ of pulses in a coupled state in the form [10]

$$I_1^{(N)}(x, \alpha = 0) = \frac{q_0}{q_1}\frac{\sigma^2 x_C^2}{\pi^2 N^2}\ \sin^2\left(\frac{\pi N x}{x_C}\right). \tag{4.20}$$

It is seen from Eq.(4.20) that, as the number $\mathbf{N}$ grows, the intensity of the scattered light component in a three-wave coupled state decreases as N^2, because the mismatch increases following Eq.(4.19a). At the same time, the spatial width $x_C/(\pi N)$ of each partial optical pulse inherent in this coupled state narrows as N^{-1}. By contrast, in the second particular case of an exact phase synchronism when $\eta = 0$ and $\alpha \neq 0$, Eq.(4.16) leads to the formula $\alpha^{-1}\sigma[1 - \exp(-\alpha x)] = \pi N$. Because the left-hand side of this formula is limited, one can find that $N \leq \sigma/(\alpha\pi)$, i.e. the whole number $\mathbf{N}$ comes to be restricted. For example, when $\alpha = 0.1$ and $\sigma = 1$, we yield $N \leq 3$, see Fig.4.1. In the general case, when $\eta \neq 0$ and $\alpha \neq 0$, a transcendental equation relative to both η and α appears from Eqs.(4.16) and (4.14). That is why this case requires numerical simulations presented in Fig.4.2.

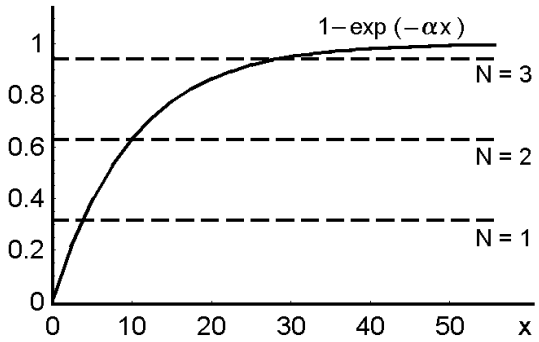

Fig.4.1 Restricting the number $\mathbf{N}$ of pulses in a coupled state in the case of $\eta = 0$ and $\alpha \neq 0$; for the taken example of $\alpha = 0.1$ and $\sigma = 1$, one can find $N \leq 3$.

Nevertheless, in the practically important case of low losses for the non-optical wave, one can develop an approximate approach illustrating the effect of losses. In this case, one can put in the first approximation that $\exp(-2\alpha x) \approx 1 - 2\alpha x$ and integrate Eq.(4.13b) as

$$\text{a)}\quad G(x, \alpha \to 0) = \sqrt{\sigma^2(1 - 2\alpha x) + \eta^2} \times \left(\frac{2x}{3} - \frac{\sigma^2 + \eta^2}{3\alpha\sigma^2} \right),$$

$$\text{b)}\quad G(x = 0, \alpha \to 0) = -\frac{\left(\sigma^2 + \eta^2\right)^{3/2}}{3\alpha\sigma^2}. \qquad (4.21)$$

Equations (4.21) lead to

$$G(x, \alpha \to 0) - G(x = 0, \alpha \to 0) = \frac{\left(\sigma^2 + \eta^2\right)^{3/2} - \left(\sigma^2 + \eta^2 - 2\alpha x\right)^{3/2}}{3\alpha\sigma^2}. \qquad (4.22)$$

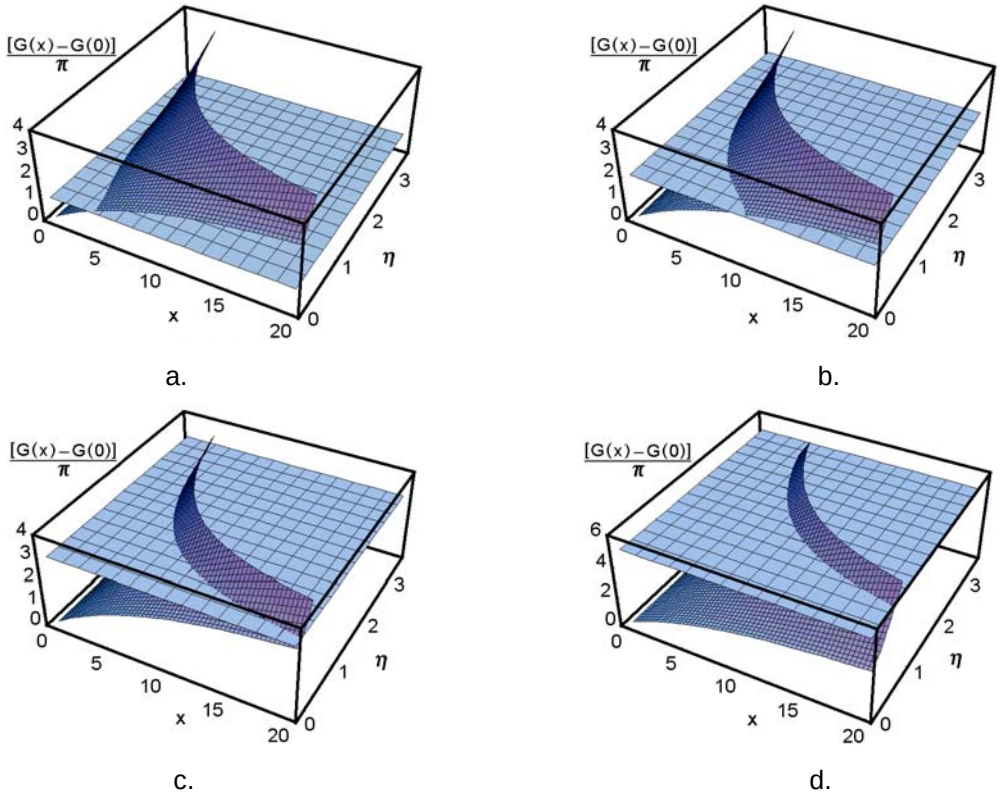

Fig.4.2 The possibility of shaping multi-pulse coupled states when $\eta \neq 0$ and $\alpha \neq 0$; i.e., $\alpha = 0.1$ and $\sigma = 1$, one can realize: a) $N = 1$, b) $N = 2$, c) $N = 3$, and d) $N = 5$.

In the first approximation with respect α, Eq.(4.22) takes the form

$$G(x, \alpha \to 0) - G(x = 0, \alpha \to 0) = x\sqrt{\sigma^2 + \eta^2} - \frac{\alpha x^2 \sigma^2}{2\sqrt{\sigma^2 + \eta^2}}. \qquad (4.23)$$

Consequently, using Eqs.(4.23) and (4.19b), one can rewrite the localization condition as

$$G(x = x_C, \alpha \to 0) - G(x = 0, \alpha \to 0) = x_C\sqrt{\sigma^2 + \eta^2} - \frac{\alpha x_C^2 \sigma^2}{2\sqrt{\sigma^2 + \eta^2}} = \pi N. \qquad (4.24)$$

Considering Eq.(4.24) as the algebraic quadratic equation relative to $\sqrt{\sigma^2 + \eta^2}$, one can find

$$\sqrt{\sigma^2+\eta^2}=\frac{\pi N}{x_C}+\frac{\alpha x_C^2\sigma^2}{2\pi N}. \tag{4.25}$$

Substituting this formula into Eq.(4.15b), one can estimate the factor

$$\frac{\sigma^2}{\sigma^2+\eta^2}\approx\frac{x_C^2\sigma^2}{\pi^2N^2+\alpha x_C^3\sigma^2}, \tag{4.26}$$

So that Eq.(4.20) takes the following approximate form [10]

$$I_1^{(N)}(x,\alpha\neq 0)=\frac{q_0}{q_1}\frac{x_C^2\sigma^2}{\pi^2N^2+\alpha x_C^3\sigma^2}\sin^2\left(\frac{\pi N x}{x_C}\right). \tag{4.27}$$

It is seen from Eq.(4.27) that as the number N of pulses in the dissipative coupled states grows, the intensity $I_1^{(N)}$ of the scattered light decreases, but now even a little bit faster than as N^2, as it was in Eq.(4.20), due to the contribution of the acoustic losses connected with the presence of the term including a small factor α in the denominator of Eq.(4.27).

4.2.3 The quasi-stationary continous-wave regime with $\Gamma\neq 0$; appearing a background

Now, one can take the case of $\Gamma\neq 0$ and consider this phenomenon again in the continuous-wave regime for the incident light and the non-optical wave with previously formulated boundary conditions. Estimating $\gamma_{0,1}$ from Eq.(4.5) approximately as above, one can now write [8-10]

a) $\gamma_{0,1}\approx\pm\eta+\Gamma_{0,1}U_0\,a_{0,1}^{-2}\exp(-\alpha x)$,

b) $-\gamma_{0,1}^2\pm 2\eta\gamma_{0,1}=\eta^2+\Gamma_{0,1}^2U_0^2\,a_{0,1}^{-4}\exp(-2\alpha x)$, (4.28)

As a result, Eqs.(4.3) take the following form

$$\frac{\partial^2 a_{0,1}}{\partial x^2} + \alpha \frac{\partial a_{0,1}}{\partial x} + \left[\sigma^2 \exp(-2\alpha x) + \eta^2 \right] a_{0,1} = \Gamma_{0,1}^2 U_0^2 a_{0,1}^{-4} \exp(-2\alpha x). \tag{4.29}$$

It is seen that Eqs.(4.29) for the amplitudes a_0 and a_1 are the same, so the indices of waves can be omitted in further analysis. Introducing a new independent variable $\zeta = \alpha^{-1}[1 - \exp(-\alpha x)]$ and converting Eqs.(4.29) into the Ermakov equation [11,12]

$$\frac{\partial^2 a}{\partial \zeta^2} + \left[\sigma^2 + \eta^2 (1 - \alpha\zeta)^{-2} \right] a = \Gamma^2 U_0^2 a^{-3}. \tag{4.30}$$

The general solution to Eq.(4.30) has the form [11]

$$a^2(\zeta) = \tilde{M}_1^{-1} \tilde{W}^2(\zeta) \left[\Gamma^2 U_0^2 + \left(\tilde{M}_2 + \tilde{M}_1 \int \tilde{W}^{-2}(\zeta)\, d\zeta \right)^2 \right], \tag{4.31}$$

where $\tilde{M}_{1,2}$ are the integration constants and $\tilde{W}(\zeta)$ is a non-trivial solution to the reduced form of Eq.(4.30), namely, to the linear differential equation

$$\frac{\partial^2 a_r}{\partial \zeta^2} + \left[\sigma^2 + \eta^2 (1 - \alpha\zeta)^{-2} \right] a_r = 0. \tag{4.32}$$

Equation (4.32) has the exact solution in terms of Bessel functions

$$a_r(\zeta) = Z_1 \sqrt{1 - \alpha\zeta}\, J_{-\nu}\left[(1 - \alpha\zeta) \frac{\sigma}{\alpha} \right] + Z_2 \sqrt{1 - \alpha\zeta}\, J_{\nu}\left[(1 - \alpha\zeta) \frac{\sigma}{\alpha} \right], \tag{4.33}$$

where $\nu = \frac{\sqrt{\alpha^2 - 4\eta^2}}{2\alpha}$ and the integration constants $Z_{1,2}$. This solution shows that one can take one of the following non-trivial functions $\tilde{W}(\zeta)$

$$\text{a)}\quad \tilde{W}_1(\zeta) = \sqrt{1-\alpha\zeta}\; J_{-\nu}\left[\left(1-\alpha\zeta\right)\frac{\sigma}{\alpha}\right],$$

$$\text{b)}\quad \tilde{W}_2(\zeta) = \sqrt{1-\alpha\zeta}\; J_{\nu}\left[\left(1-\alpha\zeta\right)\frac{\sigma}{\alpha}\right]. \qquad (4.34)$$

Unfortunately, in general, the integral term in Eq.(4.31) cannot be calculated in the closed form with $\tilde{W} = \tilde{W}_{1,2}(\zeta)$. That is why to illustrate the contributions of the factors $\Gamma_{0,1} \neq 0$ one can analyze the rather simple case for the absence of mismatches, i.e. $\eta \equiv 0$. In so doing, rather then operate over Eq.(4.34), it would be simpler to take the Ermakov equation appearing directly from Eq.(4.30) with $\eta = 0$, namely,

$$\frac{\partial^2 a}{\partial \zeta^2} + \sigma^2 a = \Gamma^2 U_0^2 a^{-3}. \qquad (4.35)$$

The corresponding non-trivial solutions to the linearized form of Eq.(4.35) can be found from

$$a_r(\zeta, \eta = 0) = Y_1 \sin(\sigma\zeta) + Y_2 \cos(\sigma\zeta), \qquad (4.36)$$

where $Y_{1,2}$ are integration constants, and one can choose

$$\text{a)}\quad \tilde{W}_1(\zeta, \eta = 0) = \sin(\sigma\zeta), \qquad \text{b)}\quad \tilde{W}_2(\zeta, \eta = 0) = \cos(\sigma\zeta). \qquad (4.37)$$

Now, one can introduce a new dependent variable $b(\zeta) = a^2(\zeta) \geq 0$ and convert Eq.(4.35) into another equivalent form

$$\frac{b}{2}\frac{\partial^2 b}{\partial \zeta^2} - \frac{1}{4}\left(\frac{\partial b}{\partial \zeta}\right)^2 + \sigma^2 b^2 = \Gamma^2 U_0^2. \qquad (4.38)$$

Equation (4.38) shows that as far as $\Gamma \neq 0$, an arbitrary solution $b(\zeta) \geq 0$ will include a background, because Eq.(4.38) with $\Gamma \neq 0$ cannot be satisfied at the points ζ_0 wherein $b(\zeta_0) = 0$ and $(db/d\zeta)(\zeta_0) = 0$ simultaneously.

Then, substituting Eqs.(4.37) into Eq.(4.31) and using the new variable $\mathbf{b}(\zeta)$, one can obtain two rather different solutions to Eq.(4.35) as well as to Eq.(4.38)

$$\mathbf{b_1}(\zeta, \eta = 0) = \tilde{\mathbf{G}}_1^{-1} \sin^2(\sigma\zeta) \left\{ \Gamma^2 \mathbf{U}_0^2 + \left[\tilde{\mathbf{H}}_1 - \sigma^{-1} \tilde{\mathbf{G}}_1 \cot(\sigma\zeta) \right]^2 \right\}, \tag{4.39}$$

$$\mathbf{b_2}(\zeta, \eta = 0) = \tilde{\mathbf{G}}_2^{-1} \cos^2(\sigma\zeta) \left\{ \Gamma^2 \mathbf{U}_0^2 + \left[\tilde{\mathbf{H}}_2 + \sigma^{-1} \tilde{\mathbf{G}}_2 \tan(\sigma\zeta) \right]^2 \right\}, \tag{4.40}$$

where $\tilde{\mathbf{G}}_{1,2}$ and $\tilde{\mathbf{H}}_{1,2}$ are integration constants. In terms of the coordinate $\mathbf{x}$, Eqs.(4.39) and (4.40) take the following forms

$$\mathbf{b_1}(\mathbf{x}, \eta = 0) = \tilde{\mathbf{G}}_1^{-1} \sin^2 \left\{ \frac{\sigma}{\alpha} \left[1 - \exp(-\alpha \mathbf{x}) \right] \right\} \times$$

$$\times \left[\Gamma^2 \mathbf{U}_0^2 + \left(\tilde{\mathbf{H}}_1 - \frac{\tilde{\mathbf{G}}_1}{\sigma} \cot \left\{ \frac{\sigma}{\alpha} \left[1 - \exp(-\alpha \mathbf{x}) \right] \right\} \right)^2 \right], \tag{4.41}$$

$$\mathbf{b_2}(\mathbf{x}, \eta = 0) = \tilde{\mathbf{G}}_2^{-1} \cos^2 \left\{ \frac{\sigma}{\alpha} \left[1 - \exp(-\alpha \mathbf{x}) \right] \right\} \times$$

$$\times \left[\Gamma^2 \mathbf{U}_0^2 + \left(\tilde{\mathbf{H}}_2 + \frac{\tilde{\mathbf{G}}_2}{\sigma} \tan \left\{ \frac{\sigma}{\alpha} \left[1 - \exp(-\alpha \mathbf{x}) \right] \right\} \right)^2 \right]. \tag{4.42}$$

Using Eqs.(4.41) and (4.42), one can find the boundary values at $\mathbf{x} = \mathbf{0}$ as $\mathbf{b_1}(\mathbf{x} = \mathbf{0}, \eta = \mathbf{0}) = \mathbf{G_1} \sigma^{-2}$ and $\mathbf{b_2}(\mathbf{x} = \mathbf{0}, \eta = \mathbf{0}) = \tilde{\mathbf{G}}_2^{-1} (\Gamma^2 \mathbf{U}_0^2 + \mathbf{H}_2^2)$. Together with this, one can estimate the frequency distribution along a wave using Eq.(4.28a). On the one hand, such an estimation will be non-trivial only when $\Gamma \neq \mathbf{0}$, while on the other hand, the regime of an exact phase synchronism with $\eta = \mathbf{0}$ is under consideration at the moment. Consequently, the expression for the frequency γ has to be written as $\gamma \approx \Gamma \mathbf{U_0} \mathbf{b}_2^{-1} \exp(-\alpha \mathbf{x})$. The corresponding plot

is shown by a dotted line only in Fig.(4.3a) related to the case $\Gamma \neq 0$, whereas for the cases depicted in Figs.(4.3b) and (4.3c) the frequency γ is equal to zero.

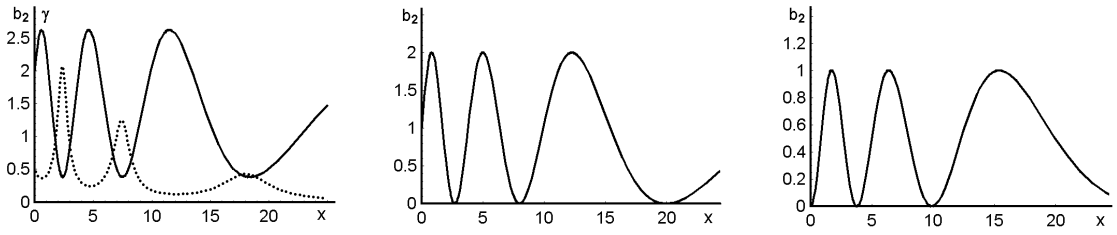

a. b. c.

Fig.4.3 Plots for $b_2(x, \eta = 0)$ with $\sigma = 1$, $\alpha = 0.1$, and $G_2 = 1$: a) $H_2 = 1$, $\Gamma^2 U_0^2 = 1$, (solid line for b_2, dotted line for the frequency γ); b) $H_2 = 1$, $\Gamma^2 U_0^2 = 0$; c) $H_2 = 0$, $\Gamma^2 U_0^2 = 0$.

Typical illustrative plots for the solution $b_2(x, \eta = 0)$ with various constants are presented in Fig.(4.3) by solid lines.

4.2.4 Non-stationary regime of the pulsed non-optical wave and localizing multi-pulse dissipative three – wave weakly coupled states

One can focus the attention on the process of localizing multi-pulse dissipative three-wave coupled states when the incident light is continuous-wave in behavior, but two facets of a medium at $x = 0$ and $x = L$ bound the area of interaction and the pulsed non-optical wave is excited in a waveguide. Let the spatial length x_0 of non-optical pulse is much shorter than L ($T_0 = x_0/V << T = L/V$) and the localizing pulse of a slow non-optical wave has a rectangular in shape, i.e., $u(x,t) = U_0\{\theta[x(1-V/c) - V\tau] - \theta[(x - x_0)(1-V/c) - V\tau]\}$. Due to $V << c$, one may put that $\partial u/\partial x \approx 0$ in Eqs.(4.3) and (4.4), excluding the points $x \in \{0, x_0\}$. These suppositions lead to three stages in the localization process; first, when the localizing non-optical pulse is incoming through the facet $x = 0$, then when the

pulse is passing along a waveguide, and finally, it is issuing through the facet $\mathbf{x = L}$. Such a process is illustrated for $|\mathbf{C_1}|^2$ in Fig.4.4 and can be described analytically by [8-10]

$$\text{a)}\ \left|\mathbf{C_0}(\mathbf{x},\tau)\right|^2 = \frac{\eta^2}{\sigma^2+\eta^2} + \frac{\sigma^2}{\sigma^2+\eta^2}\ \cos^2\left[\Phi(\mathbf{x},\tau)\right],$$

$$\text{b)}\ \left|\mathbf{C_1}(\mathbf{x},\tau)\right|^2 = \frac{q_0}{q_1}\frac{\sigma^2}{\sigma^2+\eta^2}\ \sin^2\left[\Phi(\mathbf{x},\tau)\right], \qquad (4.43)$$

where the argument of in Eqs.(4.43) can be described as

$$\Phi(\mathbf{x},\tau) = \begin{cases} \mathbf{G(x) - G(0)}, & \mathbf{0 \le \tau \le T;} \\ \mathbf{G(x) - G(x - x_0)}, & \mathbf{T \le \tau \le x(c - V)/(cV);} \\ \mathbf{G(L) - G(x - x_0)}, & \mathbf{x(c - V)/(cV) \le \tau \le T + x(c - V)/(cV);} \\ \mathbf{0}, & \mathbf{\tau < 0\ or\ \tau > T + x(c - V)/(cV).} \end{cases} \qquad (4.44)$$

The first summand in Eq.(4.43a) exhibits a background of the light wave $|\mathbf{C_0}|^2$, whose level is determined by the mismatch η; the second one represents the oscillating portion of the solution, i.e. the localized part of the incident light imposed on a background. The light wave $|\mathbf{C_1}|^2$ contains the only oscillating portion of the light field that gives the localization condition $\mathbf{G(x_C) - G(0) = \pi N}$, being perfectly analogous to Eq.(4.16); here, $\mathbf{x_C}$ is the spatial size of localization area with $\mathbf{V << c}$ and $\mathbf{N = 0,\ 1,\ 2,...}$. Figure 4.4 illustrates the numerical simulations of Eqs.(4.43b) and (4.44). The corresponding numerical plots for $|\mathbf{C_0}|^2$ can be easily created using the above-mentioned conservation law $\mathbf{q_0 a_0^2 + q_1 a_1^2 = q_0 - const}$.

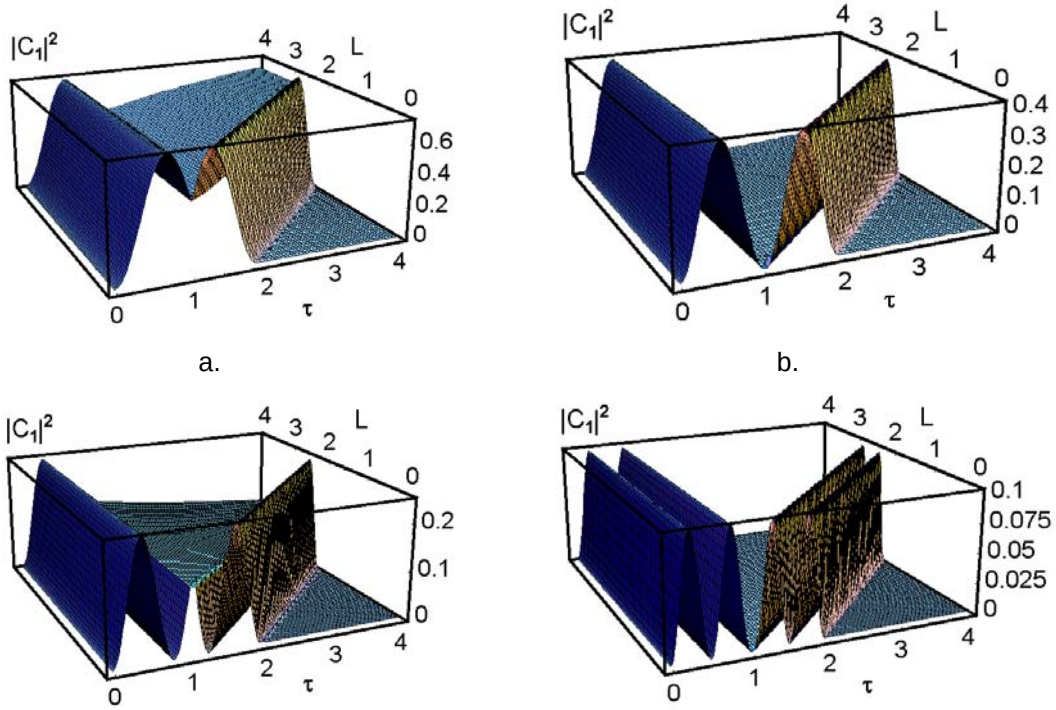

Fig.4.4 Intensity of the scattered light components vs. τ and **L** with $\sigma = 2$ and $\alpha = 0.05$. Four stages of reshaping are simulated: a) $\eta = 1.5$, the beginning of shaping a one-pulse dissipative coupled stated; b) $\eta = 2.4$, a one-pulse dissipative coupled stated; c) $\eta = 3.5$, an intermediate stage; and d) $\eta = 6.0$, a two-pulse dissipative coupled state.

From the viewpoint of further experimental verification, these plots can be interpreted rather simply. Depending on the practically fixed length **L** of a two-mode medium sample, one can consider a cross section of each of these plots with the selected plane $\mathbf{L} = \mathbf{const}$ to obtain the corresponding one-dimensional theoretical curve in time domain related to the chosen value of a mismatch. Thus, taking alone perfectly localized states presented here in Fig.4.4b for $\mathbf{N} = \mathbf{1}$ and in Fig.4.4d for $\mathbf{N} = \mathbf{2}$, one can see that it is possible to observe the localized field associated with the scattered light component $|\mathbf{C_1}|^2$ for two times, namely, when the localizing non-optical pulse is incoming or issuing through one of the facets of a medium creating or destroying, respectively, the corresponding multi-pulse three-wave dissipative coupled states.

4.2.5 Preliminary estimations

Now let us consider a few practically useful estimations related to experimental observation of the dissipative collinear three-wave coupled states in a two-mode medium with a square-law nonlinearity and linear acoustic losses. One can select such a physical phenomenon as the collinear acousto-optical interaction with linear acoustic losses in a two-mode crystalline cell made of a calcium molybdate ($CaMoO_4$) single crystal. In this case, one can observe only the anomalous process of light scattering [13] when the states of polarization for the incident and scattered light beams are orthogonal to each other, so that the parameter $q_{0,1}$ are described [14] by

$$q_{0,1} = \frac{\left|\vec{k}_{0,1}\right|}{4n_{0,1}^2}\left(\tilde{\vec{e}}_0 \,\Delta\hat{\varepsilon}\,\vec{e}_1\right). \qquad (4.45)$$

Here, $n_{0,1}$ are the refractive indices for the interacting light waves, $\left|\vec{k}_{0,1}\right| = 2\pi n_{0,1}/\lambda$, λ is the light wavelength in a vacuum and the last term in brackets describes the efficiency of interaction. This term includes the eigen-orts $\vec{e}_{0,1}$ of polarizations for the incident and scattered light beams as well as the tensor $\Delta\hat{\varepsilon}$ of perturbations of the dielectric permittivity under action of the acoustic wave in a medium. To estimate the efficiency of collinear acouto-optical interaction in a $CaMoO_4$ cell, i.e. to find the contribution in brackets of Eq.(4.45), one can consider the geometry of interaction including the shear acoustic wave with the wave normal ort $\vec{m}^*$ is passing along the $[100]$ axis, while its vector $\vec{u}$ of the transversal elastic displacements is oriented along the $[001]$ axis in that crystalline material. Consequently, one can write the deformation tensor $\hat{\gamma}$ and the unperturbed dielectric permittivity tensor $\hat{\varepsilon}$ in the main crystallographic axes as

$$\text{a)}\ \hat{\gamma} = \frac{\hat{\gamma}_0}{2}\left(\vec{u}\cdot\vec{m}^{*} + \vec{m}^{*}\cdot\vec{u}\right) = \frac{\hat{\gamma}_0}{2}\begin{pmatrix} 0 & 0 & 1 \\ 0 & 0 & 0 \\ 1 & 0 & 0 \end{pmatrix}, \qquad \text{b)}\ \hat{\varepsilon} = \begin{pmatrix} \varepsilon_0 & 0 & 0 \\ 0 & \varepsilon_0 & 0 \\ 0 & 0 & \varepsilon_e \end{pmatrix}. \tag{4.46}$$

Here, $\hat{\gamma}_0$ is the amplitude of the shear deformation, while $\varepsilon_0 = n_0^2$ and $\varepsilon_e = n_e^2$ are the eigenvalues of the unperturbed dielectric permittivity tensor $\hat{\varepsilon}$. Now, the tensor $\hat{\gamma}$ of the second rank with the components γ_{kl} $(k,l = 1,2,3)$ can be converted into a six-dimensional vector $\bar{\gamma} = \hat{\gamma}_0\ (0,\ 0,\ 0,\ 0,\ 1,\ 0)$ with the components $\bar{\gamma}_\mu$ $(\mu = 1,\ldots,6)$ using the standard procedure [15], which includes re-notating $\bar{\gamma}_\mu = \gamma_{kk}$ $(\mu = 1,2,3)$ and $\bar{\gamma}_\mu = 2\gamma_{k,l}$ $(k \neq l,\ \mu = 4,5,6)$. If one uses the same procedure [15] and takes the photo-elastic tensor p of the fourth rank for a $CaMoO_4$ single crystal in the form 6×6 matrix $\hat{p}$, it will be possible first to construct and to calculate the product $\hat{p}\bar{\gamma} = \hat{\gamma}_0\ (0,\ 0,\ 0,\ p_{45},\ p_{44},\ 0)$, and then to convert the result back to the form of a standard tensor $(\hat{p}\hat{\gamma})$ of the second rank.

The next step of our analysis is connected with finding the dielectric permittivity perturbation tensor $\Delta\hat{\varepsilon}$, whose components can be written as $\Delta\hat{\varepsilon}_{ij} = \varepsilon_{im}\,\varepsilon_{nj}\,p_{mnkl}\,\gamma_{kl}$ [14]. The result of similar calculations has the form

$$\Delta\hat{\varepsilon} = \hat{\gamma}_0\varepsilon_0\varepsilon_e\begin{pmatrix} 0 & 0 & p_{44} \\ 0 & 0 & p_{45} \\ p_{44} & p_{45} & 0 \end{pmatrix}. \tag{4.47}$$

Now, one can take into account the orts $\vec{e}_{0,1}$ of polarization for the incident and scattered light waves. When the wave vectors of these light waves are collinear to the wave normal ort $\vec{m}$ for the acoustic wave and, of course, to the $[100]$ axis in the $CaMoO_4$ crystal, the eigen-orts $\vec{e}_{0,1}$ of light polarizations should be oriented, as directly follows from Eq.(4.46b), along the $[0,\ 1,\ 0]$ and $[0,\ 0,\ 1]$ axes, so

that one can take, for example, $\vec{e}_0 = [0,\ 1,\ 0]$ and $\vec{e}_1 = [0,\ 0,\ 1]$ with $n_0 = n_o$ and $n_1 = n_e$. As a result, one can obtain the contribution of brackets to Eq.(4.45) as

$$\tilde{\vec{e}}_0 \Delta\hat{\varepsilon} \vec{e}_1 = \tilde{\vec{e}}_1 \Delta\hat{\varepsilon} \vec{e}_0 = \hat{\gamma}_0 \varepsilon_0 \varepsilon_e p_{45}. \qquad (4.48)$$

In so doing, one can find that $q_{0,1} = \pi(2\lambda)^{-1} n_{e,o} \hat{\gamma}_0 n_{o,e}^2 p_{45}$. One can see now that the difference between q_0 and q_1 is rather small, because $q_0/q_1 = n_e/n_o$. Then, because the amplitude of deformation can be explained as $\hat{\gamma}_0 = \sqrt{\frac{2P}{Lh\tilde{\rho}V^3}}$, where P/Lh is the acoustic power density, one can finally obtain [10]

$$\text{a)}\ \ q_0 = \frac{\pi}{\lambda}\sqrt{\frac{P}{2Lh}\left(\frac{n_e^2 n_o^4 p_{45}^2}{\tilde{\rho}V^3}\right)}, \qquad \text{b)}\ \ q_1 = \frac{\pi}{\lambda}\sqrt{\frac{P}{2Lh}\left(\frac{n_o^2 n_e^4 p_{45}^2}{\tilde{\rho}V^3}\right)}. \qquad (4.49)$$

It should be noted that the factors taken in brackets in Eqs.(4.49) represent the acousto-optical figures of merit M_2 peculiar to estimating the efficiency of crystalline materials in acousto-optics [16]. One can estimate the acousto-optical figures of merit peculiar to the geometry of collinear interaction under consideration at $\lambda =$ 0.532 μm in a $CaMoO_4$ cell. Taking the material density $\tilde{\rho} =$ 4.34 g cm^{-3}, acoustic velocity $V =$ 2.95 x 10^5 cm s^{-1}, $p_{45} =$ 0.06, $n_e =$ 2.0239 and $n_o =$ 2.0116 at the chosen light wavelength [17] , one can calculate $M_2 \approx 2.07 \times 10^{-18}$ s^3 g^{-1} in a quit acceptable approximation of $q_0 \approx q_1$, i.e. with an accuracy of about 1%. Then, by restricting a maximal level $P/(Lh) =$ 0.5 W mm^{-2} of the acoustic power density and estimating the factor $\sigma = U_0\sqrt{q_0 q_1}$. This level of power density is conditioned by the absolute acoustic power magnitude of about 2 W and the acoustic beam cross section of about 4 mm^2 in just a collinear acousto-optical cell. Consequently, one can find that $\sigma \approx$ 2 cm^{-1}.

Also, one can estimate the potential contributions of the angular-frequency mismatch and the acoustic losses. The maximal value of the mismatch parameter $\eta = \pi\Delta\mathbf{f}/\mathbf{V}$ for a frequency detuning $\Delta\mathbf{f}$ of 0.6 MHz is equal to about 6.4 cm^{-1}. The coefficient of linear attenuation for the chosen shear acoustic wave passing along the $[\mathbf{100}]$-axis is $\Gamma =$ 60 dB cm^{-1} GHz^{-2} in a $CaMoO_4$ [17]. The factor α of acoustic losses, measured in cm^{-1}, can be expressed as $\alpha\left(\mathbf{cm^{-1}}\right) = \mathbf{0.23}\Gamma\left(\mathbf{dB\,cm^{-1}\,GHz^{-2}}\right)\mathbf{f^2}\left(\mathbf{GHz}\right)$. Thus, at a carrier frequency $\mathbf{f}$ of about 60 MHz related to the above-mentioned light wavelength of 0.532 μm, being peculiar to the collinear acouto-optical interaction in $CaMoO_4$, one can estimate that $\alpha =$ 0.05 cm^{-1} in the case under consideration. Additionally, it should be noted that our theoretical numerical data, presented in Section 4.2.4, were normalized in such a way that those dimensionless values are in coincidence with practical numerical estimations presented in this section.

4.2.6 Experiment with multi-pulse dissipative acousto-optical coupled states in a crystal with square-law nonlinearity and linear acoustic losses

To realize experimentally shaping the multi-pulse dissipative three-wave weakly coupled states by the continuous-wave optical pump in a two-mode medium with linear losses for a relatively slow non-optical wave, the acoustic phonon mechanism of light scattering has been used. The schematic arrangement of the experimental set-up exploited is shown in Fig.4.5 and consists of a continuous-wave laser, a two-mode $CaMoO_4$-crystalline acousto-optical waveguide with polarizers (whose combined scheme is presented in detail separately in Fig.4.6), a photo-detector, and a set of electronic equipment for generating and registering the corresponding electrical radio-wave (RW) signals. This scheme has some analogies with schemes for filtering optical signals [18], but allows operation in the pulsed regime. Initially, electronic video pulse, determining a rectangular shape of envelope, is given from pulse generator. Due to applying this video pulse to the

ultra-high frequency (UHF) generator in the regime of an external modulation, a RW electronic UHF-pulse can be obtained. Then, the shaped UHF-pulse is applied to the electronic input of a two-mode crystalline waveguide, and to oscilloscope as the etalon signal, see Fig.4.5.

A two-mode co-propagating collinear $CaMoO_4$ crystalline waveguide was characterized by a crystal length **L** of **44** mm along the **[100]**-axis, an acoustic velocity $\mathbf{V = 2.95\ 10^5}$ cm/s for the shear elastic mode whose displacement vector is oriented along the **[001]**-axis. A continuous-wave beam at $\lambda =$ **532** nm was used as an optical pump during the experiments. The first polarizer was precisely aligned in correspondence with the optical axes of a crystal in a waveguide. After the interaction with an acoustic pulse, already two orthogonally polarized light beams, incident and signal ones, passed through a waveguide. The second polarizer gave us an opportunity to be aligned in correspondence with the polarization of the signal beam and to extract the output optical signal. The dynamics of shaping and localizing the optical components of multi-pulse dissipative coupled states has been sequentially followed during our experiments.

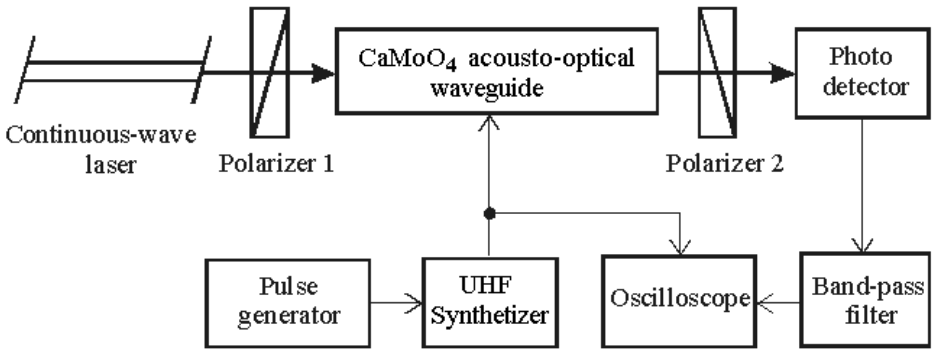

Fig.4.5 Schematic arrangement of the experimental set-up.

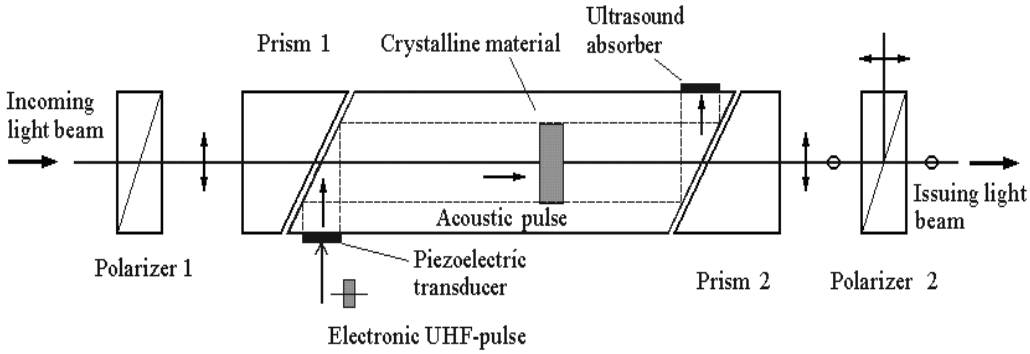

Fig.4.6 Scheme of the co-propagating collinear calcium molybdate acouto-optical cell providing the traveling-wave regime of interaction of the pumping light beam with the acoustic pulses.

A few examples of the corresponding digitized oscilloscope traces are shown in Fig.4.7 [8-10]. The maximal efficiency of shaping one-, two-, and three-pulse optical components in the scattered light wave $\mathbf{C_1}$ (shifted by the acoustic frequency from the pumping light wave $\mathbf{C_0}$) was about 50% relative to the pumping light intensity with the excited acoustic power density of up to **0.5** W/mm^2, which provided magnitudes of the parameter σ up to **2** cm^{-1}. The maximum frequency mismatch $\Delta\mathbf{f} = \eta\mathbf{V}/\pi$ was about **0.6** MHz, providing magnitudes of the phase mismatch η up to **6.32** cm^{-1}.

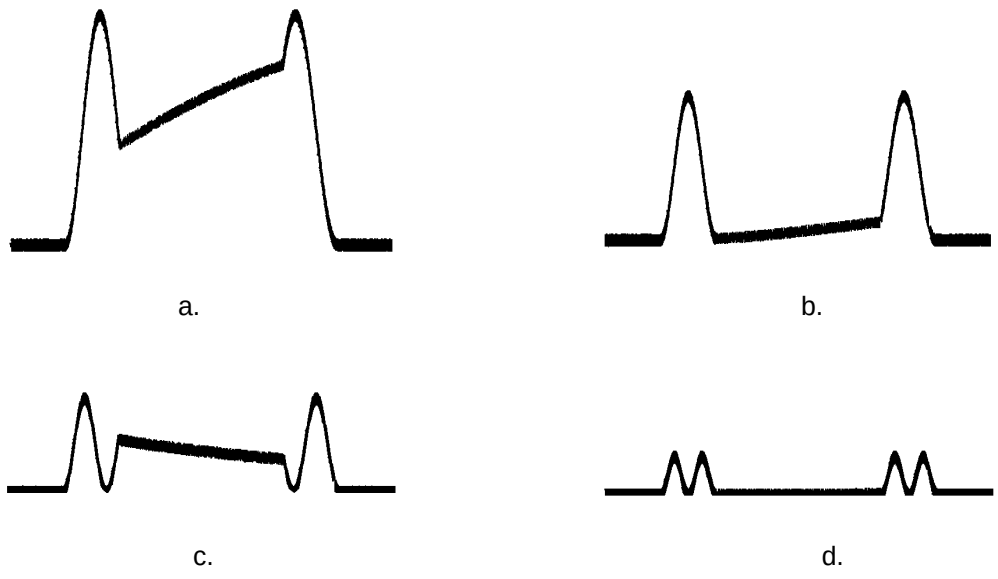

Fig.4.7 The digitized oscilloscope traces for $|C_1|^2$ in a CaMoO4-crystalline waveguide with $\alpha = 0.05$ cm^{-1} at a carrier acoustic frequency of **61.3** MHz. Four stages of reshaping are followed at the same optical pump and acoustic wave intensities and temporal scales: (a) $\eta = 1.5$ cm^{-1}, the beginning stage of shaping a one-pulse dissipative coupled stated; (b) $\eta = 2.4$ cm^{-1}, a one-pulse dissipative coupled stated; (c) $\eta = 3.5$ cm^{-1}, an intermediate stage; and (d) $\eta = 6.0$ cm^{-1}, a two-pulse dissipative coupled state.

The factor α of the linear elastic losses was about **0.05** cm^{-1} inherent in the chosen shear acoustic mode in a two-mode $CaMoO_4$ crystalline waveguide at a carrier frequency of **61.3** MHz, which was determined by $\lambda = V f^{-1} |n_o - n_e|$. The total length of a crystal is $L = 44mm$, which provides a temporal aperture T of **15** μs. The duration of the rectangular acoustic pulse is taken to be $\tau_0 = 3.75$ μs, which corresponds to a pulse spatial length l_0 of about **11** mm.

4.3 Three-wave dissipative collinear strongly coupled acousto-optical states

In this section the collinear co-directional acousto-optical interaction in presence of the linear acoustic losses in a crystal is considered in the case of strong wave

coupling, and rather adequate mathematical model, based on the real-valued evolution equations, is developed. Main attention has been paid to the analytical investigations exploiting both physically and mathematically reasonable approximations. Nevertheless, the presented approach gives a clear view of this phenomenon with mismatching the wave numbers. The evolution equations for a pair of the light waves as well as for the acoustic wave are solved analytically in the first approximation relative to the parameters of smallness inherent in this problem.

4.3.1 A strong collinear co-directional acousto-optical interaction in presence of the linear acoustic losses

The evolution equations which describe a strong co-directional collinear acousto-optical interacting, are given by a set of three nonlinear partial differential equations [7]

$$\text{a)}\quad \frac{\partial \mathbf{b_0}}{\partial \mathbf{x}} + \frac{\mathbf{1}}{\mathbf{c_0}}\frac{\partial \mathbf{b_0}}{\partial \mathbf{t}} = -\gamma_0\, \mathbf{b_1 b_2^*}\, \exp\left(2i\eta\, \mathbf{x}\right),$$

$$\text{b)}\quad \frac{\partial \mathbf{b_1}}{\partial \mathbf{x}} + \frac{\mathbf{1}}{\mathbf{c_1}}\frac{\partial \mathbf{b_1}}{\partial \mathbf{t}} = \gamma_1\, \mathbf{b_0 b_2}\, \exp\left(-2i\eta\, \mathbf{x}\right),$$

$$\text{c)}\quad \frac{\partial \mathbf{b_2}}{\partial \mathbf{x}} + \frac{\mathbf{1}}{\mathbf{v}}\frac{\partial \mathbf{b_2}}{\partial \mathbf{t}} = -\gamma_2\, \mathbf{b_1 b_0^*}\, \exp\left(2i\eta\, \mathbf{x}\right). \qquad (4.50)$$

Here $\mathbf{b_0}$, $\mathbf{b_1}$, $\mathbf{b_2}$ and $\mathbf{c_0}$, $\mathbf{c_1}$, $\mathbf{V}$ are the complex amplitudes and group velocities of two optical and acoustic waves, respectively; γ_0, γ_1, γ_2 are the factors of interactions; 2η is the wave numbers mismatch. The inequality $\mathbf{V} < \mathbf{c_1} < \mathbf{c_0}$ between the group velocities and the signs presented in the right hand sides of Eqs.(4.50) are related to the regime of decay instability when the energy exchange takes place between all the interacting waves. Even with $2\eta \neq 0$, Eqs.(4.50) can be reduced to the case of resonant interaction.

Usually, the difference in refractive indices of acousto-optic materials is too small, so it looks reasonable to approximate the velocities of light modes as $\mathbf{c_0/c_1 \approx 1}$. To determine an area of applicability for such an approximation let us consider the interaction between two optical pulses of width $\mathbf{T}$ in slightly anisotropic medium. If initially these two pulses are overlapping spatially, they will be separated from each other at the distance $\mathbf{L \approx c_{0,1} T\left(1 - c_1/c_0\right)^{-1}}$. Thus, the distance $\mathbf{L}$ characterizes the length of collinear acousto-optical interaction in the selected approximation. For typical widths of acoustic pulses exceeding 10^{-9} seconds and for the anisotropy of about $\mathbf{\left(1 - c_1/c_0\right) \le 0.1}$, one can obtain $\mathbf{L > 100}$ m. Such a length of interaction is unattainable in acousto-optics, so one can approximate the light velocities of modes as $\mathbf{c_0 \approx c_1 \approx c}$ in Eqs.(4.50). The next reduction can be realized due to the incommensurability of the group velocities of optical and acoustic waves. Let us compare summands in the left hand sides of Eqs.(4.50) for the light waves. One can assume that a spatial length x occupied by an acoustic pulse restricts the area for collinear interaction. By this it means that the first summands can be estimated as $\partial \mathbf{b_{0,1}}/\partial \mathbf{x} \approx \tilde{\mathbf{B}}/\mathbf{X}$, where $\tilde{\mathbf{B}}$ is some typical amplitude of optical waves, while the second ones are $\mathbf{c^{-1}(\partial b_{0,1}/\partial t) \approx (V/c)(\tilde{B}/X)}$, because both spatial and temporal scales in acousto-optics are determined by the motion of just acoustic pulse with the velocity $\mathbf{V}$. Because of $\mathbf{V/c \approx 10^{-5}}$, one can yield $\mathbf{c^{-1}(\partial b_{0,1}/\partial t) << \partial b_{0,1}/\partial x}$. That is why Eqs.(4.50) can be rewritten as

$$\text{a)}\ \frac{\partial \mathbf{b_0}}{\partial \mathbf{x}} = -\gamma_0 \mathbf{b_1 b_2^*} \exp\left(2i\eta \mathbf{x}\right), \qquad \text{b)}\ \frac{\partial \mathbf{b_1}}{\partial \mathbf{x}} = \gamma_1 \mathbf{b_0 b_2} \exp\left(-2i\eta \mathbf{x}\right),$$

$$\text{c)}\ \frac{\partial \mathbf{b_2}}{\partial \mathbf{x}} + \frac{1}{\mathbf{v}} \frac{\partial \mathbf{b_2}}{\partial \mathbf{t}} = -\gamma_2 \mathbf{b_1 b_0^*} \exp\left(2i\eta \mathbf{x}\right). \qquad (4.51)$$

Then, one can make the substitutions $\mathbf{b_0} = (\gamma_1 \gamma_2)^{-1/2} \mathbf{C_0}$, $\mathbf{b_1} = (\gamma_0 \gamma_2)^{-1/2} \mathbf{C_1}$,

and $\mathbf{b_2 = (\gamma_1 \gamma_0)^{-1/2} U}$ in Eq.(4.51). Finally, an additional phenomenological term, related to the contribution of acoustic losses, can be introduced into the last equation for the wave $\mathbf{U}$, so that a strong co-directional collinear acousto-optical interacting can be described by such a set of the evolution equations

$$\text{a)}\ \frac{\partial \mathbf{C_0}}{\partial \mathbf{x}} = -\mathbf{C_1 U^*}\ \mathbf{exp}\left(2\mathbf{i}\eta\ \mathbf{x}\right), \qquad \text{b)}\ \frac{\partial \mathbf{C_1}}{\partial \mathbf{x}} = \mathbf{C_0 U}\ \mathbf{exp}\left(-2\mathbf{i}\eta\ \mathbf{x}\right),$$

$$\text{c)}\ \frac{\partial \mathbf{U}}{\partial \mathbf{x}} + \frac{\mathbf{1}}{\mathbf{v}}\frac{\partial \mathbf{U}}{\partial \mathbf{t}} = -\alpha \mathbf{U} - \mathbf{C_0^*}\,\mathbf{C_1}\ \mathbf{exp}\left(2\mathbf{i}\eta\ \mathbf{x}\right), \tag{4.52}$$

here $\mathbf{C_{0,1} = A_{0,1}\ exp(i\varphi_{0,1})}$, and $\mathbf{U = U_0\ exp(i\varphi)}$ are the complex amplitudes of two light and one acoustic waves, and α is the linear acoustic losses. Let us apply the method of slowly varying profile [19] to Eq.(4.52c). In doing so, one can consider the right hand side of Eq.(4.52c) like a perturbation and assume that the amplitude $\mathbf{U}$ of acoustic wave can be presented as a function of the tracking coordinate $\mathbf{X = x - V t}$ and $\mathbf{Y} = \mu \mathbf{x}$, namely, $\mathbf{U = U(X, Y)}$, where the factor μ is considered as a parameter of smallness. In this case, one can calculate

$$\text{a)}\ \frac{\partial \mathbf{U}}{\partial \mathbf{x}} = \frac{\partial \mathbf{U}}{\partial \mathbf{X}}\frac{\partial \mathbf{X}}{\partial \mathbf{x}} + \frac{\partial \mathbf{U}}{\partial \mathbf{Y}}\frac{\partial \mathbf{Y}}{\partial \mathbf{x}} = \frac{\partial \mathbf{U}}{\partial \mathbf{X}} + \mu\,\frac{\partial \mathbf{U}}{\partial \mathbf{Y}};$$

$$\text{b)}\ \frac{\mathbf{1}}{\mathbf{V}}\frac{\partial \mathbf{U}}{\partial \mathbf{t}} = \frac{\mathbf{1}}{\mathbf{V}}\left(\frac{\partial \mathbf{U}}{\partial \mathbf{X}}\frac{\partial \mathbf{X}}{\partial \mathbf{x}} + \frac{\partial \mathbf{U}}{\partial \mathbf{Y}}\frac{\partial \mathbf{Y}}{\partial \mathbf{x}}\right) = \frac{\mathbf{1}}{\mathbf{V}}\frac{\partial \mathbf{U}}{\partial \mathbf{X}}\left(-\mathbf{V}\right) = \frac{\partial \mathbf{U}}{\partial \mathbf{X}}\ . \tag{4.53}$$

Substituting Eqs.(4.53) into Eq.(4.52c), then one can divide Eq.(4.52c) into a pair of equations in accordance with the smallness inherent in the corresponding terms in its right hand side as

$$\text{a)}\ \frac{\partial \mathbf{U}}{\partial \mathbf{x}} + \frac{\mathbf{1}}{\mathbf{V}}\frac{\partial \mathbf{U}}{\partial \mathbf{t}} = \mathbf{0}\ , \qquad \text{b)}\ \mu\,\frac{\partial \mathbf{U}}{\partial \mathbf{Y}} = -\alpha \mathbf{U} - \mathbf{C_0^*}\,\mathbf{C_1}\ \mathbf{exp}\left(2\mathbf{i}\eta\ \mathbf{x}\right)\ . \tag{4.54}$$

Because of $\mu\left(\partial \mathbf{U}/\partial \mathbf{Y}\right) = \partial \mathbf{U}/\partial \mathbf{x}$, Eq.(4.54b), determining the first order approximation, takes the form

$$\frac{\partial U}{\partial x} = -\alpha U - C_0^* C_1 \exp(2i\eta x) \ . \qquad (4.55)$$

Consequently, a set of equations such as Eqs.(4.52a), (4.52b), and (4.55) describes a three-wave system, which exhibits the following relations

$$\text{a)} \ A_0^2 + A_1^2 = J \ , \qquad \text{b)} \ A_0^2 - U_0^2 = 2\alpha \int U_0^2 \, dx + \zeta_0^* \ ,$$

$$\text{c)} \ A_1^2 + U_0^2 = -2\alpha \int U_0^2 \, dx + \zeta_1^* \ , \qquad (4.56)$$

where J and $\zeta_{0,1}^*$ are the integration constants, which are determined by the boundary conditions, so that, for example, $J = A_0^2(x=0) + A_1^2(x=0)$; then $\zeta_0^* + \zeta_1^* = J$. Now, an effort is made of separating the complex amplitudes of the waves. In doing so, a triplet set of Eqs.(4.52) of the first order with a square-low nonlinearity can be converted into a triplet of the second order equations with cubic nonlinearity as [20]

$$\text{a)} \ \frac{d^2 C_0}{dx^2} = (2i\eta - \alpha)\frac{dC_0}{dx} + C_0\left(|C_1|^2 - |U|^2\right),$$

$$\text{b)} \ \frac{d^2 C_1}{dx^2} = -(2i\eta + \alpha)\frac{dC_1}{dx} - C_1\left(|C_0|^2 + |U|^2\right) \ ,$$

$$\text{c)} \ \frac{d^2 U}{dx^2} = (2i\eta - \alpha)\frac{dU}{dx} - U\left(|C_0|^2 - |C_1|^2\right) \ . \qquad (4.57)$$

Using the relations from Eqs.(4.56) into Eqs.(4.57), one can obtain the equations with the complex amplitudes separated as

$$\text{a)} \ \frac{d^2 C_0}{dx^2} = (2i\eta - \alpha)\frac{dC_0}{dx} - 2C_0|C_0|^2 + Z_0 C_0 + 2\alpha C_0 \int |U|^2 \, dx \ ,$$

$$\text{b)}\quad \frac{d^2C_1}{dx^2} = -\left(2i\eta+\alpha\right)\frac{dC_1}{dx} + 2C_1\left|C_1\right|^2 - Z_1C_1 + 2\alpha C_1\int\left|U\right|^2 dx \ ,$$

$$\text{c)}\quad \frac{d^2U}{dx^2} = \left(2i\eta-\alpha\right)\frac{dU}{dx} - 2U\left|U\right|^2 - ZU - 4\alpha U\int\left|U\right|^2 dx + 2i\alpha\eta U \ , \tag{4.58}$$

where, $Z_0 = 2\zeta_0^* + \zeta_1^*$, $Z_1 = 2\zeta_1^* + \zeta_0^*$, $Z = \zeta_0^* - \zeta_1^*$. Equations (4.58) represent a set of combined equations that will be analyzed in the following sections.

4.3.2 The real-valued evolution equations

Let us start from the analysis of Eq.(4.58a). Using the notations after Eq.(4.52), one can extract the imaginary part of Eq.(4.58a) [21]

$$\text{a)}\quad \frac{dW_0}{dx} + W_0\left[2\frac{d(\ln A_0)}{dx} + \alpha\right] = 2\eta\frac{d(\ln A_0)}{dx} \ , \qquad \text{b)}\quad W_0 = \frac{d\varphi_0}{dx} \ . \tag{4.59}$$

The exact solution to Eq.(4.59a) is given by

$$W_0 = \frac{\tilde{\xi}_0}{A_0^2}\exp\left(-\alpha x\right) + \frac{\eta}{A_0^2}\exp\left(-\alpha x\right)\int\left[\frac{dA_0^2}{dx}\exp\left(\alpha x\right)\right]dx \ , \tag{4.60}$$

where $\tilde{\xi}_0$ is the integration constant. At this stage, it is physically reasonable to assume that spatial scale of varying the terms $\left(dA_0^2/dx\right)$ and $\exp\left(\alpha x\right)$ under the last integral are quite different, so that the exponential term is varying much slower. That is why this term can be taken out of that integral, and one get the following approximate solution

$$W_0 \approx \frac{\tilde{\xi}_0}{A_0^2}\exp\left(-\alpha x\right) + \eta \ . \tag{4.61}$$

The real part equation for Eq.(4.58a) has the following exact form

$$\frac{d^2A_0}{dx^2}+\alpha\frac{dA_0}{dx}+A_0\left(2\eta W_o-W_0^2-J\right)+A_0\left(U_0^2+A_0^2\right)=0\ . \qquad (4.62)$$

Using Eq.(4.61), one can convert Eq.(4.62) into the following approximate equation

$$\frac{d^2A_0}{dx^2}+\alpha\frac{dA_0}{dx}+A_0\left[\eta^2-J-\frac{\tilde{\xi}_0^2}{A_0^4}\exp\left(-2\alpha x\right)\right]+A_0\left(U_0^2+A_0^2\right)\approx 0\ . \qquad (4.63)$$

Exploiting similar consideration for Eq.(4.58b) with $W_1=d\varphi_1/dx$ and the integration constant $\tilde{\xi}_1$, one can obtain

$$W_1\approx\frac{\tilde{\xi}_1}{A_1^2}\exp\left(-\alpha x\right)-\eta\ , \qquad (4.64)$$

$$\frac{d^2A_1}{dx^2}+\alpha\frac{dA_1}{dx}+A_1\left[\eta^2+J-\frac{\tilde{\xi}_1^2}{A_1^4}\exp\left(-2\alpha x\right)\right]+A_1\left(U_0^2-A_1^2\right)\approx 0\ , \qquad (4.65)$$

which are completely analogous to Eqs.(4.61) and (4.63), respectively. Then, lets apply this procedure to Eq.(4.58c). The imaginary part of this equation is

$$\text{a)}\ \ \frac{dW}{dx}+W\left[2\frac{d(\ln U_0)}{dx}+\alpha\right]=2\eta\left[\frac{d(\ln A_0)}{dx}+\alpha\right],\qquad \text{b)}\ \ W=\frac{d\varphi}{dx}\ . \qquad (4.66)$$

The exact solution to Eq.(4.66a) is given by

$$W=\frac{\tilde{\xi}}{U_0^2}\exp\left(-\alpha x\right)+\frac{2\eta}{U_0^2}\exp\left(-\alpha x\right)\int\left\{\left[U_0\frac{dU_0}{dx}+\alpha U_0^2\right]\exp\left(\alpha x\right)\right\}dx, \qquad (4.67)$$

where $\tilde{\xi}$ is the integration constant. At this stage, one can again assume that spatial scale of varying the terms in the squared brackets and $\exp(\alpha x)$ under the last integral in Eq.(4.67) are quite different, so that the exponential term is varying much slower. That is why this term can be taken out of that integral, and we get an approximate solution

$$W \approx \frac{\tilde{\xi}}{U_0^2} \exp(-\alpha x) + \eta + \frac{2\alpha\eta}{U_0^2} \int U_0^2 \, dx \ . \tag{4.68}$$

The real part equation for Eq.(4.58a) has the following exact form

$$\frac{d^2 U_0}{dx^2} + \alpha \frac{dU_0}{dx} + U_0 \left(Z + 2\eta W - W^2 \right) + 2U_0^3 + 4\alpha U_0 \int U_0^2 \, dx = 0 \ . \tag{4.69}$$

Using Eq.(4.68), one can calculate approximately the contribution in the brackets of Eq.(4.69) as

$$2\eta W - W^2 = \eta^2 - \frac{\tilde{\xi}^2}{U_0^4} \exp(-2\alpha x) - \frac{4\alpha\eta\tilde{\xi}}{U_0^4} \int U_0^2 \, dx - \left(\frac{2\alpha\eta}{U_0^2} \int U_0^2 \, dx \right)^2 , \tag{4.70}$$

where the last term directly proportional to a small product $(\alpha^2 \eta^2)$ can be omitted. Hence, Eq.(4.69) takes the form

$$\frac{d^2 U_0}{dx^2} + \alpha \frac{dU_0}{dx} + U_0 \left[Z + \eta^2 - \frac{\tilde{\xi}^2}{U_0^4} \exp(-2\alpha x) \right] + 2U_0^3 + 4\alpha U_0 \left(1 - \frac{\eta\tilde{\xi}}{U_0^4} \right) \int U_0^2 \, dx \approx 0 . \tag{4.71}$$

Thus, one has obtained a sextet of the real-valued approximate evolution equations for the phases, see Eqs.(4.61), (4.64), and (4.68), as well as for the amplitudes, see Eqs.(4.63), (4.65), and (4.71), of the interacting waves [21].

4.3.3 Analysis for the light wave amplitude A_0

Let us take Eq.(4.56b), which can be considered as a differential equation connecting the amplitudes $\mathbf{U_0}$ and $\mathbf{A_0}$ as [21]

$$\frac{\mathbf{d(U_0^2)}}{\mathbf{dx}} + \mathbf{2}\alpha\,\mathbf{U_0^2} = \frac{\mathbf{d(A_0^2)}}{\mathbf{dx}} \ . \tag{4.72}$$

General solution to Eq.(4.72) is given by

$$\mathbf{U_0^2} = \mathbf{Q_0}\ \mathbf{exp}\left(-\mathbf{2}\alpha\,\mathbf{x}\right) + \mathbf{A_0^2} - \mathbf{2}\alpha\ \mathbf{exp}\left(-\mathbf{2}\alpha\,\mathbf{x}\right)\int \mathbf{exp}\left(+\mathbf{2}\alpha\,\mathbf{x}\right)\mathbf{A_0^2}\ \mathbf{dx}\ , \tag{4.73}$$

where the integration constant $\mathbf{Q_0}$ has to be taken as $\mathbf{Q_0} = -\zeta_0$ to satisfy Eq.(4.56b) with $\alpha = \mathbf{0}$. Substituting Eq.(4.73) into Eq.(4.63), assuming that $\xi_0 = \mathbf{0}$, yields

$$\frac{\mathbf{d^2A_0}}{\mathbf{dx^2}} + \alpha\,\frac{\mathbf{dA_0}}{\mathbf{dx}} + \mathbf{A_0}\left[\eta^2 - \mathbf{J} - \zeta_0\ \mathbf{exp}\left(-\mathbf{2}\alpha\,\mathbf{x}\right)\right] +$$

$$+\,\mathbf{2A_0^3} - \mathbf{2}\alpha\,\mathbf{A_0}\ \mathbf{exp}\left(-\mathbf{2}\alpha\,\mathbf{x}\right)\int \mathbf{exp}\left(+\mathbf{2}\alpha\,\mathbf{x}\right)\mathbf{A_0^2}\ \mathbf{dx} = \mathbf{0.} \tag{4.74}$$

Consider the problems in the first approximation relative to the small parameter α and expand the exponential terms as $\mathbf{exp}\ (\pm\,\mathbf{2}\alpha\,\mathbf{x}) \approx \mathbf{1} \pm \alpha\,\mathbf{x}$. Together with this, one can assume that α and η have the same order of smallness. In so doing, let us put $\mathbf{A_0} = \mathbf{a_0} + \alpha\,\mathbf{b_0}$ and divide the terms from Eq.(4.74) into a pair of the equations

$$\alpha^{\mathbf{0}}\mathbf{:}\ \ \frac{\mathbf{d^2a_0}}{\mathbf{dx^2}} - \left(\mathbf{J} + \zeta_0\right)\mathbf{a_0} + \mathbf{2a_0^3} = \mathbf{0}\ , \tag{4.75}$$

$$\alpha^1: \quad \frac{d^2 b_0}{dx^2} - \left(J + \zeta_0\right) b_0 + 6 a_0^2 b_0 = 2\alpha a_0 \int a_0^2 \, dx - \frac{da_0}{dx} - 2\alpha x \zeta_0 a_0 . \tag{4.76}$$

The zero-approximation equation (4.75) has the solution

$$a_0 = \sqrt{J + \zeta_0}\ \mathrm{sech}\left(x\sqrt{J + \zeta_0}\right) . \tag{4.77}$$

At this step, one can suppose that this pulse has unity amplitude and unity width. Correlating such a requirement with Eq.(4.56a), one has to conclude that in this case $J = 1$, $\zeta_1 = 1$, and $\zeta_0 = 0$, so that the normalized solution is given by

$$a_0 = \mathrm{sech}(x) . \tag{4.78}$$

With this result, the first-approximation equation (4.76) takes the form

$$\frac{d^2 b_0}{dx^2} - \left(1 - 6\,\mathrm{sech}^2 x\right) b_0 = 3\ \mathrm{sech}\, x\ \tanh x . \tag{4.79}$$

The homogeneous part of Eq.(4.79) is well known in the mathematical theory [22] for solitons in the form of $Z_n^{(0)''} = [\lambda_0^2 - n(n+1)\,\mathrm{sech}^2 x\,] Z_n^{(0)}$. In this case $\lambda_0 = \pm 1$ and $n = 2$ as it follows from Eq.(4.79), so one needs the solution for $Z_2^{(0)}$. Such a solution can be found as

$$\text{a)} \quad Z_2^{(0)} = \left(\frac{d}{dx} - 2\tanh x\right)\left(\frac{d}{dx} - \tanh x\right) Z_0^{(0)} ,$$

$$\text{b)} \quad Z_0^{(0)} = A_0 \exp(\lambda x) + B_0 \exp(-\lambda x) , \tag{4.80}$$

where A_0 and B_0 are arbitrary constants of integration. Exploiting this procedure, one can obtain one of the fundamental solutions to the homogeneous part of Eq.(4.79) $Z_2^{(0)} \equiv \varphi_1 = \mathrm{sech}\, x\ \tanh x$.

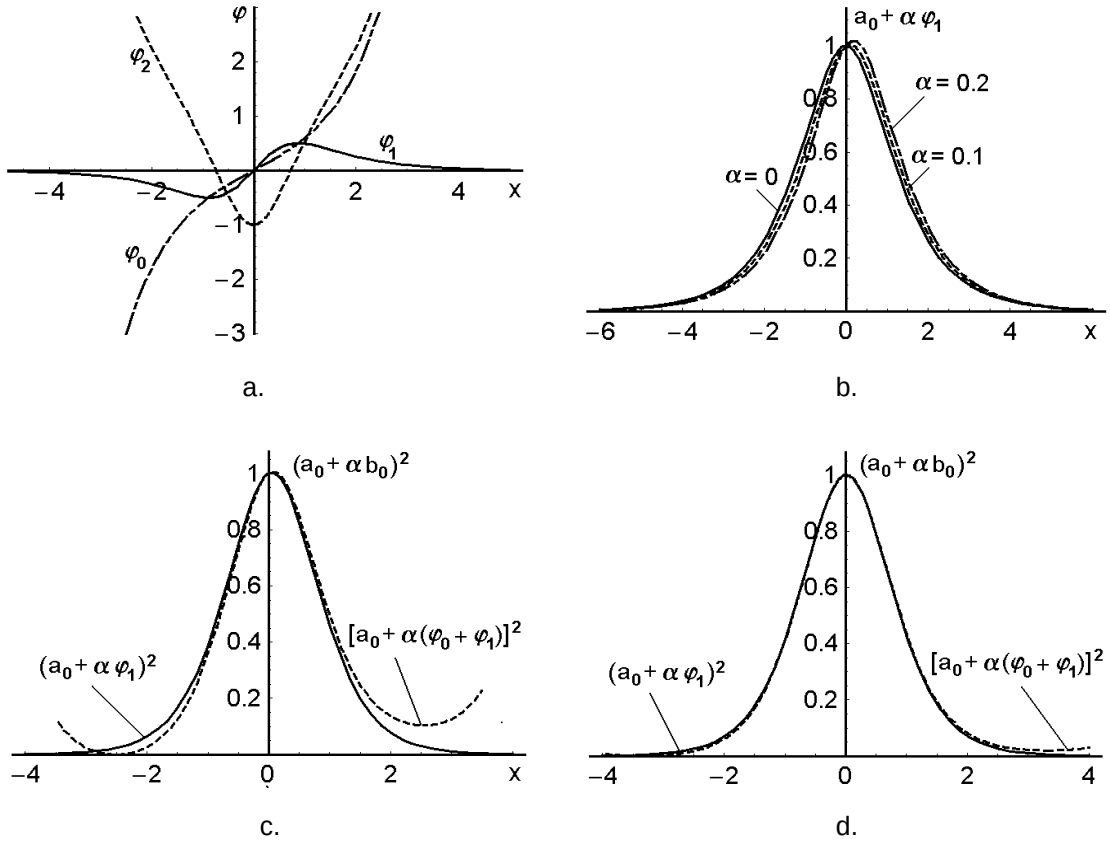

Fig.4.8. Approximate solutions to Eq.(4.93): (a) the solutions $\varphi_{0,1,2}$; (b) effect of the parameter α on the localized part of solution; the contributions inherent in the partial solution of inhomogeneous equation for $\alpha = \mathbf{0.05}$ (c) and $\alpha = \mathbf{0.01}$ (d).

The second fundamental solution φ_2, being linearly independent on the solution φ_1, can be calculated as [23]

$$\varphi_2 = \varphi_1 \int \varphi_1^{-2}\, dx = \frac{1}{2}\left[\cosh x + 3\,\mathrm{sech}\, x\,(x\tanh x - 1)\right]. \qquad (4.81)$$

The direct substitutions of both φ_1 and φ_2 in the homogeneous part of Eq.(4.79) satisfy it. The partial solution φ_0 to inhomogeneous equation (4.79) with $h_0 = 3\ \mathrm{sech}\, x\ \tanh x$ can be estimated as [23]

$$\varphi_0 = \varphi_1 \int \left[\varphi_1^{-2} \int (\varphi_1 h_0)\, dx\right] dx = \frac{1}{2}\sinh x\ . \qquad (4.82)$$

Collecting these results, one can write the general solution to Eq.(4.79) as

$$\mathbf{b_0 = C_1 \varphi_1 + C_2 \varphi_2 + \varphi_0}, \tag{4.83}$$

where $\mathbf{C_{1,2}}$ are arbitrary constants. The contributions inherent in the obtained solutions for the amplitude $\mathbf{A_0}$ are presented in Fig.4.8 [21].

4.3.4 Analysis for the light wave amplitude A_1

Now taking Eq.(4.56c), which can also be considered as a differential equation bounding the amplitudes $\mathbf{U_0}$ and $\mathbf{A_1}$ as

$$\frac{\mathbf{d(U_0^2)}}{\mathbf{dx}} + \mathbf{2\alpha U_0^2} = -\frac{\mathbf{d(A_1^2)}}{\mathbf{dx}} \ . \tag{4.84}$$

General solution to Eq.(4.84) is given by

$$\mathbf{U_0^2 = Q_1 \exp(-2\alpha x) - A_1^2 + 2\alpha \exp(-2\alpha x) \int \exp(+2\alpha x) A_1^2 \, dx} \ , \tag{4.85}$$

where the integration constant $\mathbf{Q_1}$ has to be taken as $\mathbf{Q_1 = \zeta_1}$ to satisfy Eq.(4.56c) with $\alpha = 0$. Due to substituting Eq.(4.85) in Eq.(4.65) and assuming that $\xi_1 = 0$, one can arrive at

$$\frac{\mathbf{d^2 A_1}}{\mathbf{dx^2}} + \alpha \frac{\mathbf{dA_1}}{\mathbf{dx}} + \mathbf{A_1}\left[\mathbf{J} - \eta^2 + \zeta_1 \exp(-2\alpha x)\right]$$

$$\mathbf{-2A_1^3 + 2\alpha A_1 \exp(-2\alpha x) \int \exp(+2\alpha x) A_1^2 \, dx = 0.} \tag{4.86}$$

Again, considering the problem in the first approximation relative to the small parameter α, expanding the exponential terms as $\mathbf{\exp(\pm 2\alpha x) \approx 1 \pm \alpha x}$, put $\mathbf{A_1 = a_1 + \alpha b_1}$, and dividing the terms from Eq.(4.86) into a pair of the following equations

$$\alpha^0: \qquad \frac{d^2 a_1}{dx^2} + \left(J + \zeta_1\right) a_1 - 2a_1^3 = 0 \ , \tag{4.87}$$

$$\alpha^1: \qquad \frac{d^2 b_1}{dx^2} + \left(J + \zeta_1\right) b_1 - 6a_1^2 b_1 = 2x\zeta_1 a_1 - 2a_1 \int a_1^2 \, dx - \frac{da_1}{dx} \ . \tag{4.88}$$

The exact solution to the zero-approximation equation (4.87) is given by

$$a_1 = \sqrt{(J+\zeta_1)/2} \, \tanh\left[x\sqrt{(J+\zeta_1)/2}\right] \ . \tag{4.89}$$

However, because of $J = 1$ and $\zeta_1 = 1$ (see previous section 4.3.3), this solution can be written as

$$a_1 = \tanh x \, . \tag{4.90}$$

With this result, the first-approximation equation (4.88) takes the form

$$\frac{d^2 b_1}{dx^2} - \left[4 - 6\,\mathrm{sech}^2 x\right] b_1 = 3\tanh^2 x - 1 \, . \tag{4.91}$$

The homogeneous part of Eq.(4.91) has the form of $Z_n^{(1)''} = [\lambda_1^2 - n(n+1)\,\mathrm{sech}^2 x\,]\; Z_n^{(1)}$ as before. In this case $\lambda_1 = \pm 2$ and $n = 2$ as it follows from Eq.(4.91), so again we need the solution for $Z_2^{(1)}$, which can be found using Eq.(4.80a) with $Z_0^{(1)} = A_1 \exp(\lambda_1 x) + B_1 \exp(-\lambda_1 x)$; where A_1 and B_1 are arbitrary constants of integration.

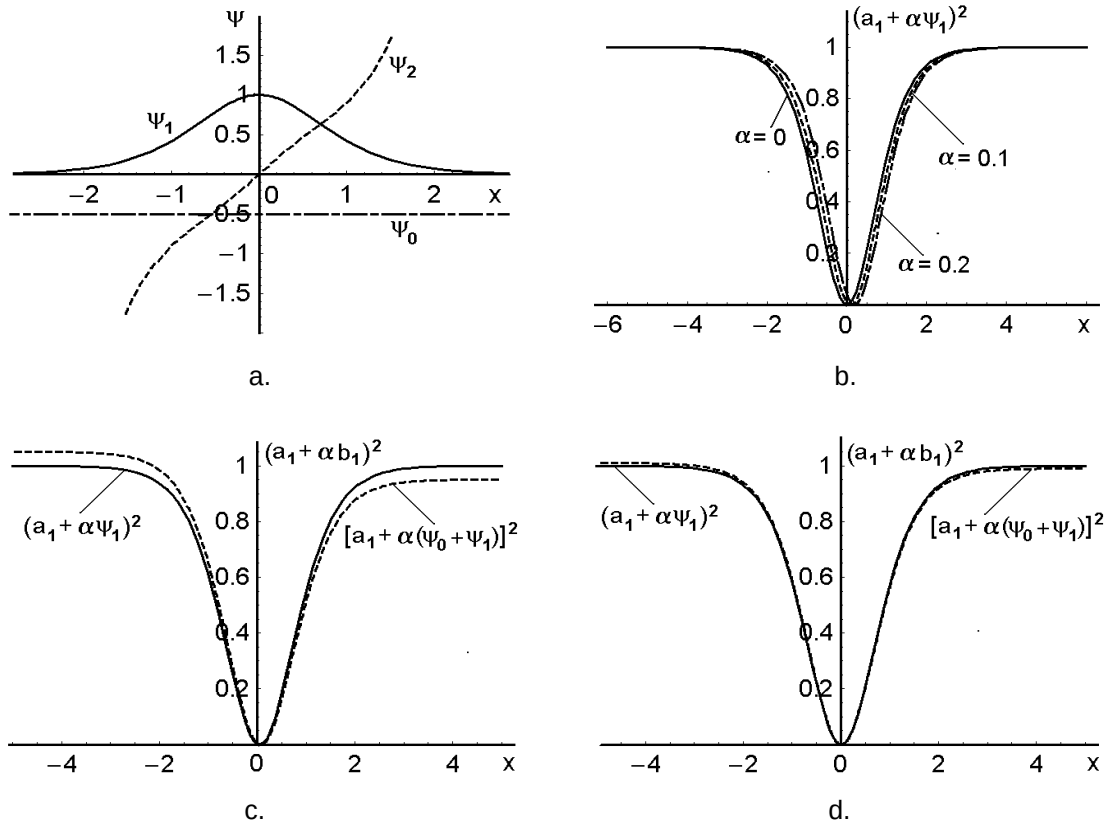

Fig.4.9. Approximate solutions to Eq.(4.86): (a) the solutions $\psi_{0,1,2}$; (b) effect of the parameter α on the localized part of solution; the contributions inherent in the partial solution of inhomogeneous equation for $\alpha = \mathbf{0.05}$ (c) and $\alpha = \mathbf{0.01}$ (d).

Exploiting that procedure, one can obtain $Z_2^{(1)} \equiv \psi_1 = \mathbf{sech}^2\,\mathbf{x}$, being one of the fundamental solutions to the homogeneous part of Eq.(4.91). The second fundamental solution ψ_2, being linearly independent on the solution ψ_1, can be found as

$$\psi_2 = \psi_1 \int \psi_1^{-2}\, \mathbf{dx} = \frac{\mathbf{1}}{\mathbf{32}}\mathbf{sech}^2\,\mathbf{x}\left[\mathbf{12x} + \mathbf{8\,sinh(2x)} + \mathbf{sinh(4x)}\right]. \qquad (4.92)$$

The direct substitutions of both ψ_1 and ψ_2 in the homogeneous part of Eq.(4.91) satisfy it. The partial solution ψ_0 to inhomogeneous equation (4.91) with $\mathbf{h_1 = 3\,tanh^2\,x - 1}$ can be estimated as [23]

$$\psi_0 = \psi_1 \int \left[\psi_1^{-2} \int (\psi_1 h_1)\, dx \right] dx = -\frac{1}{2} \ . \qquad (4.93)$$

Collecting these results, one can write the general solution to Eq.(4.91) as

$$b_1 = G_1 \psi_1 + G_2 \psi_2 + \psi_0 , \qquad (4.94)$$

where $G_{1,2}$ are arbitrary constants. Some combinations of the contributions inherent in the obtained solutions for the amplitude A_1 are presented in Fig.4.9.

4.3.5 Analysis for the acoustic wave amplitude U_0

Let us consider now Eq.(4.71) with $\xi = 0$, so that Eq.(4.71) becomes to be reduced as

$$\frac{d^2 U_0}{dx^2} + \alpha \frac{dU_0}{dx} + U_0 \left(Z + \eta^2 \right) + 2U_0^3 + 4\alpha U_0 \int U_0^2 \, dx = 0 \ , \qquad (4.95)$$

where $Z = -1$ as it follows from Section 4.3.3. One can consider the problem in the first approximation relative to the small parameter α and assume that α and η have the same order of smallness. In so doing, we put $U_0 = v_0 + \alpha v_1$ and divide the terms from Eq.(4.95) into a pair of the equations as

$$\alpha^0 : \qquad \frac{d^2 v_0}{dx^2} - v_0 + 2v_0^3 = 0 \ , \qquad (4.96)$$

$$\alpha^1 : \qquad \frac{d^2 v_1}{dx^2} - v_1 + 6 v_0^2 v_1 = -4\alpha v_0 \int v_0^2 \, dx - \frac{dv_0}{dx} \ . \qquad (4.97)$$

The zero-approximation Eq.(4.96) has the solution

$$v_0 = \operatorname{sech}(x) \ . \qquad (4.98)$$

With this result, the first-approximation equation (4.97) takes the form

$$\frac{d^2 v_1}{dx^2} - \left(1 - 6\,\mathrm{sech}^2 x\right) v_1 = -3\ \mathrm{sech}\, x\ \tanh x\ . \qquad (4.99)$$

One can see that the homogeneous parts of Eqs.(4.99) and (4.79) are exactly the same, while inhomogeneous parts of these equations differs by the sing only. By this is meant that one can directly exploit the results from Section 4.3.3 and write the fundamental solutions $\phi_{1,2}$ to Eq.(4.99) as

a) $\phi_1 = \mathrm{sech}\, x\ \tanh x$,

b) $\phi_2 = \phi_1 \int \phi_1^{-2}\, dx = \frac{1}{2}\left[\cosh x + 3\,\mathrm{sech}\, x\left(x \tanh x - 1\right)\right]$.

(4.100)

The direct substitutions of $\phi_{1,2}$ in the homogeneous part of Eq.(4.99) satisfy it. The partial solution ϕ_0 to inhomogeneous equation (4.99) with $h = -3\ \mathrm{sech}\, x\ \tanh x$ can be estimated as [23]

$$\phi_0 = \phi_1 \int \left[\phi_1^{-2} \int \left(\phi_1 h\right) dx \right] dx = -\frac{1}{2} \sinh x\ . \qquad (4.101)$$

Collecting these results, one can write the general solution to Eq.(4.95) as $v_1 = M_1 \phi_1 + M_2 \phi_2 + \phi_0$, where $M_{1,2}$ are arbitrary constants.

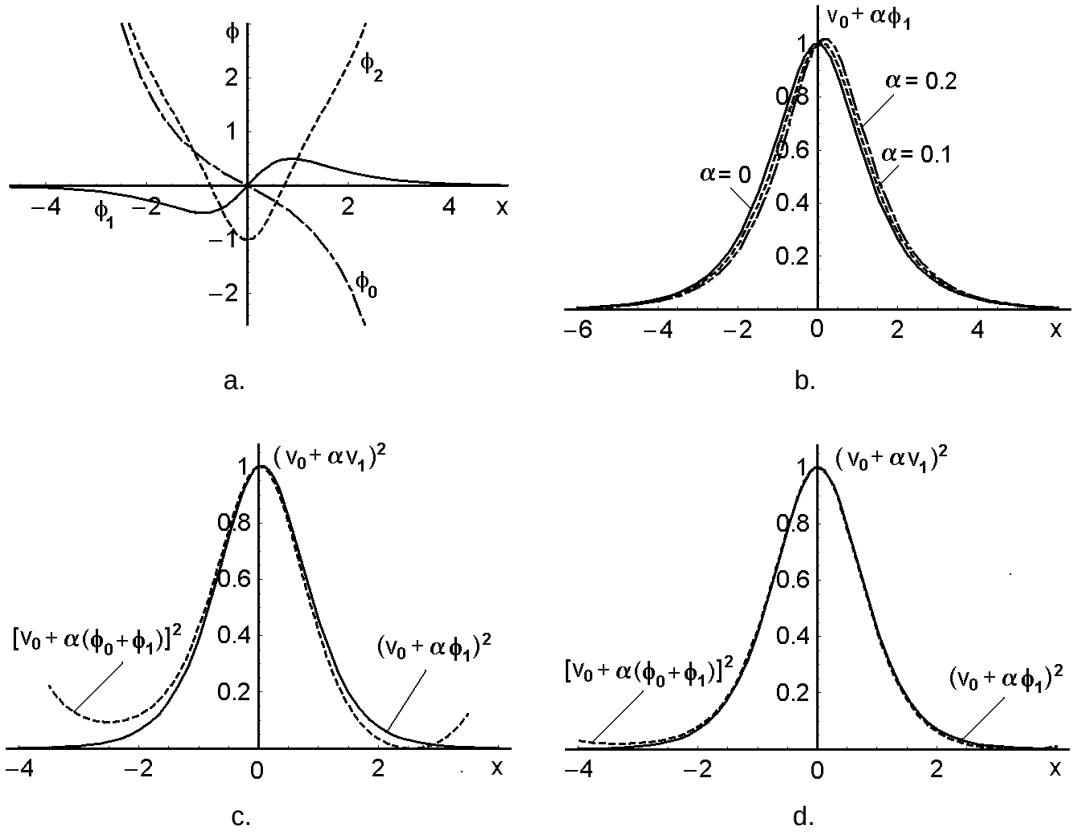

Fig.4.10. Approximate solutions to Eq.(4.95): (a) the solutions $\phi_{0,1,2}$;

(b) effect of the parameter α on the localized part of solution; the contributions inherent in the partial solution of inhomogeneous equation for $\alpha = \mathbf{0.05}$ (c) and $\alpha = \mathbf{0.01}$ (d).

The contributions inherent in the obtained solutions for the wave $\mathbf{U_0}$ are presented in Fig.4.10 [21].

4.4 Five-wave non-collinear acousto-optical coupled states

Now, the existence of another type of solitary waves, representing the most complicated multi-wave acousto-optical coupled states that can be allowed in the Bragg regime of non-collinear interaction between light and elastic waves in crystals is dicussed. Here, the quasi-stationary description for such five-wave solitary waves, including both the analytical approaches and the computer simulations are developed.

In Section 4.4.1, the localization conditions and appearing five-wave Bragg weakly coupled multi-pulse acousto-optical in the case of an exact phase synchronism are investigated.

4.4.1 Originating five-wave Bragg non-collinear weakly coupled acousto-optical states

Usually, the Bragg acousto-optic processes include the only three waves, but under certain angles of the incidence on selected crystal cuts and at a specific frequency for the acoustic wave, one can observe Bragg scattering caused by participating three phonons simultaneously [4,24], because the corresponding conservation laws become to be fulfilled. Such a five-wave process occurs at the frequency $f_0 = \lambda^{-1} V |(n_0^2 - n_1^2)/2|^{1/2}$ of acoustic wave, peculiar to just a three-phonon scattering; (here $n_0 \neq n_1$ are the refractive indices of a uniaxial crystal, V is the acoustic velocity, λ is the incident light wavelength). Polarizations of light in the zero and second orders are orthogonal to polarizations in the first and third ones, whereas the frequencies of light beams in the first, second, and third orders are shifted by f_0, $2f_0$, and $3f_0$, respectively, relative to the zero order. If the powers of waves are closely related, strongly nonlinear behavior of light waves appears with a three-phonon scattering without any observable influence on the acoustic wave, which is to say that a weak coupling of waves takes place. Assuming that an area of propagation for the acoustic wave, traveling almost perpendicularly to the light beams, is bounded by two planes $x = 0$ and $x = L$ in a crystal and take into account joint angular-frequency mismatches η_k of waves. A set of equations for the amplitudes $C_m(x)$ of light waves ($m = 0,1,2,3$) with stationary three-phonon Bragg light scattering is given by Eqs. (2.34).

Now, analyzing Eqs.(2.34) with the simplest boundary conditions $\left|\mathbf{C_0(x=0)}\right|^2=\mathbf{I^2}$, $\mathbf{C_{1,2,3}(x=0)=0}$ and exploiting the conservation law $\left|\mathbf{C_0}\right|^2+\left|\mathbf{C_1}\right|^2+\left|\mathbf{C_2}\right|^2+\left|\mathbf{C_3}\right|^2=\mathbf{I^2}$, resulting from Eqs.(2.34), where $\mathbf{I^2}$ is the intensity of the continuous-wave incident light beam. The complete analytical solution to Eqs.(2.34) is too unwieldy, so at first assuming that $\boldsymbol{\eta_0=\eta_1=\eta_2=0}$ and yield [25,26]

$$\mathbf{C_0(q_n x)}=\frac{\mathbf{I}}{\mathbf{2\sqrt{1+4q^2}}}\left[\left(\mathbf{-2q^2+P^2}\right)\mathbf{cos}\left(\frac{\mathbf{S\,q_n x}}{\sqrt{\mathbf{2}}}\right)+\left(\mathbf{2q^2-S^2}\right)\mathbf{cos}\left(\frac{\mathbf{P\,q_n x}}{\sqrt{\mathbf{2}}}\right)\right], \tag{4.102}$$

$$\mathbf{C_1(q_n x)}= =\frac{\mathbf{I}}{\mathbf{2q\sqrt{2(1+4q^2)}}}\left[\mathbf{P}\left(\mathbf{2q^2-S^2}\right)\mathbf{sin}\left(\frac{\mathbf{S\,q_n x}}{\sqrt{\mathbf{2}}}\right)+\mathbf{S}\left(\mathbf{-2q^2+P^2}\right)\mathbf{sin}\left(\frac{\mathbf{P\,q_n x}}{\sqrt{\mathbf{2}}}\right)\right]. \tag{4.103}$$

$$\mathbf{C_2(q_n x)}=\frac{\mathbf{qI}}{\sqrt{\mathbf{1+4q^2}}}\left[\mathbf{cos}\left(\frac{\mathbf{S\,q_n x}}{\sqrt{\mathbf{2}}}\right)-\mathbf{cos}\left(\frac{\mathbf{P\,q_n x}}{\sqrt{\mathbf{2}}}\right)\right], \tag{4.104}$$

$$\mathbf{C_3(q_n x)}=\frac{\mathbf{I}}{\sqrt{\mathbf{2(1+4q^2)}}}\left[\mathbf{P\,sin}\left(\frac{\mathbf{S\,q_n x}}{\sqrt{\mathbf{2}}}\right)-\mathbf{S\,sin}\left(\frac{\mathbf{P\,q_n x}}{\sqrt{\mathbf{2}}}\right)\right], \tag{4.105}$$

where $\mathbf{P}=\sqrt{\mathbf{1+2q^2}+\sqrt{\mathbf{1+4q^2}}}$ and $\mathbf{S}=\sqrt{\mathbf{1+2q^2}-\sqrt{\mathbf{1+4q^2}}}$. As follows from Eqs.(4.102) – (4.105), the light intensities $\mathbf{|C_p(x)|^2}$ are periodic in the coordinate $\mathbf{x}$, so such values $\mathbf{x_n\neq 0}$ exist that $\left|\mathbf{C_0(x_n)}\right|^2=\mathbf{I^2}$, $\mathbf{C_{1,2,3}(x_n)=0}$ with $\mathbf{n=1,2,}\ldots$. Thus, when $\mathbf{x=x_n}$, the intensities in a triplet of the scattered light waves become zero outside the area occupied by the acoustic wave, i.e. the phenomenon of localization appears for the above listed optical scattered components. Inside that area, the spatial distributions of the scattered light waves

contain a number of peaks and holes, and simultaneously the corresponding distribution of the incident light wave has holes or peaks at the same spatial positions. Equations (4.102) – (4.105) give an opportunity to search for completely localized distributions of the scattered optical components with $\eta_0 = \eta_1 = \eta_2 = 0$, i.e. exact phase synchronism. Broadly speaking, this problem can be formulated in various ways, and considering here the simplest case. One can assume that the completely localized distributions are associated with the relations $C_0(q_n L) = \pm I$, while $C_1(q_n L) = C_2(q_n L) = C_3(q_n L) = 0$ where $L \in \{x_n\}$ is the spatial length of localization. Lets start with Eq.(4.104) that is the simplest one in a set. The relation $C_2(q_n L) = 0$ leads to $\cos(S q_n x/\sqrt{2}) = \cos(P q_n x/\sqrt{2})$, but the obvious analysis shows that only the case of $\cos(S q_n x/\sqrt{2}) = \cos(P q_n x/\sqrt{2}) = \pm 1$ gives an opportunity to keep a freedom in determining both the parameters P and S as well as the length L. The last formula provides the existence of all the above-listed localized distributions and converts the associated relations into trivial equalities. That is why one arrives at two triplets of the localization conditions. The first one is given by $q_n L = 2\sqrt{2}\pi k/S = 2\sqrt{2}\pi m/P$, where k and m are the whole numbers; $m > k$, because $P > S$. If $k = 0$, yields $m = 0$ and $q_n L = 0$ that is trivial. So, we put $k \neq 0$ and using the parameters P and S obtain the formula

$$m\sqrt{1+2q^2-\sqrt{1+4q^2}} = k\sqrt{1+2q^2+\sqrt{1+4q^2}}\ , \qquad (4.106)$$

correlating the whole numbers k and m and the parameter q in the first triplet. The second triplet can be written as $q_n L = \sqrt{2}(\pi + 2\pi k)/S = \sqrt{2}(\pi + 2\pi m)/P$. Here, $m > k$ as well, but the value of $k = 0$ is now acceptable. The interrelation between the whole numbers k and m and the parameter q is given now by [25,26]

$$(1+2m)\sqrt{1+2q^2-\sqrt{1+4q^2}} = (1+2k)\sqrt{1+2q^2+\sqrt{1+4q^2}}\ . \qquad (4.107)$$

Figures 4.11 [25,26] reflect Eqs.(4.106) and (4.107), and depict various interplays between the whole number **m** and the parameter **q** for a set of the whole numbers **k**. The solutions to Eqs.(4.106) and (4.107) are presented by intersections of the curves with the fixed numbers **k** and the horizontal lines with the fixed numbers **m**. Some intersections lead to the same solutions with different values $\mathbf{q_n L}$, so the minimal value of $\mathbf{q_n L}$ will be realized in such cases. These results make it possible to conclude that spatial Bragg solitary waves in the form of five-wave weakly coupled acousto-optical states exist under the localization conditions on a discrete totality of points in a three-dimensional $(\mathbf{k}, \mathbf{m}, \mathbf{q})$-space.

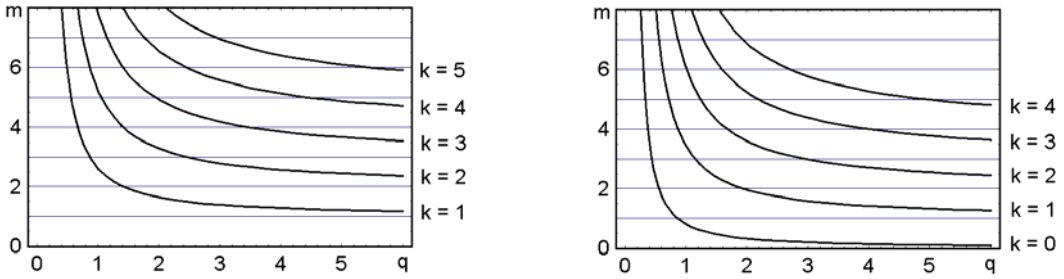

a. b.

Fig. 4.11 Graphical interpretation of the localization conditions: a) for Eq.(4.106), b) for Eq.(4.107).

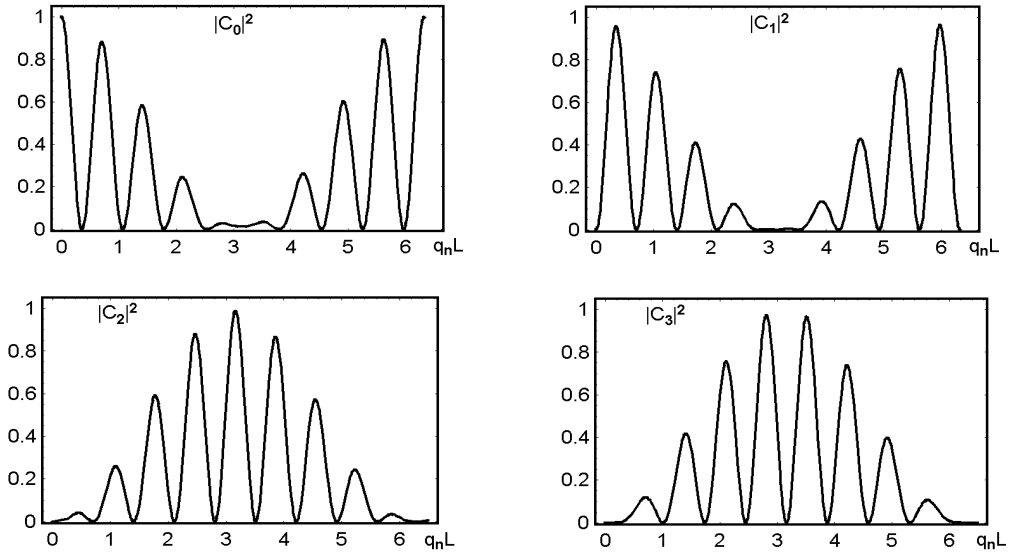

Fig.4.12. Exactly localized distributions for the intensities $\mathbf{|C_p\,(x)|^2}$ of optical components inherent in a multi-pulse weakly coupled state with $\mathbf{q = 4.44}$ for a TeO_2-crystal on $\mathbf{q_n L \in [\,0,\, 2\pi\,]}$.

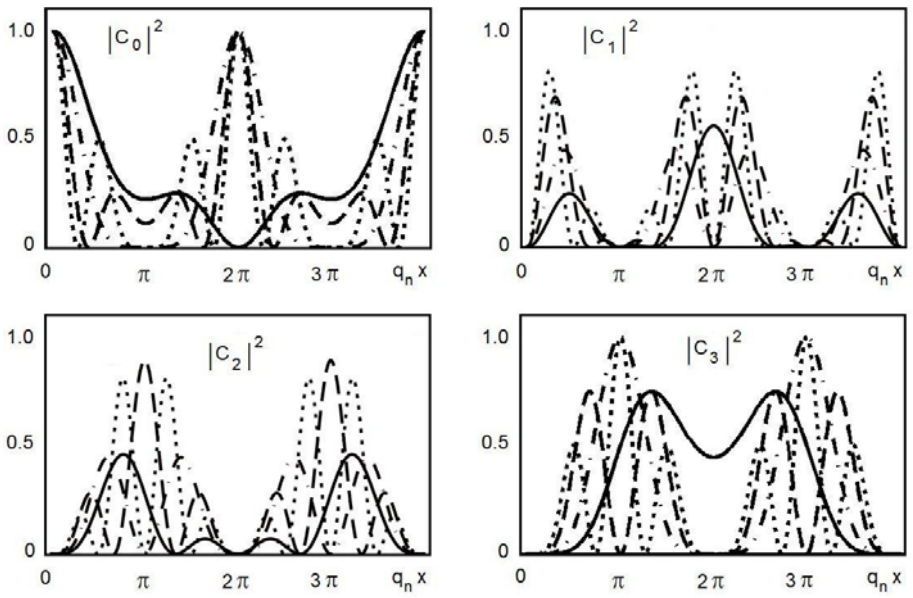

Fig.4.13 Distributions for the optical components: the doted lines are for **q = 1.936**, the dashed lines are for **q = 1.414**, the dot-dashed lines are for **q = 0.866**, and the solid lines are for **q = 0.559**.

The exactly localized distributions for the light intensities $|C_p(x)|^2$ of optical components inherent in the system, described by a set of Eqs.(4.102)-(4.105) with various values of the parameter q on the interval $q_n x \in [0, 4\pi]$, are shown in Fig.4.13 [25,26,27]. These plots represent multi-pulse dark solitary waves in zero order together with bright ones in the first, second, and third orders of scattering.

4.4.2 Five-wave non-collinear weakly coupled acousto-optical states in a TeO_2-crystal

Now taking into account the mismatches, assume the precise angular alignment of a cell, and extend η_0, η_1, and η_2 into a power series only in terms of the frequency detuning $\Delta f = |f - f_0|$ for the current frequency f relative to the frequency f_0 of exact synchronism. In the first approximation on Δf the wave vectors diagram, shown in Fig.2.3d of Chapter 2, gives us $\eta_0 = \pi \lambda f_0 \, \Delta f (n_0 V^2)^{-1}$, $\eta_1 \approx -3\eta_0$, and $\eta_2 \approx -7\eta_0$. For this approximation one

can exploit only the one parameter η_0 for estimating the mismatching effect in the form of the frequency detuning Δf.

An illustrative example of numerical simulations related to spatial-frequency distributions for the intensities of all optical components inside a rectangular acoustic pulse in the regime of a four-order light scattering is presented in Fig.4.14 for the case of $q = 4.5$.

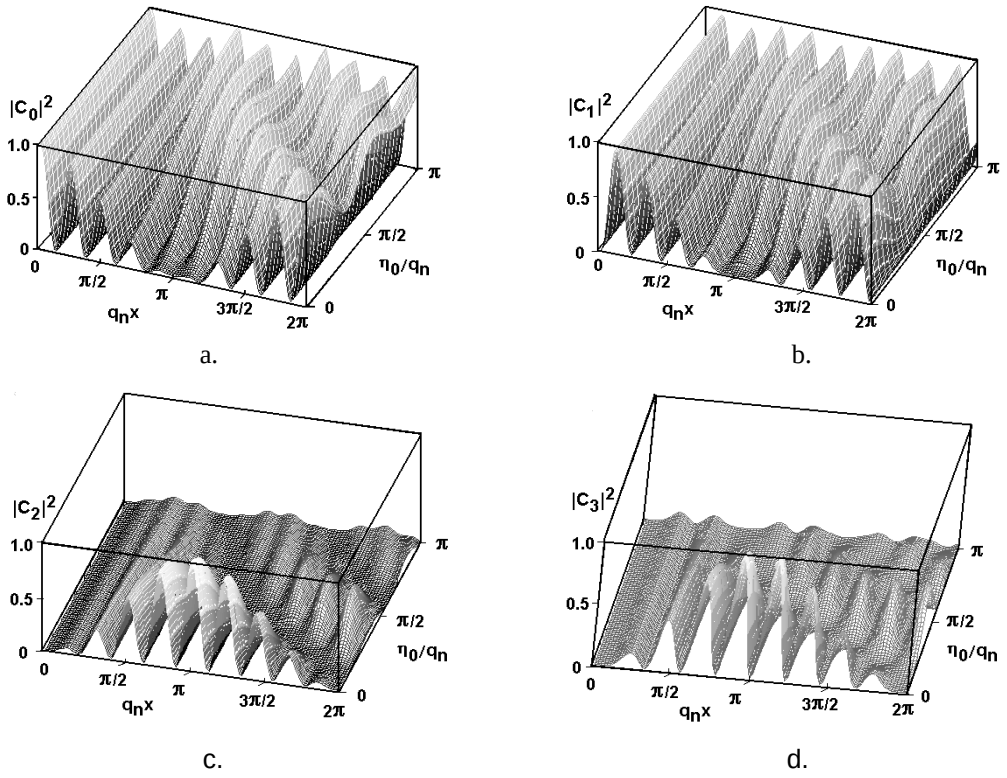

Fig.4.14. Spatial-frequency distributions for a quartet of optical components in a multi-pulse five-wave weakly coupled state with $q = 4.5$, $l = 1$, and $q_n L \le 2\pi$: an eight-pulse component in the zero order of scattering (a), a nine-pulse component in the first and the second orders (b) and (c), an eight-pulse component in the third order (d). The distributions (b), (c), and (d) are completely locked with $\eta_0 = 0$.

It is seen that initially, with $\eta_0 = 0$, well-localized and uniform distributions become to be broken due to growing the mismatch η_0, i.e. the detuning Δf, or converted into the other multi-wave states of localization.

4.4.3 Experimental data

A schematic arrangement of the experiment was quite similar to the set-up presented in [2], but in a four-order regime of light scattering, or to the scheme for optical data processing [18]. Our set-up includes a continuous-wave wide aperture laser beam, a non-collinear crystalline cell, and the CCD linear array. Its optical layout is shown in Fig.4.15.

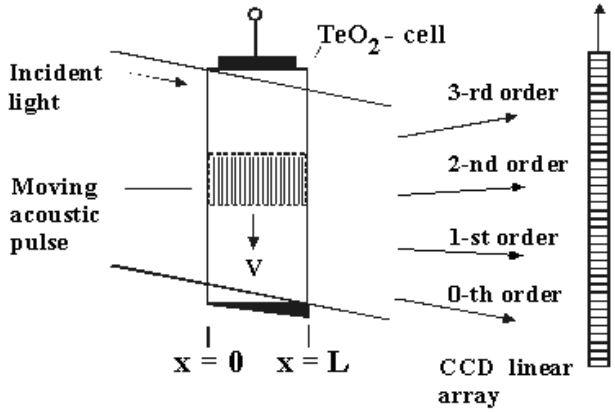

Fig.4.15. Schematic arrangement of the optical layout for the experimental set up.

The incident light beam was precisely oriented at the Bragg angle relative to the acoustic beam to minimize the influence of angular mismatches and thereby to provide just electronic control over measuring contributions of the frequency detuning. Observation of optical components inherent in stationary five-wave weakly coupled acousto-optical states has been carried out with experiments using a TeO_2 crystal cell oriented along the **[001]** and **[110]-**axis respectively as shown in Fig.2.3d, ($\mathbf{f_0 =}$ 57.8 MHz, **V =** 0.616 mm/μs [17]) and λ **=** 0.442 μm.

The Bragg scattering of circularly polarized light, resulting the maximal efficiency of acousto-optical interaction, was performed without any effect on the acoustic wave that provides the regime of weak coupling. The incident light power from a He-Cd-laser was about 20 mW, while the acoustic beam power was in excess of 4W. The intensities of the optical components peculiar to five-wave coupled states

have been measured as the functions of the product $\mathbf{q_n x}$ and the frequency detuning $\Delta\mathbf{f}$ on the first interval of localization ($\mathbf{n = 1}$).

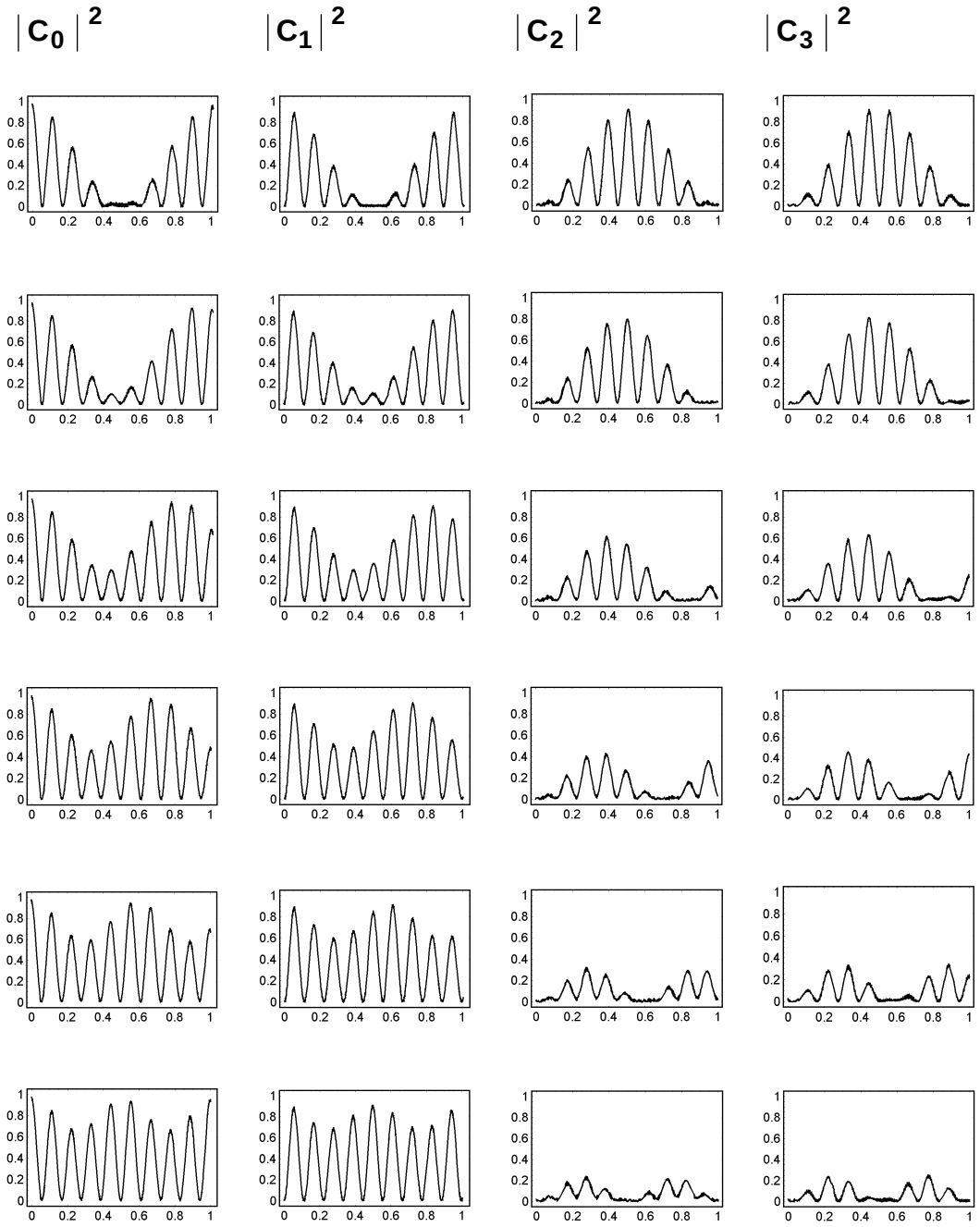

Fig.4.16. The digitized oscilloscope traces for the intensities $|C_P|^2$ of the optical components in a five-wave coupled state versus the product $\mathbf{q_n x}$ at various values of the frequency detuning $\Delta\mathbf{f}$. The magnitude of $\Delta\mathbf{f}$ is increasing from zero for the upper raw through the intermediate values 0.40, 0.75, 1.15, and 1.5 MHz to 2 MHz for the bottom one.

Figure 4.16 present the corresponding digitized oscilloscope traces [27]. Because the length of acousto-optical interaction was constant (**L =** 1.1 cm), the power density of acoustic wave was varied due to varying the applied acoustic power to control the product $\mathbf{q_n x}$.

4.5 Conclusions

- An opportunity of creating three-wave dissipative coupled states during the process of a strong co-directional collinear acousto-optical interaction between two optical modes and the suffering losses acoustic pulses in a square-law nonlinear crystal has been preliminary theoretically investigated.
- Both stationary and non-stationary analytic models for describing the localization processes for multi-pulse dissipative three-wave weakly coupled states have been elaborated, and the results of the experiments in a calcium molybdate crystalline acousto-optical waveguide have been presented and discussed.
- The five-wave Bragg weakly coupled states, occurring with a four-order non-collinear scattering of light by acoustic wave in an optically anisotropic tellurium dioxide crystal have recognized.
- The analysis which makes possible to describe originating five-wave Bragg weakly coupled acousto-optical states via the formulation of the localization conditions for multi-pulse states in the case of an exact phase synchronism have been performed.
- Theoretically predicted existence of stationary five-wave weakly coupled acousto-optical states has been experimentally observed.
- This type of multi-pulse solitary waves has been successfully shaped and identified in a non-collinear acousto-optical cell made of a tellurium dioxide single crystal.

References

1. Yu.S.Kivshar and G.P.Agrawal. *Optical Solitons. From Fibers to Photonic Crystals.* (Academic Press, New-York. 2003).
2. A.S.Shcherbakov and A.Aguirre Lopez. “Shaping the optical components of solitary three-wave weakly coupled states in a two-mode wave-guide.” Optics Express, Vol.11, p.1643-1649 (2003).
3. A.S.Shcherbakov and A.Aguirre Lopez. “Binary encoded modulation of light based on collinear three-wave acousto-optical coupled states.” Journal of Optics A: Pure and Applied Optics. Vol.5, 471-477 (2003).
4. A.S.Shcherbakov and A.Aguirre Lopez. “Observation of the optical components inherent in multi-wave non-collinear acousto-optical coupled states.” Optics Express Vol.10, 1398-1403 (2002), http://www.opticsexpress.org/abstract.cfm?URI=OPEX-10-24-1398
5. A.P.Sukhorukov. “Nonlinear Wave Interactions in Optics and Radiophysics”. (Nauka Press, Moscow. 1988).
6. A.S.Shcherbakov. *A three-wave interaction. Stationary coupled states*. (St.Petersburg State Technical University Press, St.Petersburg. 1998).
7. R.K.Dodd, J.C.Eilbeck, J.D.Gibbon, and H.C.Morris. *Solitons and Nonlinear Wave Equations*. (Academic Press, Orlando. 1984).
8. **A.S.Shcherbakov, Je.Maximov, E.Tepichin Rodriguez, S.E.Balderas Mata. “Optically pumped three-wave coupled states in a waveguide with a square-law nonlinearity and losses”, Proc. SPIE, Vol.6725, 6725-19 – 6725-29 (2007).**
9. **A.S.Shcherbakov, Je.Maximov, E.Tepichin Rodriguez, and S.E.Balderas Mata, “Collinear three-wave acousto-optical coupled states in a medium with a square-law nonlinearity and losses”, in Nonlinear Photonics, OSA Technical Digest (Optical Society of America, 2007), paper JMD24.**

10. A.S.Shcherbakov, Je.Maximov, and S.E.Balderas Mata, "Shaping the dissipative collinear three-wave coupled states in a two-mode medium with a square-law nonlinearity and linear acoustic losses", J. Opt. A: Pure Appl. Opt. Vol.10, 025001 (2008).

11. V.P.Ermakov. "Second-order differential equations; integrability conditions in the closed form." Universitetskie Izvestiya [in Russian]. Kiev. no.9, 1-25 (1880).

12. A.D.Polyanin and V.F.Zaitsev. *Handbook of Exact Solutions for Ordinary Differential Equations.* 2nd Ed. (Chapman & Hall/CRC, Boca Raton, 2003).

13. R.W.Dixon, "Acoustic diffraction of light in anisotropic media". IEEE Journal of Quantum Electronics, Vol.QE-3, 85-93 (1967).

14. V.I.Balakshy, V.N.Parygin, L.E.Chirkov. *Physical Principles of Acousto-Optics.* (Radio i Svyaz. Moscow. 1985).

15. Yu.I.Sirotin and M.P.Shaskolskaya. *Fundamentals of Crystal Physics.* (Mir Publishers. Moscow. 1982).

16. D.A. Pinnow, "Guidelines for the selection of acousto-optic materials", IEEE Journal of Quantum Electronics, Vol.QE-6, 223-38 (1970).

17. V.G.Dmitriev, G.G.Gurzadyan, and D.N.Nikogosyan. *Handbook of nonlinear optical crystals.* (Springer-Verlag,New-York, 1999).

18. F.T.S.Yu. *Introduction to Information Optics.* (Academic Press, San Diego, 2001).

19. M.B.Vinogradova, O.V.Rudenko, and A.P.Sukhorukov. *Theory of Waves.* (Nauka, Moscow, 1979).

20. A.S.Shcherbakov, S.E.Balderas Mata, Je.Maximov. "Three-wave collinear acousto-optical coupled states in a crystal with a square-law nonlinearity and losses". Proc. SPIE, Vol. 6729 (2007)

21. A.S.Shcherbakov, Je.Maximov, and S.E.Balderas Mata, "Collinear acousto-optical three-wave solitary states in a two-mode medium with a square-law nonlinearity and losses", Proc. SPIE, Vol.6875 (2008).

22. G.L.Lamb. *Elements of Soliton Theory.* (John Wiley & Sons, New-York, 1980).

23. E. Kamke, *Differentialgleichungen. Losungsmethoden und Losungen*, Part 1: Gewohnliche Differentialgleichungen (Leipzig, 1959).

24. A.Korpel. *Acousto-optics.* (Marcell Dekker, New-York, 1997).

25. A.S.Scherbakov, S.E.Balderas Mata, Je.Maximov. "Shaping five-wave non-collinear weakly coupled acousto-optical states in a TeO_2 single crystal", Proc. SPIE, Vol.6729 (2007).

26. A.S.Shcherbakov, A.Aguirre Lopez, and S.E.Balderas Mata, "Revealing non-collinear five-wave Bragg coupled states and studying their multi-pulse optical components in crystals", in Nonlinear Photonics, OSA Technical Digest (Optical Society of America, 2007), paper JMD18.

27. A.S.Shcherbakov, S.E.Balderas Mata, Je.Maximov, and A.Aguirre Lopez, "The existance of five-wave non-collinear acousto-optical weakly coupled states", J. Opt. A: Pure Appl. Opt. Vol.10, 085106 (2008).

General conclusions

Estimations of the bandwidth for one- two- and three-phonon interactions have been performed and they have been experimentally compared.

The combined influence of both the geometric limitations and the acoustic attenuation on the number of resolvable elements for the regime of a one-phonon anomalous light scattering and for two-phonon has been created for the first time.

Gaussian apodization as well as the acoustic attenuation factor in connection with the dynamic range of the acousto-optical cell have been studied.

The theoretical analysis of three-wave collinear acousto-optical coupled states in a medium with acoustic losses under localization conditions has been studied for the first time.

The existence of Bragg solitary waves in the form of five-wave non-collinear coupled states under localization conditions is analytically and experimentally demonstrated.

FIGURE INDEX

Chapter 1

Fig.1.1. Bragg interaction geometry. 19

Fig.1.2. Wave vector diagram for Bragg interaction: a) frequency upshifted, b) frequency downshifted. 20

Fig.1.3. Wave vector surfaces and wave vector diagrams inherent in a one-fold (a), two-fold (b), and three-fold scattering of a photon by acoustic phonons in a single-axis crystal. 23

Fig.1.4. General arrangement of optical beams in a two-phonon (a) and three-phonon (b) processes of light scattering; light arrows show the corresponding acoustic waves passing through crystals from the piezo-electric transducers to the absorbers. 23

Fig.1.5. Anisotropic interaction in positive uniaxial crystal. a) Shear wave along optical axis, light wave in **xy** plane, b) all waves in **xy** plane. 24

Fig.1.6. a) Collinear coupling between a **z**-polarized and a **y**-polarized optical beams by a shear acoustic, b) collinear phase matching in a birefringent crystal 26

Fig.1.7. Basic acousto-optic spectrum analyzer. 32

Chapter 2

Fig.2.1 General diagram of originating the orders of scattering governed by Eq.(2.8) with $\mathbf{C(0) = (0, 0, \ldots, 0, 1, 0, \ldots, 0)}$. 45

Fig.2.2. Diagram of originating the scattered orders governed by Eq.(2.8) in the regime of a one-phonon light scattering with $\mathbf{C(0) = (1, 0)}$. 45

Fig.2.3. Feasible geometries of the acousto-optical interaction in a tellurium dioxide single crystal: normal (a) and anomalous, (b) one-phonon regime; a two-phonon regime (c), and a three-phonon regime (d). 47

Fig.2.4. Diagrams of originating the scattered orders, Eq.(2.8): (a) two-phonon light scattering regime with $\mathbf{C(0) = (1, 0, 0)}$; b) three-phonon light scattering regime with $\mathbf{C(0) = (1, 0, 0, 0)}$. 48

Fig.2.5. Intensity distributions: (a) one-phonon light scattering regime with $q = \sqrt{q_0\, q_1}$ (dot-dashed line for $|C_0(qx)|^2$ and solid line for $|C_1(qx)|^2$); (b) a two-phonon light scattering regime (dot-dashed line for $|C_0(q_0 x)|^2$, dashed line for $|C_1(q_0 x)|^2$, and solid line for $|C_2(q_0 x)|^2$). 49

Fig.2.6. A three-dimensional distribution (a) for $|C_2(qx, \eta_1 x)|^2$ and the cross-section of that distribution at $qx = \pi/\sqrt{2}$ (b). 53

Fig.2.7. Distributions of the light intensity $|C_3(x)|^2$ vs. $q_n x$: dashed line: **q = 0.559**, solid line: **q = 0.866**, dotted line: **q = 1.414**, and dot-dashed line: **q = 1.936.** 55

Fig.2.8. Distributions of the light intensities with a three-phonon light scattering vs. $q_n x$: (a) **q = 0.866**, and (b) **q = 1.936**. Dot-dashed lines for $|C_0(x)|^2$; dashed lines for $|C_1(x)|^2$; dotted lines for $|C_2(x)|^2$; and solid lines for $|C_3(x)|^2$. 55

Fig.2.9. (a) Distribution of the light intensity $|C_3(x)|^2$ vs. $q_n x$ with **q = 4.44**; (b) dependence of $|C_3(x)|^2$ on $\eta_0 x$ with $q_n x = 2.82$. 58

Fig.2.10. Two cross-sections of the refractive index surfaces inherent in a tellurium dioxide crystal: (a) hypothetic plot without the effect of optical activity; (b) illustration to the effect of optical activity. 61

Fig.2.11. The ellipticity ρ of polarization of the light waves vs. the angle ϑ of a tip from the **[001]**-axis in a TeO_2-crystal. 63

Fig.2.12. A wide-band geometry for the anomalous regime of light scattering in a TeO_2-crystal. 63

Fig.2.13. Squared moduli of the normalized effective photo-elastic constants (a) $|p^*_{eff}(i \to i)|$, (b) $|p^*_{eff}(i \to j)|$ versus the ellipticity ρ_i of the polarization of an external light beam as well as the rotation angle ϕ, and (c) the moduli of the normalized effective 69

photo-elastic constants $\left|\tilde{p}_{eff}(i \to i)\right|$ and $\left|\tilde{p}_{eff}(i \to j)\right|$ versus the ellipticity ρ of the eigen states of polarization in a TeO_2-crystal.

Fig.2.14. General schematic arrangement for measuring the frequency bandwidths of a TeO2-modulator in various regimes of multi-phonon light scattering. 74

Fig.2.15. The intensity-frequency distributions for a one-phonon (a), two-phonon (b), and three-phonon (c) light scattering processes in tellurium dioxide single crystal. 74

Fig.2.16. Schematic arrangement to measure the intensity profile of an individual spot. 76

Fig.2.17. The intensity distributions of an individual spot in focal plane of the integrating lens for a two-phonon light scattering in a TeO_2 acousto-optical modulator: (a) experimental plot, (b) numerical simulation. 77

Chapter 3

Fig.3.1 Schematic arrangement for the implementation of an acousto-optical spectrum analyzer. 81

Fig.3.2. Diagram of the interaction of a light beam passing through a prism. 82

Fig.3.3. The light beam passing through a glass prism: (a) $\mathbf{m=1}$, (b) $\mathbf{m=2}$. 84

Fig.3.4. Linear expanding factor $\mathbf{B_m}$ for $\mathbf{m}$ prisms with $\mathbf{n=1.5}$ and $\alpha = \mathbf{30^0}$. 85

Fig.3.5. Comparison of the transmissions inherent in one glass prism with $\mathbf{n=1.5}$ and $\alpha = \mathbf{30^0}$ for two states of light polarization. 89

Fig.3.6. The combined diagram illustrating the beam expanding and the transmission in glass prism shapers with $\mathbf{m=\{1,2,4\}}$, $\mathbf{n=1.5}$, and $\alpha = \mathbf{30^0}$. 89

Fig.3.7. Diagrams illustration the effect of varying the prism top angle α: (a) $\mathbf{m=2}$, and (b) $\mathbf{m=4}$. 90

Fig.3.8. Scheme to perform the Fourier transform with a thick positive lens, which is illuminated by a plane wave. 91

Fig.3.9. Side view of a thick lens and how it is possible to split it in three parts. 92

Fig.3.10. Calculation of the thickness function. Geometry for Δ_1 and Δ_3. 93

Fig.3.11. Vector diagram for a one-phonon light scattering, being non-degenerated by a two-phonon process, in a tellurium dioxide crystal. 96

Fig.3.12. The combined diagram illustrating effect of a triplet of the restricting factors. Solid slowly growing lines are for $\mathbf{N_1}$ with **D = 1, 2, 3,** and **4** cm. Dashed line are for $\mathbf{N_2}$ with **Q = 2** π. Solid hyperbolic-like falling curves illustrate $\mathbf{N_3}$ and reflect contributions of the acoustic attenuation; **B = 3, 4**, and **6** dB along the aperture. 99

Fig.3.13. Combined diagram illustrating the effect of a triplet of the restricting factors. Solid straight lines for $\mathbf{N_1}$**, D = 1, 2, 3,** and **4** cm. Dashed line for $\mathbf{N_2}$ with **Q = 4** π. Solid hyperbolic-like for $\mathbf{N_3}$ and **B = 3, 4,** and **6** dB along the aperture. 103

Fig.3.14. The profiles of transfer functions: solid line is for a two-phonon light scattering, dashed line for a one phonon regime is presented for a comparison. 106

Fig.3.15. Optical scheme for scattering light by a thick dynamic acoustic grating (a) and the corresponding light intensity distributions (b). 107

Fig.3.16. Effect of acoustic attenuation: (a) normalized light intensity in the focal spot; solid line, $\alpha = \mathbf{0}$ dB/cm, dashed line, $\alpha = \mathbf{3}$ dB/cm, dash-dotted line, $\alpha = \mathbf{6}$ dB/cm, and dotted line, $\alpha = \mathbf{10}$ dB/cm; (b) light intensity in a maximum of the focal spot as a function of $\alpha\mathbf{D}$. 109

Fig.3.17. Optical arrangement of lighting the acousto-optical cell (a) and a role of the parameter β (b). 112

Fig. 3.18. Available optical powers. 114

Fig. 3.19. Light intensity plots for: $\beta = \mathbf{0}$ (dashed line), $\beta = \mathbf{2}$ (dotted line), and $\beta = \mathbf{10}$ (solid line). 114

Fig.3.20. A three-dimensional plot of the lobes illustrating the tendency of dominating the second lobe. 115

Fig.3.21. Estimations for the maximal side lobe and spot's width with varying β; the level of the side lobes is measured relative to the maximal intensity of the main lobe. 115

Fig.3.22. Level of the maximal side lobe relative to the maximum intensity of the main lobe. 116

Fig.3.23. Broadening of a resolvable spot at the intensity level of half a-maximum of the main lobe. 116

Fig.3.24. Combined effects of the incident light apodization and the acoustic attenuation on the normalized light intensity in the focal plane: (a) and (b) are for $\beta = 0$, (c) and (d) for $\beta = 2$, (e) and (f) for $\beta = 6$. Then, everywhere, solid lines for $\alpha_0 = 0$, dashed lines for $\alpha_0 = 3$ dB, dashed-dotted lines for $\alpha_0 = 6$ dB, and dotted lines for $\alpha_0 = 10$ dB. 118

Fig.3.25. The general plot of the first side lobe inherent in an individual resolvable spot in a Fourier plane (a) and maximal levels of the first side lobe versus the apodization parameter β (b), solid line for $\alpha_0 = 0$, dashed line for $\alpha_0 = 3$ dB, dashed-dotted line for $\alpha_0 = 6$ dB, and dotted line for $\alpha_0 = 10$ dB. 119

Chapter 4

Fig.4.1. Restricting the number $\mathbf{N}$ of pulses in a coupled state in the case of $\eta = 0$ and $\alpha \neq 0$; for the taken example of $\alpha = 0.1$ and $\sigma = 1$, one can find $N \leq 3$. 130

Fig.4.2. The possibility of shaping multi-pulse coupled states when $\eta \neq 0$ and $\alpha \neq 0$; i.e., $\alpha = 0.1$ and $\sigma = 1$, one can realize: a) $N = 1$, b) $N = 2$, c) $N = 3$, and d) $N = 5$. 131

Fig.4.3. Plots for $b_2(x, \eta = 0)$ with $\sigma = 1$, $\alpha = 0.1$, and $G_2 = 1$: a) $H_2 = 1$, $\Gamma^2 U_0^2 = 1$, (solid line for b_2, dotted line for the frequency γ); b) $H_2 = 1$, $\Gamma^2 U_0^2 = 0$; c) $H_2 = 0$, $\Gamma^2 U_0^2 = 0$. 136

Fig.4.4. Intensity of the scattered light components vs. τ and L with $\sigma = 2$ and $\alpha = 0.05$. Four stages of reshaping are simulated: a) $\eta = 1.5$, the beginning of shaping a one-pulse coupled stated; b) $\eta = 2.4$, a one-pulse coupled stated; c) $\eta = 3.5$, an intermediate stage; and d) $\eta = 6.0$, a two-pulse coupled state. 138

Fig.4.5. Schematic arrangement of the experimental set-up. 143

Fig.4.6. Scheme of the co-propagating collinear calcium molybdate acousto-optical cell providing the traveling-wave regime of interaction of the pumping light beam with the acoustic pulses. 144

Fig.4.7. The digitized oscilloscope traces for $|C_1|^2$ in a CaMoO4-crystalline waveguide with $\alpha = 0.05$ cm^{-1} at a carrier acoustic frequency of 61.3 MHz. Four stages of reshaping are followed at the same optical pump and acoustic wave intensities and temporal scales: (a) $\eta = 1.5$ cm^{-1}, the beginning stage of shaping a one-pulse coupled stated; (b) $\eta = 2.4$ cm^{-1}, a one-pulse coupled stated; (c) $\eta = 3.5$ cm^{-1}, an intermediate stage; and (d) $\eta = 6.0$ cm^{-1}, a two-pulse coupled state. 145

Fig.4.8. Approximate solutions to Eq.(4.93): (a) the solutions $\varphi_{0,1,2}$; (b) effect of the parameter α on the localized part of solution; the contributions inherent in the partial solution of inhomogeneous equation for $\alpha = 0.05$ (c) and $\alpha = 0.01$ (d). 155

Fig.4.9. Approximate solutions to Eq.(4.86): (a) the solutions $\psi_{0,1,2}$; (b) effect of the parameter α on the localized part of solution; the contributions inherent in the partial solution of inhomogeneous equation for $\alpha = 0.05$ (c) and $\alpha = 0.01$ (d). 158

Fig.4.10. Approximate solutions to Eq.(4.95): (a) the solutions $\phi_{0,1,2}$; (b) effect of the parameter α on the localized part of solution; the contributions inherent in the partial solution of inhomogeneous equation for $\alpha = 0.05$ (c) and $\alpha = 0.01$ (d). 161

Fig.4.11. Graphical interpretation of the localization conditions: a) for Eq.(4.106), b) for Eq.(4.107). 165

Fig.4.12. Exactly localized distributions for the intensities $|C_p(x)|^2$ of optical components inherent in a multi-pulse weakly coupled state with **q = 4.44** for a TeO_2-crystalon the interval $q_n L \in [0, 2\pi]$. 165

Fig.4.13. Distributions for the optical components: the doted lines are for **q = 1.936**, the dashed lines are for **q = 1.414**, the dot-dashed lines are for **q = 0.866**, and the solid lines are for **q = 0.559**. 166

Fig.4.14. Spatial-frequency distributions for a quartet of optical components in a multi-pulse five-wave weakly coupled state with **q = 4.5**, **I = 1**, and $q_n L \leq 2\pi$: an eight-pulse component in the zero order of scattering (a), a nine-pulse component in the first and the second orders (b) and (c), an eight-pulse component in the third order (d). The distributions (b), (c), and (d) are completely locked with $\eta_0 = 0$. 167

Fig.4.15. Schematic arrangement of the optical layout for the experimental set up. 168

Fig.4.16. The digitized oscilloscope traces for the intensities $|C_P|^2$ of the optical components in a five-wave coupled state versus the product $q_n x$ at various values of the frequency detuning Δf. The magnitude of Δf is increasing from zero for the upper raw through the intermediate values 0.40, 0.75, 1.15, and 1.5 MHz to 2 MHz for the bottom one. 169

TABLE INDEX

Chapter 1

Table I. Summary of features of different types of spectrometers used for radio-astronomy 35